Serotonergic circuits: Role in sleep and enhanced genetic tools for access and optical recording

Thesis by

Michael Altermatt

In Partial Fulfillment of the Requirements for

the degree of

Doctor of Philosophy

CALIFORNIA INSTITUTE OF TECHNOLOGY

Pasadena, California

2021

(Defended December 16, 2020)

Michael Altermatt
ORCID: 0000-0003-2841-5374

ACKNOWLEDGEMENTS

Caltech has been an incredibly inspiring place to work at and has had an enormous impact on the way I think about science and life in general. The memory of my first day on campus during the Neurobiology recruitment event is still very vivid. The harmonious blend of beautiful gardens and ancient buildings, the intense conversations about the ongoing innovative research, and the amazing bright people from all around the world made me immediately want to leave my country to pursue my graduate studies here. I will deeply miss the feeling of being part of this small scientific community of diverse people from different backgrounds, who share a deep passion for science and come together to relentlessly push the boundaries of knowledge.

When I joined Dr. Viviana Gradinaru's lab, I decided to take on a systems neuroscience project aiming to understand the role of a certain peptide in sleep. Having never been exposed to research involving animal behavior, I had no idea what I was getting myself into, and I was about to learn the difficulties of it. The project heavily relied on a transgenic mouse line that still had to be imported from New Zealand. Due to several unfortunate events, I could not conduct experiments with these animals until one year after I officially joined the lab. Moreover, the outcome of these experiments was sobering to say the least and we quickly realized that the project was not worth pursuing any further. All experiments performed over the course of my first year in preparation for the arrival of the animals did not bring me any closer to graduating. But Viviana has a unique gift of making you see such experiences in a positive light, lifting your spirits even though everything seems lost and making you persevere. I am most grateful for her clear and reassuring guidance over the years through several (more successful) subsequent projects and collaborations. I have great respect and admiration for her mentoring style which is tailored to the personal goals of each individual graduate student. She was most supportive of my decision to change my direction of research from a behavior-focused systems neuroscience project to an AAV-related project due to changes in my personal future plans. Viviana was also instrumental in paving the way to find an excellent position for my time after graduation. Words cannot do justice to how grateful I am for the opportunities that are open to me now due to her mentoring and training over the past years.

I would like to thank my committee members Dr. David Prober, Dr. David Anderson, and Dr. Elizabeth Hong for their time, critical feedback, and advice given during meetings. Furthermore, I am incredibly grateful for Dr. David Anderson's devotion to teaching in his class on genetic dissection of neural circuit function, which was crucial in developing my skills of critically evaluating scientific publications.

I am grateful to Dr. David Prober and his postdoc, Dr. Grigorios Oikonomou for their support throughout our collaboration on the project investigating the role of the serotonergic system in sleep. Dr. David Prober's advice on experiments and his inputs during the manuscript writing process were invaluable and helped me grow as a researcher. In particular, I would like to acknowledge Dr. Grigorios Oikonomou. I could not have wished for a better colleague. Your friendly nature and uplifting spirit were pivotal for keeping me motivated

through the rough patches. All these nights in the animal facility conducting (and subjecting myself to) sleep deprivation experiments will hopefully soon be forgotten, but I will hold on to the many joyful memories of conversations with you about conceiving more such experiments and the confusing serotonin literature.

I would also like to thank Dr. Lin Tian and her postdoc, Dr. Elizabeth Unger for giving me the opportunity of being part of the team bringing forward iSeroSnFR. This project taught me much on the benefits and challenges of collaborating across many labs at distant geographical locations.

To my 10x teammates, David Brown and Tatyana Dobreva, it has been a thrill fighting with you in the trenches, both inside and outside the lab. I will forever be in awe of your creativity and out-of-the-box thinking.

I would also like to recognize Dr. Ryan Cho who as a graduate student a few years above me has been a great mentor throughout my graduate studies and taught me everything I needed to know before embarking on a mammalian sleep project. His passion for neuroscience is contagious and his devotion to basic sciences are remarkable. As someone who spends too much time in the lab, I envy most his unique skill of achieving so much while making it look like he barely works.

I am appreciative of the good times I had over the years with Elisha Mackey, Dr. Anat Kahan, Dr. Elliott Robinson, and Gerry Coughlin while sharing the same (way too narrow) aisle in the Alles office. I will miss our lunch time chats the most.

Dr. Máté Borsos, our projects in the lab barely overlapped and as a consequence we unfortunately started to interact rather late. Our adventures into the wild, although life-threatening at times, were one of my best moments here in California! I wish our paths had overlapped for longer.

Furthermore, I am deeply grateful for the general support of Elisha Mackey and Pat Anguiano throughout the years. My graduate experience would not have been nearly as good without your help.

Finally, I am thankful for other former and current lab members with whom I had the opportunity to interact and work with over the years: Dr. Nicholas Flytzanis, Dr. Nick Goedon, Dr. Claire Bedbrook, Dr. Alon Greenbaum, Dr. Ben Deverman, Dr. Priya Kumar, Dr. Min Jee Jang, Xiaozhe Ding, Xinhong Chen, Miggy Chuapoco, Acacia Hori, David Goertsen, Dr. Tim Miles, Dr. Ken Chan, Dr. Jennifer Treweek, Keith Beadle, Dr. Qin Huang, Yaping Lei, Dr. Zhe Qu, Damien Wolfe, Erin Sullivan, Nathan Appling, Dr. Collin Challis, Dr. Rose Challis, Dr. Rajib Schubert, Dr. Cheng Xiao, and Dr. Chunyi Zhou.

ABSTRACT

Overall, this thesis encompasses three main directions: the study of neural circuits in sleep (Chapter 2), the development and testing of tools for measuring neuromodulator release (Chapter 3), and methods for *in vivo* characterization of gene delivery vehicles (Chapter 5).

The role of the neuromodulator serotonin in sleep has been debated for over 60 years. Until recently, the serotonergic system was widely thought to be part of the arousal system and promote wakefulness. In Chapter 2, we investigate the function of serotonin-producing neurons in murine and zebrafish sleep with tools featuring superior specificity and precision compared to previously employed techniques. Our results demonstrate that the serotonergic raphe are sleep-promoting and required for sleep homeostasis. Intriguingly, serotonergic neurons in mice can have opposing effects on sleep depending on the firing mode.

The release of serotonin from neurons can be regulated by the frequency of neuronal firing and can occur at classical synapses, varicosities, soma, and dendrites. Further examination of the complex signaling mechanism of serotonin would benefit from tools capable of measuring the release of serotonin *in vivo* with long-term stability and high spatiotemporal resolution. To this end, we developed and characterized iSeroSnFR, an intensity-based genetically encoded serotonin indicator. In Chapter 3, we demonstrate that iSeroSnFR can detect serotonin release in freely behaving mice during fear conditioning, social interaction, and sleep-wake transitions.

Adeno-associated viruses (AAVs) have been extensively used as gene delivery vehicles in basic neuroscience and gene therapy. However, optimization of transduction efficiency and target specificity remain a key challenge to overcome. Several AAV vector engineering approaches have been devised for this purpose and yield large collections of candidates that require further *in vivo* characterization. However, conventional characterization methods fall short with regard to in-depth cell type tropism analysis and/or high-throughput capabilities. In Chapter 5, we address this shortcoming with single-cell RNA sequencing technologies based on the Drop-seq method. We established an experimental and computational pipeline that allows us to profile the viral tropism of multiple AAV variants in parallel across numerous complex cell types.

PUBLISHED CONTENT AND CONTRIBUTIONS

[1] Oikonomou, G.*, **Altermatt**, **M.*** et al. (2019). The serotonergic raphe promote sleep in zebrafish and mice. Neuron *103,* 686-701.e8. doi: 10.1016/j.neuron.2019.05.038.

M.A. designed and performed mouse experiments, analyzed mouse data, prepared figures, and wrote a significant portion of the manuscript as a co-first author.

[2] Unger, K.U.*, Keller, J.P.*, **Altermatt**, **M.*** et al. (2020). Directed evolution of a selective and sensitive serotonin sensor via machine learning. Cell *183,* 1986-2002.e26. doi: 10.1016/j.cell.2020.11.040.

M.A. participated in the conception and design of the study, performed and analyzed in vivo fiber photometry and EEG/EMG recordings in BLA and mPFC in fear learning and sleep-wake cycles, prepared figures, and provided significant input in the manuscript writing process.

*equal contribution

Published conference abstracts

[1] **Altermatt**, **M.** et al., (2020). In-depth parallel profiling of tissue and cell-type tropism of AAV variants by single-cell RNA sequencing. Molecular Therapy *28,* 1-592. doi: 10.1016/j.ymthe.2020.04.019.

M.A. gave oral presentation. M.A. co-designed, performed, and analyzed the data.

[2] Brown, D., **Altermatt**, **M.** et al. (2020). A computational and experimental platform for detecting full transcriptome cell type tropism of lowly expressed barcoded and pooled AAV variants via single-cell RNA sequencing. Molecular Therapy *28,* 1-592. doi: 10.1016/j.ymthe.2020.04.019.

M.A. co-designed, performed, and analyzed the data.

TABLE OF CONTENTS

C h a p t e r 1

INTRODUCTION

1.1 The neuromodulator serotonin

Neuromodulation

Animals need to constantly adjust their behavior to the demands of their internal and external environment, demands that emerge on various time scales. These behavioral adaptations arise from changes in the activity of neuronal cell groups in the central nervous system (CNS). Different neuronal circuits are being recruited for specific sets of behaviors, however, the same neuronal element can be active across multiple behaviors. For example, thalamocortical circuits display rhythmic oscillating activity during sleep, which is replaced by desynchronized activity at the transition to wakefulness. This shift in circuit activity is mediated by modulatory cholinergic and noradrenergic neurotransmitter systems (McCormick, 1989, 1992; McCormick and Bal, 1997). Such observations led to the view that the anatomical network of neuronal circuits provides the physical backbone, and neuromodulators recruit, reconfigure, or manipulate these circuits at any given time to produce the required behavioral output. Neuromodulators are chemicals exerting their action on neurons in various forms, such as by altering the strength of synapses between neurons (Dudel, 1965; Glusman and Kravitz, 1982; Kandel and Schwartz, 1982; Klein and Kandel, 1978; Klein et al., 1982), by manipulating the intracellular concentrations of second messengers, for example cyclic adenosine monophosphate (cAMP), which affects action potential waveforms and membrane currents (DeRiemer et al., 1985; Hockberger and Connor, 1984; Kaczmarek et al., 1986; Siegelbaum et al., 1982), or by increasing or decreasing the amplitude of voltage-dependent currents (Adams and Brown, 1980; Brown and Adams, 1980; Camardo et al., 1983; Dunlap and Fischbach, 1981).

Biosynthesis of serotonin

A central topic in Chapters 2 and 3 is the neuromodulator serotonin, a phylogenetically ancient signaling molecule (Hay-Schmidt, 2000). Serotonin was first described in the periphery (Rapport, 1949; Rapport et al., 1948; Vialli and Erspamer, 1937) where 95% of the total amount of this molecule is localized (Murphy et al., 2008). Its name is derived from this first description: source is serum and its activity is one of causing constriction. Later, it was discovered to be present in the

CNS (Amin et al., 1954; Twarog and Page, 1953), followed by the description of the anatomical location of serotonin-producing neurons in the lower brain stem (Dahlstroem and Fuxe, 1964). Approximately 26,000 serotonin-producing neurons are present in the mouse brain (Ishimura et al., 1988). During development, these neurons derive from embryonic precursors that produce the transcription factor PET1 (also referred to as FEV) upon terminal cell division (Hendricks et al., 1999). PET1 shapes the serotonergic identity of neurons by regulating the expression of genes required for serotonin biosynthesis, packaging in synaptic vesicles, reuptake, and metabolism (Hendricks et al., 2003; Krueger and Deneris, 2008; Liu et al., 2010; Wyler et al., 2015, 2016). Tryptophan hydroxylase (TPH) enzyme is the first-step and rate-limiting enzyme in the serotonin synthesis (Grahame-Smith, 1964; Jequier et al., 1969; Lovenberg et al., 1967). It hydroxylates L-tryptophan generating 5-hydroxy-L-tryptophan (5-HTP). TPH comes in two isoforms, TPH1 and TPH2. The raphe neurons of the adult brain use TPH2 (Alenina et al., 2009; Gutknecht et al., 2009; Walther and Bader, 2003, 2003). Once TPH2 hydroxylates L-tryptophan, 5-HTP is decarboxylated by aromatic L-amino-acid decarboxylase (AADC) to 5-hydroxytryptamine (5-HT) or serotonin (Walther et al., 2003). 5-HT is then concentrated in synaptic vesicles in neurons by the vesicular monoamine transporter (VMAT), which also exists in two different forms, VMAT2 and VMAT1; VMAT2 is the dominant isoform in the brain, while VMAT1 is essentially expressed in the periphery (Erickson et al., 1996). After 5-HT is being released into the extracellular medium, the 5-HT reuptake transporter (SERT) moves 5-HT across the plasma membrane back into neurons (Blakely et al., 1991; Hoffman et al., 1991). In the adult animal, SERT is localized on presynaptic 5-HT nerve terminals as well as on axons and 5-HT cell bodies in the raphe (Blakely et al., 1998). Finally, degradation of 5-HT is mediated by the mitochondrial membrane-bound monoamine oxidase (MAO), for which there are again two isoforms, MAOA and MAOB. MAOA is the main variant responsible for 5-HT degradation in the CNS (Shih et al., 2011; Vitalis et al., 2003).

Activity pattern of serotonergic neurons

The electrical activity of most neurons expressing 5-HT (5-HT neurons) is characterized by a highly regular and tonic low-frequency (1-6 Hz) firing pattern that is highest during wakefulness, decreases during non-rapid eye movement sleep (NREM), and almost ceases during rapid eye movement sleep (REM) (McGinty and Harper, 1976; Trulson and Jacobs, 1979). In specific contexts, however, 5-HT

neurons are capable of transiently increasing their firing rate up to 30 Hz (Liu et al., 2014; Schweimer and Ungless, 2010).

Although many 5-HT neurons share a similar tonic low-frequency firing pattern, differences in electrophysiological characteristics have been demonstrated for 5-HT neurons in the median raphe nucleus (MRN) versus dorsal raphe nucleus (DRN), as well as for 5-HT neurons within these nuclei. Their electrophysiological properties can differ in resting potential, membrane resistance, rheobase, delay to first spike, spike-frequency adaptation, maximum firing rate, and reaction to chemical substances such as the 5-HT_{1A} receptor agonist (Beck et al., 2004; Calizo et al., 2011; Challis et al., 2013; Crawford et al., 2010; Fernandez et al., 2016; Okaty et al., 2015, 2020; Rood et al., 2014; Shikanai et al., 2012; Trulson and Frederickson, 1987). Based on these features, at least four distinct electrophysiological types could be distinguished so far (Okaty et al., 2020). In addition to electrophysiological properties varying with anatomy, these characteristics have been shown to vary according to the projection patterns (Fernandez et al., 2016).

Serotonin release mechanisms

Projections of 5-HT neurons form classical synaptic connections as well as varicosities with no associated postsynaptic structures, and the ratio between the two structures varies according to the brain region (Descarries et al., 2010; Dinopoulos et al., 1993; Moukhles et al., 1997; Muller et al., 2007, 2007; Papadopoulos et al., 1987; Ridet et al., 1993; Steinbusch, 1981). Given the large number of varicosities allowing for non-synaptic release (Beaudet and Descarries, 1981; Chazal and Ralston, 1987; Fuxe et al., 2010), 5-HT neurons are thought to mainly transmit 5-HT by volume conduction (Bunin and Wightman, 1998, 1999; Dankoski and Wightman, 2013). Interestingly, 5-HT can also be released by dendrites, through an action potential-independent mechanism (Colgan et al., 2012; de Kock et al., 2006), as well as by the soma (Kaushalya et al., 2008). A few studies also suggest that the release of 5-HT from axons is dependent on the frequency of action potentials (Sengupta et al., 2017; Trueta and De-Miguel, 2012).

Co-release of serotonin with other neurochemicals

While the focus of Chapters 2 and 3 will be on 5-HT, it is important to note that 5-HT neurons have the capacity to co-release other neurochemicals based on evidence collected by several studies using

immunohistochemistry (IHC), mRNA *in situ* hybridization (ISH), transcriptional profiling, and *in vitro* and *in vivo* electrophysiology.

About two-thirds of 5-HT neurons in the DRN express VGLUT3, which allows for filling of synaptic vesicles with the excitatory neurotransmitter glutamate. This VGLUT3+ 5-HT subpopulation is concentrated in the ventromedial portion of the DRN and MRN (Amilhon et al., 2010; Commons, 2009; Gras et al., 2002; Hioki et al., 2004, 2010; Jackson et al., 2009; Mintz and Scott, 2006; Okaty et al., 2019; Prouty et al., 2017; Schäfer et al., 2002; Shutoh et al., 2008). Several studies have also provided functional demonstration of 5-HT and glutamate co-release upon stimulation in the basolateral amygdala (BLA), ventral tegmental area (VTA), nucleus accumbens (NAc), the olfactory bulb, orbital prefrontal cortex, and the hippocampus (Kapoor et al., 2016; Liu et al., 2014; Ren et al., 2018; Sengupta et al., 2017; Varga et al., 2009; Wang et al., 2019b). Intriguingly, VGLUT3+ and 5-HT+ terminals can be segregated in individual 5-HT neurons depending on projection target area (Gagnon and Parent, 2014).

IHC and single-cell RNA sequencing (scRNA-seq) observed the co-expression of γ-aminobutyric acid (GABA)-related genes and *Tph2* (Belin et al., 1983; Fernandez et al., 2016; Fu et al., 2010; Hioki et al., 2004, 2010; Kachidian et al., 1991; Niederkofler et al., 2016; Okaty et al., 2015; Ren et al., 2019; Shikanai et al., 2012, 2012; Weissbourd et al., 2014). In contrast to glutamate, GABA-release by 5-HT neurons has not been reported yet.

In addition, 5-HT neurons were observed to co-produce galanin, somatostatin, nitric oxide synthase 1, corticotropin-releasing hormone, substance P, thyrotropin-releasing hormone, proenkephalin, neuropeptide B, prodynorphin, growth hormone releasing hormone, and neuromedin B (Commons et al., 2003; Fu et al., 2010; Kachidian et al., 1991; Okaty et al., 2015, 2020; Ren et al., 2019).

Serotonin receptors

5-HT binds to receptors belonging to 7 different gene families comprising of at least 14 distinct receptor subtypes in mammals (Green, 2006; Hayes and Greenshaw, 2011; Lesch and Waider, 2012). These receptors include both ionotropic and G protein-coupled receptors engaging with diverse signal transduction pathways and are found throughout the CNS on dendrites, soma, and axon terminals (Filip and Bader, 2009; Hannon and Hoyer, 2008; Hoyer, 2017). 5-HT_3 receptors (Pentamer of 5-HT_{3A} with 5-HT_{3B}, 5-HT_{3C}, 5-HT_{3D}, and 5-HT_{3E}) are the only family of ionotropic

receptors consisting of ligand-gated cation channels that lead to rapid depolarization of the plasma membrane. The two receptor families 5-HT_1 (5-HT_{1A}, 5-HT_{1B}, 5-HT_{1D}, 5-HT_{1E}, 5-HT_{1F}) and 5-HT_5 (5-HT_{5A}, 5-HT_{5B}) are connected to $G_{i/o}$ proteins, inhibit adenylate cyclase, decrease cellular levels of cAMP, and evoke a membrane hyperpolarization due to activation of G protein-coupled K^+ channels. The 5-HT_2 receptors (5-HT_{2A}, 5-HT_{2B}, 5-HT_{2C}) couple to $G_{q/11}$ proteins and the phosphoinositol hydrolysis signal transduction system to stimulate the inositol 1,4,5-trisphosphate accumulation and intracellular Ca^{2+} release which results in neuronal depolarization. The three receptor families, 5-HT_4, 5-HT_6, and 5-HT_7 are positively coupled to adenylate cyclase via G_s proteins, enhance cAMP formation, and lead to depolarization of the cell. In addition to this range of different receptors, 5-HT receptors are expressed on inhibitory and excitatory neurons, and individual neurons can express receptors with both inhibitory and excitatory effects which renders it difficult to determine the net outcome of 5-HT on circuit activity (Lesch and Waider, 2012).

Anatomical groups of serotonergic neurons

The first study describing the anatomical location of 5-HT neurons defined nine distinct nuclei (B1-B9) which spatially ranged from the caudal medulla through the pons up into the midbrain (Dahlstroem and Fuxe, 1964). Further studies proposed an updated anatomical nomenclature for 5-HT neurons (Alonso et al., 2013; Hale and Lowry, 2011; Jacobs and Azmitia, 1992). The following describes a commonly used and recently described categorization of 5-HT neurons (Okaty et al., 2019). The serotonergic system is broadly subdivided into a rostral superior and a caudal inferior brainstem group. The rostral group consists of the DRN (B6 and B7), the MRN (B5 and B8), the caudal linear nucleus (CLi; B8), and the B9 nucleus. The caudal group is divided into the nucleus raphe magnus (RMg; B3), the nucleus raphe obscurus (ROb; B2), the nucleus raphe pallidus (RPa; B1), and the ventrolateral medulla (VLM; B1 and B3). The caudal superior brainstem group is most relevant for Chapters 2 and 3, hence this group will receive more attention in the following paragraphs.

Targets of serotonergic projections

In its entirety, the serotonergic system innervates nearly every region of the CNS (Azmitia and Segal, 1978; Jacobs and Azmitia, 1992; Steinbusch, 1981). Although individual 5-HT neurons have diffuse and highly collateralized projections (Fallon and Loughlin, 1982; Imai et al., 1986a; Vertes Robert

P. et al., 1999), different 5-HT subpopulations are topographically organized (Bang et al., 2012; Brust et al., 2014; Fernandez et al., 2016; Imai et al., 1986a; Lowry, 2002; Lowry et al., 2008; Muzerelle et al., 2016; Niederkofler et al., 2016; O'Hearn and Molliver, 1984; Ren et al., 2018). For example, the prefrontal cortex, BLA, and dorsal hippocampus are innervated by largely non-overlapping 5-HT subpopulations (Fernandez et al., 2016; Ren et al., 2018).

Overall, the rostral superior group is providing projections to the forebrain, and the caudal inferior group is providing the principle descending projections to the spinal cord (Aitken and Törk, 1988; Lidov and Molliver, 1982; Törk, 1990). Within the rostral region, DRN and MRN vary again significantly in their distribution of projections. The MRN 5-HT neurons project to structures near the midline, including hippocampus, septum, and mesopontine tegmental nuclei, whereas the DRN 5-HT neurons target more lateral regions, such as the amygdala, substantia innominate, and lateral preoptic area (Jacobs and Azmitia, 1992; Muzerelle et al., 2016; Vertes, 1991; Vertes Robert P. et al., 1999). Furthermore, the DRN consists of different subcomponents with distinctive anatomical profiles as described by Muzerelle et al. The dorsal DRN innervates several hypothalamic and preoptic nuclei, as well as the amygdala, areas that are avoided by the ventral region. On the other hand, the ventral DRN innervates neocortical structures that are almost entirely devoid of inputs from the dorsal DRN. The lateral wings of the DRN distinguish themselves by selective input to the lateral and medial geniculate nuclei. Similarly to the MRN, the posterior region of the DRN (B6) projects to the hippocampus and the lateral septal nuclei, which are almost devoid of projections from the rest of the DRN neurons (Imai et al., 1986b, 1986a; Muzerelle et al., 2016; de Olmos and Heimer, 1980). Importantly, accumulating evidence indicates that subpopulations with differing projection patterns can affect distinct behavioral functions, receive biased inputs from presynaptic partners, and respond differently to external stimuli (Niederkofler et al., 2016; Ren et al., 2018).

Inputs to serotonergic neurons

Inputs to DRN and MRN have been thoroughly characterized and were found to be overall from similar brain regions, although with biased contributions (Celada et al., 2001; Commons, 2015; Gonçalves et al., 2009; Levine and Jacobs, 1992; Mosko et al., 1977; Ogawa et al., 2014; Peyron et al., 1997, 2018; Pollak Dorocic et al., 2014; Weissbourd et al., 2014). The DRN alone receives inputs from as many as eighty distinct anatomical brain regions, including other brainstem raphe nuclei. The vast number of brain regions sending inputs to 5-HT neurons suggests that in general these

neurons are sensitive to neural activity across the brain. However, there is some evidence that 5-HT subpopulations in the rostral DRN receive inputs from different projections than the one in the caudal DRN (Commons, 2015, 2016). Other studies report proportionally different innervation of the ventromedial and dorsal DRN (Ren et al., 2018).

Transcriptome of serotonergic neurons

The advent of scRNA-seq has allowed to characterize and compare the entire transcriptome of individual 5-HT neurons and use this detailed information to categorize the serotonergic system into different subpopulations. For now, however, the field has not reached a consensus on how many 5-HT subpopulations exist based on transcriptomic profiles. Recent studies conducting transcriptomic analysis reported between five to fourteen distinct 5-HT sub-cell type clusters with distinct molecular, electrophysiological, and anatomical properties (Huang et al., 2019; Okaty et al., 2020; Ren et al., 2019; Zeisel et al., 2018). Identified clusters can be distinguished by genes related to neurotransmitters (e.g. *Vglut3* and *Gad1/2*), neuropeptides (e.g. *Trh* and *Crh*), neurotransmitter receptors (e.g. *Grin3a* and *Drd2*), and neuropeptide receptors (e.g. *Tacr3* and *Oxtr*). An important finding made by these studies are genetic handles for projection-specific targeting. Axons from VGLUT3+ 5-HT population preferentially target cortical regions, TRH+ 5-HT population project to subcortical regions in particular the hypothalamus (Ren et al., 2019), while PDYN+ 5-HT population selectively innervate structures that are part of or functionally linked to the basal ganglia (Huang et al., 2019). Another conclusion drawn from these studies is that the distribution of cell bodies from molecularly distinct 5-HT cell types spatially overlap with each other and occupy multiple anatomical subdomains requiring intersectional genetic approaches to dissect the function of each subtype.

Serotonin's role in different behaviors

As suggested by the large number of brain regions receiving inputs from and projecting to 5-HT neurons, the serotonergic system is involved in numerous behaviors, such as ingestion control (Lee and Clifton, 2010), sexual behavior (Liu et al., 2011; Uphouse and Guptarak, 2010; Zhang et al., 2013), mood and emotion (Hensler, 2010), and motor control (Carey, 2010). For example, loss of 5-HT in the rostral superior group was shown to result in a robust hyperactivity phenotype (Whitney et al., 2016). Furthermore, 5-HT is implicated in the regulation of anxiety, where it seems to have a

bidirectional effect; it can either facilitate or attenuate anxious states depending on the site of action and receptor type involved (Lowry and Hale, 2010; Lowry et al., 2005; Teissier et al., 2015). 5-HT is also involved in reward (Liu et al., 2020; McBride, 2010), impulsivity and compulsivity (Angoa-Pérez et al., 2012; Miyazaki et al., 2011a, 2012a, 2011b, 2012b; Robbins and Crockett, 2010), learning (Cassel, 2010), social behavior (Duman and Canli, 2010; Kane et al., 2012), and pain (Sommer, 2010). Interestingly, for the latter behavior it has been demonstrated that different 5-HT subpopulations in the DRN respond oppositely towards aversive stimuli (Ren et al., 2018). A central topic of Chapter 2 is the role of 5-HT in sleep, a subject that has been debated for over 60 years (Ursin, 2008). To put the work presented in Chapter 2 into context, the following section will summarize the main discoveries that led to our current understanding of the function of 5-HT in sleep.

1.2 The role of serotonin in sleep

Serotonin is sleep-promoting

The neuromodulator 5-HT is well-positioned to have a major influence on fundamental behavioral states such as sleep-wake states. Endowed with a vast efferent and afferent system, the serotonergic system has the ability to directly integrate information from most brain areas and in response synchronize or disrupt synchronized activity of many functionally diverse brain areas (Celada et al., 2013; Koella and Czicman, 1966; Ogawa et al., 2014; Pollak Dorocic et al., 2014; Puig and Gener, 2015; Weissbourd et al., 2014). Brain-wide changes in oscillations of neuronal activity are a hallmark of sleep-wake states.

Early studies based on lesion of the brainstem raphe nuclei and the effects of 5-HT depleting drugs established the concept of 5-HT as a sleep neurotransmitter. After lesions of raphe nuclei in cats, a state of permanent wakefulness in conjunction with a decrease in cerebral 5-HT was observed for multiple days followed by short periods of sleep (<5% per day) (Jouvet, 1968). REM sleep was usually not seen and the reduction in NREM sleep was proportional to the size of the lesion. In a pharmacology experiment, cats were depleted of 5-HT with a single intraperitoneal *para*-chlorophenylalanine (pCPA, an irreversible inhibitor of TPH) injection which resulted in dose-related reduction of sleep for several days (Koella et al., 1968; Pujol et al., 1971). Importantly, after injection of 5-HTP in animals depleted of 5-HT, cats went to sleep within minutes for several hours.

Subsequent studies corroborated findings from these early studies (Borbely et al., 1981; Mouret et al., 1968; Pujol et al., 1971; Torda, 1967; Ursin, 1972, 1980; Weitzman et al., 1968).

Serotonergic neurons are wake-active

Following the early studies supporting the sleep-promoting role of 5-HT, a few studies started to challenge the prevailing view at the time. One study showed that cooling of the raphe nucleus in cats induced sleep when it was performed during waking (Cespuglio et al., 1976). In addition, raphe lesions in rats induced hyperactivity, but failed to display a sleep phenotype (Bouhuys and Van Den Hoofdakker, 1977). The advent of single-unit recordings then finally shifted the paradigm to 5-HT being viewed as a wake-promoting neurotransmitter (Monti, 2011; Ursin, 2008). In spontaneously sleeping animals, 5-HT neurons showed highest activity during waking, reduced activity during NREM sleep, and almost cessation of firing during REM sleep (Cespuglio et al., 1981; Guzmán-Marín et al., 2000; Jacobs and Azmitia, 1992; McGinty and Harper, 1976; McGinty et al., 1973; Trulson and Jacobs, 1979). In addition, electrical stimulation of the DRN induced wakefulness (Houdouin et al., 1991). As a side note, while the majority of 5-HT neurons follow this firing pattern, a few 5-HT subpopulations exist that retain high firing rates during NREM and REM sleep or even display higher firing rates during NREM sleep (Sakai and Crochet, 2001). Later, microdialysis studies confirmed the correlation of extracellular 5-HT concentration with behavioral states; 5-HT release in several brain regions was highest in waking animals, was reduced during NREM sleep, and decreased further during REM sleep (Iwakiri et al., 1993; Park et al., 1999; Portas and McCarley, 1994; Portas et al., 1998; Strecker et al., 1999). Furthermore, sleep deprivation lead to increased levels of extracellular 5-HT (Peñalva et al., 2003; Zant et al., 2011). At the time, these results were taken as evidence that 5-HT neurons could not be sleep-promoting.

Pharmacology experiments with 5-HT receptor agonists and antagonists, as well as 5-HT reuptake inhibitors, complicated the picture of 5-HT's role in sleep-wake regulation. For example, 5-HT_{1A} receptor activation may increase waking, NREM, or REM sleep, depending on where the receptor is located (Bjorvatn and Ursin, 1998). In addition, administration of several selective 5-HT reuptake inhibitors has been shown to increase waking followed by increased NREM sleep and reduction of REM sleep (Cespuglio et al., 2005; Hilakivi et al., 1987; Lelkes et al., 1994; Maudhuit et al., 1994; Sommerfelt and Ursin, 1987, 1991; Ursin et al., 1989).

In spite of these inconsistencies, the 5-HT raphe were widely thought to promote wakefulness as part of the ascending arousal system (Saper et al., 2005; Scammell et al., 2017) up until recently.

Current view

Chapter 2 summarizes our results of revisiting the role of 5-HT neurons in murine and zebrafish sleep using modern optogenetic and chemogenetic tools that allow probing and manipulation of 5-HT neurons with superior spatial and temporal precision when compared to previously employed methods. Given the enormous complexity of the serotonergic system and at the time a lack of thorough investigations of genetic handles for accessing 5-HT subpopulations, we decided to readdress the question by manipulating the 5-HT population in its entirety. We demonstrate that the serotonergic raphe are sleep-promoting and are required for sleep homeostasis, but can also induce wakefulness in specific contexts. Subsequent studies from another laboratory further consolidated our findings of a sleep-promoting function for 5-HT neurons (Venner et al., 2019, 2020) leading to a renewed appreciation of this particular role in sleep-wake regulation (Bandarabadi et al., 2020; Deboer, 2020; Kashiwagi and Hayashi, 2020; Lyons and Rihel, 2020; Park and Weber, 2020; Peng et al., 2020).

1.3 Tools for measuring serotonin release

As mentioned in previous paragraphs, the serotonergic system innervates nearly every region of the CNS (Azmitia and Segal, 1978; Jacobs and Azmitia, 1992; Steinbusch, 1981) while forming both classical synaptic connections and varicosities (Chazal and Ralston, 1987; Descarries et al., 2010; Dinopoulos et al., 1993; Moukhles et al., 1997; Muller et al., 2007, 2007; Papadopoulos et al., 1987; Ridet et al., 1993; Steinbusch, 1981). Besides varicosities, the detection of 5-HT receptors and transporters at a distance from the release site support the volume transmission theory (Bunin and Wightman, 1999; Ridet et al., 1994). Observations of 5-HT release add to the complexity of the serotonergic system by showing that the amount of 5-HT release from axons is dependent on the frequency of action potentials (Bunin and Wightman, 1998; Gartside et al., 2000; John et al., 2006; O'Connor and Kruk, 1991; Sengupta et al., 2017; Trueta and De-Miguel, 2012), while release of 5-HT at dendritic sites can even be independent of action potentials (Colgan et al., 2012; de Kock et al., 2006). Studies in the Retzius neurons of the leech indicate that distinct 5-HT-release mechanisms may underlie the difference in the amount of release between high- and low-frequency firing of 5-

HT neurons (De-Miguel and Trueta, 2005; Leon-Pinzon et al., 2014), thus, aggregating evidence points to a very complex mode of action of the neuromodulator 5-HT. Its understanding necessitates the development of tools capable of detecting 5-HT release at high spatiotemporal resolution. In the following, different approaches taken over the last decades to measure serotonin release are introduced in preparation for Chapter 3 (Beyene et al., 2019).

Device-based sensors

One of the first methods employed for characterizing extracellular serotonin was **microdialysis**. In this technique, the interstitial space of brain tissue is sampled through dialysis followed by characterization using established analytical approaches such as liquid chromatography, capillary electrophoresis, mass spectrometry, and electrochemistry (Benveniste, 1989; Chefer et al., 2009; Plock and Kloft, 2005). The sampling is performed by a dialysis probe with a tubular semipermeable membrane that is inserted into the brain tissue. The probe is perfused with a solution resembling the extracellular fluid but devoid of the analyte molecules (e.g. 5-HT). As a consequence, 5-HT diffuses along its concentration gradient from the extracellular space into the flowing perfusate and is collected via outlet tubing for further analytical quantification. The ability to continuously collect perfusate endows microdialysis with the advantage of being compatible with sophisticated downstream characterization methods that provide multiplexed, highly selective, and reliable identification of various molecules, such as 5-HT (Chefer et al., 2009). In addition, the dialysis probe can be repeatedly used for chronic analysis during behavioral studies. However, its working principle is based on diffusion which results in poor temporal resolution (Chefer et al., 2009; Plock and Kloft, 2005). To date, the fastest reported time resolutions are still around a minute (Harstad and Bowser, 2016; Ngo et al., 2017; Saylor and Lunte, 2015; Wang et al., 2008, 2010; Yang et al., 2015). For this reason, microdialysis is most suited for studying changes in basal levels of serotonin that occur on the scale of several minutes and hours, such as extracellular 5-HT concentrations across sleep-wake cycles (Portas et al., 1998). Furthermore, microdialysis has limited spatial resolution due to the size of the probe which is in the order of millimeters in length and several hundreds of micrometers in width. Microdialysis usually samples from volumes that extend several hundred of micrometers from the probe, considerably larger than a synaptic cleft. The sampling procedure may also lead to depletion of 5-HT from tissue surrounding the probe.

An alternative approach to microdialysis is **voltammetry**. The principle of this technique is applying a voltage at the tip of a microelectrode which oxidizes electroactive molecules such as 5-HT (Jackson et al., 1995). The current generated by the redox reaction can be measured providing information on the local analyte concentration. Typically, the applied voltage is varied as a function of time and the corresponding current-voltage plot serves as a readout for both analyte concentration and chemical identity. Rapidly changing the applied voltage enables high temporal resolution and is known as fast-scan cyclic voltammetry (FSCV) (Baur et al., 1988; Ewing et al., 1983; Stamford et al., 1984). This technique provides a tremendous improvement in temporal resolution and can measure millisecond-scale transients in 5-HT concentration (Baur et al., 1988; Kawagoe et al., 1993). A recent study used FSCV to measure optically-evoked 5-HT release in the bed nucleus of stria terminalis and how 5-HT reuptake is affected by application of the selective serotonin reuptake inhibitor fluoxetine (Marcinkiewcz et al., 2016). Owing to the relatively large size of FSCV electrodes (Armstrong-James and Millar, 1979; Ponchon et al., 1979; Wightman, 1981), application of this method to serotonergic systems is functionally limited to measure ensemble-averaged activity, and as a result spatially limited to regions that exhibit robust and dense innervation (Dankoski and Wightman, 2013). Nevertheless, FSCV provides much improved spatial resolution compared to microdialysis. Carbon fiber electrodes can be constructed at the scale of single-digit micrometer width scales, resulting in improved spatial resolutions of more than an order of magnitude compared to microdialysis as well as reduced tissue damage (Kozai et al., 2015; Peters et al., 2004).

A more recent device-based approach is the **field effect transistor** (FET) that senses changes in electric fields induced by molecule binding. In principle, once the molecule binds to the sensitized surface, the charge of the molecule will change the gate bias and therefore change the source-drain current which generates a signal indicative of binding (Kim et al., 2013). A FET sensor modified with a 5-HT aptamer was reported to exhibit a highly sensitive and selective electrochemical response to 5-HT under physiological conditions (10 pM to 100 nM) for several hours (Nakatsuka et al., 2018). So far, however, FET sensors for 5-HT have only been tested in *in vitro* conditions.

Synthetic molecule-based sensors

Single-walled carbon nanotubes (SWNT) are made of carbon with diameters in the range of nanometers and possess useful photoluminescence properties for biosensors (Heller et al., 2005).

SWNT-based sensors fluoresce in the near infrared (NIR), a wavelength window which provides considerable advantages in probing sensor response within tissues, both *in vivo* and *in vitro* (Bonis-O'Donnell et al., 2017; Giraldo et al., 2015; Landry et al., 2017). The NIR II region (1000-1350) presents a local minimum in the tissue absorption spectrum and sensors operating in this regime enable relatively deep tissue imaging at high resolution (Welsher et al., 2011). An additional advantage of SWNT-based sensors is their resistance to photobleaching, showing no attenuation in fluorescence even after 10 h of continuous excitation (Heller et al., 2005). Modulation of SWNT fluorescence by 5-HT binding can be achieved by functionalizing the surface of SWNT with single-stranded DNA sensitive to 5-HT. nIRHT, a SWNT-based 5-HT sensor, has been developed and demonstrated $\Delta F/F_0$ of up to 194±6% in the emission window of 1000 to 1300 nm with a K_d of 6.3 µM. Currently, the performance of this sensor has only been tested in *in vitro* environments and also lacks specificity due to relatively strong responses to dopamine. These sensors, however, are interesting due to their temporal resolution which is comparable to the one of FSCV and due to their high spatial resolution.

Gold nanoparticles, defined as particles with dimensions ranging from 1 to 100 nm, are an attractive alternative synthetic molecule-based sensor due to their tunable absorption and emission properties (Nune et al., 2009). A 5-HT sensor developed by Chávez et al. incorporates a 5-HT-binding DNA aptamer as a 5-HT recognition element on their gold nanoparticles (Chávez et al., 2017). In the absence of 5-HT, 5-HT-binding DNA aptamers are free to adopt a variety of conformations and absorb onto the gold nanoparticle surface. To a certain extent, aptamers already protect gold nanoparticles from aggregation. In the presence of 5-HT, however, the 5-HT-binding DNA aptamers are increasing the aptamer shielding and are decreasing the gold nanoparticle aggregation which is changing their plasmon resonance frequency and generating a colorimetric response that scales with the concentration of 5-HT. This strategy yields a linear sensor response in the physiologically relevant 5-HT concentration range of 750 nM-2.5 µM. The drawback of current sensors based on gold nanoparticles is that the host serum interferes with the sensor response. Samples need to undergo a filtration step in order for the sensor to perform properly. The limited testing in realistic biological environments remains a major challenge for these gold nanoparticle-based sensors. At their current state, gold nanoparticle sensors are only suited for *ex vivo* studies where samples can be pretreated to ensure robust sensor performance.

Hettie and Glass developed a 5-HT sensor, NS715, with a fluorophore based on a coumarin-3-aldehyde scaffold that exhibits a near-infrared fluorescence response toward 5-HT (Hettie and Glass, 2016). Exciting NS715 at 559 nm affords an emission maximum at 674 nm, which is in the NIR spectral region. Addition of 5-HT to NS715 produced a marked increase in fluorescence intensity with a red-shift in its emission maximum to 715 nm. A weakness of this sensor is its considerable affinity to other neurochemicals, such as dopamine and norepinephrine, and a lack of testing its performance beyond chromaffin cells in an *in vitro* setting.

Overall, due to their non-biological origin, synthetic molecule-based sensors face the major challenge of maintaining their performance in a complex biological setting.

Protein-based sensors

Protein-based fluorescent sensors typically have an analyte recognition moiety that is covalently conjugated to a fluorophore. During analyte binding, the recognition domain undergoes a conformational change that alters the photophysical properties of the fluorophore, which can be read out. In contrast to previously introduced sensors, protein-based sensors can target specific neuronal populations by genetic handles (Marvin et al., 2013).

Forster resonance energy transfer (FRET) is a form of nonradiative energy transfer that can occur between two fluorophores in close proximity with overlapping absorption and emission spectra. The FRET efficiency between a pair of fluorophores is ultrasensitive to the distance between them, affording a precise readout of nanometer-scale conformational changes that follow protein-ligand binding events (Spiering et al., 2013). This principle was employed to detect conformational changes in a genetically engineered 5-HT_{1B} receptor sensor containing an intramolecular GPCR conformation-sensitive FRET pair (Candelario and Chachisvilis, 2012). The **FRET based-sensor** was constructed with Citrine fluorescent protein inserted into the third cytoplasmic loop and Cerulean fluorescent protein fused to the C-terminus of the 5-HT_{1B} receptor. The sensor was tested in HEK293 cells and demonstrated an increase in fluorescence at 530 nm and a decrease at 480 nm upon exposure to 5-HT concentrations ranging from 5 to 500 μM. A drawback of the sensor is the low 5-HT sensitivity in the nanomolar range. Furthermore, no attempts were made to characterize

the sensor *in vivo* or investigate whether the natural intracellular interactions of the $5HT_{1B}$ receptor are preserved.

In contrast to FRET-based sensors, single wavelength sensors relay an optical signal via changes in a single fluorophore, rather than changes in donor-acceptor pair FRET efficiency. This readout results in a sensor with relatively compact optical excitation and emission spectra that make them more amenable to multiplexing.

Similarly to the FRET-based sensor described above, a recent study used the $5\text{-}HT_{2C}$ receptor as the 5-HT sensing moiety and inserted a circular permutated GFP (cpGFP) into the third intracellular loop to create a genetically encoded GPCR-activation-based 5-HT (**$GRAB_{5\text{-}HT}$**) sensor (Wan et al., 2020). The $GRAB_{5\text{-}HT}$ sensor has no detectable coupling to either intracellular G-protein or β-arresting signaling pathways. During *in vivo* recordings in Drosophila, they observed τ_{on} and τ_{off} values of 0.07 s and 4.08s, respectively. Furthermore, $GRAB_{5\text{-}HT}$ was shown to selectively and reliably report to endogenous 5-HT release in response to a variety of stimuli and behaviors in Drosophila as well as mice. In a direct comparison with FSCV, $GRAB_{5\text{-}HT}$ showed better signal to noise ratio (SNR). Some of their fluorescent imaging experiments were conducted over several hours suggesting that $GRAB_{5\text{-}HT}$ is suitable for stable, long-term imaging *in vivo*. A drawback of GPCR-based biosensors is that they respond to all molecules that interact with the parental GPCR, resulting in artifacts when GPCR antagonists or agonists are concurrently used. In addition, GPCR-based biosensors tend to suffer from slow dissociation kinetics (Borden et al., 2020). Finally, there are concerns about the overexpression of GPCRs, which may perturb cell signaling that is highly organized and tightly controlled (Tubio et al., 2010).

An alternative strategy which alleviates the undesired interactions of endogenous 5-HT-binding proteins is to look for orthogonal 5-HT-binding proteins in other organisms. This strategy was exploited in the development of the green fluorescent, genetically encoded serotonin sensor (**G-GESS**) from a 5-HT-binding lipocalin in the soft tick (Zhang et al., 2020). A cpGPF was inserted into the 5-HT-binding lipcalin such that allosteric coupling of 5-HT binding results in cpGFP fluorescence. Using insertion linker optimization and whole-gene random mutagenesis, the sensor was evolved over multiple rounds to reach the current G-GESS sensor. In HEK293T cells, G-GESS displayed a ~350% ($\Delta F/F_0$) fluorescence increase in response to 5-HT with a K_d of ~120 nM and a

half-time for association and dissociation of 27 ms and 840 ms, respectively. Furthermore, G-GESS demonstrated a fluorescence increase in the mouse brain upon methylenedioxy-methamphetamine (MDMA) administration and an increase upon footshock in a fear conditioning paradigm. Overall, G-GESS displays good fluorescence change, brightness, photostability, and specificity.

In Chapter 3, we developed a fluorescent 5-HT sensor, **iSeroSnFR**, using a binding-pocket redesign strategy guided by machine learning. Similarly to G-GESS, the scaffold of iSeroSnFR is not based on a host protein but on microbial periplasmic binding proteins (PBPs). In contrast to GPCR-based sensors, PBPs typically bind few, if any, drugs targeting host proteins. We demonstrate that iSeroSnFR can be used to detect serotonin release in freely behaving mice during fear conditioning, social interaction, and sleep/wake transitions. Finally, we also established a robust assay of 5-HT transporter function and modulation by drugs.

1.4 AAVs as gene delivery vectors

Since its discovery in 1965, AAVs have been successfully repurposed as safe gene delivery vehicles leading to novel gene therapy treatments and facilitation of interrogation of neuronal circuits (such as the serotonergic system) in basic neuroscience (Bedbrook et al., 2018; Hastie and Samulski, 2015; Maguire et al., 2019; Mahajan, 2019; Samulski and Muzyczka, 2014; Samulski et al., 1989; Wang et al., 2019a; Weitzman and Linden, 2011; Ylä-Herttuala, 2012).

For **basic neuroscience**, AAVs are excellent gene delivery vectors due to their stable and long-term expression of transgenes, and the ability to transduce terminally differentiated or nondividing cells, such as neurons with high efficiency; some serotypes also transduce astrocytes, endothelial cells, oligodendrocytes, and ependymal cells (Alisky et al., 2000; Burger et al., 2004; Davidson et al., 2000; Lawlor et al., 2009; McCown et al., 1996; Van der Perren et al., 2011). AAVs were instrumental in advancing our understanding of, for example, the serotonergic system in several aspects. Employing AAVs with axon terminal-transducing properties enabled to specifically access and investigate over long term a 5-HT subpopulation projecting to a particular downstream brain area (Ren et al., 2018). These retrograde AAVs complement the Canine adenovirus-2 (CAV-2), which allows only modest levels of transgene expression and shows some toxicity (Piersanti et al., 2013; Simão et al., 2016; Tervo et al., 2016). Furthermore, in adult animals neuronal activity sensors were delivered by AAVs to spatially-defined 5-HT neurons to report their natural activity pattern

during various behaviors and stimuli (Li et al., 2016; Matias et al., 2017; Moriya et al., 2019; Oikonomou et al., 2019; Ren et al., 2018; Seo et al., 2019; Wei et al., 2018; Zhong et al., 2017). The activity of 5-HT neurons could be precisely manipulated over short- and long-term with AAV-mediated expression of actuators such as light-sensitive cation channels or designer receptors exclusively activated by designer drugs (DREADDS) (Baskin et al., 2020; Browne et al., 2019; Cai et al., 2014; Chowdhury and Yamanaka, 2016; Correia et al., 2017; Garcia-Garcia et al., 2018; Giorgi et al., 2017; Hasegawa et al., 2017; Liu et al., 2014; Lottem et al., 2016; Miyazaki et al., 2014; Ohmura et al., 2014; Oikonomou et al., 2019; Ren et al., 2018; Seo et al., 2019; Teissier et al., 2015; Urban et al., 2016; Venner et al., 2020). Loss-of-function experiments were performed using AAVs delivering transgenes to eliminate the synthesis of *Tph2* or ablate cells in specific 5-HT subpopulations (Oikonomou et al., 2019; Whitney et al., 2016). Besides the advantage of spatial control of transgene expression with intracranial injection of AAVs, transgenes can be delivered and expressed in adult animals which is essential for the serotonergic system due to its involvement in development (Alenina et al., 2009). However, basic neuroscience could benefit from developing optimized AAVs with more efficient retrograde infection (Tervo et al., 2016), improved anterograde transsynaptic spread efficiency (Zingg et al., 2016), and increased efficiency and specificity for cell types such as microglia which are a critical component of neurodegenerative diseases, but are currently not accessible to manipulation with AAVs (Maes et al., 2019; Wang et al., 2020).

Compared to other available gene delivery vectors for **gene therapy**, AAVs have the strongest potential for *in vivo* systemic gene delivery due to their latent infection, low immunogenicity, non-pathogenicity, low probability of integrating into the host genome, ability to transduce both dividing and non-dividing cells, broad tropism, their capability of ensuring long-term transgene expression, and ease of production compared to other viral vectors (Atchison et al., 1965; Carter and Samulski, 2000; Hastie and Samulski, 2015; Hermonat and Muzyczka, 1984; Hoggan, 1970; Hoggan et al., 1966; Lykken et al., 2018; McCarty et al., 2004; Naso et al., 2017; Schultz and Chamberlain, 2008; Van Vliet et al., 2008; Vance et al., 2015; Wang et al., 2019a; Wu et al., 2006, 2010). In total, three AAV-based gene therapies have been approved for gene therapy treatment in humans. In 2012, the European Regulatory Commission (ERC) approved Glybera to treat lipoprotein lipase deficiency (LPLD), and Glybera thereby became the first approved AAV-based gene therapy (Ylä-Herttuala, 2012). In 2017, the Food and Drug Administration (FDA) approved Luxturna (voretigene neparvovec-rzyl) to correct RPE65 mutation-associated inherited retinal dystrophy and

made it the first AAV-based gene therapy in the US (Maguire et al., 2019). In 2019, the FDA approved Zolgensma (onasemnogene abeparvovec) to treat spinal muscular atrophy (Mahajan, 2019). The recognition of the potential impact of AAVs for gene therapy has led to more than 200 phase I, II, and III clinical trials (Wang et al., 2020). The approval of these AAV-based gene therapies is encouraging and it increased investment in AAV-based therapies. Current limitations that hinder the application of AAV delivery vehicles to other diseases or improve treatment outcome for approved therapies are the transduction efficiency and target specificity (Lisowski et al., 2015). At present, there are 12 known serotypes of AAVs with overlapping tropisms and sequence similarity between 50-99% (Gao et al., 2004; Vance et al., 2015). Contributing to the difference in viral tropism are varying affinities of the AAV capsids towards endogenous receptors (Pillay and Carette, 2017; Wu et al., 2006). For example, AAV2 binds to heparin sulfate receptor (Summerford and Samulski, 1998) and has other co-receptors (Qing et al., 1999; Summerford et al., 1999), while AAV9 binds to galactose receptor (Shen et al., 2011). AAVR, on the other hand, is considered a universal receptor essential for AAV transduction (Pillay et al., 2016). These receptors are expressed across a vast array of cell and tissue types which is explaining the broad viral tropism of natural AAVs. In order to tailor the tropism of AAVs to the specific needs of a particular disease, several capsid engineering approaches have been developed to optimize binding to defined receptors, to improve intracellular trafficking and second-strand synthesis in target cells and tissues.

1.5 Engineering of AAV tissue and cell type tropism

AAV cassette engineering

The AAV vector tropism can be altered by engineering either the AAV cassette or the capsid. The AAV cassette engineering can involve a rational *in silico* design of promoters (Chuah et al., 2014; Jüttner et al., 2019; Rincon et al., 2015) or the discovery of cell-type-specific enhancers leveraging ATAC- and scRNA-seq (Hrvatin et al., 2019; Mich et al., 2020). Both strategies have been employed to obtain target tissue or cell type specific transgene expression with AAVs. For example, Ple67 (Portales-Casamar et al., 2010), a MiniPromoter based on the FEV regulatory regions, conferred selective transgene expression in 5-HT neurons after systemic AAV injection (Chan et al., 2017; de Leeuw et al., 2016).

AAV capsid engineering

Investigations of the receptor-binding domains on some AAV serotypes spurred efforts to create AAVs with altered viral tropism by **rational engineering** (Herrmann and Grimm, 2018). For instance, to increase the efficiency of AAV2 to transduce mouse skeletal muscle, several natural AAV serotypes with a higher efficiency of transducing skeletal muscle than AAV2 were closely examined for conserved regions in the structurally variable region on the capsid surface (Bowles et al., 2012). Engrafting five conserved residues from AAV1 into the AAV2 capsid transduced muscles more efficiently than AAV2 (Bowles et al., 2012). Another study demonstrated that engrafting the glycan-binding residues from the AAV9 capsid into the AAV2 capsid conferred the ability to bind glycan to AAV2 which increased its transduction efficiency (Shen et al., 2013). An alternative rational engineering approach is the incorporation of cell-targeting peptides into permissive sites of the AAV capsid genome (Davis et al., 2015; White Stephen J. et al., 2004).

Often, insufficient information is available for a rational design of capsid optimization. An attractive alternative to rational engineering is **directed evolution** which requires little to no knowledge of a receptor target or mechanism of entry (Bedbrook et al., 2018; Kwon and Schaffer, 2008). The directed evolution technique incorporates several different methodologies, including error-prone PCR (Maheshri et al., 2006; Pulicherla et al., 2011), SCHEMA-based gene shuffling (Ojala et al., 2018), and Cre recombination-based AAV targeted evolution (CREATE) (Deverman et al., 2016).

CREATE was devised to apply positive selective pressure for capsids to cross the BBB and functionally transduce specific cell types. An AAV capsid genome couples the full-length AAV *cap* gene with a Cre-invertible switch. Capsid libraries are built and the corresponding virus libraries are injected into animals with Cre expression in a defined cell population. Cre-recombination enables the selective amplification and recovery of sequences that have transduced the cell type of interest. Multiplexed-CREATE (M-CREATE) builds upon the CREATE platform by several modifications, including the incorporation of next-generation sequencing (NGS) (Ravindra Kumar et al., 2020). The improvements enabled a better interpretation of relative infection efficiencies of different variants across a broad range of enrichments in multiple positive selections. Most importantly, it allowed post-hoc negative screening by comparing capsid libraries recovered from several cell types and organs.

1.6 *In vivo* characterization of AAV tropism

The engineering approaches described above yield a large collection of candidates that require further *in vivo* characterization. Various techniques have been employed over the years to study the viral tropism based on visualization of the viral capsid, RNA/DNA, or transgene expression product.

Visualization of viral capsid

Radioactive molecules, such as iodine-124 (Kothari et al., 2017) or Cu-64 (Seo et al., 2020), can be linked to the AAV capsid by covalent binding of tyrosines, lysines, or cysteines. Following the systemic injection of radioactively labeled AAVs, positron emission tomography (PET) can be utilized to non-invasively and repeatedly study the biodistribution of AAV capsids across the entire murine body (Seo et al., 2020). PET's non-invasiveness represents a clear advantage over most other tropism profiling techniques described below which are invasive and rely on small quantities of tissue at a single site and/or time point. However, PET has limited spatial resolution, provides no information regarding cell type tropism and due to the radiation of tracers, wide-spread application in research is limited (Xu et al., 2011). Another concern is that labels attached to the capsid surface may alter the viral tropism.

Visualization of viral nucleic acid

Viral nucleic acid spread across the host tissue can be detected using Southern blotting (Bernt et al., 2003; Cichon et al., 1999), quantitative-PCR (qPCR) (Hackett et al., 2000; Senoo et al., 2000), and NGS (Adachi et al., 2014; Davidsson et al., 2019; De Alencastro et al., 2020; Herrmann et al., 2019; Körbelin et al., 2016a; Marsic et al., 2015; Paulk et al., 2018; Ravindra Kumar et al., 2020; Westhaus et al., 2020). Although these techniques have proven valuable due to their sensitivity and specificity, as well as the high-throughput capabilities of NGS, without modifications they merely report a quantitative measure of presence in the homogenized tissue and ignore putative heterogeneity across cell types within the tissue. In contrast, ISH allows to study the heterogeneity in transduction of various cell types residing within a tissue and preserves spatial information by labeling nucleic acids within an intact tissue (Arruda et al., 2001; Deleage et al., 2016, 2018; Grabinski et al., 2015; Hinderer et al., 2018; Hunter et al., 2019; Miao et al., 2000; Polinski et al., 2015, 2016; Puray-Chavez et al., 2017; Wang et al., 2020; Zhang et al., 2016; Zhao et al., 2020). Due to technical challenges,

ISH studies usually focus on transcripts of a few gene markers and thus fall short of precisely characterizing viral tropism across the many complex cell types present in the CNS.

Visualization of viral transgene expression

PET can also visualize viral transgene expressions by intravenously injecting radioactive agents that bind to the viral transgene product (Horst et al., 2006; Yoon et al., 2014). For example, pyruvate kinase (*Pkm2*) has low background expression in the brain and can be packaged into an AAV (Haywood et al., 2019). The reporter probe [^{18}F]DASA-23, which permeates the blood-brain barrier, binds to PKM2 and allows long-term monitoring of brain transduction by AAVs using PET (Haywood et al., 2019). To avoid radioactive reporters, bioluminescence imaging can be applied for non-invasive whole-body viral tropism profiling. The feasibility of this approach has been demonstrated by systemically injecting mice with different AAV serotypes packaging the *luciferase* reporter, followed by D-luciferin injection and repeated imaging with special equipment capable of detecting emitted photons (Körbelin et al., 2016b; Zincarelli et al., 2008). However, reporter-based characterization of AAV transduction profiles using Western blotting (Shen Fanxia et al., 2006; Xu et al., 2011) or IHC are the most frequently applied techniques. Often, AAV tropism profiling is conducted across a few canonical marker genes representing major cell types (Chan et al., 2017; Deverman et al., 2016; Ravindra Kumar et al., 2020). To avoid the problem of failing to detect low levels of reporter expression, AAVs carrying Cre-recombinase can be injected in report mice instead (Lang et al., 2019).

Current limitations

All currently applied *in vivo* vector characterization methods fall short of efficiently profiling the tropism of multiple AAVs in parallel across complex cell types and states present in the CNS. To date, the characterization often entails the injection of one AAV variant per animal followed by histological analysis using IHC with a few canonical cell type markers - a highly time-consuming procedure. As a consequence, only a small and manually-selected fraction of the enriched AAV variants emerging from engineering methods is characterized, possibly missing some useful variants and certainly loosing capsid-tropism correlation information. Ideally, the tropism of large pools of AAV variants should be profiled across tissue and cell types at single-cell resolution with the entire transcriptome available for each cell.

Single-cell RNA sequencing as a promising viral tropism profiling method

Before the advent of scRNA-seq, transcriptomic analysis was based on entire tissue samples composed of many different cell types or a collection of sorted cells sharing a defined gene marker (Cahoy et al., 2008; Lovatt et al., 2007). The increased resolution provided by scRNA-seq revealed cell states and subtypes not previously known or described (Herring et al., 2018; Treutlein et al., 2014; Usoskin et al., 2015; Villani et al., 2017; Zeisel et al., 2015). Refinement of the experimental setup and reduction in cost led to dramatic increases in the scale of experiments over the years. In 2009, scRNA-seq protocols examined just six cells (Tang et al., 2009, 2010). By 2015, plate-based automated liquid handling protocols enabled hundreds of cells to be sequenced (Paul et al., 2015; Satija et al., 2015), followed by droplet-based protocols with up to tens of thousands of cells (Klein et al., 2015; Macosko et al., 2015). More recently, combinatorial barcoding of messenger RNAs (mRNAs) within cells were enabled to sequence hundreds of thousands of cells (Cao et al., 2017; Dixit et al., 2016; Rosenberg et al., 2018). Plate-based protocols, in particular SMART-seq2, have the greatest sensitivity in terms of the number of detectable mRNAs per cell, but they also have the lowest throughput in terms of cell numbers. Droplet-based protocols, such as Drop-seq, can routinely sequence tens of thousands of cells based on 3' sequences, but their capture rate at 65% is lower than plate-based protocols (Zheng et al., 2017; Ziegenhain et al., 2017).

In Chapter 5, we address the shortcoming of current *in vivo* viral tropism profiling techniques with scRNA-seq technologies based on the Drop-seq method. We establish an experimental and computational pipeline that allows us to profile the viral tropism of multiple AAV variants in parallel across complex cell type hierarchies. Although we tested our approach by characterizing AAVs, the method can be employed more broadly for gene delivery vehicles.

1.7 References

Adachi, K., Enoki, T., Kawano, Y., Veraz, M., and Nakai, H. (2014). Drawing a high-resolution functional map of adeno-associated virus capsid by massively parallel sequencing. Nat. Commun. *5*, 3075.

Adams, P.R., and Brown, D.A. (1980). Luteinizing hormone-releasing factor and muscarinic agonists act on the same voltage-sensitive K+ -current in bullfrog sympathetic neurones. Br. J. Pharmacol. *68*, 353–355.

Aitken, A.R., and Törk, I. (1988). Early development of serotonin-containing neurons and pathways as seen in wholemount preparations of the fetal rat brain. J. Comp. Neurol. *274*, 32–47.

Alenina, N., Kikic, D., Todiras, M., Mosienko, V., Qadri, F., Plehm, R., Boyé, P., Vilianovitch, L., Sohr, R., Tenner, K., et al. (2009). Growth retardation and altered autonomic control in mice lacking brain serotonin. Proc. Natl. Acad. Sci. U.S.A. *106*, 10332–10337.

Alisky, J.M., Hughes, S.M., Sauter, S.L., Jolly, D., Dubensky, T.W.J., Staber, P.D., Chiorini, J.A., and Davidson, B.L. (2000). Transduction of murine cerebellar neurons with recombinant FIV and AAV5 vectors. NeuroReport *11*, 2669–2673.

Alonso, A., Merchán, P., Sandoval, J.E., Sánchez-Arrones, L., Garcia-Cazorla, A., Artuch, R., Ferrán, J.L., Martínez-de-la-Torre, M., and Puelles, L. (2013). Development of the serotonergic cells in murine raphe nuclei and their relations with rhombomeric domains. Brain Struct. Funct. *218*, 1229–1277.

Amilhon, B., Lepicard, È., Renoir, T., Mongeau, R., Popa, D., Poirel, O., Miot, S., Gras, C., Gardier, A.M., Gallego, J., et al. (2010). VGLUT3 (vesicular glutamate transporter type 3) contribution to the regulation of serotonergic transmission and anxiety. J. Neurosci. *30*, 2198–2210.

Amin, A.H., Crawford, T.B.B., and Gaddum, J.H. (1954). The distribution of substance P and 5-hydroxytryptamine in the central nervous system of the dog. J. Physiol. *126*, 596–618.

Angoa-Pérez, M., Kane, M.J., Briggs, D.I., Sykes, C.E., Shah, M.M., Francescutti, D.M., Rosenberg, D.R., Thomas, D.M., and Kuhn, D.M. (2012). Genetic depletion of brain 5HT reveals a common molecular pathway mediating compulsivity and impulsivity. J. Neurochem. *121*, 974–984.

Armstrong-James, M., and Millar, J. (1979). Carbon fibre microelectrodes. J. Neurosci. Methods *1*, 279–287.

Arruda, V.R., Fields, P.A., Milner, R., Wainwright, L., De Miguel, M.P., Donovan, P.J., Herzog, R.W., Nichols, T.C., Biegel, J.A., Razavi, M., et al. (2001). Lack of germline transmission of vector sequences following systemic administration of recombinant AAV-2 vector in males. Mol. Ther. *4*, 586–592.

Atchison, R.W., Casto, B.C., and Hammon, W.M. (1965). Adenovirus-associated defective virus particles. Science *149*, 754–756.

Azmitia, E.C., and Segal, M. (1978). An autoradiographic analysis of the differential ascending projections of the dorsal and median raphe nuclei in the rat. J. Comp. Neurol. *179*, 641–667.

Bandarabadi, M., Vassalli, A., and Tafti, M. (2020). Sleep as a default state of cortical and subcortical networks. Curr. Opin. Physiol. *15*, 60–67.

Bang, S.J., Jensen, P., Dymecki, S.M., and Commons, K.G. (2012). Projections and interconnections of genetically defined serotonin neurons in mice. Eur. J. Neurosci. *35*, 85–96.

Baskin, B.M., Mai, J.J., Dymecki, S.M., and Kantak, K.M. (2020). Cocaine reward and memory after chemogenetic inhibition of distinct serotonin neuron subtypes in mice. Psychopharmacology *237*, 2633–2648.

Baur, J.E., Kristensen, E.W., May, L.J., Wiedemann, D.J., and Wightman, R.Mark. (1988). Fast-scan voltammetry of biogenic amines. Anal. Chem. *60*, 1268–1272.

Beaudet, A., and Descarries, L. (1981). The fine structure of central serotonin neurons. J. Physiol. (Paris) *77*, 193–203.

Beck, S.G., Pan, Y.-Z., Akanwa, A.C., and Kirby, L.G. (2004). Median and dorsal raphe neurons are not electrophysiologically identical. J. Neurophysiol. *91*, 994–1005.

Bedbrook, C.N., Deverman, B.E., and Gradinaru, V. (2018). Viral strategies for targeting the central and peripheral nervous systems. Annu. Rev. Neurosci. *41*, 323–348.

Belin, M.F., Nanopoulos, D., Didier, M., Aguera, M., Steinbusch, H., Verhofstad, A., Maitre, M., and Pujol, J.F. (1983). Immunohistochemical evidence for the presence of gamma-aminobutyric acid and serotonin in one nerve cell. A study on the raphe nuclei of the rat using antibodies to glutamate decarboxylase and serotonin. Brain Res. *275*, 329–339.

Benveniste, H. (1989). Brain microdialysis. J. Neurochem. *52*, 1667–1679.

Bernt, K.M., Ni, S., Li, Z.-Y., Shayakhmetov, D.M., and Lieber, A. (2003). The effect of sequestration by nontarget tissues on anti-tumor efficacy of systemically applied, conditionally replicating adenovirus vectors. Mol. Ther. *8*, 746–755.

Beyene, A.G., Yang, S.J., and Landry, M.P. (2019). Review article: Tools and trends for probing brain neurochemistry. J. Vac. Sci. Technol. A *37*, 040802.

Bjorvatn, B., and Ursin, R. (1998). Changes in sleep and wakefulness following 5-HT1A ligands given systemically and locally in different brain regions. Rev. Neurosci. *9*, 265–273.

Blakely, R.D., Berson, H.E., Fremeau, R.T., Caron, M.G., Peek, M.M., Prince, H.K., and Bradley, C.C. (1991). Cloning and expression of a functional serotonin transporter from rat brain. Nature *354*, 66–70.

Blakely, R.D., Ramamoorthy, S., Schroeter, S., Qian, Y., Apparsundaram, S., Galli, A., and DeFelice, L.J. (1998). Regulated phosphorylation and trafficking of antidepressant-sensitive serotonin transporter proteins. Biol. Psychiatry *44*, 169–178.

Bonis-O'Donnell, J.T.D., Page, R.H., Beyene, A.G., Tindall, E.G., McFarlane, I.R., and Landry, M.P. (2017). Dual near-infrared two-photon microscopy for deep-tissue dopamine nanosensor imaging. Adv. Funct. Mater. *27*, 1702112.

Borbely, A.A., Neuhaus, H.U., and Tobler, I. (1981). Effect of p-chlorophenylalanine and tryptophan on sleep, EEG and motor activity in the rat. Behav. Brain Res. *2*, 1–22.

Borden, P.M., Zhang, P., Shivange, A.V., Marvin, J.S., Cichon, J., Dan, C., Podgorski, K., Figueiredo, A., Novak, O., Tanimoto, M., et al. (2020). A fast genetically encoded fluorescent sensor for faithful in vivo acetylcholine detection in mice, fish, worms and flies. bioRxiv. https://doi.org/10.1101/2020.02.07.939504.

Bouhuys, A.L., and Van Den Hoofdakker, R.H. (1977). Effects of midbrain raphe destruction on sleep and locomotor activity in rats. Physiol. Behav. *19*, 535–541.

Bowles, D.E., McPhee, S.W., Li, C., Gray, S.J., Samulski, J.J., Camp, A.S., Li, J., Wang, B., Monahan, P.E., Rabinowitz, J.E., et al. (2012). Phase 1 gene therapy for duchenne muscular dystrophy using a translational optimized AAV vector. Mol. Ther. *20*, 443–455.

Brown, D.A., and Adams, P.R. (1980). Muscarinic suppression of a novel voltage-sensitive K + current in a vertebrate neurone. Nature *283*, 673–676.

Browne, C.J., Abela, A.R., Chu, D., Li, Z., Ji, X., Lambe, E.K., and Fletcher, P.J. (2019). Dorsal raphe serotonin neurons inhibit operant responding for reward via inputs to the ventral tegmental area but not the nucleus accumbens: Evidence from studies combining optogenetic stimulation and serotonin reuptake inhibition. Neuropsychopharmacology *44*, 793–804.

Brust, R.D., Corcoran, A.E., Richerson, G.B., Nattie, E., and Dymecki, S.M. (2014). Functional and developmental identification of a molecular subtype of brain serotonergic neuron specialized to regulate breathing dynamics. Cell Rep. *9*, 2152–2165.

Bunin, M.A., and Wightman, R.M. (1998). Quantitative evaluation of 5-hydroxytryptamine (serotonin) neuronal release and uptake: An investigation of extrasynaptic transmission. J. Neurosci. *18*, 4854–4860.

Bunin, M.A., and Wightman, R.M. (1999). Paracrine neurotransmission in the CNS: Involvement of 5-HT. Trends Neurosci. *22*, 377–382.

Burger, C., Gorbatyuk, O.S., Velardo, M.J., Peden, C.S., Williams, P., Zolotukhin, S., Reier, P.J., Mandel, R.J., and Muzyczka, N. (2004). Recombinant AAV viral vectors pseudotyped with viral

capsids from serotypes 1, 2, and 5 display differential efficiency and cell tropism after delivery to different regions of the central nervous system. Mol. Ther. *10*, 302–317.

Cahoy, J.D., Emery, B., Kaushal, A., Foo, L.C., Zamanian, J.L., Christopherson, K.S., Xing, Y., Lubischer, J.L., Krieg, P.A., Krupenko, S.A., et al. (2008). A transcriptome database for astrocytes, neurons, and oligodendrocytes: A new resource for understanding brain development and function. J. Neurosci. *28*, 264–278.

Cai, Y.-Q., Wang, W., Hou, Y.-Y., and Pan, Z.Z. (2014). Optogenetic activation of brainstem serotonergic neurons induces persistent pain sensitization. Mol. Pain *10*, 1–9.

Calizo, L.H., Akanwa, A., Ma, X., Pan, Y.Z., Lemos, J.C., Craige, C., Heemstra, L.A., and Beck, S.G. (2011). Raphe serotonin neurons are not homogenous: Electrophysiological, morphological and neurochemical evidence. Neuropharmacology *61*, 524–543.

Camardo, J.S., Shuster, M.J., Siegelbaum, S.A., and Kandel, E.R. (1983). Modulation of a specific potassium channel in sensory neurons of Aplysia by serotonin and cAMP-dependent protein phosphorylation. Cold Spring Harb. Symp. Quant. Biol. *48*, 213–220.

Candelario, J., and Chachisvilis, M. (2012). Mechanical stress stimulates conformational changes in 5-hydroxytryptamine receptor 1B in bone cells. Cell. Mol. Bioeng. *5*, 277–286.

Cao, J., Packer, J.S., Ramani, V., Cusanovich, D.A., Huynh, C., Daza, R., Qiu, X., Lee, C., Furlan, S.N., Steemers, F.J., et al. (2017). Comprehensive single-cell transcriptional profiling of a multicellular organism. Science *357*, 661–667.

Carey, R.J. (2010). Chapter 3.2 - Serotonin and basal sensory–motor control. In handbook of the behavioral neurobiology of serotonin, C.P. Müller, and B.L. Jacobs, eds. (Elsevier), pp. 325–330.

Carter, P.J., and Samulski, R.J. (2000). Adeno-associated viral vectors as gene delivery vehicles. Int. J. Mol. Med. *6*, 17–27.

Cassel, J.-C. (2010). Chapter 3.9 - Experimental studies on the role(s) of serotonin in learning and memory functions. In handbook of the behavioral neurobiology of serotonin, C.P. Müller, and B.L. Jacobs, eds. (Elsevier), pp. 429–447.

Celada, P., Puig, M.V., Casanovas, J.M., Guillazo, G., and Artigas, F. (2001). Control of dorsal raphe serotonergic neurons by the medial prefrontal cortex: Involvement of serotonin-1A, GABAA, and glutamate receptors. J. Neurosci. *21*, 9917–9929.

Celada, P., Puig, M.V., and Artigas, F. (2013). Serotonin modulation of cortical neurons and networks. Front. Integr. Neurosci. *7*, 25.

Cespuglio, R., Walker, E., Gomez, M.-E., and Musolino, R. (1976). Cooling of the nucleus raphe dorsalis induces sleep in the cat. Neurosci. Lett. *3*, 221–227.

Cespuglio, R., Faradji, H., Gomez, M.-E., and Jouvet, M. (1981). Single unit recordings in the nuclei raphe dorsalis and magnus during the sleep-waking cycle of semi-chronic prepared cats. Neurosci. Lett. *24*, 133–138.

Cespuglio, R., Rousset, C., Debilly, G., Rochat, C., and Millan, M.J. (2005). Acute administration of the novel serotonin and noradrenaline reuptake inhibitor, S33005, markedly modifies sleep–wake cycle architecture in the rat. Psychopharmacology *181*, 639–652.

Challis, C., Boulden, J., Veerakumar, A., Espallergues, J., Vassoler, F.M., Pierce, R.C., Beck, S.G., and Berton, O. (2013). Raphe GABAergic neurons mediate the acquisition of avoidance after social defeat. J. Neurosci. *33*, 13978–13988.

Chan, K.Y., Jang, M.J., Yoo, B.B., Greenbaum, A., Ravi, N., Wu, W.-L., Sánchez-Guardado, L., Lois, C., Mazmanian, S.K., Deverman, B.E., et al. (2017). Engineered AAVs for efficient noninvasive gene delivery to the central and peripheral nervous systems. Nat. Neurosci. *20*, 1172–1179.

Chávez, J.L., Hagen, J.A., and Kelley-Loughnane, N. (2017). Fast and selective plasmonic serotonin detection with aptamer-gold nanoparticle conjugates. Sensors *17*, 681.

Chazal, G., and Ralston, H.J. (1987). Serotonin-containing structures in the nucleus raphe dorsalis of the cat: An ultrastructural analysis of dendrites, presynaptic dendrites, and axon terminals. J. Comp. Neurol. *259*, 317–329.

Chefer, V.I., Thompson, A.C., Zapata, A., and Shippenberg, T.S. (2009). Overview of brain microdialysis. Curr. Protoc. Neurosci. *47*, 7.1.1-7.1.28.

Chowdhury, S., and Yamanaka, A. (2016). Optogenetic activation of serotonergic terminals facilitates GABAergic inhibitory input to orexin/hypocretin neurons. Sci. Rep. *6*, 36039.

Chuah, M.K., Petrus, I., De Bleser, P., Le Guiner, C., Gernoux, G., Adjali, O., Nair, N., Willems, J., Evens, H., Rincon, M.Y., et al. (2014). Liver-specific transcriptional modules identified by genome-wide in silico analysis enable efficient gene therapy in mice and non-human primates. Mol. Ther. *22*, 1605–1613.

Cichon, G., Schmidt, H.H., Benhidjeb, T., Löser, P., Ziemer, S., Haas, R., Grewe, N., Schnieders, F., Heeren, J., Manns, M.P., et al. (1999). Intravenous administration of recombinant adenoviruses causes thrombocytopenia, anemia and erythroblastosis in rabbits. J. Gene Med. *1*, 360–371.

Colgan, L.A., Cavolo, S.L., Commons, K.G., and Levitan, E.S. (2012). Action potential-independent and pharmacologically unique vesicular serotonin release from dendrites. J. Neurosci. *32*, 15737–15746.

Commons, K.G. (2009). Locally collateralizing glutamate neurons in the dorsal raphe nucleus responsive to substance P contain vesicular glutamate transporter 3 (VGLUT3). J. Chem. Neuroanat. *38*, 273–281.

Commons, K.G. (2015). Two major network domains within the dorsal raphe nucleus. J. Comp. Neurol. *523*, 1488–1504.

Commons, K.G. (2016). Ascending serotonin neuron diversity under two umbrellas. Brain Struct. Funct. *221*, 3347–3360.

Commons, K.G., Connolley, K.R., and Valentino, R.J. (2003). A neurochemically distinct dorsal raphe-limbic circuit with a potential role in affective disorders. Neuropsychopharmacology *28*, 206–215.

Correia, P.A., Lottem, E., Banerjee, D., Machado, A.S., Carey, M.R., and Mainen, Z.F. (2017). Transient inhibition and long-term facilitation of locomotion by phasic optogenetic activation of serotonin neurons. eLife *6*, e20975.

Crawford, L.K., Craige, C.P., and Beck, S.G. (2010). Increased intrinsic excitability of lateral wing serotonin neurons of the dorsal raphe: A mechanism for selective activation in stress circuits. J. Neurophysiol. *103*, 2652–2663.

Dahlstroem, A., and Fuxe, K. (1964). Evidence for the existence of monoamine-containing neurons in the central nervous system. I. Demonstration of monoamines in the cell bodies of brain stem neurons. Acta Physiol. Scand. Suppl. SUPPL 232:1-55.

Dankoski, E.C., and Wightman, R.M. (2013). Monitoring serotonin signaling on a subsecond time scale. Front. Integr. Neurosci. *7*, 44.

Davidson, B.L., Stein, C.S., Heth, J.A., Martins, I., Kotin, R.M., Derksen, T.A., Zabner, J., Ghodsi, A., and Chiorini, J.A. (2000). Recombinant adeno-associated virus type 2, 4, and 5 vectors: Transduction of variant cell types and regions in the mammalian central nervous system. Proc. Natl. Acad. Sci. U.S.A. *97*, 3428–3432.

Davidsson, M., Wang, G., Aldrin-Kirk, P., Cardoso, T., Nolbrant, S., Hartnor, M., Mudannayake, J., Parmar, M., and Björklund, T. (2019). A systematic capsid evolution approach performed in vivo for the design of AAV vectors with tailored properties and tropism. Proc. Natl. Acad. Sci. U.S.A. *116*, 27053–27062.

Davis, A.S., Federici, T., Ray, W.C., Boulis, N.M., O'Connor, D., Clark, K.R., and Bartlett, J.S. (2015). Rational design and engineering of a modified adeno-associated virus (AAV1)-based vector system for enhanced retrograde gene delivery. Neurosurgery *76*, 216–225.

De Alencastro, G., Pekrun, K., Valdmanis, P., Tiffany, M., Xu, J., and Kay, M.A. (2020). Tracking adeno-associated virus capsid evolution by high-throughput sequencing. Hum. Gene Ther. *31*, 553–564.

Deboer, T. (2020). Circadian regulation of sleep in mammals. Curr. Opin. Physiol. *15*, 89–95.

Deleage, C., Wietgrefe, S.W., Del Prete, G., Morcock, D.R., Hao, X.P., Piatak, M., Bess, J., Anderson, J.L., Perkey, K.E., Reilly, C., et al. (2016). Defining HIV and SIV reservoirs in lymphoid tissues. Pathog. Immun. *1*, 68–106.

Deleage, C., Chan, C.N., Busman-Sahay, K., and Estes, J.D. (2018). Next-generation in situ hybridization approaches to define and quantify HIV and SIV reservoirs in tissue microenvironments. Retrovirology *15*, 4.

De-Miguel, F.F., and Trueta, C. (2005). Synaptic and extrasynaptic secretion of serotonin. Cell. Mol. Neurobiol. *25*, 297–312.

DeRiemer, S.A., Strong, J.A., Albert, K.A., Greengard, P., and Kaczmarek, L.K. (1985). Enhancement of calcium current in Aplysia neurones by phorbol ester and protein kinase C. Nature *313*, 313–316.

Descarries, L., Riad, M., and Parent, M. (2010). Chapter 1.4 - Ultrastructure of the serotonin innervation in the mammalian central nervous system. In handbook of behavioral neuroscience, C.P. Müller, and B.L. Jacobs, eds. (Elsevier), pp. 65–101.

Deverman, B.E., Pravdo, P.L., Simpson, B.P., Kumar, S.R., Chan, K.Y., Banerjee, A., Wu, W.L., Yang, B., Huber, N., Pasca, S.P., et al. (2016). Cre-dependent selection yields AAV variants for widespread gene transfer to the adult brain. Nat. Biotechnol. *34*, 204–209.

Dinopoulos, A., Dori, I., and Parnavelas, J.G. (1993). Serotonergic innervation of the mature and developing lateral septum of the rat: A light and electron microscopic immunocytochemical analysis. Neuroscience *55*, 209–222.

Dixit, A., Parnas, O., Li, B., Chen, J., Fulco, C.P., Jerby-Arnon, L., Marjanovic, N.D., Dionne, D., Burks, T., Raychowdhury, R., et al. (2016). Perturb-seq: Dissecting molecular circuits with scalable single-cell RNA profiling of pooled genetic screens. Cell *167*, 1853-1866.e17.

Dudel, J. (1965). Facilitatory effects of 5-hydroxy-tryptamine on the crayfish neuromuscular junction. Naunyn - Schmiedebergs Arch *249*, 515–528.

Duman, E.A., and Canli, T. (2010). Chapter 3.10 - Social behavior and serotonin. In handbook of the behavioral neurobiology of serotonin, C.P. Müller, and B.L. Jacobs, eds. (Elsevier), pp. 449–456.

Dunlap, K., and Fischbach, G.D. (1981). Neurotransmitters decrease the calcium conductance activated by depolarization of embryonic chick sensory neurones. J. Physiol. *317*, 519–535.

Erickson, J.D., Schafer, M.K., Bonner, T.I., Eiden, L.E., and Weihe, E. (1996). Distinct pharmacological properties and distribution in neurons and endocrine cells of two isoforms of the human vesicular monoamine transporter. Proc. Natl. Acad. Sci. U.S.A. *93*, 5166–5171.

Ewing, A.G., Bigelow, J.C., and Wightman, R.M. (1983). Direct in vivo monitoring of dopamine released from two striatal compartments in the rat. Science *221*, 169–171.

Fallon, J.H., and Loughlin, S.E. (1982). Monoamine innervation of the forebrain: Collateralization. Brain Res. Bull. *9*, 295–307.

Fernandez, S.P., Cauli, B., Cabezas, C., Muzerelle, A., Poncer, J.C., and Gaspar, P. (2016). Multiscale single-cell analysis reveals unique phenotypes of raphe 5-HT neurons projecting to the forebrain. Brain Struct. Funct. *221*, 4007–4025.

Filip, M., and Bader, M. (2009). Overview on 5-HT receptors and their role in physiology and pathology of the central nervous system. Pharmacol. Rep. *61*, 761–777.

Fu, W., Le Maitre, E., Fabre, V., Bernard, J.F., David Xu, Z.Q., and Hokfelt, T. (2010). Chemical neuroanatomy of the dorsal raphe nucleus and adjacent structures of the mouse brain. J. Comp. Neurol. *518*, 3464–3494.

Fuxe, K., Dahlström, A.B., Jonsson, G., Marcellino, D., Guescini, M., Dam, M., Manger, P., and Agnati, L. (2010). The discovery of central monoamine neurons gave volume transmission to the wired brain. Prog. Neurobiol. *90*, 82–100.

Gagnon, D., and Parent, M. (2014). Distribution of VGLUT3 in highly collateralized axons from the rat dorsal raphe nucleus as revealed by single-neuron reconstructions. PLoS One *9*, e87709.

Gao, G., Vandenberghe, L.H., Alvira, M.R., Lu, Y., Calcedo, R., Zhou, X., and Wilson, J.M. (2004). Clades of adeno-associated viruses are widely disseminated in human tissues. J. Virol. *78*, 6381–6388.

Garcia-Garcia, A.L., Canetta, S., Stujenske, J.M., Burghardt, N.S., Ansorge, M.S., Dranovsky, A., and Leonardo, E.D. (2018). Serotonin inputs to the dorsal BNST modulate anxiety in a 5-HT 1A receptor-dependent manner. Mol. Psychiatry *23*, 1990–1997.

Gartside, S.E., Hajos-Korcsok, E., Bagdy, E., Harsing, L.G., Jr., Sharp, T., and Hajos, M. (2000). Neurochemical and electrophysiological studies on the functional significance of burst firing in serotonergic neurons. Neuroscience *98*, 295–300.

Giorgi, A., Migliarini, S., Galbusera, A., Maddaloni, G., Mereu, M., Margiani, G., Gritti, M., Landi, S., Trovato, F., Bertozzi, S.M., et al. (2017). Brain-wide mapping of endogenous serotonergic transmission via chemogenetic fMRI. Cell Rep. *21*, 910–918.

Giraldo, J.P., Landry, M.P., Kwak, S.-Y., Jain, R.M., Wong, M.H., Iverson, N.M., Ben-Naim, M., and Strano, M.S. (2015). A ratiometric sensor using single chirality near-infrared fluorescent carbon nanotubes: Application to in vivo monitoring. Small *11*, 3973–3984.

Glusman, S., and Kravitz, E.A. (1982). The action of serotonin on excitatory nerve terminals in lobster nerve-muscle preparations. J. Physiol. *325*, 223–241.

Gonçalves, L., Nogueira, M.I., Shammah-Lagnado, S.J., and Metzger, M. (2009). Prefrontal afferents to the dorsal raphe nucleus in the rat. Brain Res. Bull. *78*, 240–247.

Grabinski, T.M., Kneynsberg, A., Manfredsson, F.P., and Kanaan, N.M. (2015). A method for combining RNAscope in situ hybridization with immunohistochemistry in thick free-floating brain sections and primary neuronal cultures. PLoS One *10*, e0120120.

Grahame-Smith, D.G. (1964). Tryptophan hydroxylation in brain. Biochem. Biophys. Res. Commun. *16*, 586–592.

Gras, C., Herzog, E., Bellenchi, G.C., Bernard, V., Ravassard, P., Pohl, M., Gasnier, B., Giros, B., and El Mestikawy, S. (2002). A third vesicular glutamate transporter expressed by cholinergic and serotoninergic neurons. J. Neurosci. *22*, 5442–5451.

Green, A.R. (2006). Neuropharmacology of 5-hydroxytryptamine. Br. J. Pharmacol. *147 Suppl 1*, S145-152.

Gutknecht, L., Kriegebaum, C., Waider, J., Schmitt, A., and Lesch, K.-P. (2009). Spatio-temporal expression of tryptophan hydroxylase isoforms in murine and human brain: Convergent data from Tph2 knockout mice. Eur. Neuropsychopharmacol. *19*, 266–282.

Guzmán-Marín, R., Alam, Md.N., Szymusiak, R., Drucker-Colín, R., Gong, H., and McGinty, D. (2000). Discharge modulation of rat dorsal raphe neurons during sleep and waking: Effects of preoptic/basal forebrain warming. Brain Res. *875*, 23–34.

Hackett, N.R., Sawy, T.E., Lee, L.Y., Silva, I., O'Leary, J., Rosengart, T.K., and Crystal, R.G. (2000). Use of quantitative TaqMan real-time PCR to track the time-dependent distribution of gene transfer vectors in vivo. Mol. Ther. *2*, 649–656.

Hale, M.W., and Lowry, C.A. (2011). Functional topography of midbrain and pontine serotonergic systems: Implications for synaptic regulation of serotonergic circuits. Psychopharmacology *213*, 243–264.

Hannon, J., and Hoyer, D. (2008). Molecular biology of 5-HT receptors. Behav. Brain Res. *195*, 198–213.

Harstad, R.K., and Bowser, M.T. (2016). High-speed microdialysis–capillary electrophoresis assays for measuring branched chain amino acid uptake in 3T3-L1 cells. Anal. Chem. *88*, 8115–8122.

Hasegawa, E., Maejima, T., Yoshida, T., Masseck, O.A., Herlitze, S., Yoshioka, M., Sakurai, T., and Mieda, M. (2017). Serotonin neurons in the dorsal raphe mediate the anticataplectic action of orexin neurons by reducing amygdala activity. Proc. Natl. Acad. Sci. U.S.A. *114*, E3526–E3535.

Hastie, E., and Samulski, R.J. (2015). Adeno-associated virus at 50: A golden anniversary of discovery, research, and gene therapy success—A personal perspective. Hum. Gene Ther. *26*, 257–265.

Hayes, D.J., and Greenshaw, A.J. (2011). 5-HT receptors and reward-related behaviour: A review. Neurosci. Biobehav. Rev. *35*, 1419–1449.

Hay-Schmidt, A. (2000). The evolution of the serotonergic nervous system. Proc. Royal Soc. B *267*, 1071–1079.

Haywood, T., Beinat, C., Gowrishankar, G., Patel, C.B., Alam, I.S., Murty, S., and Gambhir, S.S. (2019). Positron emission tomography reporter gene strategy for use in the central nervous system. Proc. Natl. Acad. Sci. U.S.A. *116*, 11402–11407.

Heller, D.A., Baik, S., Eurell, T.E., and Strano, M.S. (2005). Single-walled carbon nanotube spectroscopy in live cells: Towards long-term labels and optical sensors. Adv. Mater. *17*, 2793–2799.

Hendricks, T., Francis, N., Fyodorov, D., and Deneris, E.S. (1999). The ETS domain factor Pet-1 is an early and precise marker of central serotonin neurons and interacts with a conserved element in serotonergic genes. J. Neurosci. *19*, 10348–10356.

Hendricks, T.J., Fyodorov, D.V., Wegman, L.J., Lelutiu, N.B., Pehek, E.A., Yamamoto, B., Silver, J., Weeber, E.J., Sweatt, J.D., and Deneris, E.S. (2003). Pet-1 ETS gene plays a critical role in 5-HT neuron development and is required for normal anxiety-like and aggressive behavior. Neuron *37*, 233–247.

Hensler, J.G. (2010). Chapter 3.5 - Serotonin in mood and emotion. In handbook of the behavioral neurobiology of serotonin, C.P. Müller, and B.L. Jacobs, eds. (Elsevier), pp. 367–378.

Hermonat, P.L., and Muzyczka, N. (1984). Use of adeno-associated virus as a mammalian DNA cloning vector: Transduction of neomycin resistance into mammalian tissue culture cells. Proc. Natl. Acad. Sci. U.S.A. *81*, 6466–6470.

Herring, C.A., Banerjee, A., McKinley, E.T., Simmons, A.J., Ping, J., Roland, J.T., Franklin, J.L., Liu, Q., Gerdes, M.J., Coffey, R.J., et al. (2018). Unsupervised trajectory analysis of single-cell RNA-seq and imaging data reveals alternative tuft cell origins in the gut. Cell Syst. *6*, 37-51.e9.

Herrmann, A.-K., and Grimm, D. (2018). High-throughput dissection of AAV–host interactions: The fast and the curious. J. Mol. Biol. *430*, 2626–2640.

Herrmann, A.-K., Bender, C., Kienle, E., Grosse, S., El Andari, J., Botta, J., Schürmann, N., Wiedtke, E., Niopek, D., and Grimm, D. (2019). A robust and all-inclusive pipeline for shuffling of adeno-associated viruses. ACS Synth. Biol. *8*, 194–206.

Hettie, K.S., and Glass, T.E. (2016). Turn-on near-infrared fluorescent sensor for selectively imaging serotonin. ACS Chem. Neurosci. *7*, 21–25.

Hilakivi, I., Kovala, T., Leppävuori, A., and Shvaloff, A. (1987). Effects of serotonin and noradrenaline uptake blockers on wakefulness and sleep in cats. Pharmacol. Toxicol. *60*, 161–166.

Hinderer, C., Katz, N., Buza, E.L., Dyer, C., Goode, T., Bell, P., Richman, L.K., and Wilson, J.M. (2018). Severe toxicity in nonhuman primates and piglets following high-dose intravenous administration of an adeno-associated virus vector expressing human SMN. Hum. Gene Ther. *29*, 285–298.

Hioki, H., Fujiyama, F., Nakamura, K., Wu, S.-X., Matsuda, W., and Kaneko, T. (2004). Chemically specific circuit composed of vesicular glutamate transporter 3- and preprotachykinin B-producing interneurons in the rat neocortex. Cereb. Cortex *14*, 1266–1275.

Hioki, H., Nakamura, H., Ma, Y.F., Konno, M., Hayakawa, T., Nakamura, K.C., Fujiyama, F., and Kaneko, T. (2010). Vesicular glutamate transporter 3-expressing nonserotonergic projection neurons constitute a subregion in the rat midbrain raphe nuclei. J. Comp. Neurol. *518*, 668–686.

Hockberger, P., and Connor, J.A. (1984). Alteration of calcium conductances and outward current by cyclic adenosine monophosphate (cAMP) in neurons of Limax maximus. Cell. Mol. Neurobiol. *4*, 319–338.

Hoffman, B.J., Mezey, E., and Brownstein, M.J. (1991). Cloning of a serotonin transporter affected by antidepressants. Science *254*, 579–580.

Hoggan, M.D. (1970). Adenovirus associated viruses. Prog. Med. Virol. *12*, 211–239.

Hoggan, M.D., Blacklow, N.R., and Rowe, W.P. (1966). Studies of small DNA viruses found in various adenovirus preparations: Physical, biological, and immunological characteristics. Proc. Natl. Acad. Sci. U.S.A. *55*, 1467–1474.

Horst, M. ter, Verwijnen, S.M., Brouwer, E., Hoeben, R.C., Jong, M. de, Leeuw, B.H.C.G.M. de, and Smitt, P.A.E.S. (2006). Locoregional delivery of adenoviral vectors. J. Nucl. Med. *47*, 1483–1489.

Houdouin, F., Cespuglio, R., and Jouvet, M. (1991). Effects induced by the electrical stimulation of the nucleus raphe dorsalis upon hypothalamic release of 5-hydroxyindole compounds and sleep parameters in the rat. Brain Res. *565*, 48–56.

Hoyer, D. (2017). 5-HT receptor nomenclature: Naming names, does it matter? A tribute to Maurice Rapport. ACS Chem. Neurosci. *8*, 908–919.

Hrvatin, S., Tzeng, C.P., Nagy, M.A., Stroud, H., Koutsioumpa, C., Wilcox, O.F., Assad, E.G., Green, J., Harvey, C.D., Griffith, E.C., et al. (2019). A scalable platform for the development of cell-type-specific viral drivers. eLife *8*, e48089.

Huang, K.W., Ochandarena, N.E., Philson, A.C., Hyun, M., Birnbaum, J.E., Cicconet, M., and Sabatini, B.L. (2019). Molecular and anatomical organization of the dorsal raphe nucleus. eLife *8*, e46464.

Hunter, J.E., Gurda, B.L., Yoon, S.Y., Castle, M.J., and Wolfe, J.H. (2019). In situ hybridization for detection of AAV-mediated gene expression. Methods Mol. Biol. *1950*, 107–122.

Imai, H., Steindler, D.A., and Kitai, S.T. (1986a). The organization of divergent axonal projections from the midbrain raphe nuclei in the rat. J. Comp. Neurol. *243*, 363–380.

Imai, H., Park, M.R., Steindler, D.A., and Kitai, S.T. (1986b). The morphology and divergent axonal organization of midbrain raphe projection neurons in the rat. Brain Dev. *8*, 343–354.

Ishimura, K., Takeuchi, Y., Fujiwara, K., Tominaga, M., Yoshioka, H., and Sawada, T. (1988). Quantitative analysis of the distribution of serotonin-immunoreactive cell bodies in the mouse brain. Neurosci. Lett. *91*, 265–270.

Iwakiri, H., Matsuyama, K., and Mori, S. (1993). Extracellular levels of serotonin in the medial pontine reticular formation in relation to sleep-wake cycle in cats: A microdialysis study. J. Neurosci. Res. *18*, 157–170.

Jackson, B.P., Dietz, S.M., and Wightman, R.M. (1995). Fast-scan cyclic voltammetry of 5-hydroxytryptamine. Anal. Chem. *67*, 1115–1120.

Jackson, J., Bland, B.H., and Antle, M.C. (2009). Nonserotonergic projection neurons in the midbrain raphe nuclei contain the vesicular glutamate transporter VGLUT3. Synapse *63*, 31–41.

Jacobs, B.L., and Azmitia, E.C. (1992). Structure and function of the brain serotonin system. Physiol. Rev. *72*, 165–229.

Jequier, E., Robinson, D.S., Lovenberg, W., and Sjoerdsma, A. (1969). Further studies on tryptophan hydroxylase in rat brainstem and beef pineal. Biochem. Pharmacol. *18*, 1071–1081.

John, C.E., Budygin, E.A., Mateo, Y., and Jones, S.R. (2006). Neurochemical characterization of the release and uptake of dopamine in ventral tegmental area and serotonin in substantia nigra of the mouse. J. Neurochem. *96*, 267–282.

Jouvet, M. (1968). Insomnia and decrease of cerebral 5-hydroxytryptamine after destruction of the raphe system in the cat. Adv. Pharmacol. *6*, 265–279.

Jüttner, J., Szabo, A., Gross-Scherf, B., Morikawa, R.K., Rompani, S.B., Hantz, P., Szikra, T., Esposti, F., Cowan, C.S., Bharioke, A., et al. (2019). Targeting neuronal and glial cell types with synthetic promoter AAVs in mice, non-human primates and humans. Nat. Neurosci. *22*, 1345–1356.

Kachidian, P., Poulat, P., Marlier, L., and Privat, A. (1991). Immunohistochemical evidence for the coexistence of substance P, thyrotropin-releasing hormone, GABA, methionine-enkephalin, and leucin-enkephalin in the serotonergic neurons of the caudal raphe nuclei: A dual labeling in the rat. J. Neurosci. Res. *30*, 521–530.

Kaczmarek, L.K., Strong, J.A., and Kauer, J.A. (1986). Chapter 7 The role of protein kinases in the control of prolonged changes in neuronal excitability. In progress in brain research, W.H. Gispen, and A. Routtenberg, eds. (Elsevier), pp. 77–90.

Kandel, E.R., and Schwartz, J.H. (1982). Molecular biology of learning: Modulation of transmitter release. Science *218*, 433–443.

Kane, M.J., Angoa-Peréz, M., Briggs, D.I., Sykes, C.E., Francescutti, D.M., Rosenberg, D.R., and Kuhn, D.M. (2012). Mice genetically depleted of brain serotonin display social impairments, communication deficits and repetitive behaviors: Possible relevance to autism. PLoS One *7*, e48975.

Kapoor, V., Provost, A.C., Agarwal, P., and Murthy, V.N. (2016). Activation of raphe nuclei triggers rapid and distinct effects on parallel olfactory bulb output channels. Nat. Neurosci. *19*, 271–282.

Kashiwagi, M., and Hayashi, Y. (2020). The existence of two states of sleep as a common trait in various animals and its molecular and neuronal mechanisms. Curr. Opin. Physiol. *15*, 197–202.

Kaushalya, S.K., Desai, R., Arumugam, S., Ghosh, H., Balaji, J., and Maiti, S. (2008). Three-photon microscopy shows that somatic release can be a quantitatively significant component of serotonergic neurotransmission in the mammalian brain. J. Neurosci. Res. *86*, 3469–3480.

Kawagoe, K.T., Zimmerman, J.B., and Wightman, R.M. (1993). Principles of voltammetry and microelectrode surface states. J. Neurosci. Methods *48*, 225–240.

Kim, B., Song, H.S., Jin, H.J., Park, E.J., Lee, S.H., Lee, B.Y., Park, T.H., and Hong, S. (2013). Highly selective and sensitive detection of neurotransmitters using receptor-modified single-walled carbon nanotube sensors. Nanotechnology *24*, 285501.

Klein, M., and Kandel, E.R. (1978). Presynaptic modulation of voltage-dependent Ca2+ current: Mechanism for behavioral sensitization in Aplysia californica. Proc. Natl. Acad. Sci. U.S.A. *75*, 3512–3516.

Klein, A.M., Mazutis, L., Akartuna, I., Tallapragada, N., Veres, A., Li, V., Peshkin, L., Weitz, D.A., and Kirschner, M.W. (2015). Droplet barcoding for single-cell transcriptomics applied to embryonic stem cells. Cell *161*, 1187–1201.

Klein, M., Camardo, J., and Kandel, E.R. (1982). Serotonin modulates a specific potassium current in the sensory neurons that show presynaptic facilitation in Aplysia. Proc. Natl. Acad. Sci. U.S.A. *79*, 5713–5717.

de Kock, C.P.J., Cornelisse, L.N., Burnashev, N., Lodder, J.C., Timmerman, A.J., Couey, J.J., Mansvelder, H.D., and Brussaard, A.B. (2006). NMDA receptors trigger neurosecretion of 5-HT within dorsal raphé nucleus of the rat in the absence of action potential firing. J. Physiol. *577*, 891–905.

Koella, W., and Czicman, J. (1966). Mechanism of the EEG-synchronizing action of serotonin. Am. J. Physiol. Renal Physiol. *211*, 926–934.

Koella, W.P., Feldstein, A., and Czicman, J.S. (1968). The effect of para-chlorophenylalanine on the sleep of cats. Electroencephalogr. Clin. Neurophysiol. *25*, 481–490.

Körbelin, J., Sieber, T., Michelfelder, S., Lunding, L., Spies, E., Hunger, A., Alawi, M., Rapti, K., Indenbirken, D., Müller, O.J., et al. (2016a). Pulmonary targeting of adeno-associated viral vectors by next-generation sequencing-guided screening of random capsid displayed peptide libraries. Mol. Ther. *24*, 1050–1061.

Körbelin, J., Dogbevia, G., Michelfelder, S., Ridder, D.A., Hunger, A., Wenzel, J., Seismann, H., Lampe, M., Bannach, J., Pasparakis, M., et al. (2016b). A brain microvasculature endothelial cell-specific viral vector with the potential to treat neurovascular and neurological diseases. EMBO Mol. Med. *8*, 609–625.

Kothari, P., De, B.P., He, B., Chen, A., Chiuchiolo, M.J., Kim, D., Nikolopoulou, A., Amor-Coarasa, A., Dyke, J.P., Voss, H.U., et al. (2017). Radioiodinated capsids facilitate in vivo non-invasive tracking of adeno-associated gene transfer vectors. Sci. Rep. *7*, 39594.

Kozai, T.D.Y., Jaquins-Gerstl, A.S., Vazquez, A.L., Michael, A.C., and Cui, X.T. (2015). Brain tissue responses to neural implants impact signal sensitivity and intervention strategies. ACS Chem. Neurosci. *6*, 48–67.

Krueger, K.C., and Deneris, E.S. (2008). Serotonergic transcription of human FEV reveals direct GATA factor interactions and fate of Pet-1-deficient serotonin neuron precursors. J. Neurosci. *28*, 12748–12758.

Kwon, I., and Schaffer, D.V. (2008). Designer gene delivery vectors: Molecular engineering and evolution of adeno-associated viral vectors for enhanced gene transfer. Pharm. Res. *25*, 489–499.

Landry, M.P., Ando, H., Chen, A.Y., Cao, J., Kottadiel, V.I., Chio, L., Yang, D., Dong, J., Lu, T.K., and Strano, M.S. (2017). Single-molecule detection of protein efflux from microorganisms using fluorescent single-walled carbon nanotube sensor arrays. Nat. Nanotechnol. *12*, 368–377.

Lang, J.F., Toulmin, S.A., Brida, K.L., Eisenlohr, L.C., and Davidson, B.L. (2019). Standard screening methods underreport AAV-mediated transduction and gene editing. Nat. Commun. *10*, 3415.

Lawlor, P.A., Bland, R.J., Mouravlev, A., Young, D., and During, M.J. (2009). Efficient gene delivery and selective transduction of glial cells in the mammalian brain by AAV serotypes isolated from nonhuman primates. Mol. Ther. *17*, 1692–1702.

Lee, M.D., and Clifton, P.G. (2010). Chapter 3.3 - Role of the serotonergic system in appetite and ingestion control. In handbook of the behavioral neurobiology of serotonin, C.P. Müller, and B.L. Jacobs, eds. (Elsevier), pp. 331–345.

de Leeuw, C.N., Korecki, A.J., Berry, G.E., Hickmott, J.W., Lam, S.L., Lengyell, T.C., Bonaguro, R.J., Borretta, L.J., Chopra, V., Chou, A.Y., et al. (2016). rAAV-compatible MiniPromoters for restricted expression in the brain and eye. Mol. Brain *9*, 52.

Lelkes, Z., Obál, F., Alföldi, P., Erdös, A., Rubicsek, G., and Benedek, G. (1994). Effects of acute and chronic treatment with trazodone, an antidepressant, on the sleep-wake activity in rats. Pharmacol. Res. *30*, 105–115.

Leon-Pinzon, C., Cercós, M.G., Noguez, P., Trueta, C., and De-Miguel, F.F. (2014). Exocytosis of serotonin from the neuronal soma is sustained by a serotonin and calcium-dependent feedback loop. Front. Cell. Neurosci. *8*, 169.

Lesch, K.P., and Waider, J. (2012). Serotonin in the modulation of neural plasticity and networks: Implications for neurodevelopmental disorders. Neuron *76*, 175–191.

Levine, E.S., and Jacobs, B.L. (1992). Neurochemical afferents controlling the activity of serotonergic neurons in the dorsal raphe nucleus: Microiontophoretic studies in the awake cat. J. Neurosci. *12*, 4037–4044.

Li, Y., Zhong, W., Wang, D., Feng, Q., Liu, Z., Zhou, J., Jia, C., Hu, F., Zeng, J., Guo, Q., et al. (2016). Serotonin neurons in the dorsal raphe nucleus encode reward signals. Nat. Commun. *7*, 10503.

Lidov, H.G.W., and Molliver, M.E. (1982). Immunohistochemical study of the development of serotonergic neurons in the rat CNS. Brain Res. Bull. *9*, 559–604.

Lisowski, L., Tay, S.S., and Alexander, I.E. (2015). Adeno-associated virus serotypes for gene therapeutics. Curr. Opin. Pharmacol. *24*, 59–67.

Liu, C., Maejima, T., Wyler, S.C., Casadesus, G., Herlitze, S., and Deneris, E.S. (2010). Pet-1 is required across different stages of life to regulate serotonergic function. Nat. Neurosci. *13*, 1190–1198.

Liu, Y., Jiang, Y., Si, Y., Kim, J.-Y., Chen, Z.-F., and Rao, Y. (2011). Molecular regulation of sexual preference revealed by genetic studies of 5-HT in the brains of male mice. Nature *472*, 95–99.

Liu, Z., Zhou, J., Li, Y., Hu, F., Lu, Y., Ma, M., Feng, Q., Zhang, J.E., Wang, D., Zeng, J., et al. (2014). Dorsal raphe neurons signal reward through 5-HT and glutamate. Neuron *81*, 1360–1374.

Liu, Z., Lin, R., and Luo, M. (2020). Reward contributions to serotonergic functions. Annu. Rev. Neurosci. *43*, 141–162.

Lottem, E., Lörincz, M.L., and Mainen, Z.F. (2016). Optogenetic activation of dorsal raphe serotonin neurons rapidly inhibits spontaneous but not odor-evoked activity in olfactory cortex. J. Neurosci. *36*, 7–18.

Lovatt, D., Sonnewald, U., Waagepetersen, H.S., Schousboe, A., He, W., Lin, J.H.-C., Han, X., Takano, T., Wang, S., Sim, F.J., et al. (2007). The transcriptome and metabolic gene signature of protoplasmic astrocytes in the adult murine cortex. J. Neurosci. *27*, 12255–12266.

Lovenberg, W., Jequier, E., and Sjoerdsma, A. (1967). Tryptophan hydroxylation: Measurement in pineal gland, brainstem, and carcinoid tumor. Science *155*, 217–219.

Lowry, C.A. (2002). Functional subsets of serotonergic neurones: Implications for control of the hypothalamic-pituitary-adrenal axis. J. Neuroendocrinol. *14*, 911–923.

Lowry, C.A., and Hale, M.W. (2010). Chapter 3.6 - Serotonin and the neurobiology of anxious states. In handbook of the behavioral neurobiology of serotonin, C.P. Müller, and B.L. Jacobs, eds. (Elsevier), pp. 379–397.

Lowry, C.A., Johnson, P.L., Hay-Schmidt, A., Mikkelsen, J., and Shekhar, A. (2005). Modulation of anxiety circuits by serotonergic systems. Stress *8*, 233–246.

Lowry, C.A., Evans, A.K., Gasser, P.J., Hale, M.W., Staub, D.R., and Shekhar, A. (2008). Topographic organization and chemoarchitecture of the dorsal raphe nucleus and the median raphe nucleus. In serotonin and sleep: Molecular, functional and clinical aspects, J.M. Monti, S.R. Pandi-Perumal, B.L. Jacobs, and D.J. Nutt, eds. (Basel: Birkhäuser), pp. 25–67.

Lykken, E.A., Shyng, C., Edwards, R.J., Rozenberg, A., and Gray, S.J. (2018). Recent progress and considerations for AAV gene therapies targeting the central nervous system. J. Neurodev. Disord. *10*, 16.

Lyons, D.G., and Rihel, J. (2020). Sleep circuits and physiology in non-mammalian systems. Curr. Opin. Physiol. *15*, 245–255.

Macosko, E.Z., Basu, A., Satija, R., Nemesh, J., Shekhar, K., Goldman, M., Tirosh, I., Bialas, A.R., Kamitaki, N., Martersteck, E.M., et al. (2015). Highly parallel genome-wide expression profiling of individual cells using nanoliter droplets. Cell *161*, 1202–1214.

Maes, M.E., Colombo, G., Schulz, R., and Siegert, S. (2019). Targeting microglia with lentivirus and AAV: Recent advances and remaining challenges. Neurosci. Lett. *707*, 134310.

Maguire, A.M., Russell, S., Wellman, J.A., Chung, D.C., Yu, Z.-F., Tillman, A., Wittes, J., Pappas, J., Elci, O., Marshall, K.A., et al. (2019). Efficacy, safety, and durability of voretigene neparvovec-

rzyl in RPE65 mutation-associated inherited retinal dystrophy: Results of phase 1 and 3 trials. Ophthalmology *126*, 1273–1285.

Mahajan, R. (2019). Onasemnogene abeparvovec for spinal muscular atrophy: The costlier drug ever. Int. J. Appl. Basic Med. Res. *9*, 127–128.

Maheshri, N., Koerber, J.T., Kaspar, B.K., and Schaffer, D.V. (2006). Directed evolution of adeno-associated virus yields enhanced gene delivery vectors. Nat. Biotechnol. *24*, 198–204.

Marcinkiewcz, C.A., Mazzone, C.M., D'Agostino, G., Halladay, L.R., Hardaway, J.A., DiBerto, J.F., Navarro, M., Burnham, N., Cristiano, C., Dorrier, C.E., et al. (2016). Serotonin engages an anxiety and fear-promoting circuit in the extended amygdala. Nature *537*, 97–101.

Marsic, D., Méndez-Gómez, H.R., and Zolotukhin, S. (2015). High-accuracy biodistribution analysis of adeno-associated virus variants by double barcode sequencing. Mol. Ther. *2*, 15041.

Marvin, J.S., Borghuis, B.G., Tian, L., Cichon, J., Harnett, M.T., Akerboom, J., Gordus, A., Renninger, S.L., Chen, T.-W., Bargmann, C.I., et al. (2013). An optimized fluorescent probe for visualizing glutamate neurotransmission. Nat. Methods *10*, 162–170.

Matias, S., Lottem, E., Dugue, G.P., and Mainen, Z.F. (2017). Activity patterns of serotonin neurons underlying cognitive flexibility. eLife *6*, e20552.

Maudhuit, C., Jolas, T., Lainey, E., Hamon, M., and Adrien, J. (1994). Effects of acute and chronic treatment with amoxapine and cericlamine on the sleep-wakefulness cycle in the rat. Neuropharmacology *33*, 1017–1025.

McBride, W.J. (2010). Chapter 3.7 - Role of serotonin in brain reward and regulation of alcohol drinking behavior. In handbook of the behavioral neurobiology of serotonin, C.P. Müller, and B.L. Jacobs, eds. (Elsevier), pp. 399–414.

McCarty, D.M., Young, S.M., and Samulski, R.J. (2004). Integration of adeno-associated virus (AAV) and recombinant AAV vectors. Annu. Rev. Genet. *38*, 819–845.

McCormick, D.A. (1989). Cholinergic and noradrenergic modulation of thalamocortical processing. Trends Neurosci. *12*, 215–221.

McCormick, D.A. (1992). Cellular mechanisms underlying cholinergic and noradrenergic modulation of neuronal firing mode in the cat and guinea pig dorsal lateral geniculate nucleus. J. Neurosci. *12*, 278–289.

McCormick, D.A., and Bal, T. (1997). Sleep and arousal: Thalamocortical mechanisms. Annu. Rev. Neurosci. *20*, 185–215.

McCown, T.J., Xiao, X., Li, J., Breese, G.R., and Jude Samulski, R. (1996). Differential and persistent expression patterns of CNS gene transfer by an adeno-associated virus (AAV) vector. Brain Res. *713*, 99–107.

McGinty, D.J., and Harper, R.M. (1976). Dorsal raphe neurons: Depression of firing during sleep in cats. Brain Res. *101*, 569–575.

McGinty, D.J., Harper, R.M., and Fairbanks, M.K. (1973). 5-HT-containing neurons: Unit activity in behaving cats. In serotonin and behavior, J. Barchas, and E. Usdin, eds. (Academic Press), pp. 267–279.

Miao, C.H., Nakai, H., Thompson, A.R., Storm, T.A., Chiu, W., Snyder, R.O., and Kay, M.A. (2000). Nonrandom transduction of recombinant adeno-associated virus vectors in mouse hepatocytes in vivo: Cell cycling does not influence hepatocyte transduction. J. Virol. *74*, 3793–3803.

Mich, J.K., Graybuck, L.T., Hess, E.E., Mahoney, J.T., Kojima, Y., Ding, Y., Somasundaram, S., Miller, J.A., Weed, N., Omstead, V., et al. (2020). Functional enhancer elements drive subclass-selective expression from mouse to primate neocortex. bioRxiv. https://doi.org/10.1101/555318.

Mintz, E.M., and Scott, T.J. (2006). Colocalization of serotonin and vesicular glutamate transporter 3-like immunoreactivity in the midbrain raphe of Syrian hamsters (Mesocricetus auratus). Neurosci. Lett. *394*, 97–100.

Miyazaki, K., Miyazaki, K.W., and Doya, K. (2011a). Activation of dorsal raphe serotonin neurons underlies waiting for delayed rewards. J. Neurosci. *31*, 469–479.

Miyazaki, K., Miyazaki, K.W., and Doya, K. (2012a). The role of serotonin in the regulation of patience and impulsivity. Mol. Neurobiol. *45*, 213–224.

Miyazaki, K.W., Miyazaki, K., and Doya, K. (2011b). Activation of the central serotonergic system in response to delayed but not omitted rewards. Eur. J. Neurosci. *33*, 153–160.

Miyazaki, K.W., Miyazaki, K., and Doya, K. (2012b). Activation of dorsal raphe serotonin neurons is necessary for waiting for delayed rewards. J. Neurosci. *32*, 10451–10457.

Miyazaki, K.W., Miyazaki, K., Tanaka, K.F., Yamanaka, A., Takahashi, A., Tabuchi, S., and Doya, K. (2014). Optogenetic activation of dorsal raphe serotonin neurons enhances patience for future rewards. Curr. Biol. *24*, 2033–2040.

Monti, J.M. (2011). Serotonin control of sleep-wake behavior. Sleep Med. Rev. *15*, 269–281.

Moriya, S., Yamashita, A., Nishi, R., Ikoma, Y., Yamanaka, A., and Kuwaki, T. (2019). Acute nociceptive stimuli rapidly induce the activity of serotonin and noradrenalin neurons in the brain stem of awake mice. IBRO Rep. *7*, 1–9.

Mosko, S.S., Haubrich, D., and Jacobs, B.L. (1977). Serotonergic afferents to the dorsal raphe nucleus: Evidence from HRP and synaptosomal uptake studies. Brain Res. *119*, 269–290.

Moukhles, H., Bosler, O., Bolam, J.P., Vallée, A., Umbriaco, D., Geffard, M., and Doucet, G. (1997). Quantitative and morphometric data indicate precise cellular interactions between serotonin terminals and postsynaptic targets in rat substantia nigra. Neuroscience *76*, 1159–1171.

Mouret, J., Bobillier, P., and Jouvet, M. (1968). Insomnia following parachlorophenylalanine in the rat. Eur. J. Pharmacol. *5*, 17–22.

Muller, J.F., Mascagni, F., and McDonald, A.J. (2007). Serotonin-immunoreactive axon terminals innervate pyramidal cells and interneurons in the rat basolateral amygdala. J. Comp. Neurol. *505*, 314–335.

Murphy, D.L., Fox, M.A., Timpano, K.R., Moya, P.R., Ren-Patterson, R., Andrews, A.M., Holmes, A., Lesch, K.-P., and Wendland, J.R. (2008). How the serotonin story is being rewritten by new gene-based discoveries principally related to SLC6A4, the serotonin transporter gene, which functions to influence all cellular serotonin systems. Neuropharmacology *55*, 932–960.

Muzerelle, A., Scotto-Lomassese, S., Bernard, J.F., Soiza-Reilly, M., and Gaspar, P. (2016). Conditional anterograde tracing reveals distinct targeting of individual serotonin cell groups (B5-B9) to the forebrain and brainstem. Brain. Struct. Funct. *221*, 535–561.

Nakatsuka, N., Yang, K.-A., Abendroth, J.M., Cheung, K.M., Xu, X., Yang, H., Zhao, C., Zhu, B., Rim, Y.S., Yang, Y., et al. (2018). Aptamer–field-effect transistors overcome Debye length limitations for small-molecule sensing. Science *362*, 319–324.

Naso, M.F., Tomkowicz, B., Perry, W.L., and Strohl, W.R. (2017). Adeno-associated virus (AAV) as a vector for gene therapy. BioDrugs *31*, 317–334.

Ngo, K.T., Varner, E.L., Michael, A.C., and Weber, S.G. (2017). Monitoring dopamine responses to potassium ion and nomifensine by in vivo microdialysis with online liquid chromatography at one-minute resolution. ACS Chem. Neurosci. *8*, 329–338.

Niederkofler, V., Asher, T.E., Okaty, B.W., Rood, B.D., Narayan, A., Hwa, L.S., Beck, S.G., Miczek, K.A., and Dymecki, S.M. (2016). Identification of serotonergic neuronal modules that affect aggressive behavior. Cell Rep. *17*, 1934–1949.

Nune, S.K., Gunda, P., Thallapally, P.K., Lin, Y.-Y., Forrest, M.L., and Berkland, C.J. (2009). Nanoparticles for biomedical imaging. Expert Opin. Drug Deliv. *6*, 1175–1194.

O'Connor, J.J., and Kruk, Z.L. (1991). Frequency dependence of 5-HT autoreceptor function in rat dorsal raphe and suprachiasmatic nuclei studied using fast cyclic voltammetry. Brain Res. *568*, 123–130.

Ogawa, S.K., Cohen, J.Y., Hwang, D., Uchida, N., and Watabe-Uchida, M. (2014). Organization of monosynaptic inputs to the serotonin and dopamine neuromodulatory systems. Cell Rep. *8*, 1105–1118.

O'Hearn, E., and Molliver, M.E. (1984). Organization of raphe-cortical projections in rat: A quantitative retrograde study. Brain Res. Bull. *13*, 709–726.

Ohmura, Y., Tanaka, K.F., Tsunematsu, T., Yamanaka, A., and Yoshioka, M. (2014). Optogenetic activation of serotonergic neurons enhances anxiety-like behaviour in mice. Int. J. Neuropsychopharmacol. *17*, 1777–1783.

Oikonomou, G., Altermatt, M., Zhang, R., Coughlin, G.M., Montz, C., Gradinaru, V., and Prober, D.A. (2019). The serotonergic raphe promote sleep in zebrafish and mice. Neuron *103*, 686-701.e8.

Ojala, D.S., Sun, S., Santiago-Ortiz, J.L., Shapiro, M.G., Romero, P.A., and Schaffer, D.V. (2018). In vivo selection of a computationally designed SCHEMA AAV library yields a novel variant for infection of adult neural stem cells in the SVZ. Mol. Ther. *26*, 304–319.

Okaty, B.W., Freret, M.E., Rood, B.D., Brust, R.D., Hennessy, M.L., deBairos, D., Kim, J.C., Cook, M.N., and Dymecki, S.M. (2015). Multi-scale molecular deconstruction of the serotonin neuron system. Neuron *88*, 774–791.

Okaty, B.W., Commons, K.G., and Dymecki, S.M. (2019). Embracing diversity in the 5-HT neuronal system. Nat. Rev. Neurosci. *20*, 397.

Okaty, B.W., Sturrock, N., Escobedo Lozoya, Y., Chang, Y., Senft, R.A., Lyon, K.A., Alekseyenko, O.V., and Dymecki, S.M. (2020). A single-cell transcriptomic and anatomic atlas of mouse dorsal raphe Pet1 neurons. eLife *9*, e55523.

de Olmos, J., and Heimer, L. (1980). Double and triple labeling of neurons with fluorescent substances; The study of collateral pathways in the ascending raphe system. Neurosci. Lett. *19*, 7–12.

Papadopoulos, G.C., Parnavelas, J.G., and Buijs, R.M. (1987). Light and electron microscopic immunocytochemical analysis of the serotonin innervation of the rat visual cortex. J. Neurocytol. *16*, 883–892.

Park, S.-H., and Weber, F. (2020). Neural and homeostatic regulation of REM sleep. Front. Psychol. *11*.

Park, S.P., Lopez-Rodriguez, F., Wilson, C.L., Maidment, N., Matsumoto, Y., and Engel, J. (1999). In vivo microdialysis measures of extracellular serotonin in the rat hippocampus during sleep–wakefulness. Brain Res. *833*, 291–296.

Paul, F., Arkin, Y., Giladi, A., Jaitin, D.A., Kenigsberg, E., Keren-Shaul, H., Winter, D., Lara-Astiaso, D., Gury, M., Weiner, A., et al. (2015). Transcriptional heterogeneity and lineage commitment in myeloid progenitors. Cell *163*, 1663–1677.

Paulk, N.K., Pekrun, K., Zhu, E., Nygaard, S., Li, B., Xu, J., Chu, K., Leborgne, C., Dane, A.P., Haft, A., et al. (2018). Bioengineered AAV capsids with combined high human liver transduction in vivo and unique humoral seroreactivity. Mol. Ther. *26*, 289–303.

Peñalva, R.G., Lancel, M., Flachskamm, C., Reul, J.M.H.M., Holsboer, F., and Linthorst, A.C.E. (2003). Effect of sleep and sleep deprivation on serotonergic neurotransmission in the hippocampus: A combined in vivo microdialysis/EEG study in rats. Eur. J. Neurosci. *17*, 1896–1906.

Peng, W., Wu, Z., Song, K., Zhang, S., Li, Y., and Xu, M. (2020). Regulation of sleep homeostasis mediator adenosine by basal forebrain glutamatergic neurons. Science *369*, eabb0556.

Peters, J.L., Miner, L.H., Michael, A.C., and Sesack, S.R. (2004). Ultrastructure at carbon fiber microelectrode implantation sites after acute voltammetric measurements in the striatum of anesthetized rats. J. Neurosci. Methods *137*, 9–23.

Peyron, C., Petit, J.-M., Rampon, C., Jouvet, M., and Luppi, P.-H. (1997). Forebrain afferents to the rat dorsal raphe nucleus demonstrated by retrograde and anterograde tracing methods. Neuroscience *82*, 443–468.

Peyron, C., Rampon, C., Petit, J.-M., and Luppi, P.-H. (2018). Sub-regions of the dorsal raphé nucleus receive different inputs from the brainstem. Sleep Med. *49*, 53–63.

Piersanti, S., Astrologo, L., Licursi, V., Costa, R., Roncaglia, E., Gennetier, A., Ibanes, S., Chillon, M., Negri, R., Tagliafico, E., et al. (2013). Differentiated neuroprogenitor cells incubated with human or canine adenovirus, or lentiviral vectors have distinct transcriptome profiles. PLoS One *8*, e69808.

Pillay, S., and Carette, J.E. (2017). Host determinants of adeno-associated viral vector entry. Curr. Opin. Virol. *24*, 124–131.

Pillay, S., Meyer, N.L., Puschnik, A.S., Davulcu, O., Diep, J., Ishikawa, Y., Jae, L.T., Wosen, J.E., Nagamine, C.M., Chapman, M.S., et al. (2016). An essential receptor for adeno-associated virus infection. Nature *530*, 108–112.

Plock, N., and Kloft, C. (2005). Microdialysis—theoretical background and recent implementation in applied life-sciences. Eur. J. Pharm. Sci. *25*, 1–24.

Polinski, N.K., Gombash, S.E., Manfredsson, F.P., Lipton, J.W., Kemp, C.J., Cole-Strauss, A., Kanaan, N.M., Steece-Collier, K., Kuhn, N.C., Wohlgenant, S.L., et al. (2015). Recombinant adenoassociated virus 2/5-mediated gene transfer is reduced in the aged rat midbrain. Neurobiol. Aging *36*, 1110–1120.

Polinski, N.K., Manfredsson, F.P., Benskey, M.J., Fischer, D.L., Kemp, C.J., Steece-Collier, K., Sandoval, I.M., Paumier, K.L., and Sortwell, C.E. (2016). Impact of age and vector construct on striatal and nigral transgene expression. Mol. Ther. Methods Clin. Dev. *3*, 16082.

Pollak Dorocic, I., Furth, D., Xuan, Y., Johansson, Y., Pozzi, L., Silberberg, G., Carlen, M., and Meletis, K. (2014). A whole-brain atlas of inputs to serotonergic neurons of the dorsal and median raphe nuclei. Neuron *83*, 663–678.

Ponchon, J.Luc., Cespuglio, Raymond., Gonon, Francois., Jouvet, Michel., and Pujol, J.Francois. (1979). Normal pulse polarography with carbon fiber electrodes for in vitro and in vivo determination of catecholamines. Anal. Chem. *51*, 1483–1486.

Portales-Casamar, E., Swanson, D.J., Liu, L., Leeuw, C.N. de, Banks, K.G., Sui, S.J.H., Fulton, D.L., Ali, J., Amirabbasi, M., Arenillas, D.J., et al. (2010). A regulatory toolbox of MiniPromoters to drive selective expression in the brain. Proc. Natl. Acad. Sci. U.S.A. *107*, 16589–16594.

Portas, C.M., and McCarley, R.W. (1994). Behavioral state-related changes of extracellular serotonin concentration in the dorsal raphe nucleus: A microdialysis study in the freely moving cat. Brain Res. *648*, 306–312.

Portas, C.M., Bjorvatn, B., Fagerland, S., Grønli, J., Mundal, V., Sørensen, E., and Ursin, R. (1998). On-line detection of extracellular levels of serotonin in dorsal raphe nucleus and frontal cortex over the sleep/wake cycle in the freely moving rat. Neuroscience *83*, 807–814.

Prouty, E.W., Chandler, D.J., and Waterhouse, B.D. (2017). Neurochemical differences between target-specific populations of rat dorsal raphe projection neurons. Brain Res. *1675*, 28–40.

Puig, M.V., and Gener, T. (2015). Serotonin modulation of prefronto-hippocampal rhythms in health and disease. ACS Chem. Neurosci. *6*, 1017–1025.

Pujol, J.F., Buguet, A., Froment, J.L., Jones, B., and Jouvet, M. (1971). The central metabolism of serotonin in the cat during insomnia. A neurophysiological and biochemical study after administration of p-chlorophenylalanine or destruction of the raphe system. Brain Res. *29*, 195–212.

Pulicherla, N., Shen, S., Yadav, S., Debbink, K., Govindasamy, L., Agbandje-McKenna, M., and Asokan, A. (2011). Engineering liver-detargeted AAV9 vectors for cardiac and musculoskeletal gene transfer. Mol. Ther. *19*, 1070–1078.

Puray-Chavez, M., Tedbury, P.R., Huber, A.D., Ukah, O.B., Yapo, V., Liu, D., Ji, J., Wolf, J.J., Engelman, A.N., and Sarafianos, S.G. (2017). Multiplex single-cell visualization of nucleic acids and protein during HIV infection. Nat. Commun. *8*, 1882.

Qing, K., Mah, C., Hansen, J., Zhou, S., Dwarki, V., and Srivastava, A. (1999). Human fibroblast growth factor receptor 1 is a co-receptor for infection by adeno-associated virus 2. Nat. Med. *5*, 71–77.

Rapport, M.M. (1949). Serum vasoconstrictor (serotonin) the presence of creatinine in the complex; A proposed structure of the vasoconstrictor principle. J. Biol. Chem. *180*, 961–969.

Rapport, M.M., Green, A.A., and Page, I.H. (1948). Crystalline serotonin. Science *108*, 329–330.

Ravindra Kumar, S., Miles, T.F., Chen, X., Brown, D., Dobreva, T., Huang, Q., Ding, X., Luo, Y., Einarsson, P.H., Greenbaum, A., et al. (2020). Multiplexed Cre-dependent selection yields systemic AAVs for targeting distinct brain cell types. Nat. Methods *17*, 541–550.

Ren, J., Friedmann, D., Xiong, J., Liu, C.D., Ferguson, B.R., Weerakkody, T., DeLoach, K.E., Ran, C., Pun, A., Sun, Y., et al. (2018). Anatomically defined and functionally distinct dorsal raphe serotonin sub-systems. Cell *175*, 472-487.e20.

Ren, J., Isakova, A., Friedmann, D., Zeng, J., Grutzner, S.M., Pun, A., Zhao, G.Q., Kolluru, S.S., Wang, R., Lin, R., et al. (2019). Single-cell transcriptomes and whole-brain projections of serotonin neurons in the mouse dorsal and median raphe nuclei. eLife *8*, e49424.

Ridet, J.-L., Rajaofetra, N., Teilhac, J.-R., Geffard, M., and Privat, A. (1993). Evidence for nonsynaptic serotonergic and noradrenergic innervation of the rat dorsal horn and possible involvement of neuron-glia interactions. Neuroscience *52*, 143–157.

Ridet, J.-L., Tamir, H., and Privat, A. (1994). Direct immunocytochemical localization of 5-hydroxytryptamine receptors in the adult rat spinal cord: A light and electron microscopic study using an anti-idiotypic antiserum. J. Neurosci. Res. *38*, 109–121.

Rincon, M.Y., Sarcar, S., Danso-Abeam, D., Keyaerts, M., Matrai, J., Samara-Kuko, E., Acosta-Sanchez, A., Athanasopoulos, T., Dickson, G., Lahoutte, T., et al. (2015). Genome-wide computational analysis reveals cardiomyocyte-specific transcriptional Cis-regulatory motifs that enable efficient cardiac gene therapy. Mol. Ther. *23*, 43–52.

Robbins, T.W., and Crockett, M.J. (2010). Chapter 3.8 - Role of central serotonin in impulsivity and compulsivity: Comparative studies in experimental animals and humans. In handbook of the behavioral neurobiology of serotonin, C.P. Müller, and B.L. Jacobs, eds. (Elsevier), pp. 415–427.

Rood, B.D., Calizo, L.H., Piel, D., Spangler, Z.P., Campbell, K., and Beck, S.G. (2014). Dorsal raphe serotonin neurons in mice: Immature hyperexcitability transitions to adult state during first three postnatal weeks suggesting sensitive period for environmental perturbation. J. Neurosci. *34*, 4809–4821.

Rosenberg, A.B., Roco, C.M., Muscat, R.A., Kuchina, A., Sample, P., Yao, Z., Graybuck, L.T., Peeler, D.J., Mukherjee, S., Chen, W., et al. (2018). Single-cell profiling of the developing mouse brain and spinal cord with split-pool barcoding. Science *360*, 176–182.

Sakai, K., and Crochet, S. (2001). Differentiation of presumed serotonergic dorsal raphe neurons in relation to behavior and wake-sleep states. Neuroscience *104*, 1141–1155.

Samulski, R.J., and Muzyczka, N. (2014). AAV-mediated gene therapy for research and therapeutic purposes. Annu. Rev. Virol. *1*, 427–451.

Samulski, R.J., Chang, L.S., and Shenk, T. (1989). Helper-free stocks of recombinant adeno-associated viruses: Normal integration does not require viral gene expression. J. Virol. *63*, 3822–3828.

Saper, C.B., Scammell, T.E., and Lu, J. (2005). Hypothalamic regulation of sleep and circadian rhythms. Nature *437*, 1257–1263.

Satija, R., Farrell, J.A., Gennert, D., Schier, A.F., and Regev, A. (2015). Spatial reconstruction of single-cell gene expression data. Nat. Biotechnol. *33*, 495–502.

Saylor, R.A., and Lunte, S.M. (2015). A review of microdialysis coupled to microchip electrophoresis for monitoring biological events. J. Chromatogr. A *1382*, 48–64.

Scammell, T.E., Arrigoni, E., and Lipton, J.O. (2017). Neural circuitry of wakefulness and sleep. Neuron *93*, 747–765.

Schäfer, M.K.-H., Varoqui, H., Defamie, N., Weihe, E., and Erickson, J.D. (2002). Molecular cloning and functional identification of mouse vesicular glutamate transporter 3 and its expression in subsets of novel excitatory neurons. J. Biol. Chem. *277*, 50734–50748.

Schultz, B.R., and Chamberlain, J.S. (2008). Recombinant adeno-associated virus transduction and integration. Mol. Ther. *16*, 1189–1199.

Schweimer, J.V., and Ungless, M.A. (2010). Phasic responses in dorsal raphe serotonin neurons to noxious stimuli. Neuroscience *171*, 1209–1215.

Sengupta, A., Bocchio, M., Bannerman, D.M., Sharp, T., and Capogna, M. (2017). Control of amygdala circuits by 5-HT neurons via 5-HT and glutamate cotransmission. J. Neurosci. *37*, 1785–1796.

Senoo, M., Matsubara, Y., Fujii, K., Nagasaki, Y., Hiratsuka, M., Kure, S., Uehara, S., Okamura, K., Yajima, A., and Narisawa, K. (2000). Adenovirus-mediated in utero gene transfer in mice and guinea pigs: Tissue distribution of recombinant adenovirus determined by quantitative TaqMan–polymerase chain reaction assay. Mol. Genet. Metab. *69*, 269–276.

Seo, C., Guru, A., Jin, M., Ito, B., Sleezer, B.J., Ho, Y.-Y., Wang, E., Boada, C., Krupa, N.A., Kullakanda, D.S., et al. (2019). Intense threat switches dorsal raphe serotonin neurons to a paradoxical operational mode. Science *363*, 538–542.

Seo, J.W., Ingham, E.S., Mahakian, L., Tumbale, S., Wu, B., Aghevlian, S., Shams, S., Baikoghli, M., Jain, P., Ding, X., et al. (2020). Positron emission tomography imaging of novel AAV capsids maps rapid brain accumulation. Nat. Commun. *11*, 2102.

Shen, S., Bryant, K.D., Brown, S.M., Randell, S.H., and Asokan, A. (2011). Terminal N-linked galactose is the primary receptor for adeno-associated virus 9. J. Biol. Chem. *286*, 13532–13540.

Shen, S., Horowitz, E.D., Troupes, A.N., Brown, S.M., Pulicherla, N., Samulski, R.J., Agbandje-McKenna, M., and Asokan, A. (2013). Engraftment of a galactose receptor footprint onto adeno-associated viral capsids improves transduction efficiency. J. Biol. Chem. *288*, 28814–28823.

Shen Fanxia, Su Hua, Fan Yongfeng, Chen Yongmei, Zhu Yiqian, Liu Weizhong, Young William L., and Yang Guo-Yuan (2006). Adeno-associated viral vector-mediated hypoxia-inducible vascular endothelial growth factor gene expression attenuates ischemic brain injury after focal cerebral ischemia in mice. Stroke *37*, 2601–2606.

Shih, J.C., Wu, J.B., and Chen, K. (2011). Transcriptional regulation and multiple functions of MAO genes. J. Neural Transm. *118*, 979–986.

Shikanai, H., Yoshida, T., Konno, K., Yamasaki, M., Izumi, T., Ohmura, Y., Watanabe, M., and Yoshioka, M. (2012). Distinct neurochemical and functional properties of GAD67-containing 5-HT neurons in the rat dorsal raphe nucleus. J. Neurosci. *32*, 14415–14426.

Shutoh, F., Ina, A., Yoshida, S., Konno, J., and Hisano, S. (2008). Two distinct subtypes of serotonergic fibers classified by co-expression with vesicular glutamate transporter 3 in rat forebrain. Neurosci. Lett. *432*, 132–136.

Siegelbaum, S.A., Camardo, J.S., and Kandel, E.R. (1982). Serotonin and cyclic AMP close single K + channels in Aplysia sensory neurones. Nature *299*, 413–417.

Simão, D., Pinto, C., Fernandes, P., Peddie, C.J., Piersanti, S., Collinson, L.M., Salinas, S., Saggio, I., Schiavo, G., Kremer, E.J., et al. (2016). Evaluation of helper-dependent canine adenovirus vectors in a 3D human CNS model. Gene Ther. *23*, 86–94.

Sommer, C. (2010). Chapter 3.11 - Serotonin in pain and pain control. In handbook of the behavioral neurobiology of serotonin, C.P. Müller, and B.L. Jacobs, eds. (Elsevier), pp. 457–471.

Sommerfelt, L., and Ursin, R. (1987). The effects of zimeldine and alaproclate combined with a small dose of 5-HTP on waking and sleep stages in cats. Behav. Brain Res. *24*, 1–10.

Sommerfelt, L., and Ursin, R. (1991). Behavioral, sleep-waking and EEG power spectral effects following the two specific 5-HT uptake inhibitors zimeldine and alaproclate in cats. Behav. Brain Res. *45*, 105–115.

Spiering, D., Bravo-Cordero, J.J., Moshfegh, Y., Miskolci, V., and Hodgson, L. (2013). Chapter 25 - Quantitative ratiometric imaging of FRET-biosensors in living cells. In methods in cell biology, G. Sluder, and D.E. Wolf, eds. (Academic Press), pp. 593–609.

Stamford, J.A., Kruk, Z.L., Millar, J., and Wightman, R.M. (1984). Striatal dopamine uptake in the rat: In vivo analysis by fast cyclic voltammetry. Neurosci. Lett. *51*, 133–138.

Steinbusch, H.W. (1981). Distribution of serotonin-immunoreactivity in the central nervous system of the rat—Cell bodies and terminals. Neuroscience *6*, 557–618.

Strecker, R.E., Thakkar, M.M., Porkka-Heiskanen, T., Dauphin, L.J., Bjørkum, A.A., and McCarley, R.W. (1999). Behavioral state-related changes of extracellular serotonin concentration in the pedunculopontine tegmental nucleus: A microdialysis study in freely moving animals. Sleep Res. Online *2*, 21–27.

Summerford, C., and Samulski, R.J. (1998). Membrane-associated heparan sulfate proteoglycan is a receptor for adeno-associated virus type 2 virions. J. Virol. *72*, 1438–1445.

Summerford, C., Bartlett, J.S., and Samulski, R.J. (1999). AlphaVbeta5 integrin: A co-receptor for adeno-associated virus type 2 infection. Nat. Med. *5*, 78–82.

Tang, F., Barbacioru, C., Wang, Y., Nordman, E., Lee, C., Xu, N., Wang, X., Bodeau, J., Tuch, B.B., Siddiqui, A., et al. (2009). mRNA-seq whole-transcriptome analysis of a single cell. Nat. Methods *6*, 377–382.

Tang, F., Barbacioru, C., Nordman, E., Li, B., Xu, N., Bashkirov, V.I., Lao, K., and Surani, M.A. (2010). RNA-seq analysis to capture the transcriptome landscape of a single cell. Nat. Protoc. *5*, 516–535.

Teissier, A., Chemiakine, A., Inbar, B., Bagchi, S., Ray, R.S., Palmiter, R.D., Dymecki, S.M., Moore, H., and Ansorge, M.S. (2015). Activity of raphe serotonergic neurons controls emotional behaviors. Cell Rep. *13*, 1965–1976.

Tervo, D.G., Hwang, B.Y., Viswanathan, S., Gaj, T., Lavzin, M., Ritola, K.D., Lindo, S., Michael, S., Kuleshova, E., Ojala, D., et al. (2016). A designer AAV variant permits efficient retrograde access to projection neurons. Neuron *92*, 372–382.

Torda, C. (1967). Effect of brain serotonin depletion on sleep in rats. Brain Res. *6*, 375–377.

Törk, I. (1990). Anatomy of the serotonergic systema. Ann. N. Y. Acad. Sci. *600*, 9–34.

Treutlein, B., Brownfield, D.G., Wu, A.R., Neff, N.F., Mantalas, G.L., Espinoza, F.H., Desai, T.J., Krasnow, M.A., and Quake, S.R. (2014). Reconstructing lineage hierarchies of the distal lung epithelium using single-cell RNA-seq. Nature *509*, 371–375.

Trueta, C., and De-Miguel, F.F. (2012). Extrasynaptic exocytosis and its mechanisms: A source of molecules mediating volume transmission in the nervous system. Front. Physiol. *3*, 319.

Trulson, M.E., and Frederickson, C.J. (1987). A comparison of the electrophysiological and pharmacological properties of serotonin-containing neurons in the nucleus raphe dorsalis, raphe medianus and raphe pallidus recorded from mouse brain slices in vitro: Role of autoreceptors. Brain Res. Bull. *18*, 179–190.

Trulson, M.E., and Jacobs, B.L. (1979). Raphe unit activity in freely moving cats: Correlation with level of behavioral arousal. Brain Res. *163*, 135–150.

Tubio, M.R., Fernandez, N., Fitzsimons, C.P., Copsel, S., Santiago, S., Shayo, C., Davio, C., and Monczor, F. (2010). Expression of a G protein-coupled receptor (GPCR) leads to attenuation of signaling by other GPCRs. J. Biol. Chem. *285*, 14990–14998.

Twarog, B.M., and Page, I.H. (1953). Serotonin content of some mammalian tissues and urine and a method for its determination. Am. J. Physiol. *175*, 157–161.

Uphouse, L., and Guptarak, J. (2010). Chapter 3.4 - Serotonin and sexual behavior. In handbook of the behavioral neurobiology of serotonin, C.P. Müller, and B.L. Jacobs, eds. (Elsevier), pp. 347–365.

Urban, D.J., Zhu, H., Marcinkiewcz, C.A., Michaelides, M., Oshibuchi, H., Rhea, D., Aryal, D.K., Farrell, M.S., Lowery-Gionta, E., Olsen, R.H., et al. (2016). Elucidation of the behavioral program and neuronal network encoded by dorsal raphe serotonergic neurons. Neuropsychopharmacology *41*, 1404–1415.

Ursin, R. (1972). Differential effect of para-chlorophenylalanine on the two slow wave sleep stages in the cat. Acta Physiol. Scand. *86*, 278–285.

Ursin, R. (1980). Does para-chlorophenylalanine produce disturbed waking, disturbed sleep or activation by ponto-geniculo-occipital waves in cats? Waking Sleeping *4*, 211–221.

Ursin, R. (2008). Changing concepts on the role of serotonin in the regulation of sleep and waking. In serotonin and sleep: Molecular, functional and clinical aspects, J.M. Monti, S.R. Pandi-Perumal, B.L. Jacobs, and D.J. Nutt, eds. (Basel: Birkhäuser Basel), pp. 3–21.

Ursin, R., Bjorvatn, B., Sommerfelt, L., and Underland, G. (1989). Increased waking as well as increased synchronization following administration of selective 5-HT uptake inhibitors to rats. Behav. Brain Res. *34*, 117–130.

Usoskin, D., Furlan, A., Islam, S., Abdo, H., Lönnerberg, P., Lou, D., Hjerling-Leffler, J., Haeggström, J., Kharchenko, O., Kharchenko, P.V., et al. (2015). Unbiased classification of sensory neuron types by large-scale single-cell RNA sequencing. Nat. Neurosci. *18*, 145–153.

Van der Perren, A., Toelen, J., Carlon, M., Van den Haute, C., Coun, F., Heeman, B., Reumers, V., Vandenberghe, L.H., Wilson, J.M., Debyser, Z., et al. (2011). Efficient and stable transduction of dopaminergic neurons in rat substantia nigra by rAAV 2/1, 2/2, 2/5, 2/6.2, 2/7, 2/8 and 2/9. Gene Ther. *18*, 517–527.

Van Vliet, K.M., Blouin, V., Brument, N., Agbandje-McKenna, M., and Snyder, R.O. (2008). The role of the adeno-associated virus capsid in gene transfer. Drug Deliv. Syst. *437*, 51–91.

Vance, M.A., Mitchell, A., and Samulski, R.J. (2015). AAV biology, infectivity and therapeutic use from bench to clinic. In gene therapy - Principles and challenges, D. Hashad, ed. (InTech), pp. 119–143.

Varga, V., Losonczy, A., Zemelman, B.V., Borhegyi, Z., Nyiri, G., Domonkos, A., Hangya, B., Holderith, N., Magee, J.C., and Freund, T.F. (2009). Fast synaptic subcortical control of hippocampal circuits. Science *326*, 449–453.

Venner, A., De Luca, R., Sohn, L.T., Bandaru, S.S., Verstegen, A.M.J., Arrigoni, E., and Fuller, P.M. (2019). An inhibitory lateral hypothalamic-preoptic circuit mediates rapid arousals from sleep. Curr. Biol. *29*, 4155-4168.e5.

Venner, A., Broadhurst, R.Y., Sohn, L.T., Todd, W.D., and Fuller, P.M. (2020). Selective activation of serotoninergic dorsal raphe neurons facilitates sleep through anxiolysis. Sleep *43*, zsz231.

Vertes, R.P. (1991). A PHA-L analysis of ascending projections of the dorsal raphe nucleus in the rat. J. Comp. Neurol. *313*, 643–668.

Vertes Robert P., Fortin William J., and Crane Alison M. (1999). Projections of the median raphe nucleus in the rat. J. Comp. Neurol. *407*, 555–582.

Vialli, M., and Erspamer, V. (1937). Ricerche sul secreto delle cellule enterocromaffini. Z. f. Zellforschung u. mikr. Anatomie. *27*, 81–99.

Villani, A.-C., Satija, R., Reynolds, G., Sarkizova, S., Shekhar, K., Fletcher, J., Griesbeck, M., Butler, A., Zheng, S., Lazo, S., et al. (2017). Single-cell RNA-seq reveals new types of human blood dendritic cells, monocytes, and progenitors. Science *356*, eaah4573.

Vitalis, T., Alvarez, C., Chen, K., Shih, J.C., Gaspar, P., and Cases, O. (2003). Developmental expression pattern of monoamine oxidases in sensory organs and neural crest derivatives. J. Comp. Neurol. *464*, 392–403.

Walther, D.J., and Bader, M. (2003). A unique central tryptophan hydroxylase isoform. Biochem. Pharmacol. *66*, 1673–1680.

Walther, D.J., Peter, J.-U., Bashammakh, S., Hörtnagl, H., Voits, M., Fink, H., and Bader, M. (2003). Synthesis of serotonin by a second tryptophan hydroxylase isoform. Science *299*, 76.

Wan, J., Peng, W., Li, X., Qian, T., Song, K., Zeng, J., Deng, F., Hao, S., Feng, J., Zhang, P., et al. (2020). A genetically encoded GRAB sensor for measuring serotonin dynamics in vivo. bioRxiv. https://doi.org/10.1101/2020.02.24.962282.

Wang, D., Tai, P.W.L., and Gao, G. (2019a). Adeno-associated virus vector as a platform for gene therapy delivery. Nat. Rev. Drug Discov. *18*, 358–378.

Wang, H.-L., Zhang, S., Qi, J., Wang, H., Cachope, R., Mejias-Aponte, C.A., Gomez, J.A., Mateo-Semidey, G.E., Beaudoin, G.M.J., Paladini, C.A., et al. (2019b). Dorsal raphe dual serotonin-glutamate neurons drive reward by establishing excitatory synapses on VTA mesoaccumbens dopamine neurons. Cell Rep. *26*, 1128-1142.e7.

Wang, M., Roman, G.T., Schultz, K., Jennings, C., and Kennedy, R.T. (2008). Improved temporal resolution for in vivo microdialysis by using segmented flow. Anal. Chem. *80*, 5607–5615.

Wang, M., Slaney, T., Mabrouk, O., and Kennedy, R.T. (2010). Collection of nanoliter microdialysate fractions in plugs for off-line in vivo chemical monitoring with up to 2s temporal resolution. J. Neurosci. Methods *190*, 39–48.

Wang, S.K., Lapan, S.W., Hong, C.M., Krause, T.B., and Cepko, C.L. (2020). In situ detection of adeno-associated viral vector genomes with SABER-FISH. Mol. Ther. Methods Clin. Dev. *19*, 376–386.

Wei, C., Han, X., Weng, D., Feng, Q., Qi, X., Li, J., and Luo, M. (2018). Response dynamics of midbrain dopamine neurons and serotonin neurons to heroin, nicotine, cocaine, and MDMA. Cell Discov. *4*, 1–16.

Weissbourd, B., Ren, J., DeLoach, K.E., Guenthner, C.J., Miyamichi, K., and Luo, L. (2014). Presynaptic partners of dorsal raphe serotonergic and GABAergic neurons. Neuron *83*, 645–662.

Weitzman, M.D., and Linden, R.M. (2011). Adeno-associated virus biology. In adeno-associated virus: Methods and protocols, R.O. Snyder, and P. Moullier, eds. (Totowa, NJ: Humana Press), pp. 1–23.

Weitzman, E.D., Rapport, M.M., McGregor, P., and Jacoby, J. (1968). Sleep patterns of the monkey and brain serotonin concentration: Effect of p-chlorophenylalanine. Science *160*, 1361–1363.

Welsher, K., Sherlock, S.P., and Dai, H. (2011). Deep-tissue anatomical imaging of mice using carbon nanotube fluorophores in the second near-infrared window. Proc. Natl. Acad. Sci. U.S.A. *108*, 8943–8948.

Westhaus, A., Cabanes-Creus, M., Rybicki, A., Baltazar, G., Navarro, R.G., Zhu, E., Drouyer, M., Knight, M., Albu, R.F., Ng, B.H., et al. (2020). High-throughput in vitro, ex vivo, and in vivo screen of adeno-associated virus vectors based on physical and functional transduction. Hum. Gene Ther. *31*, 575–589.

White Stephen J., Nicklin Stuart A., Büning Hildegard, Brosnan M. Julia, Leike Kristen, Papadakis Emmanuel D., Hallek Michael, and Baker Andrew H. (2004). Targeted gene delivery to vascular tissue in vivo by tropism-modified adeno-associated virus vectors. Circulation *109*, 513–519.

Whitney, M.S., Shemery, A.M., Yaw, A.M., Donovan, L.J., Glass, J.D., and Deneris, E.S. (2016). Adult brain serotonin deficiency causes hyperactivity, circadian disruption, and elimination of siestas. J. Neurosci. *36*, 9828–9842.

Wightman, R.M. (1981). Microvoltammetric electrodes. Anal. Chem. *53*, 1125A-1134A.
Wu, Z., Asokan, A., and Samulski, R.J. (2006). Adeno-associated virus serotypes: Vector toolkit for human gene therapy. Mol. Ther. *14*, 316–327.

Wu, Z., Yang, H., and Colosi, P. (2010). Effect of genome size on AAV vector packaging. Mol. Ther. *18*, 80–86.

Wyler, S.C., Donovan, L.J., Yeager, M., and Deneris, E. (2015). Pet-1 controls tetrahydrobiopterin pathway and Slc22a3 transporter genes in serotonin neurons. ACS Chem. Neurosci. *6*, 1198–1205.

Wyler, S.C., Spencer, W.C., Green, N.H., Rood, B.D., Crawford, L., Craige, C., Gresch, P., McMahon, D.G., Beck, S.G., and Deneris, E. (2016). Pet-1 switches transcriptional targets postnatally to regulate maturation of serotonin neuron excitability. J. Neurosci. *36*, 1758–1774.

Xu, X., Jingwen, Y., and Yuanguo, C. (2011). Pharmacokinetic study of viral vectors for gene therapy: Progress and challenges. Viral Gene Ther.

Yang, H., Sampson, M.M., Senturk, D., and Andrews, A.M. (2015). Sex- and SERT-mediated differences in stimulated serotonin revealed by fast microdialysis. ACS Chem. Neurosci. *6*, 1487–1501.

Ylä-Herttuala, S. (2012). Endgame: Glybera finally recommended for approval as the first gene therapy drug in the European union. Mol. Ther. *20*, 1831–1832.

Yoon, S.Y., Gay-Antaki, C., Ponde, D.E., Poptani, H., Vite, C.H., and Wolfe, J.H. (2014). Quantitative, noninvasive, in vivo longitudinal monitoring of gene expression in the brain by co-AAV transduction with a PET reporter gene. Mol. Ther. Methods Clin. Dev. *1*, 14016.

Zant, J.C., Leenaars, C.H.C., Kostin, A., Van Someren, E.J.W., and Porkka-Heiskanen, T. (2011). Increases in extracellular serotonin and dopamine metabolite levels in the basal forebrain during sleep deprivation. Brain Res. *1399*, 40–48.

Zeisel, A., Muñoz-Manchado, A.B., Codeluppi, S., Lönnerberg, P., Manno, G.L., Juréus, A., Marques, S., Munguba, H., He, L., Betsholtz, C., et al. (2015). Cell types in the mouse cortex and hippocampus revealed by single-cell RNA-seq. Science *347*, 1138–1142.

Zeisel, A., Hochgerner, H., Lönnerberg, P., Johnsson, A., Memic, F., van der Zwan, J., Häring, M., Braun, E., Borm, L.E., La Manno, G., et al. (2018). Molecular architecture of the mouse nervous system. Cell *174*, 999-1014.e22.

Zhang, S., Liu, Y., and Rao, Y. (2013). Serotonin signaling in the brain of adult female mice is required for sexual preference. Proc. Natl. Acad. Sci. U.S.A. *110*, 9968–9973.

Zhang, S., Li, X., Drobizhev, M., and Ai, H. (2020). A fast high-affinity fluorescent serotonin biosensor engineered from a tick lipocalin. bioRxiv. https://doi.org/10.1101/2020.04.18.048397.

Zhang, X., Lu, W., Zheng, Y., Wang, W., Bai, L., Chen, L., Feng, Y., Zhang, Z., and Yuan, Z. (2016). In situ analysis of intrahepatic virological events in chronic hepatitis B virus infection. J. Clin. Invest. *126*, 1079–1092.

Zhao, J., Yue, Y., Patel, A., Wasala, L., Karp, J.F., Zhang, K., Duan, D., and Lai, Y. (2020). High-resolution histological landscape of AAV DNA distribution in cellular compartments and tissues following local and systemic injection. Mol. Ther. Methods Clin. Dev. *18*, 856–868.

Zheng, G.X.Y., Terry, J.M., Belgrader, P., Ryvkin, P., Bent, Z.W., Wilson, R., Ziraldo, S.B., Wheeler, T.D., McDermott, G.P., Zhu, J., et al. (2017). Massively parallel digital transcriptional profiling of single cells. Nat. Commun. *8*, 14049.

Zhong, W., Li, Y., Feng, Q., and Luo, M. (2017). Learning and stress shape the reward response patterns of serotonin neurons. J. Neurosci. *37*, 8863–8875.

Ziegenhain, C., Vieth, B., Parekh, S., Reinius, B., Guillaumet-Adkins, A., Smets, M., Leonhardt, H., Heyn, H., Hellmann, I., and Enard, W. (2017). Comparative analysis of single-cell RNA sequencing methods. Mol. Cell *65*, 631-643.e4.

Zincarelli, C., Soltys, S., Rengo, G., and Rabinowitz, J.E. (2008). Analysis of AAV serotypes 1–9 mediated gene expression and tropism in mice after systemic injection. Mol. Ther. *16*, 1073–1080.

Zingg, B., Chou, X.L., Zhang, Z.G., Mesik, L., Liang, F., Tao, H.W., and Zhang, L.I. (2016). AAV-mediated anterograde transsynaptic tagging: Mapping corticocollicular input-defined neural pathways for defense behaviors. Neuron *93*, 33–47.

Chapter 2

THE SEROTONERGIC RAPHE PROMOTE SLEEP IN ZEBRAFISH AND MICE

Oikonomou, G.*, Altermatt, M.*, Zhang, R., Coughlin, G.M., Montz, C., Gradinaru, V., and Prober, D.A. (2019). The serotonergic raphe promote sleep in zebrafish and mice. Neuron 103, 686-701.e8. doi: 10.1016/j.neuron.2019.05.038.
*equal contribution

2.1 Summary

The role of serotonin (5-HT) in sleep is controversial: early studies suggested a sleep-promoting role, but eventually the paradigm shifted toward a wake-promoting function for the serotonergic raphe. Here, we provide evidence from zebrafish and mice that the raphe are critical for the initiation and maintenance of sleep. In zebrafish, genetic ablation of 5-HT production by the raphe reduces sleep, sleep depth, and the homeostatic response to sleep deprivation. Pharmacological inhibition or ablation of the raphe reduces sleep, while optogenetic stimulation increases sleep. Similarly, in mice, ablation of the raphe increases wakefulness and impairs the homeostatic response to sleep deprivation, whereas tonic optogenetic stimulation at a rate similar to baseline activity induces sleep. Interestingly, burst optogenetic stimulation induces wakefulness in accordance with previously described burst activity of the raphe during arousing stimuli. These results indicate that the serotonergic system promotes sleep in both diurnal zebrafish and nocturnal rodents.

2.2 Introduction

The role of serotonin (5-HT) in sleep has been debated for over 50 years (Ursin, 2008). The multiple roles of the serotonergic system (STS) in animal physiology and behavior (Monti et al., 2008; Müller and Jacobs, 2010) make dissection of any specific aspect a challenge. In the CNS, the raphe, a diffuse network of brainstem nuclei, synthesize 5-HT and send projections to almost every region of the brain (Azmitia and Segal, 1978). Initial studies reported that ablation of the raphe in cats reduced 5-HT levels and sleep, in proportion to the size of the lesion (Jouvet, 1968). Intraperitoneal injections of *para*-chlorophenylalanine (pCPA), an irreversible inhibitor of tryptophan hydroxylase (TPH; the

rate limiting enzyme in 5-HT synthesis), also reduced sleep (Koella et al., 1968; Mouret et al., 1968; Torda, 1967; Weitzman et al., 1968). This work, combined with studies of other neurotransmitters, gave rise to the monoaminergic theory of sleep (Jouvet, 1972), in which 5-HT plays an important sleep-promoting role. However, this paradigm eventually came into doubt (Monti, 2011; Ursin, 2008). Cooling of the dorsal raphe was shown to induce sleep in cats (Cespuglio et al., 1976), while in rats, raphe lesions were reported to cause hyperactivity with no effect on sleep (Bouhuys and Van Den Hoofdakker, 1977). The finding that most serotonergic raphe neurons are active during wakefulness, less active during non-rapid eye movement (NREM) sleep, and mostly silent during rapid eye movement (REM) sleep (McGinty and Harper, 1976; Trulson and Jacobs, 1979), was taken as support for a wake-promoting role for 5-HT and the raphe. In addition, microdialysis studies showed that brain 5-HT levels follow a similar pattern with levels highest during waking, lower during NREM, and lowest during REM (Portas et al., 2000). Currently, the raphe are widely thought to promote wakefulness as part of the ascending arousal system (Saper et al., 2005; Scammell et al., 2017), although the debate is far from resolved (see Discussion).

We decided to investigate the role of 5-HT and the raphe in sleep using modern optogenetic and chemogenetic tools that enable neuronal manipulation with superior spatial and temporal precision. The conserved nature of both the STS and the sleep/wake cycle suggests that using a simple vertebrate system, which lacks the complex behavioral repertoire of murine systems that can confound interpretation of sleep studies, could provide insights translatable to mammals. The zebrafish is a well-established model system for the study of sleep (Oikonomou and Prober, 2017), with extensive anatomical and neurochemical homology to mammals, and has proven useful in uncovering conserved neuromodulatory circuits (Lovett-Barron et al., 2017). Here we show, using both zebrafish and mice, that the serotonergic raphe are a sleep-promoting system that is required for sleep homeostasis but can also induce wakefulness in specific contexts. Our results support an evolutionarily conserved and mode-dependent role for the STS in regulating sleep.

2.3 Results

Serotonin receptor agonists increase sleep and inhibition of 5-HT synthesis reduces sleep in zebrafish

We first sought to verify and expand upon previous pharmacological studies demonstrating a role for the STS in zebrafish sleep (Rihel et al., 2010). We treated zebrafish larvae with the broad-

spectrum serotonergic receptor agonist quipazine, while monitoring their behavior using a video-tracking system (Prober et al., 2006). Animals treated with quipazine showed a reduction in locomotor activity and increase in sleep compared to vehicle-treated controls (Figures S1A-S1E). A reduction in waking activity (i.e. locomotor activity while awake) was also observed, indicating that activation of the STS induces an overall reduction in locomotion during wakefulness. Treatment with buspirone, a broad serotonergic receptor agonist with partial specificity for the inhibitory receptor 5-HT1A, gave similar results (Figures S1F-S1J). In both cases, night sleep phenotypes were associated with longer sleep bouts and reduced sleep latency (time to first sleep bout at night).

To broadly impair serotonergic signaling we used pCPA. Treated larvae had reduced 5-HT immunoreactivity (Figures S2A and S2B) (Airhart et al., 2012), as well as a significant increase in locomotor activity and decrease in sleep, due to fewer and shorter sleep bouts and a longer sleep latency (Figures S2C-S2G). These experiments suggest that the STS promotes sleep in zebrafish.

tph2$^{-/-}$ zebrafish do not produce 5-HT in the raphe and lack serotonergic brain innervation

In most vertebrates, 5-HT is synthesized in several brain regions, including the pineal gland, preoptic area, posterior tuberculum, hypothalamus, midbrain/pons, and medulla oblongata, with the raphe nuclei spanning the midbrain/pons boundary and medulla (Lillesaar, 2011). In placental mammals, brain 5-HT synthesis is limited to the pineal gland and the raphe nuclei. Hypothalamic (Vanhatalo and Soinila, 1998) and thalamic (Lebrand et al., 1996) neurons in mammals are 5-HT positive although they do not express TPH; instead they appear to take up 5-HT through the action of serotonin transporters (Vanhatalo and Soinila, 1998).

Staining for 5-HT in the larval zebrafish brain (Figure 1A) revealed several populations of 5-HT positive cells (Lillesaar et al., 2009; McLean and Fetcho, 2004). These include a small pretectal population and large groups in the posterior tuberculum/hypothalamus that form a prominent horseshoe-like pattern. The pineal gland, where 5-HT serves as a substrate for the production of melatonin (Figure S3A), is also 5-HT positive (Figure 1A). In mammals, the raphe is subdivided into a rostral or superior group that lies on the midbrain/pons boundary (groups B5-B9) (Dahlstroem and Fuxe, 1964) and includes the DRN and the median raphe nuclei (MRN), and a caudal or inferior group in the medulla (groups B1-B3). In zebrafish larvae, the raphe nuclei are also subdivided into superior raphe (SRa) and inferior raphe (IRa) (Figure 1A), while the dispersed medullary 5-HT-

positive neurons have been excluded from the raphe designation, presumably because they do not express *tryptophan hydroxylase* (*tph*).

The zebrafish genome contains three *tph* paralogs (Bellipanni et al., 2002; Teraoka et al., 2004), of which only *tph2* is expressed in the raphe (Teraoka et al., 2004). We used genome editing to generate a zebrafish *tph2* predicted null mutant line (Chen et al., 2013). *tph2*$^{-/-}$ mice show severe developmental retardation and postnatal lethality (Alenina et al., 2009) that make interpretation of behavioral assays problematic. In contrast, *tph2*$^{-/-}$ zebrafish are healthy, develop normally, and are born in Mendelian ratios, although some adults eventually develop scoliosis (data not shown). *tph2* mutant zebrafish lacked 5-HT immunoreactivity in the raphe and showed a dramatic reduction of 5-HT positive fibers throughout the brain (Figure 1A). *tph2* is also expressed in the pretectal group and the pineal gland (Teraoka et al., 2004). In *tph2*$^{-/-}$ animals, 5-HT immunoreactivity was absent from the pretectal group, but the pineal gland still contained 5-HT, presumably due to expression of *tph1a* (Bellipanni et al., 2002), although the signal was reduced compared to sibling controls (Figure 1A). Interestingly, the medullary cells also lost 5-HT signal in *tph2*$^{-/-}$ animals even though these cells do not express *tph2*, suggesting that they take up extracellular 5-HT, similar to thalamic and hypothalamic populations in mammals. These observations corroborate previous studies demonstrating that the *tph2*-expressing raphe are the main source of serotonergic innervation in the zebrafish brain, similar to mammals (Lillesaar et al., 2009).

tph2$^{-/-}$ zebrafish show reduced sleep and altered sleep architecture

We next asked whether genetic loss of 5-HT affects sleep by in-crossing *tph2*$^{+/-}$ animals and monitoring their progeny. *tph2*$^{-/-}$ animals showed increased locomotor and waking activity and reduced sleep (Figures 1B-1F) compared to sibling controls. We observed no such differences between *tph2*$^{+/-}$ and *tph2*$^{+/+}$ animals. The mutant phenotype at night was due to shorter sleep bouts, with no effect on the number of sleep bouts (Figure 1F), suggesting that *tph2*$^{-/-}$ mutants enter sleep as often as controls but fail to maintain the sleep state for the normal amount of time. The mutants also showed an increase in sleep latency at night (Figure 1F). Thus, *tph2*$^{-/-}$ animals are defective in both initiating and maintaining the sleep state.

In the pineal gland, 5-HT is converted by arylalkylamine N-acetyltransferase 2 (AANAT2) to N-acetylserotonin, the substrate for the biosynthesis of melatonin (Figure S3A), a hormone that regulates sleep in mammals (Fisher et al., 2013) and zebrafish (Zhdanova et al., 2001; Gandhi et al.,

2015). We hypothesized that the reduced sleep in *tph2* mutants could be caused not by reduced 5-HT in the raphe, but rather by reduced melatonin levels in the pineal gland due to reduced 5-HT. To test this hypothesis, we used *aanat2* mutant animals, which fail to synthesize melatonin and exhibit reduced sleep at night (Gandhi et al., 2015). We reasoned that if the *tph2* phenotype is caused solely by reduced melatonin levels, *aanat2* should be epistatic to *tph2*, that is, *aanat2*; *tph2* double mutants should show the same sleep phenotype as *aanat2* single mutants. Instead, we found that animals mutant for both *tph2* and *aanat2* slept less than either single mutant (Figures S3B-S3F), indicating that the sleep phenotypes of *tph2* and *aanat2* are additive and not epistatic to each other. This demonstrates that the *tph2*$^{-/-}$ phenotype is not due to reduced melatonin levels.

tph2$^{-/-}$ zebrafish show increased arousal, lighter sleep, and attenuated sleep homeostasis

Because *tph2* mutants show reduced sleep, we asked whether they also exhibit a change in overall arousal. To assess this, we delivered mechano-acoustic stimuli of variable intensities at 1-min intervals during the night, while monitoring behavior (Singh et al., 2015). We determined the fraction of animals that responded to each stimulus, constructed stimulus-response curves (Figure 2A), and calculated the tapping power that resulted in half-maximal response (effective power 50 [EP_{50}]). The EP_{50} of *tph2*$^{-/-}$ animals was not significantly different from that of sibling controls, suggesting that although *tph2* mutants sleep less, they have a normal arousal threshold. However, the *tph2*$^{-/-}$ response curve had an elevated plateau (Figure 2A), suggesting that *tph2* mutants exhibit increased arousal in response to strong stimuli.

To assay sleep depth, we applied the mechano-acoustic stimulus with an inter-trial interval of 5 min. This allows the animals to enter the sleep state between trials; thus, we were able to assay the response of awake or sleeping fish to a mild stimulus. We found that awake *tph2*$^{-/-}$ animals responded as efficiently as controls (Figure 2B, left), but sleeping *tph2*$^{-/-}$ animals showed a significantly higher probability of responding to the stimulus (Figure 2B, right). The observation that *tph2* mutants exit the sleep state more readily suggests a reduction in sleep depth.

The STS has been implicated in sleep homeostasis (see Discussion), so we asked whether zebrafish *tph2* mutants are defective in their response to sleep deprivation. To assay this, we crossed *tph2*$^{+/-}$ to *tph2*$^{-/-}$ animals and monitored the sleep profile of their progeny over a 48-hour period. On the beginning of the second night, we subjected the animals to 6 h of sleep deprivation (SD) by maintaining full daylight conditions and then allowed them to enter recovery sleep by turning off the

lights (Figure 2C). The normalized SD response (see STAR Methods) was significantly reduced in *tph2*$^{-/-}$ animals compared to sibling controls (Figure 2C). This reduced homeostatic response to sleep deprivation is in accordance with a previously-proposed role for the STS in sleep homeostasis (Jouvet, 1999). According to this hypothesis, STS activity and concomitant 5-HT release during the wake period are part of the build-up of homeostatic sleep pressure (see Discussion).

Zebrafish raphe neurons have higher firing rates during the day

Electrophysiological studies have shown that mammalian DRN serotonergic neurons have higher firing rates during wakefulness than during sleep (McGinty and Harper, 1976; Trulson and Jacobs, 1979). Serotonergic neurons have a "distinctive neuronal signature" that is used to identify them (Jacobs and Fornal, 2010), consisting of slow tonic firing (1-6 Hz) that is highly regular, and a long-duration action potential (2-3 ms). We asked whether larval zebrafish raphe 5-HT neurons show similar properties. We used a *Tg(tph2:eGFP)* line and fluorescence microscopy to identify such neurons and performed *in vivo* cell-attached recording to examine their spontaneous activity (Figure 2D). We found that they fire at 1-2 Hz (Figure 2E), with an action potential half-duration of 1-1.5 ms during the day (Figure 2F), similar to mammals. The firing rate was significantly reduced at night (Figure 2E), the main rest phase of zebrafish, similar to sleeping mammals. We also observed a reduction in the length of spontaneous action potentials during the night (Figure 2F). These observations demonstrate conserved electrophysiological properties between raphe 5-HT neurons of zebrafish and mammals.

Ablation of the raphe results in reduced sleep in zebrafish

Having established a sleep-promoting role for *tph2* in zebrafish, we asked whether cellular ablation of the raphe has a similar effect on behavior as genetic ablation of *tph2*. The *tph2* promoter is subject to positional effects (Yokogawa et al., 2012); thus using a 1.2 kb promoter fragment and screening multiple lines, we generated a *Tg(tph2:eNTR-YFP)* line in which the *tph2* promoter drives expression of enhanced nitroreductase (Mathias et al., 2014; Tabor et al., 2014) in the raphe, with no expression observed in the pineal gland or pretectal area (Figures 3A and 3A'). As previously described (Montgomery et al., 2016; Yokogawa et al., 2012)), we observed sparse expression in the spinal cord for this and other *tph2* transgenic lines (data not shown). Unlike a previous transgene (Yokogawa et al., 2012), expression was not limited to the SRa, but instead included both the SRa and the IRa

(Figure 3A). Nitroreductase converts the inert pro-drug metronidazole (MTZ) into a cytotoxic compound that causes cell-autonomous ablation (Curado et al., 2008). Following treatment with MTZ (Figures 3D-3F'), but not vehicle (Figures 3A-3C'), *Tg(tph2:eNTR-YFP)* animals lost both YFP and 5-HT immunoreactivity within the raphe soma and projections**.** Some 5-HT immunoreactive projections remained in the medulla, suggesting that these projections originate from medullary 5-HT positive cells and not the raphe (Figure 3E). After treatment with MTZ, *Tg(tph2:eNTR-YFP)* animals showed increased locomotor and waking activity and reduced sleep, compared to non-transgenic sibling controls (Figures 3G-3K), similar to *tph2* mutants. These behavioral phenotypes were not simply due to the presence of the transgene, as vehicle-treated *Tg(tph2:eNTR-YFP)* animals behaved similarly to non-transgenic siblings (Figures S4A-S4E).

In order to verify that this phenotype is specific to loss of the raphe, we performed 2-photon laser ablation of the superior and inferior raphe at 4 dpf in *Tg(tph2:eGFP)* animals (Figure S4F) and assayed their behavior the next day. These animals showed increased locomotor activity and reduced sleep (Figure S4G-S4K), similar to the chemogenetic ablation phenotype. These results suggest that the raphe are necessary for normal sleep patterns and have an overall sleep-promoting role in zebrafish.

Optogenetic stimulation of the raphe promotes sleep in zebrafish

Having shown that the raphe are necessary for normal amounts of sleep, we next asked whether their stimulation is sufficient to drive sleep. To address this question, we created a *Tg(tph2:ChR2-YFP)* transgenic line in which ChR2 (Lin et al., 2009) is expressed in the raphe (Figures 4A-4C). We used a modification of the video-tracking system (Singh et al., 2015) to expose *Tg(tph2:ChR2-YFP)* animals and non-transgenic sibling controls to 30-min pulses of blue light during the night, with a 90-min inter-trial interval. These animals were maintained under dim light during the day in order to minimize background activation of ChR2; this still allows for normal wake/sleep cycles (Figures S5A-S5E). Upon exposure to blue light, both populations of animals showed a brief spike in locomotor activity (presumably due to a startle response) followed by a return to baseline and then a steady increase in activity during the period of illumination (Figure 4D). Transgenic animals showed reduced locomotor activity (Figure 4D) and increased sleep (Figure 4E) during illumination compared to sibling controls, suggesting that stimulation of the raphe promotes sleep. Interestingly, when we repeated this experiment using *tph2*$^{-/-}$ animals, stimulation of the raphe resulted in reduced

locomotor activity (Figure 4F) but no increase in sleep (Figure 4G). A fraction of larval zebrafish raphe neurons produce GABA (Kawashima et al., 2016), which could mediate 5-HT-independent inhibition of locomotor activity. These results demonstrate that stimulation of the raphe is sufficient to both suppress locomotor activity and increase sleep, and the sleep-promoting effect requires 5-HT.

The *Tg(tph2:ChR2-YFP)* line that we used showed YFP immunoreactivity in the pineal gland (Figures 4A'-4C') in addition to the raphe, although no expression was observed in the pretectal *tph2*-expressing population (Figures 4A-4C). Melatonin has high membrane permeability (Yu et al., 2016) and is thought to be released by passive diffusion (Simonneaux and Ribelayga, 2003), as opposed to being stored in vesicles that fuse with the cell membrane upon membrane depolarization. It is therefore unlikely that the sleep increase observed during exposure of *Tg(tph2:ChR2-YFP)* animals to blue light is due to an increase in melatonin release by the pineal gland. However, to experimentally address this possibility, we created *Tg(aanat2:ChR2-YFP)* animals, which express ChR2 exclusively in the pineal gland (Figures S5F-S5H'), and repeated the optogenetic experiment. We observed no difference in behavior between transgenic animals and non-transgenic sibling controls during blue light exposure (Figures S5I and S5J).

DRN neuronal activity correlates with sleep-wake states in mice

Encouraged by our zebrafish studies, we decided to revisit the question of sleep regulation by the STS in mammals. Previous studies used electrophysiology to record the activity of a few 5-HT neurons across sleep-wake states (McGinty and Harper, 1976) with cell-type determination based on electrophysiological characteristics, which do not allow for unequivocal identification of serotonergic neurons (Allers and Sharp, 2003; Kirby et al., 2003). To confirm these findings using genetically identified serotonergic neurons and to investigate how the combined activity of large numbers of these neurons changes across sleep-wake states, we performed simultaneous polysomnographic (electroencephalogram/electromyogram [EEG/EMG]) and fiber photometry (GCaMP) recordings in the DRN.

SERT-cre mice (Zhuang et al., 2005), in which the serotonin transporter (SERT) promoter drives Cre expression specifically in 5-HT neurons, were implanted with EEG and EMG electrodes and injected with AAV5-Syn-Flex-GCaMP6s or AAV5-EF1a-DIO-eYFP, followed by optical fiber implantation targeting the DRN (Figures 5A, 5B and S6A). We quantified the specificity and

efficiency of GCaMP6s^{+} neurons in the DRN of SERT-cre mice (DRN$^{SERT\text{-}GCaMP6s}$), and found that 93% ± 1% of GCaMP6s-expressing neurons co-expressed TPH2, and that 81% ± 3% of TPH2-expressing neurons co-expressed GCaMP6s. A representative example of an EEG spectrogram, behavioral state classification, EMG, and DRN$^{SERT\text{-}GCaMP6s}$ signal is shown in Figure 5C. In agreement with electrophysiological studies, we observed the highest activity of DRN^{SERT} during wakefulness, followed by NREM and REM. Even though the baseline GCaMP6s signal decreased when animals transitioned from wake to NREM, we still observed bouts of increased DRN^{SERT} activity during periods classified as NREM. However, spectral analysis of EEG signals at a finer timescale suggests that these fluorescence peaks actually mark micro-awakenings (Figure S6B). Due to the short duration (<2 s; window size used for sleep/wake classification is 5 s) and small magnitude of changes in EMG, these periods were classified as NREM. DRN$^{SERT\text{-}eYFP}$ fiber photometry recordings displayed no such fluorescent variations (Figure S6C). To examine the dynamics of DRN^{SERT} population activity over the course of a particular state, fluorescent signals were extracted for each state, normalized with regard to time, and averaged across animals (Figure 5D). The summed neuronal activity level normalized by time was higher during wakefulness than in NREM and REM (Figure S6D). Changes over time in DRN$^{SERT\text{-}GCaMP6s}$ fluorescence was observed for all states (Figure 5D), but only the decreases over the wake and NREM states were statistically significant (Figure S6E).

Next, we focused on changes in DRN^{SERT} activity at state transitions. Fluorescent signal of DRN$^{SERT\text{-}GCaMP6s}$ gradually decreased when an animal transitioned from wake to NREM (Figure 5E). Conversely, a time-locked increase in DRN^{SERT} activity occurred at the transition from NREM to wake (Figure 5F). When considering the activity during NREM >90 s before the transition to REM, DRN^{SERT} activity was lower during REM than in NREM (Figure 5G). Interestingly, DRN$^{SERT\text{-}GCaMP6s}$ fluorescence was lowest just before the transition from NREM to REM (Figure 5G), in agreement with single unit recordings (Trulson and Jacobs, 1979). When an animal transitioned from REM to wake, there was a time-locked increase in fluorescence (Figure 5H), similar to the NREM-to-wake transition. Taken together, these results verify and expand upon observations of putative 5-HT DRN neurons identified based on electrophysiological criteria and provide insights into population activity across states and state transitions.

Ablation of serotonergic neurons leads to increased wakefulness and impairs the homeostatic response to sleep deprivation in mice

Early raphe physical ablation experiments resulted in reduced sleep (Jouvet, 1968), but this phenotype is complicated by the role of the medullary raphe in thermoregulation (Tan and Knight, 2018). Indeed, animals genetically engineered to lack all 5-HT neurons sleep less at an ambient temperature of 23°C but not at 33°C (Buchanan and Richerson, 2010), presumably due to shivering at 23°C, but not at the thermoneutral temperature of 33°C. We reasoned that targeted ablation of the superior raphe (groups B5-B9) while sparing the medullary populations (groups B1-B3) would avoid this complication. Therefore, we implanted SERT-cre mice with EEG and EMG electrodes and performed injections targeting the superior raphe with either AAV5-EF1a-mCherry-FLEX-dtA, which ablates cells expressing Cre recombinase, or a negative control virus (AAV5-EF1a-DIO-eYFP or AAV5-CAG-GFP) (Figures 6A and 6B). Two weeks later, sleep-wake patterns were recorded for 24 h. Subsequent histological analysis showed that only 5-HT neurons in the B5-B9 groups were ablated (B5-B9$^{SERT\text{-}dtA}$: 4% ± 1%, n=8; B5-B9$^{SERT\text{-}eYFP}$ or B5-B9^{GFP} 100% ± 3%, n=9; unpaired t test, $p<0.001$), whereas no change was observed in the B1-B3 groups (B1-B3$^{SERT\text{-}dtA}$: 104% ± 6%, n = 8; B1-B3$^{SERT\text{-}eYFP}$ or B1-B3^{GFP} 100% ± 5%, n=9; unpaired t test, $p>0.05$). The amount of wakefulness in experimental animals was increased at the expense of NREM and REM sleep during both the day and night (Figure 6C), in accordance with a sleep-promoting role for the superior raphe. B5-B9$^{SERT\text{-}dtA}$ animals had fewer wake bouts than controls (Figure 6E), but these wake bouts were longer than those of controls (Figure 6D, note log scale for y axis), resulting in increased time spent in wakefulness (Figure 6C).

To investigate the consequences of STS ablation on sleep homeostasis, animals were subjected to 6 h of SD at the beginning of the light phase following 24 h of baseline polysomnographic recordings. As expected, both B5-B9$^{SERT\text{-}dtA}$ and B5-B9$^{SERT\text{-}eYFP}$ or B5-B9^{GFP} animals showed an increase in sleep following SD (recovery sleep), and the amount of time spent in wake, NREM, or REM state during recovery was similar in both populations (data not shown). A critical feature of recovery sleep is an increase in delta power during NREM (Borbély and Neuhaus, 1979). Indeed, both B5-B9$^{SERT\text{-}dtA}$ and B5-B9$^{SERT\text{-}eYFP}$ or B5-B9^{GFP} animals showed a significant increase in delta power during recovery sleep compared to baseline, although this effect was only significant for the first 2 h of recovery sleep for B5-B9$^{SERT\text{-}dtA}$ animals, whereas it remained significant for at least 6 h for B5-B9$^{SERT\text{-}eYFP}$ or B5-B9^{GFP} animals (Figures S7J and S7K).

Furthermore, B5-B9$^{SERT\text{-}dtA}$ animals showed a significantly smaller increase in delta power compared to B5-B9$^{SERT\text{-}eYFP}$ or B5-B9^{GFP} (Figure 6F), suggesting that SD led to a smaller increase in homeostatic sleep pressure in B5-B9$^{SERT\text{-}dtA}$ animals. These results suggest that STS activity is normally involved in generating homeostatic sleep pressure, in accordance with the hypothesis put forward by Jouvet (1999) (see Discussion).

Optogenetic stimulation of DRN neurons has bidirectional mode-dependent effects on mouse sleep

In addition to a tonic (~1-6 Hz) baseline firing pattern during wakefulness (McGinty and Harper, 1976), 5-HT neurons also fire in bursts (up to ~30 Hz) (Cohen et al., 2015; Liu et al., 2014; Schweimer and Ungless, 2010; Veasey et al., 1995). Therefore, we asked whether different stimulation modes can have different effects on sleep/wake states. To answer this question, we implanted SERT-cre mice with EEG and EMG electrodes, performed bilateral injections with either AAV5-EF1a-DIO-ChR2-eYFP or AAV5-EF1a-DIO-eYFP, and then implanted two optical fibers targeting the DRN (Figures 7A, 7B and S6A). We quantified the specificity and efficiency of ChR2^{+} neurons in the DRN of SERT-cre mice and found that 94% ± 1% of ChR2-expressing neurons co-expressed TPH2, and that 90% ± 1% of TPH2-expressing neurons co-expressed ChR2. We then stimulated the raphe with either a burst or a tonic pattern (Figure 7C). Importantly, the number of stimuli per trial was the same for both stimulation modes. Based on results from preliminary experiments, burst stimulation experiments were conducted during the light phase, when mice are mostly asleep, and tonic stimulation experiments were conducted during the dark phase, when wake states dominate.

Burst optogenetic stimulation of DRN$^{SERT\text{-}ChR2}$ animals caused a sudden decrease in NREM and REM probability and an increase in wake probability (Figure 7D). Changes in probability of sleep-wake states during the first minute of optogenetic stimulation were significantly different between DRN$^{SERT\text{-}ChR2}$ and DRN$^{SERT\text{-}eYFP}$ mice (Figure 7F). Tonic optogenetic stimulation of DRN$^{SERT\text{-}ChR2}$ caused an inhibition of REM similar to burst stimulation, however, it also caused an increase in NREM probability at the expense of wake probability over the course of stimulation (Figure 7G). Changes in probability of sleep-wake states during the last 5 min of optogenetic stimulation were different between DRN$^{SERT\text{-}ChR2}$ and DRN$^{SERT\text{-}eYFP}$ mice (Figure 7I). In DRN$^{SERT\text{-}eYFP}$ animals, neither burst nor tonic optogenetic stimulation affected behavioral states (Figures 7E,

7F, 7H and 7I). In order to determine whether optogenetic stimulation promotes initiation of a particular state, we investigated the latency to state transitions. We found that burst stimulation reduced the latency from NREM or REM to wake (Figure 7J), while tonic stimulation reduced the latency from wake to NREM (Figure 7J). We also asked whether optogenetic stimulation affects the duration of a particular state. Burst stimulation increased the duration of wake bouts (Figure S7A) and decreased the duration of NREM bouts (Figure S7B) while tonic stimulation increased the duration of NREM bouts (Figure S7B) and decreased the duration of wake bouts (Figure S7A).

Spectral analysis demonstrated that burst stimulation of $DRN^{SERT\text{-}ChR2}$ animals reduced delta power, whereas tonic stimulation increased delta power, compared to $DRN^{SERT\text{-}eYFP}$ controls (Figure 7K). Conversely, burst stimulation increased high-frequency power, and tonic stimulation decreased high-frequency power (Figure 7L). These effects on patterns of brain activity are consistent with wake- and NREM-promoting effects of burst and tonic stimulation, respectively. Furthermore, as delta power is a measure of homeostatic sleep pressure (Borbély and Neuhaus, 1979), the increase observed under tonic stimulation is consistent with the idea that baseline STS activity (predominately 1-6 Hz) serves to build homeostatic sleep pressure (Jouvet, 1999).

To corroborate our results with an independent transgenic line, we performed similar experiments using the ePet-cre transgenic mouse line (Scott et al., 2005; Figures S7E, S7F and S7H). Like the SERT-cre line (Zhuang et al., 2005), Cre recombinase is specifically expressed in CNS 5-HT neurons in ePet-cre mice. Surprisingly, neither burst nor tonic optogenetic stimulation of $DRN^{ePet\text{-}ChR2}$ animals had an effect on wake or sleep probability. The ePet-cre mouse line can show imperfect recombination efficiency (Narboux-Neme et al., 2013), so it is possible that fewer neurons were activated in this transgenic background. Indeed, histological quantification revealed that even though 96% ± 1% ChR2-expressing neurons co-expressed TPH2, similar to the SERT-cre line (Figure S7C), only 28% ± 2% TPH2-expressing neurons co-expressed ChR2 in ePet-cre mice, compared to 90% ± 1% in SERT-cre mice (Figure S7D). This suggests that the lack of behavioral phenotypes during stimulation of $DRN^{ePet\text{-}ChR2}$ animals could be due to low levels of 5-HT release compared to SERT-cre mice. To test this hypothesis, we injected the selective serotonin reuptake inhibitor (SSRI) fluoxetine in $DRN^{ePet\text{-}ChR2}$ animals immediately prior to optogenetic stimulation to boost the optogenetically induced increase in extracellular 5-HT concentration (Marcinkiewcz et al., 2016). In this context, burst and tonic stimulation resulted in increased wake and NREM probability (Figures S7G and S7I), respectively, similar to SERT-cre animals.

2.4 Discussion

The debate regarding the role of the STS in sleep regulation has been carefully chronicled elsewhere (Ursin, 2008). In short, initial studies based on lesions and pharmacological inhibition of TPH supported a sleep-promoting role, but later the paradigm shifted in support of a wake-promoting role, mostly due to the wake-active nature of 5-HT DRN neurons. The debate has continued in the modern era with pharmacological work generating conflicting results. For example, ritanserin, an antagonist of the excitatory 5-HT2 receptor family, promotes sleep in humans (Idzikowski et al., 1986) and rats (Dugovic and Wauquier, 1987), but wakefulness in cats (Sommerfelt and Ursin, 1993), while agonists of the inhibitory 5-HT1A receptor decrease wakefulness when administered locally, but increase wakefulness when administered systemically (Portas and Grønli, 2008). Genetic models have often contradicted pharmacology (Adrien, 2008): mice mutant for 5-HT2A show reduced sleep, but treatment with a 5-HT2A receptor antagonist increases sleep (Popa, 2005). However, genetic studies can also be difficult to interpret: while embryonic ablation of *tph2* was reported to not alter total sleep levels in mice (Solarewicz et al., 2015), these results are complicated by severe developmental retardation and postnatal lethality in these animals (Alenina et al., 2009). Genetic ablation of *tph2* in the pons/midbrain raphe nuclei (groups B5-B9) of adult mice was shown to cause hyperactivity and eliminate siestas (Whitney et al., 2016), although ablation of the majority of serotonergic neurons in both the midbrain/pons and medulla of adults using an ePet-cre line caused a reduction only in REM sleep (Iwasaki et al., 2018). Optogenetic inhibition of 5-HT DRN neurons using ePet-cre blocked arousal in response to high levels of CO_2 (Smith et al., 2018), suggesting that the DRN is required for wakefulness induced by hypercapnia.

To limit confounds generated by the diverse role of the STS in animal behavior (Müller and Jacobs, 2010), we first investigated sleep-regulating aspects of the STS in the larval zebrafish, a diurnal vertebrate that displays robust sleep cycles (Prober et al., 2006) but lacks a complicated behavioral repertoire (Dreosti et al., 2015). Our larval zebrafish work supports a sleep-promoting role for the STS. Serotonin receptor agonists increase sleep and TPH inhibition reduces sleep. *tph2* mutant animals exhibit reduced and lighter sleep, increased maximal arousal, and reduced homeostatic response to sleep deprivation. Ablation of the raphe phenocopies the *tph2* mutant phenotype, while optogenetic stimulation increases sleep in a *tph2*-dependent fashion. Interestingly, the electrophysiological properties of the 5-HT raphe neurons of larval zebrafish are similar to those

of mammals: they fire at a regular and slow rate which is elevated during the wake period, and their action potentials are long-lasting.

In mammals, early studies describing the firing pattern of 5-HT neurons were based on single-unit recordings and used electrophysiological criteria to differentiate between serotonergic neurons and other DRN cell types. However, these criteria do not allow for unequivocal identification of serotonergic neurons as non-serotonergic DRN neurons can have similar firing properties (Allers and Sharp, 2003; Kirby et al., 2003). We therefore used fiber photometry to record the activity of genetically identified 5-HT neurons. Our findings confirm results from single-unit recordings (McGinty and Harper, 1976; Trulson and Jacobs, 1979), wherein serotonergic DRN neurons display the highest activity level during the wake state, followed by NREM and REM. Early studies in which 5-HT production was pharmacologically inhibited or the DRN were physically ablated showed a reduction in sleep (Jouvet, 1968; Mouret et al., 1968), but this phenotype was later attributed to increased shivering due to disrupted thermoregulation (Buchanan and Richerson, 2010; Murray et al., 2015). To avoid this complication, we selectively targeted the superior raphe, while leaving intact the thermoregulatory populations in the medulla, and observed a reduction in sleep. Optogenetic activation of the DRN in a tonic pattern, at a frequency similar to that of endogenous baseline activity, reduced wake, and REM probability with a concurrent increase in NREM probability. Thus, in both zebrafish and mice, the STS appears to play a sleep-promoting role.

Our work in zebrafish and mice, as well as classical studies in mammals (McGinty and Harper, 1976; Trulson and Jacobs, 1979), generates an apparent paradox: how can a sleep-promoting system be more active during wakefulness? Jouvet (1999) sought to reconcile this paradox by proposing a role for the STS in sleep homeostasis. According to the two-process model (Borbély, 1982), sleep is regulated by a circadian component (process C), which gates the timing of sleep, and a homeostatic component (process S), which builds sleep pressure during wakefulness. The sleep pressure generated by process S is eventually relieved when the animal enters the sleep state at the time prescribed by process C. Jouvet (1999) proposed that the activity of the STS and concomitant release of 5-HT during wakefulness are part of process S and serve to build sleep pressure by measuring the duration and intensity of waking, presumably along with other somnogenic molecules such as adenosine (Porkka-Heiskanen et al., 1997). Indeed in *Drosophila*, 5-HT promotes sleep and *5HT1* mutants show reduced sleep, as well as reduced rebound sleep following sleep deprivation, in accordance with a role for 5-HT in measuring sleep debt (Yuan et al., 2006). Flies mutant for *trh*

(equivalent to *tph*) or the serotonin receptor *5HT2b* have reduced homeostatic response to sleep deprivation, and a small group of *5HT2b*-expressing neurons in the dorsal fan-shaped body is necessary for rebound sleep (Qian et al., 2017). Mice mutant for *5-HT2A* sleep less and, following sleep deprivation, show a smaller delta power increase compared to controls (Popa, 2005), suggesting a reduced homeostatic sleep drive. Mice mutant for *5-HT2C* also show reduced sleep and disrupted sleep homeostasis (Frank et al., 2002). Here we show that *tph2* mutant zebrafish have reduced response to sleep deprivation, that raphe-ablated mice show reduced increase in delta power after sleep deprivation, and that tonic optogenetic activation of the raphe in mice increases delta power. These results support the hypothesis of Jouvet (1999) that the STS promotes sleep, despite being wake-active, by forming part of the sleep homeostasis system. Thus, the induction of sleep during optogenetic activation of the STS in zebrafish and mice, described here, could be due to a transient increase in sleep pressure.

Distinct and even opposing effects during tonic versus burst activity have been reported for other monoaminergic systems, including dopamine (Goto et al., 2007) and noradrenaline (Aston-Jones and Cohen, 2005). Recently, tonic activation of centromedial thalamic neurons in mice was shown to induce wakefulness, while burst activation induced slow-wave-like activity and enhanced cortical synchrony (Gent et al., 2018). These studies suggest that different activity modes of the same circuit can have opposite behavioral outcomes. Indeed, contrary to tonic stimulation, burst stimulation of the DRN in mice increased wake probability at the expense of NREM and REM. Whereas tonic activity is the typical mode observed in the raphe (Jacobs and Azmitia, 1992), burst activity occurs in specific contexts including reward/punishment (Cohen et al., 2015; Liu et al., 2014), treadmill-induced locomotion (Veasey et al., 1995), and noxious stimuli (Schweimer and Ungless, 2010), all of which are presumably arousing. Thus, we propose that the endogenous baseline mode of tonic activity mediates the sleep-promoting role of the STS, while burst activity is a component of arousal-inducing behaviors. The correlation between burst activity and noxious stimuli suggests that hypercapnia-induced arousal might involve burst firing of STS neurons.

The mechanisms that enable different modes of activity by the STS to generate opposing behavioral outcomes are unclear. In the leech Retzius neuron, tonic stimulation at 1 Hz generates only synaptic release of 5-HT, but burst stimulation at 10 or 20 Hz generates extrasynaptic release of 5-HT from the soma and axonal varicosities (Trueta and De-Miguel, 2012). Thus, different modes of STS activity could translate into different spatial or quantitative patterns of 5-HT release.

Alternatively, tonic and burst modes of activity could recruit different serotonergic sub-systems. It has recently been shown that the DRN consists of anatomic subdivisions with distinct inputs, outputs and functionalities (Ren et al., 2018). It is possible that these sub-systems employ inherently different modes of activity and hence are preferentially recruited by burst versus tonic inputs. Considering that these two hypotheses are not mutually exclusive, and that the number of sub-systems that comprise the STS is likely to increase along with our understanding of it, a significant effort will be required in order to fully elucidate the bimodal effects of the STS on sleep/wake states and on other behaviors.

2.5 Acknowledgements

We thank the Gradinaru and Prober labs for helpful discussions; Viveca Sapin, Uyen Pham, Hannah Hurley, and Tasha Cammidge for zebrafish husbandry assistance; Chanpreet Singh for generating the *Tg(aanat2:ChR2-YFP)* line; Elisha D. Mackey for supervising mouse breeding; Andres Collazo for advice on 2-photon laser ablation; Justin S. Bois for advice on statistics; and Catherine M. Oikonomou for critical reading of the manuscript. This work was supported by the NIH (F32NS082010 to G.O.; NIH BRAIN RF1MH117069 to V.G.; and R01NS070911, R01NS101158, R01NS095824, and R01NS101665 to D.A.P.), Center for Molecular and Cellular Neuroscience of the Chen Institute (to V.G.) and the Beckman Institute for CLARITY, Optogenetics and Vector Engineering Research (to V.G.). G.M.C. is supported by a PGS-D from the National Science and Engineering Research Council (NSERC) of Canada. V.G. is a Heritage Principal Investigator supported by the Heritage Medical Research Institute.

2.6 Author contributions

G.O., M.A., D.A.P., and V.G. designed experiments. G.O. performed zebrafish experiments. M.A. performed mouse experiments. R.Z. performed zebrafish electrophysiology. G.M.C. performed mouse histology and quantification. C.M. isolated the zebrafish *tph2* promoter. V.G. supervised rodent aspects of the project. D.A.P. supervised zebrafish aspects of the project. G.O., M.A., V.G., and D.A.P. wrote the paper with input from R.Z. and G.M.C.

2.7 Declaration of interests

The authors declare no competing interests.

2.8 Main figures

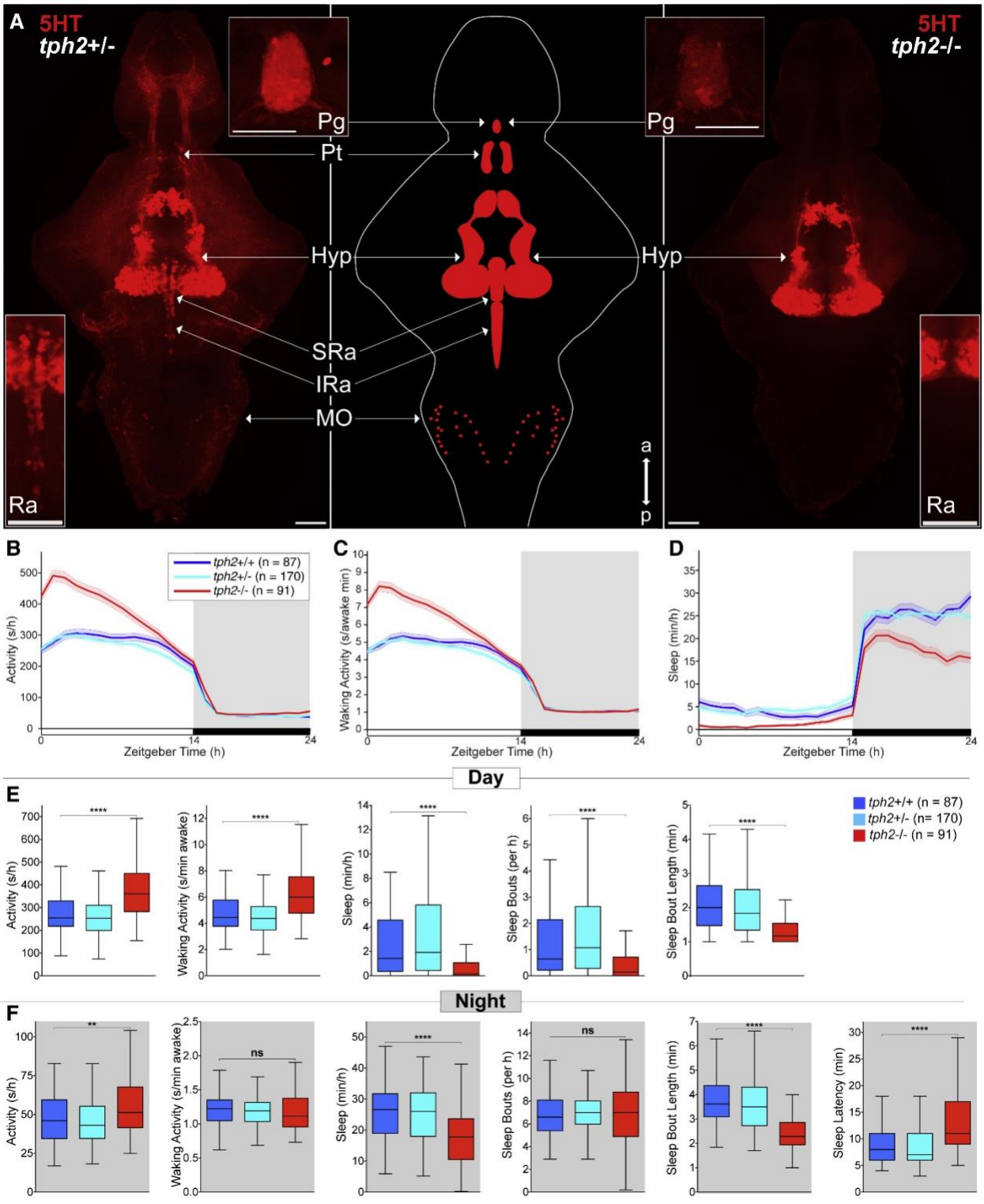

Figure 1. *tph2*$^{-/-}$ zebrafish are more active and sleep less

(A) Maximum intensity projections of 5 days post-fertilization (dpf) *tph2*$^{+/-}$ (left) or *tph2*$^{-/-}$ (right) zebrafish brains immunostained for 5-HT. Middle: brain schematic. Top insets: 5-HT immunostaining of the pineal gland. Bottom insets: magnified view of the raphe. Scale bars, 50 μm; a, anterior; p, posterior; Pg, pineal gland; Pt, pretectal area; Hyp, hypothalamus; Ra, raphe; SRa, superior raphe; IRa, inferior raphe; MO, medulla oblongata.

(B-D) Activity (B), waking activity (C), and sleep (D) for *tph2*$^{+/+}$ (blue), *tph2*$^{+/-}$ (cyan), and *tph2*$^{-/-}$ (red) zebrafish. Line and shading represent mean ± S.E.M.

(E and F) Activity, waking activity, sleep, sleep bout number, sleep bout length during day (E) and night (F) and sleep latency at night (F).

n, number of animals. Not significant (ns) $p>0.05$, *$p<0.05$, **$p<0.01$, ***$p<0.001$, ****$p<0.0001$, Kruskal-Wallis test with Dunn's multiple comparisons test.

See also Figures S1-S3.

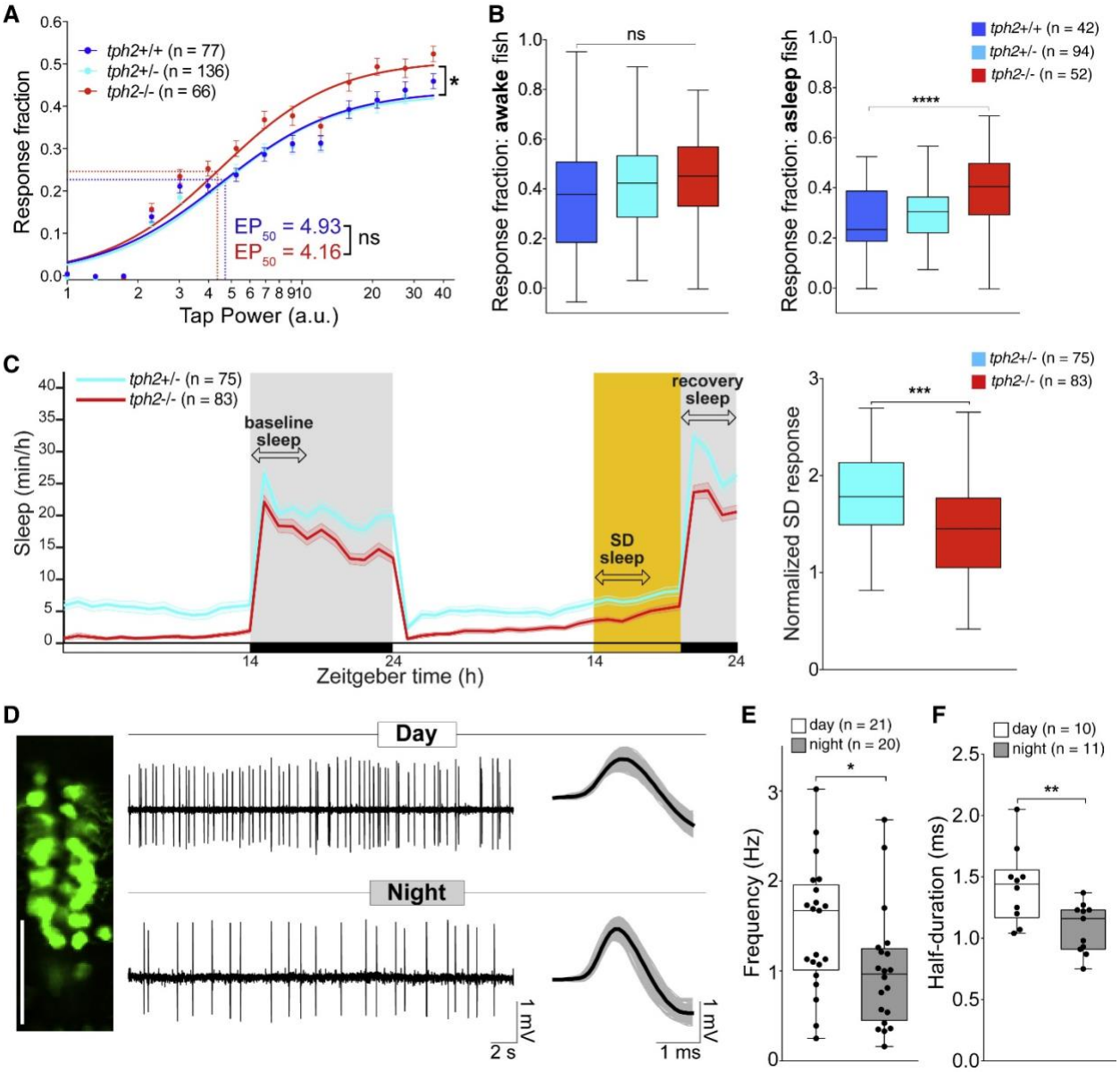

Figure 2. Zebrafish *tph2* mutants show lighter sleep and reduced rebound sleep; zebrafish raphe neurons have higher firing rates during the day

(A) Stimulus-response curves generated using a mechano-acoustic stimulus. *tph2*$^{-/-}$ and sibling control animals were not significantly different in EP_{50}, but mutants exhibited increased maximal response. Data points represent mean ± S.E.M. for 30 trials at each stimulus intensity (extra sum-of-squares F test).

(B) Response of awake (left) and sleeping (right) zebrafish to a mechano-acoustic stimulus. When awake, *tph2*$^{-/-}$ and sibling control animals responded similarly to the stimulus, but when asleep,

tph2$^{-/-}$ animals were significantly more likely to respond (Kruskal-Wallis test with Dunn's multiple comparisons test).

(C) Sleep of *tph2*$^{+/-}$ (cyan) and *tph2*$^{-/-}$ (red) siblings over a 48 h period (5-6 dpf); line and shading represent mean ± S.E.M. Baseline sleep levels were established during the first 4 h (arrow in first gray box) of the first night (first grey box). Sleep deprivation during the first 6 h of the second night was achieved by maintaining daytime white light illumination (yellow shaded box). SD sleep is defined as the sleep during the first 4 h of the sleep deprivation period (arrow in yellow box). Recovery sleep is sleep during the first 4 h after lights-off (arrow in second gray box). Normalized SD response (right) is calculated as recovery sleep / (baseline sleep – SD sleep) (unpaired t test).

(D) Spontaneous firing of representative GFP-positive raphe neurons of *Tg(tph2:eGFP)* zebrafish during the day (top) and night (bottom). A single plane image of the raphe from a *Tg(tph2:eGFP)* 5 dpf zebrafish immunostained for eGFP is shown. Traces on the right show the waveform of action potentials. Black traces represent the average and gray traces represent 748 sorted events during the day and 420 sorted events at night.

(E-F) Spontaneous spike firing frequency (E) and half-duration of spontaneous action potentials (F) of GFP-positive raphe neurons of *Tg(tph2:eGFP)* animals during the day and night (Mann-Whitney test).

n, number of animals (A-C) or neurons (E, F). ns $p>0.05$, *$p<0.05$, **$p<0.01$, ***$p<0.001$, ****$p<0.0001$.

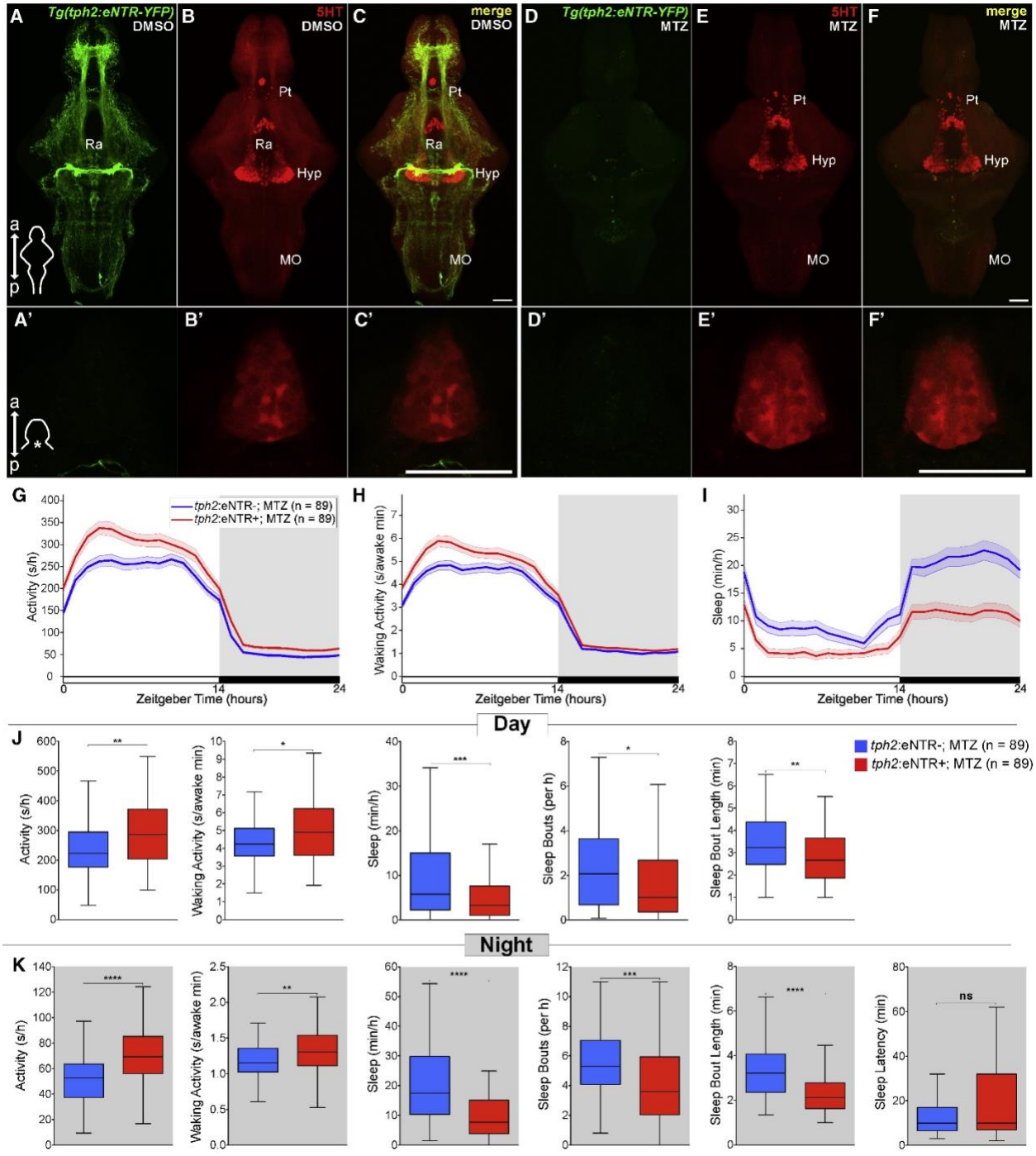

Figure 3. Chemogenetic ablation of the raphe results in decreased sleep in zebrafish

(A-F) Maximum intensity projections of brains (A-F) and single plane images of pineal glands (A'-F') from 5 dpf *Tg(tph2:eNTR-YFP)* zebrafish treated with DMSO vehicle (A-C and A'-C') or MTZ (D-F, D'-F'), and immunostained for 5-HT and YFP. Scale bars, 50 μm; a, anterior; p, posterior; Pt, pretectal area; Hyp, hypothalamus; Ra, raphe; MO, medulla oblongata.

(G-I) Activity (G), waking activity (H), and sleep (I) for 5 dpf *Tg(tph2:eNTR-YFP)* (red) and non-transgenic sibling control (blue) zebrafish treated with MTZ. Line and shading represent mean ± S.E.M.

(J and K) Activity, waking activity, sleep, sleep bout number, sleep bout length during day (J) and night (K), and sleep latency at night (K). n, number of animals. ns $p>0.05$, *$p<0.05$, **$p<0.01$, ***$p<0.001$, ****$p<0.0001$, Mann-Whitney test.

See also Figure S4.

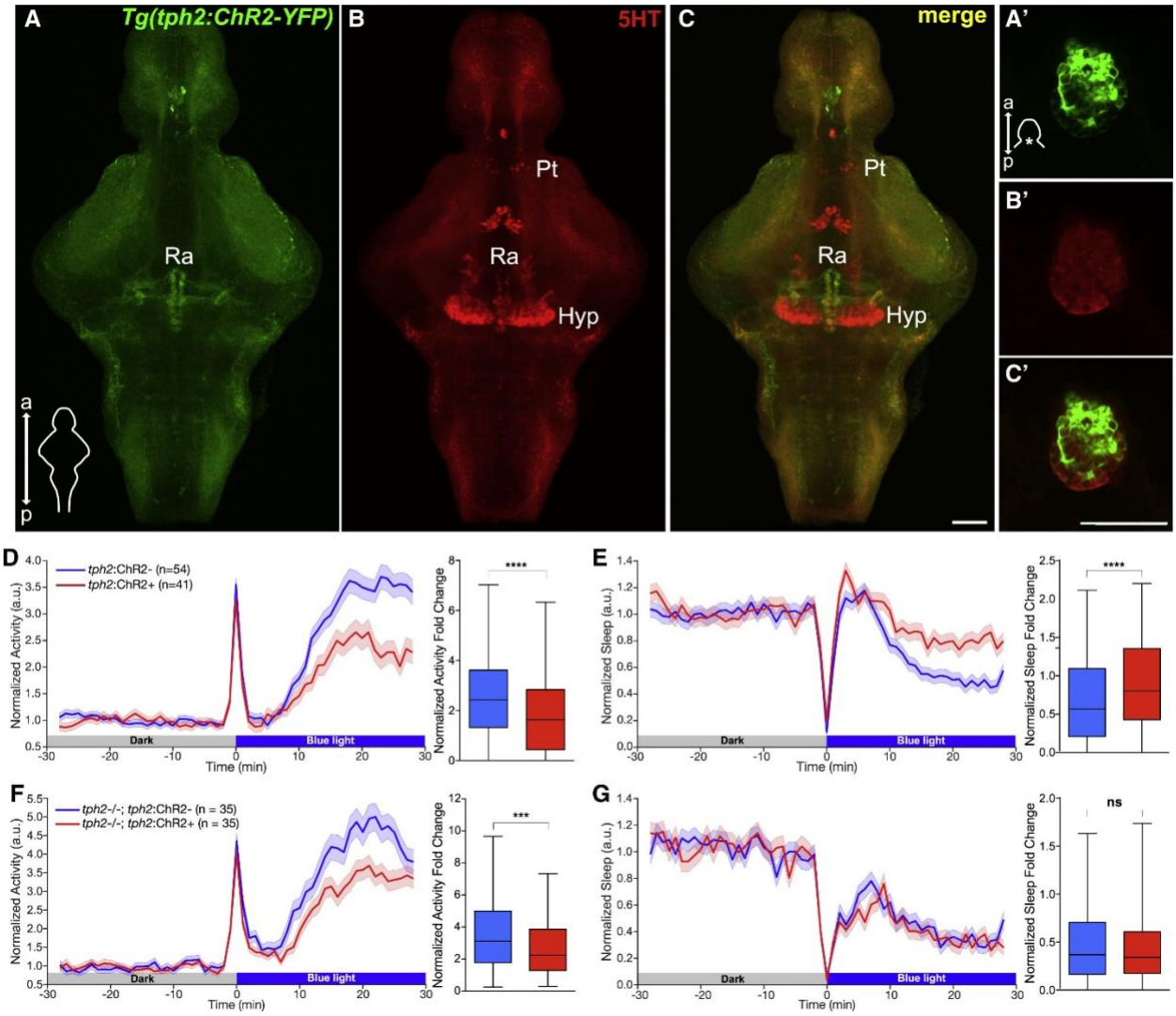

Figure 4. Optogenetic stimulation of the raphe results in reduced locomotor activity and increased sleep in zebrafish

Maximum intensity projections of brains (A-C) and single plane images of pineal glands (A'-C') from 5 dpf *Tg(tph2:ChR2-YFP)* zebrafish immunostained for 5-HT and YFP. Scale bars, 50 µm; a, anterior; p, posterior; Pt, pretectal area; Hyp, hypothalamus; Ra, raphe.

(D and E) Left: normalized locomotor activity (D) and sleep (E) of 5 dpf *Tg(tph2:ChR2)* (red) and non-transgenic sibling control (blue) zebrafish before and during exposure to blue light. Right: normalized locomotor activity (D) and sleep (E) fold change during illumination.

(F and G) Same as (D) and (E) but in *tph2*$^{-/-}$ animals.

n, number of animals; 6 trials per animal. ns $p>0.05$, ***$p<0.001$, ****$p<0.0001$, Mann-Whitney test. See also Figure S5.

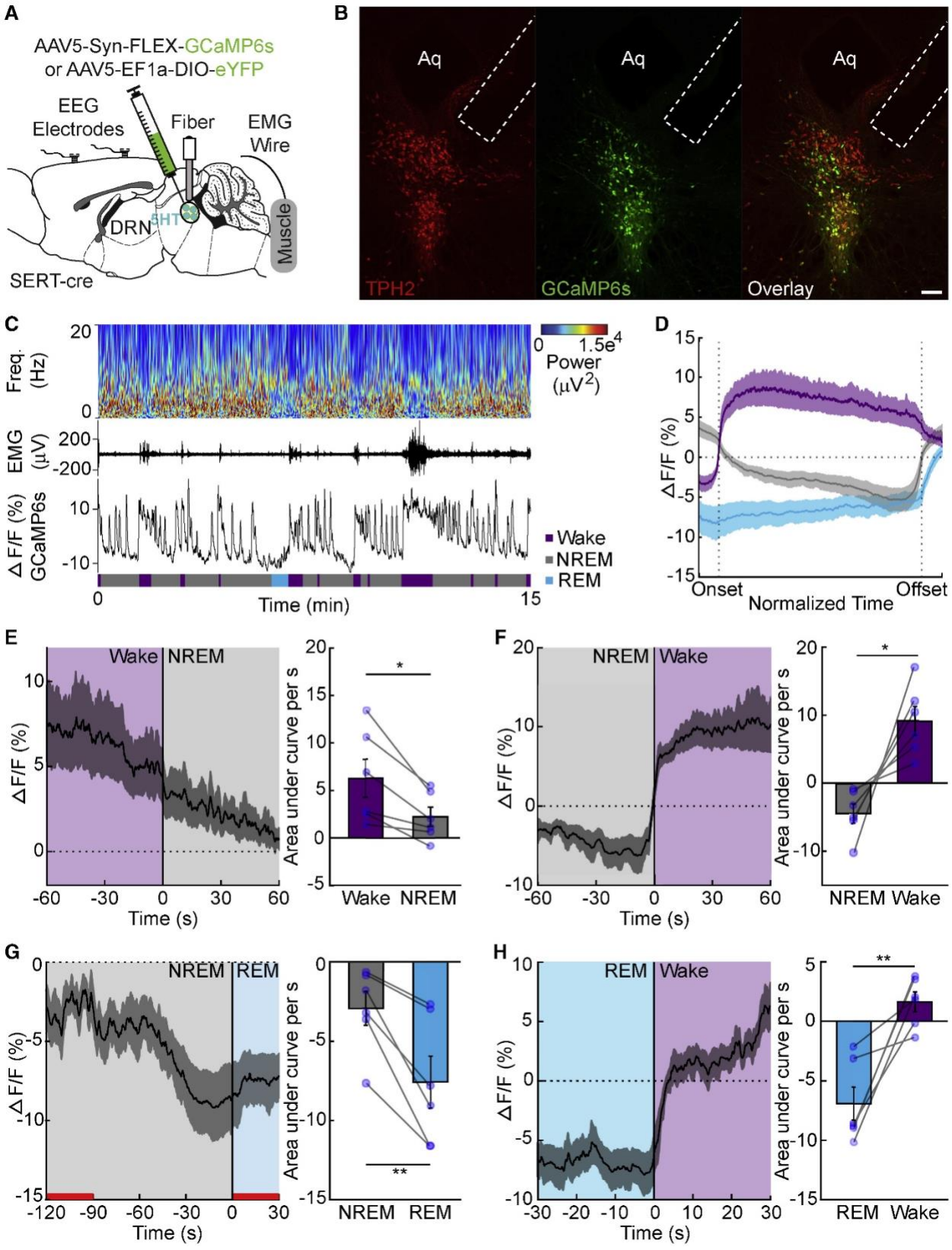

Figure 5. DRN neuronal activity correlates with sleep-wake states in mice

(A) Experimental setup.

(B) Representative images of GCaMP6s^{+} neurons (green) co-localized with TPH2^{+} neurons (red). Scale bar, 100 μm. Aq, aqueduct.

(C) Representative DRN$^{SERT\text{-}GCaMP6s}$ mouse spectrogram, EMG and fiber photometry traces over time across different sleep-wake states.

(D) Temporal dynamics of DRN^{SERT} activity during wake (purple), NREM (grey) and REM (blue) episodes within normalized time.

(E-H) DRN^{SERT} activity across wake to NREM (E), NREM to wake (F), NREM to REM (G), and REM to wake (H) transitions (left) and quantification of area under the curve (right). Statistical comparisons are based on the full time window shown (E,F and H) or on the time periods indicated by red lines (G).

Data represent mean ± S.E.M. n = 6 mice, paired t test, *$p<0.05$, **$p<0.01$.

See also Figure S6.

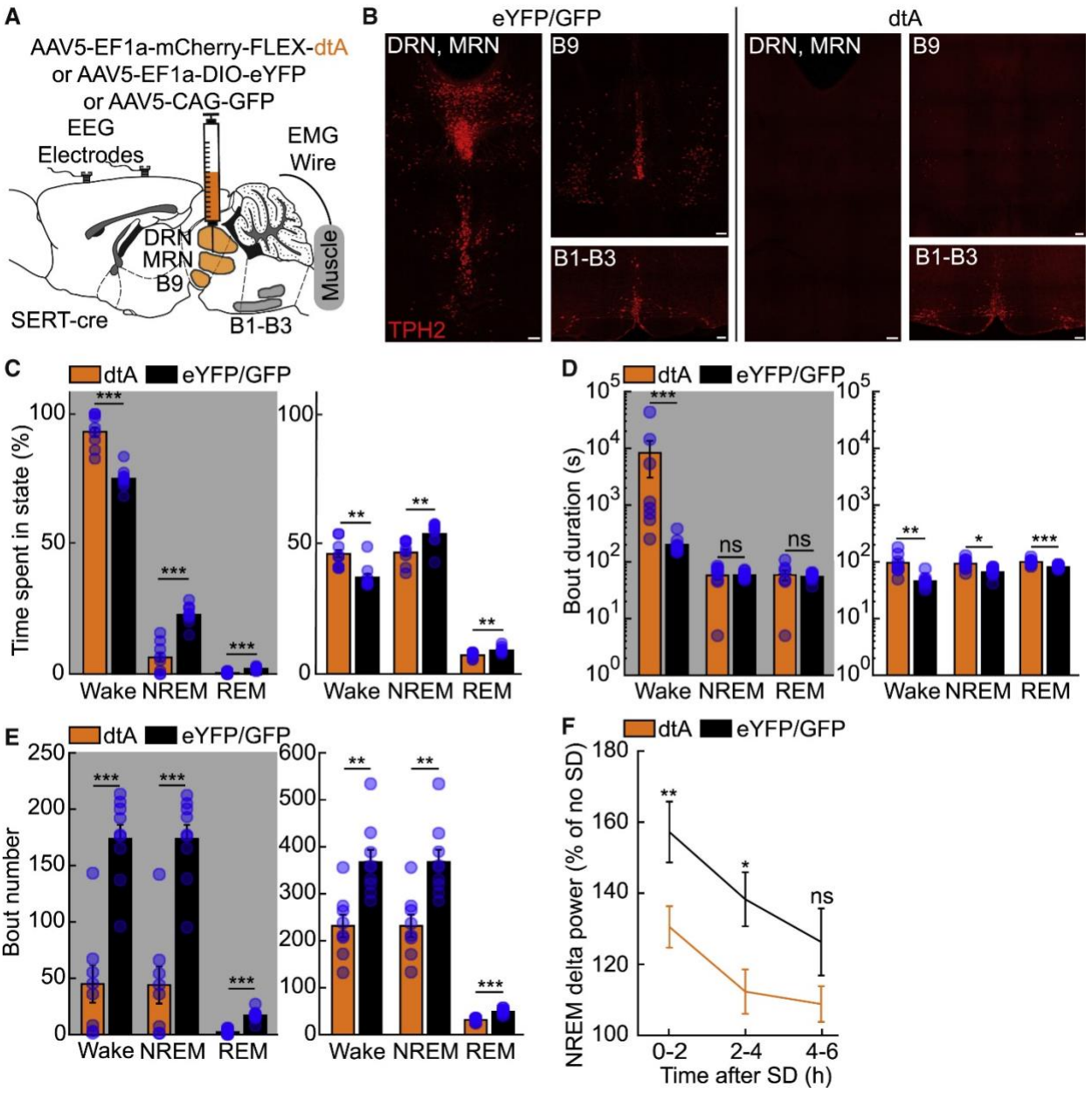

Figure 6. Ablation of murine raphe leads to increased wakefulness and impairs the homeostatic response to sleep deprivation

(A) Experimental setup.

(B) Representative images of $TPH2^{+}$ neurons (red) from SERT-cre mice injected with either AAV5-EF1a-DIO-eYFP (left) or AAV5-EF1a-mCherry-FLEX-dtA (right). Scale bar, 100 μm.

(C) Percentage of time spent in the wake, NREM, and REM states during the dark (grey shading) and light phase from 24 h polysomnographic recordings.

(D and E) Duration (D) and number (E) of wake, NREM, and REM bouts during the dark and light phase.

(F) Change in delta power across NREM episodes in animals subjected to 6 h of sleep deprivation (SD) at the beginning of the light phase compared to undisturbed sleep from previous light phase (no SD).

n = 8 for B5-B9$^{SERT\text{-}dtA}$, n = 9 for B5-B9$^{SERT\text{-}eYFP}$ or B5-B9^{GFP}, two-sided Wilcoxon rank-sum test, ns $p>0.05$, *$p<0.05$, **$p<0.01$, ***$p<0.001$. See also Figure S7.

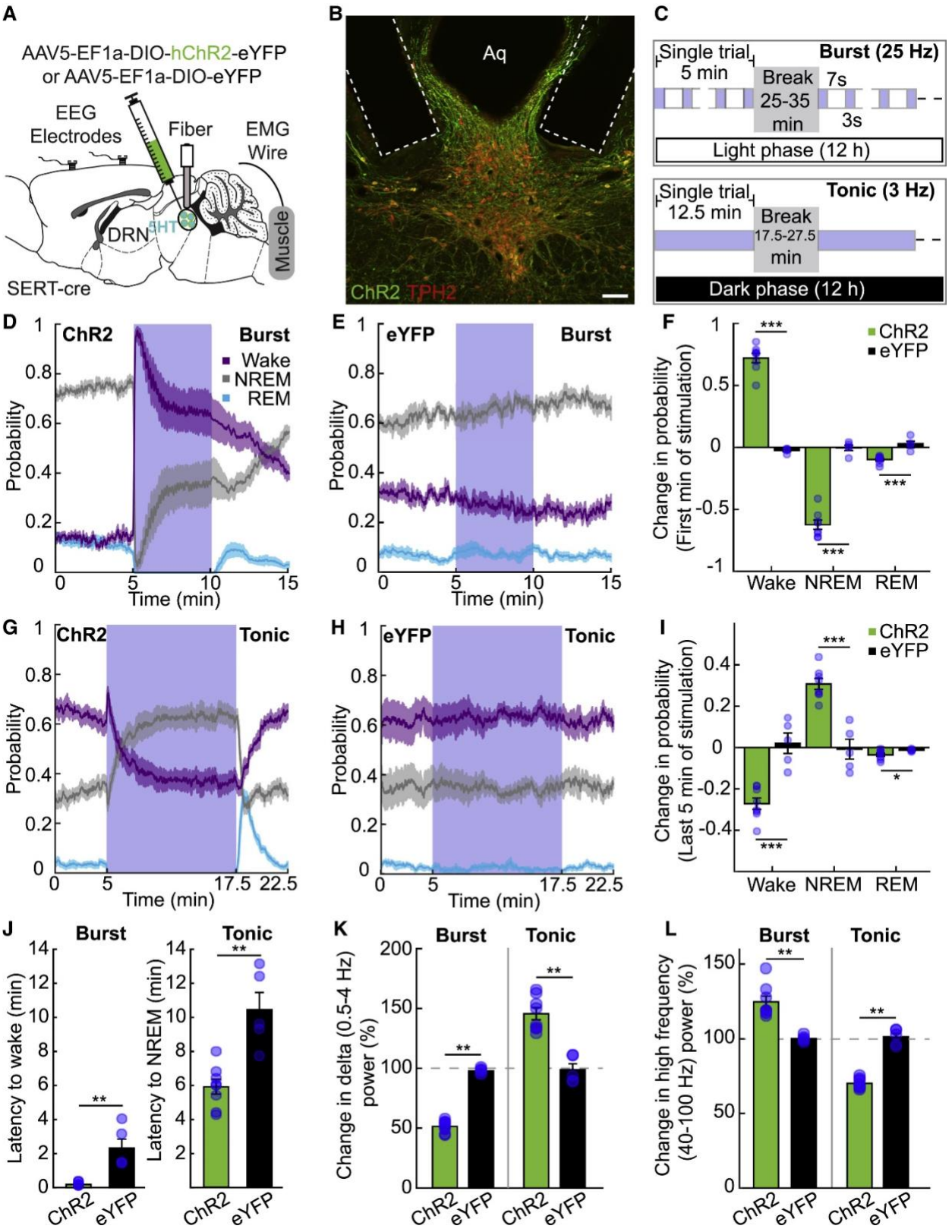

Figure 7. Optogenetic stimulation of DRN neurons has bidirectional mode-dependent effects on mouse sleep

(A) Experimental setup.

(B) Representative images of $ChR2^+$ neurons (green) co-localized with $TPH2^+$ neurons (red) from a SERT-cre mouse. Scale bar, 100 μm.

(C) Burst and tonic stimulation paradigms.

(D and E) State probability trace before, during, and after burst stimulation of $DRN^{SERT\text{-}ChR2}$ (D) or $DRN^{SERT\text{-}eYFP}$ (E) mice. Blue box indicates laser stimulation period.

(F) Quantification of (D) and (E) (unpaired t test).

(G and H) State probability trace before, during, and after tonic stimulation of $DRN^{SERT\text{-}ChR2}$ (G) or $DRN^{SERT\text{-}EYFP}$ (H) mice.

(I) Quantification of (G) and (H) (unpaired t test).

(J) Latency to wake after burst stimulation onset in $DRN^{SERT\text{-}ChR2}$ compared to $DRN^{SERT\text{-}eYFP}$ mice (left); latency to NREM after tonic stimulation onset in $DRN^{SERT\text{-}ChR2}$ mice compared to $DRN^{SERT\text{-}eYFP}$ mice (right) (two-sided Wilcoxon rank-sum test).

(K and L) Power spectral density of frontal EEG delta (K) or high-frequency (L) power upon burst stimulation onset (first min of stimulation) and over the course of tonic stimulation (last 5 min of stimulation) (two-sided Wilcoxon rank-sum test).

n = 8 for $DRN^{SERT\text{-}ChR2}$; n = 5 for $DRN^{SERT\text{-}eYFP}$; *$p<0.05$, **$p<0.01$, ***$p<0.001$.

See also Figures S6 and S7.

2.9 Supplementary figures

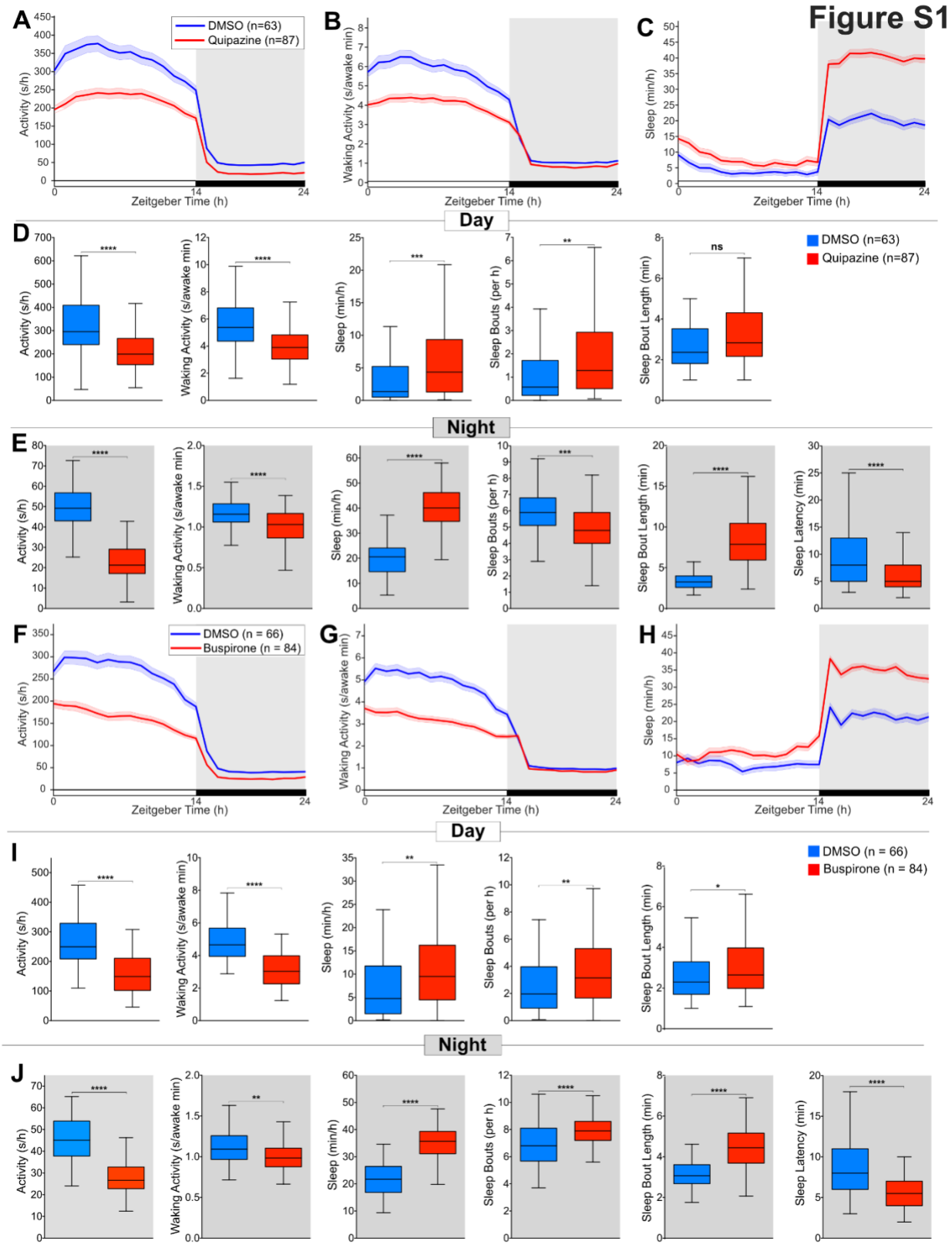

Figure S1. 5-HT receptor agonists increase zebrafish sleep, related to Figure 1

(A-C) Activity (A), waking activity (B), and sleep (C) for zebrafish treated with DMSO vehicle (blue) or 10 μM quipazine (red). Line and shading represent mean ± S.E.M. n = number of animals. (D and E) Boxplots quantifying activity, waking activity, sleep, sleep bout number, sleep bout length during day (D) and night (E) and sleep latency during night (E).

(F-J) Same as above but for animals treated with DMSO vehicle (blue) or 25 μM buspirone (red). n = number of animals. ns $p>0.05$, *$p<0.05$, **$p<0.01$, ***$p<0.001$, ****$p<0.0001$, Mann-Whitney test.

Figure S2

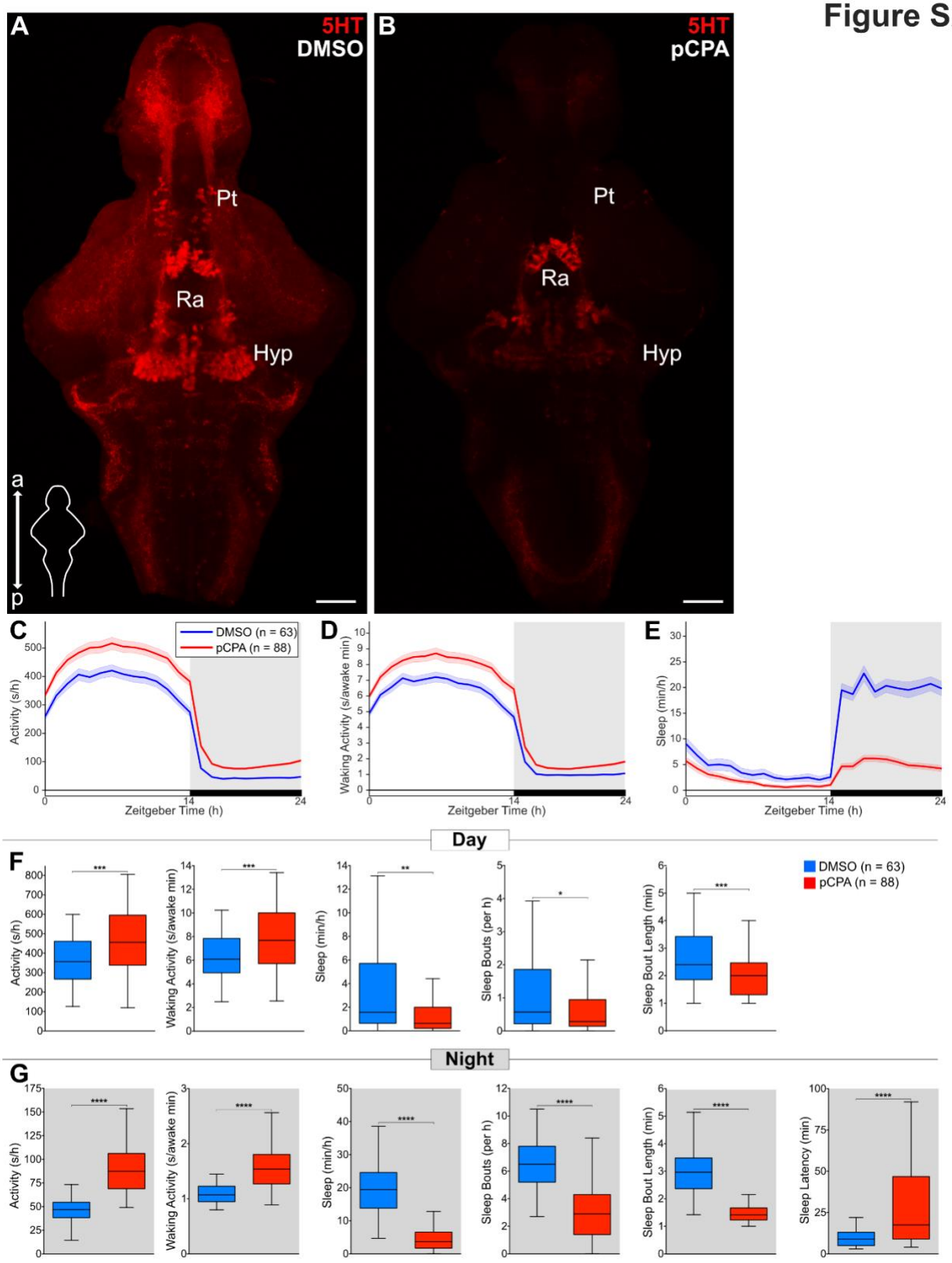

Figure S2. pCPA treatment depletes brain 5-HT and decreases sleep in zebrafish, related to Figure 1

(A and B) Maximum intensity projections of dissected brains from 5 dpf zebrafish treated with either DMSO vehicle (A) or pCPA (B) and immunostained for 5-HT. Scale bar, 50 μm; a, anterior; p, posterior; Ra, raphe; Hyp, hypothalamus; Pt, pretectal area.

(C-E) Activity (C), waking activity (D), and sleep (E) for zebrafish treated with DMSO vehicle (blue) or 7.5 μM pCPA (red). Line and shading represent mean ± S.E.M. n = number of animals.

(F and G) Boxplots quantifying activity, waking activity, sleep, sleep bout number, sleep bout length during day (F) and night (G) and sleep latency during night (G). n = number of animals. ns $p>0.05$, *$p<0.05$, **$p<0.01$, ***$p< 0.001$, ****$p<0.0001$, Mann-Whitney test.

Figure S3

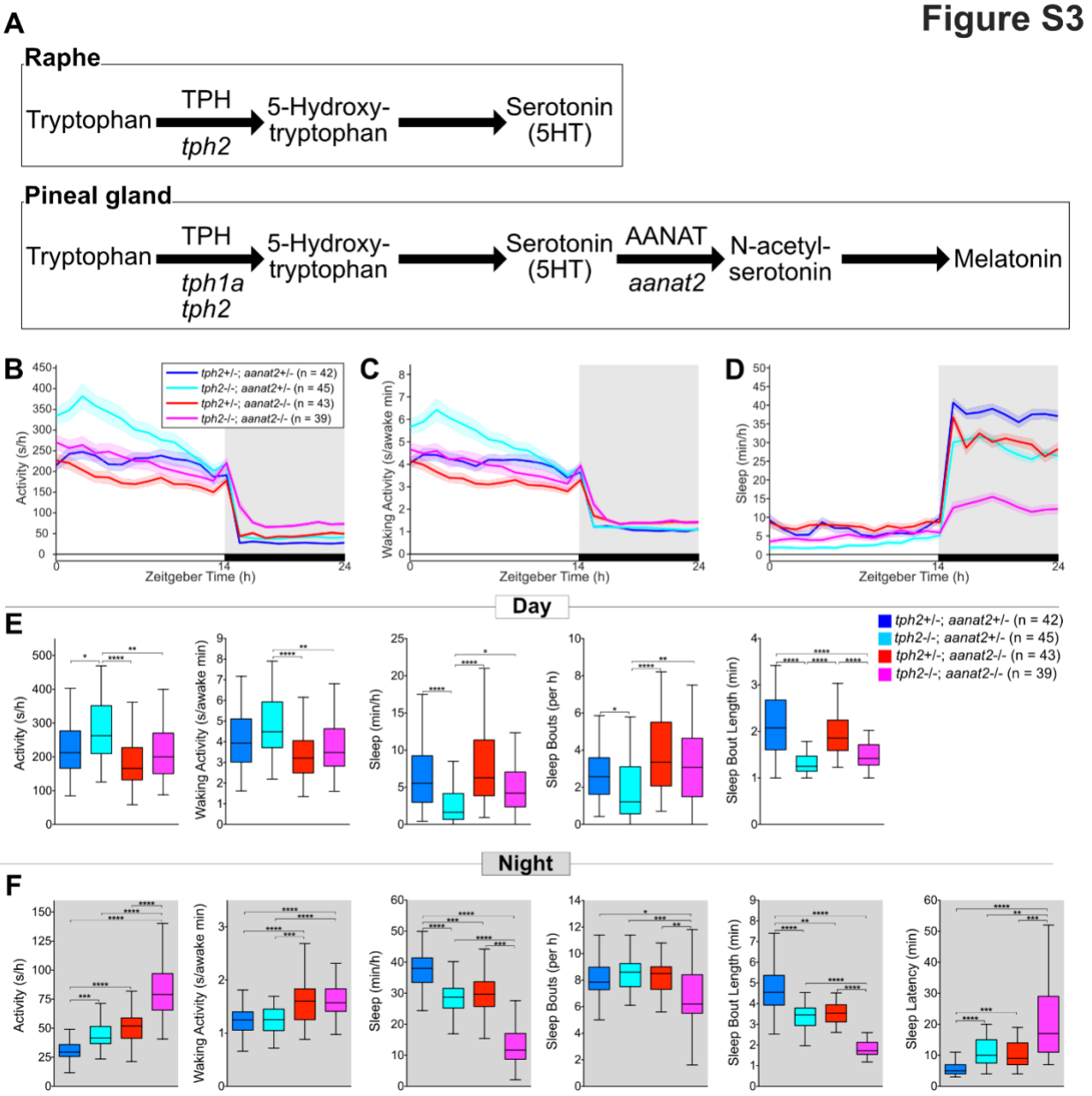

Figure S3. Loss of melatonin enhances the *tph2* mutant zebrafish night sleep phenotype, related to Figure 1

(A) Schematic of the serotonin biosynthetic pathway in the raphe (top) where the TPH enzymatic activity originates exclusively from transcription of the *tph2* paralog, and the melatonin biosynthetic pathway in the pineal gland (bottom) where the TPH enzymatic activity originates from both *tph1a* and *tph2*. *aanat2* is expressed in the pineal and encodes for arylalkylamine N-acetyltransferase (AANAT).

(B-D) Activity (B), waking activity (C), and sleep (D) for *tph2*$^{+/-}$; *aanat2*$^{+/-}$ (blue), *tph2*$^{-/-}$; *aanat2*$^{+/-}$ (cyan), *tph2*$^{+/-}$; *aanat2*$^{-/-}$ (red), and *tph2*$^{-/-}$; *aanat2*$^{-/-}$ (magenta) zebrafish. Line and shading represent mean ± S.E.M. n = number of animals.

(E and F) Boxplots quantifying activity, waking activity, sleep, sleep bout number, sleep bout length during day (E) and night (F) and sleep latency at night (F). n = number of animals. *p<0.05, **p<0.01, ***p<0.001, ****p<0.0001, Kruskal-Wallis test followed by Dunn's multiple comparisons test. All pair-wise comparisons were performed; only those with significant differences are indicated.

Figure S4

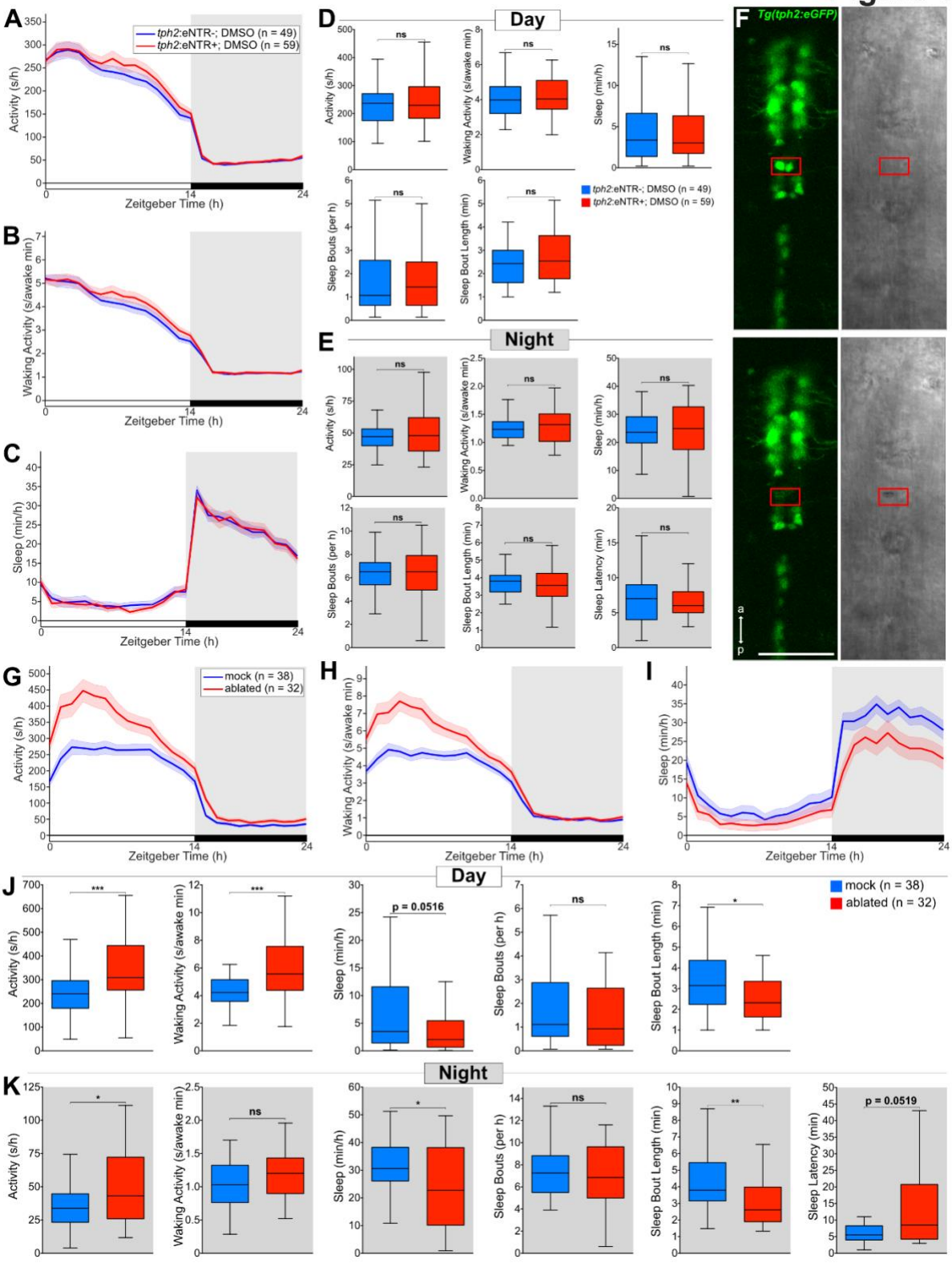
A
B
C
D
E
F
G
H
I
J
K
Day
Night
tph2:eNTR-; DMSO (n = 49)
tph2:eNTR+; DMSO (n = 59)
mock (n = 38)
ablated (n = 32)
Tg(tph2:eGFP)
Activity (s/h)
Waking Activity (s/awake min)
Sleep (min/h)
Sleep Bouts (per h)
Sleep Bout Length (min)
Sleep Latency (min)
Zeitgeber Time (h)
ns
p = 0.0516
p = 0.0519
a
p

Figure S4. Vehicle treatment of *Tg(tph2:eNTR-YFP)* animals does not affect behavior; 2-photon laser ablation of the raphe results in increased locomotor activity and decreased sleep in zebrafish, related to Figure 3

(A-C) Activity (A), waking activity (B), and sleep (C) for *Tg(tph2:eNTR-YFP)* (red) and non-transgenic sibling control (blue) zebrafish treated with DMSO. Line and shading represent mean ± S.E.M.

(D and E) Boxplots quantifying activity, waking activity, sleep, sleep bout number, sleep bout length during day (D) and night (E) and sleep latency during night (E).

(F) Top: Image of *Tg(tph2:eGFP)* fish (green channel on left, transmitted light image on right) before ablation of cells in red box. Bottom: Same as above but after 2-photon laser ablation; note small cavitation in transmitted light image (red box). The same process was repeated until all GFP+ cells in the shown area were ablated. Scale bar, 50 μm; a, anterior; p, posterior.

(G-I) Activity (G), waking activity (H), and sleep (I) for raphe laser-ablated (red) and mock laser-ablated sibling control (blue) zebrafish. Line and shading represent mean ± S.E.M.

(J and K) Boxplots quantifying activity, waking activity, sleep, sleep bout number, sleep bout length during day (J) and night (K) and sleep latency during night (K).

n = number of animals. ns $p>0.05$, *$p<0.05$, **$p<0.01$, ***$p<0.001$, Mann-Whitney test.

Figure S5

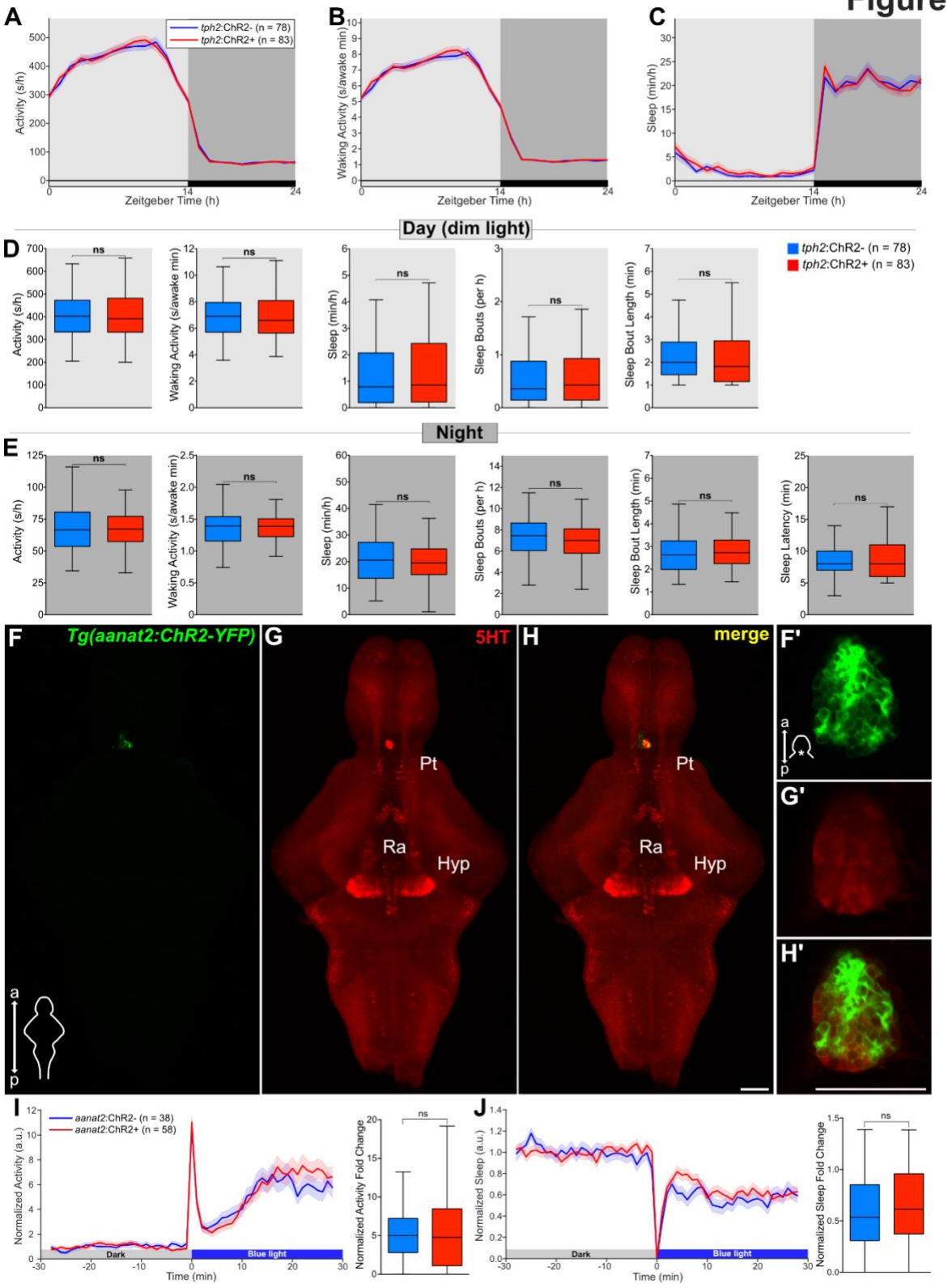
A
B
C
tph2:ChR2- (n = 78)
tph2:ChR2+ (n = 83)
Activity (s/h)
Waking Activity (s/awake min)
Sleep (min/h)
Zeitgeber Time (h)
Day (dim light)
Night
D
E
Sleep Bouts (per h)
Sleep Bout Length (min)
Sleep Latency (min)
ns
F
Tg(aanat2:ChR2-YFP)
G
5HT
H
merge
F'
G'
H'
Pt
Ra
Hyp
a
p
I
J
aanat2:ChR2- (n = 38)
aanat2:ChR2+ (n = 58)
Normalized Activity (a.u.)
Normalized Activity Fold Change
Normalized Sleep (a.u.)
Normalized Sleep Fold Change
Time (min)
Dark
Blue light

Figure S5. *Tg(tph2:ChR2-YFP)* zebrafish show normal wake/sleep cycles when maintained in dim light/dark cycles; blue light exposure does not affect behavior in zebrafish that express ChR2 in the pineal gland, related to Figure 4

(A-C) Activity (A), waking activity (B), and sleep (C) for *Tg(tph2:ChR2-eGFP)* (red) and non-transgenic sibling control (blue) zebrafish maintained in a dim light/dark cycle. Line and shading represent mean ± S.E.M. n = number of animals.

(D and E) Boxplots quantifying activity, waking activity, sleep, sleep bout number, sleep bout length during day (D) and night (E) and sleep latency during night (E). n = number of animals. ns $p>0.05$, Mann-Whitney test.

(F-H') Maximum intensity projections of dissected brains from 5 dpf *Tg(aanat2:ChR2-YFP)* zebrafish immunostained for 5-HT and YFP. a, anterior; p, posterior; Pt, pretectal area; Hyp, hypothalamus; Ra, raphe. The 5-HT+ structure above the Pt is the remnants of the pineal gland that was damaged during dissection. (F'-H') Single plane images of the pineal gland from 5 dpf *Tg(aanat2:ChR2-YFP)* whole zebrafish immunostained for 5-HT and YFP. Scale bars, 50 μm.

(I, J) Left: Normalized locomotor activity (I) and sleep (J) traces of 5 dpf *Tg(aanat2:ChR2)* zebrafish (red) and non-transgenic siblings (blue) before and during exposure to blue light. Right: boxplots quantifying normalized locomotor activity (I) and sleep (J) fold change during illumination. Line and shading represent mean ± S.E.M.

n = number of animals; 3 trials per animal. ns $p>0.05$, Mann-Whitney test.

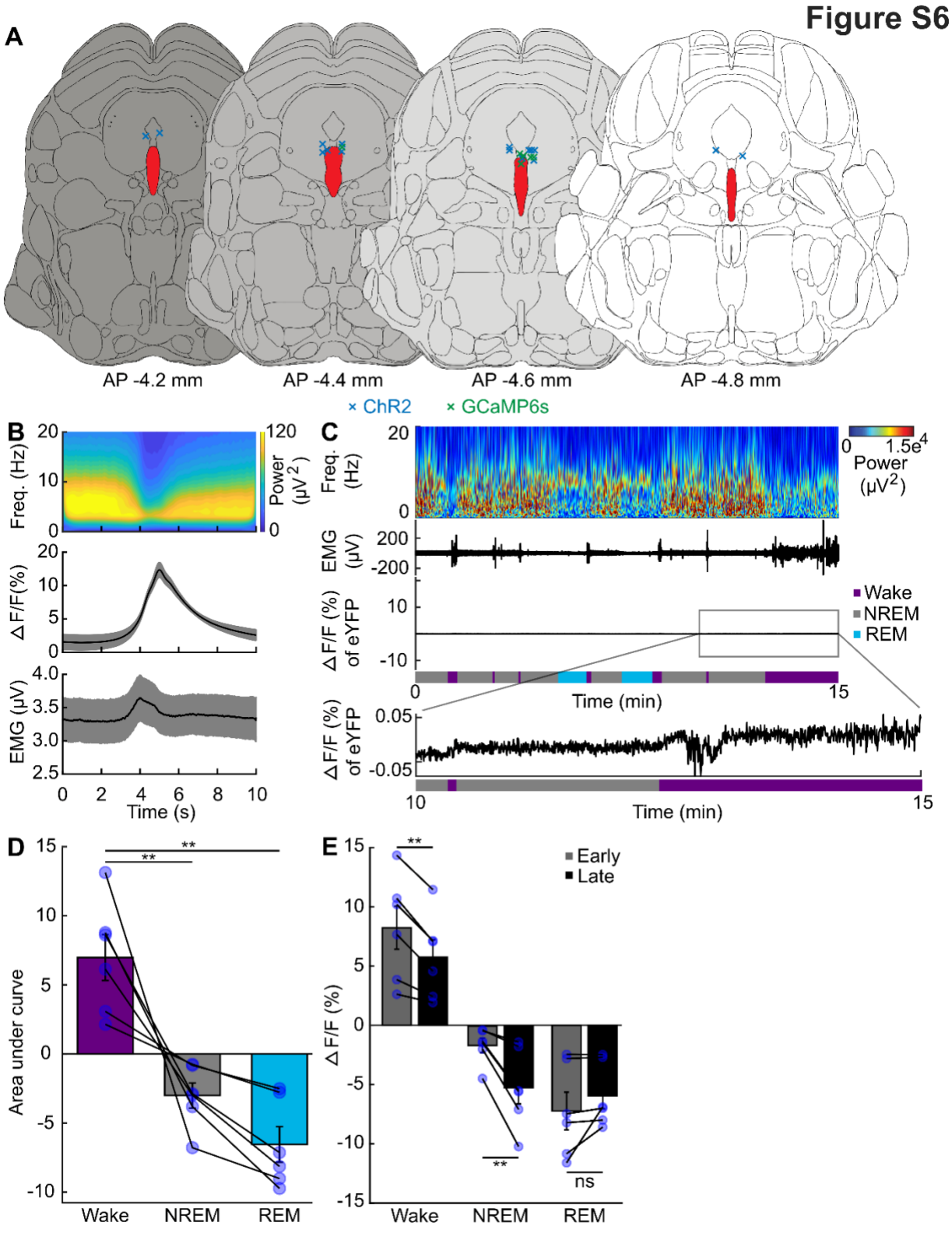

Figure S6. Large fluorescence changes of DRN$^{SERT\text{-}GCaMP6s}$, but not DRN$^{SERT\text{-}eYFP}$, across and within behavioral states, related to Figure 5

(A) Fiber-tip locations of $DRN^{SERT\text{-}ChR2}$ (blue) and $DRN^{SERT\text{-}GCaMP6s}$ (green) mice.

(B) EMG signal and spectral analysis of EEG traces around fluorescent peaks from $DRN^{SERT\text{-}GCaMP6s}$ during NREM episodes.

(C) Representative example from a $DRN^{SERT\text{-}eYFP}$ mouse of spectrogram, EMG and fiber photometry traces over time across different sleep-wake states. Last 5 min of ΔF/F (%) of eYFP are magnified to illustrate minor locomotion-induced artifacts.

(D) Activity level of DRN^{SERT} averaged across normalized time per state (one-way ANOVA followed by Bonferroni post hoc test).

(E) Comparison of DRN^{SERT} activity levels early and late (10-20 and 80-90 percentile time ranges, respectively) within episodes of wake, NREM and REM states (paired t test).

n = 6 $DRN^{SERT\text{-}GCaMP6s}$ mice; ns $p>0.05$, $^{**}p< 0.01$. Data represent mean ± S.E.M.

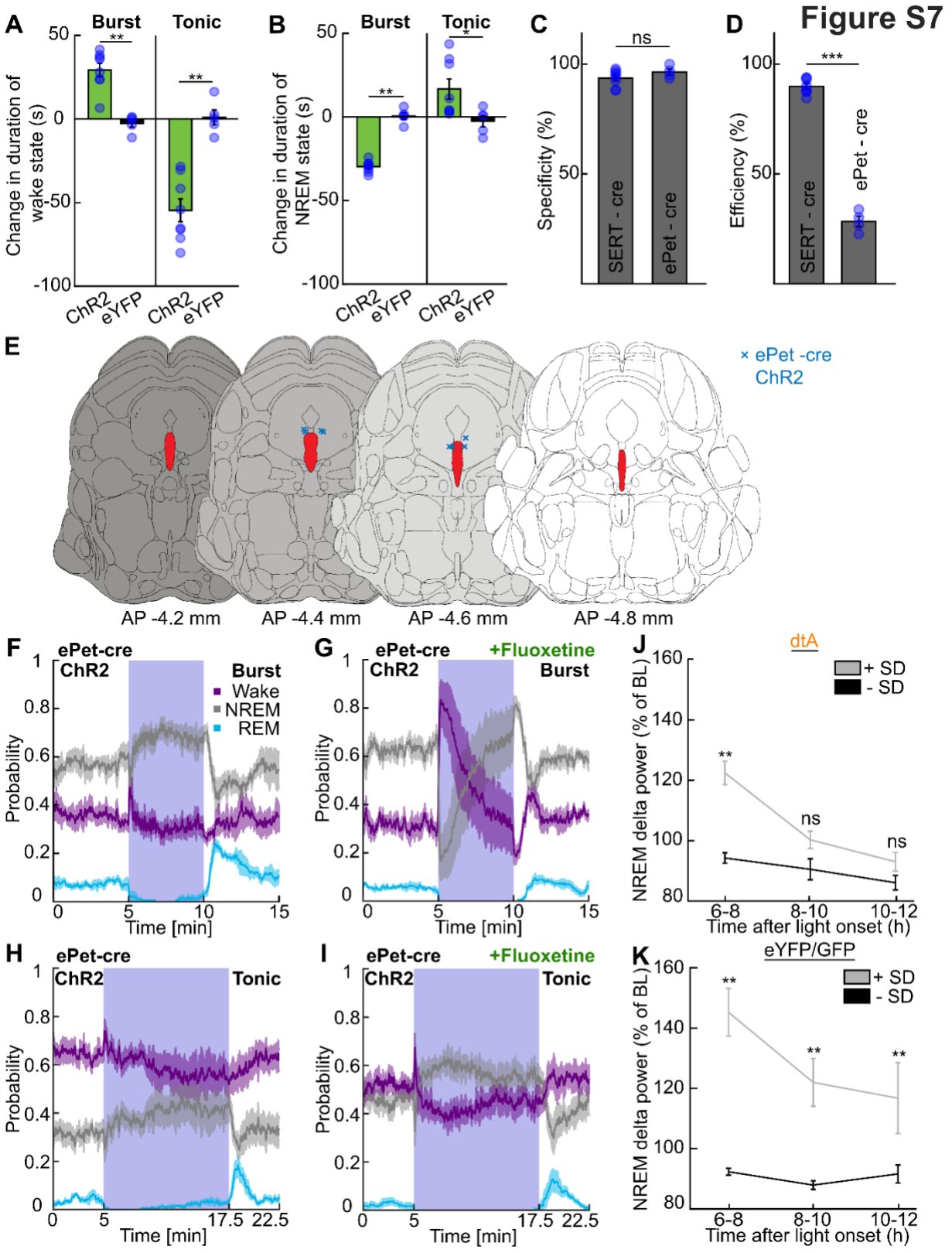
Figure S7
A
Burst
Tonic
Change in duration of wake state (s)
ChR2
eYFP
B
Change in duration of NREM state (s)
C
Specificity (%)
ns
SERT - cre
ePet - cre
D
Efficiency (%)
E
× ePet -cre
ChR2
AP -4.2 mm
AP -4.4 mm
AP -4.6 mm
AP -4.8 mm
F
ePet-cre
ChR2
Burst
Wake
NREM
REM
Probability
Time [min]
G
+Fluoxetine
J
dtA
+ SD
- SD
NREM delta power (% of BL)
Time after light onset (h)
H
Tonic
I
K
eYFP/GFP

Figure S7. Optogenetic stimulation of DRN using different transgenic mouse lines; change in delta power after SD of B5-B9$^{SERT\text{-}dtA}$ and B5-B9$^{SERT\text{-}eYFP}$ or B5-B9^{GFP} mice, related to Figures 6 and 7

(A) Change in duration of wake state during burst or tonic stimulation of DRN$^{SERT\text{-}ChR2}$ and DRN$^{SERT\text{-}eYFP}$ mice (n = 8 for DRN$^{SERT\text{-}ChR2}$; n = 5 for DRN$^{SERT\text{-}eYFP}$; two-sided Wilcoxon rank sum test, **p<0.01).

(B) Change in duration of NREM state during burst or tonic stimulation of DRN$^{SERT\text{-}ChR2}$ and DRN$^{SERT\text{-}eYFP}$ mice (n = 8 for DRN$^{SERT\text{-}ChR2}$, n = 5 for DRN$^{SERT\text{-}eYFP}$ two-sided Wilcoxon rank sum test, **p<0.01, *p<0.05).

(C-D) Quantification of viral transduction efficiency ((ChR2+ & TPH2+)/TPH2+) and ChR2-eYFP expression specificity ((ChR2+ & TPH2+)/ChR2+) in SERT-cre (Zhuang et al., 2005) and ePet-cre (Scott et al., 2005) mice (n = 8 for DRN$^{SERT\text{-}ChR2}$, n = 4 for DRN$^{ePet\text{-}ChR2}$, paired t test, ns p>0.05, ***p<0.001).

(E) Fiber-tip locations of ePet-cre (Scott et al., 2005) mice injected with AAV5-EF1a-DIO-ChR2-eYFP (n = 4 for DRN$^{ePet\text{-}ChR2}$).

(F) Burst stimulation of DRN$^{ePet\text{-}ChR2}$ neurons. Blue box highlights laser stimulation period (n = 4 DRN$^{ePet\text{-}ChR2}$).

(G) Same experiment as (F), but with prior i.p. injection of 10-20 mg/kg fluoxetine (n = 4 DRN$^{ePet\text{-}ChR2}$).

(H) Tonic stimulation of DRN$^{ePet\text{-}ChR2}$ neurons (n = 4 DRN$^{ePet\text{-}ChR2}$).

(I) Same experiment as (H), but with prior i.p. injection of 10-20 mg/kg fluoxetine (n = 4 DRN$^{ePet\text{-}ChR2}$).

(J) Delta power in NREM episodes across the last 6 h of the light phase with and without prior 6 h SD of B5-B9$^{SERT\text{-}dtA}$. Delta power is shown as percentage of average delta power across all NREM episodes during the light phase (n = 8 for B5-B9$^{SERT\text{-}dtA}$, two-sided Wilcoxon signed rank test, ns p>0.05, **p<0.01).

(K) Delta power in NREM episodes across the last 6 h of the light phase with and without prior 6 h SD of B5-B9$^{SERT\text{-}eYFP}$ or B5-B9^{GFP}. Delta power is shown as percentage of average delta power across all NREM episodes during the light phase (n = 8 for B5-B9$^{SERT\text{-}eYFP}$ or B5-B9^{GFP}, two-sided Wilcoxon signed rank test, **p<0.01). Data represent mean ± S.E.M.

2.10 STAR methods

KEY RESOURCES TABLE

REAGENT or RESOURCE	SOURCE	IDENTIFIER
Antibodies		
Rabbit polyclonal anti-5-HT	MilliporeSigma	Cat# S5545; RRID:AB_477522
Chicken polyclonal anti-GFP	Aves Labs	Cat# GFP-1020; RRID: AB_10000240
Chicken polyclonal anti-mCherry	Abcam	Cat# ab205402; RRID: AB_2722769
Rabbit polyclonal anti-Tryptophan Hydroxylase 2	Millipore	Cat# ABN60; RRID: AB_10806898
Goat anti-Chicken IgY (H+L) Secondary Antibody, Alexa Fluor 488	Invitrogen	Cat# A-11039; RRID: AB_2534096
Goat anti-Rabbit IgG (H+L) Cross-Adsorbed Secondary Antibody, Alexa Fluor 568	Invitrogen	Cat# A-11011; RRID: AB_143157
Goat anti-chicken IgY H&L Alexa Fluor 488	Abcam	Cat# ab150169; RRID: AB_2636803
Goat anti-chicken IgY H&L Alexa Fluor 647	Abcam	Cat# ab150175; RRID: AB_2732800
Goat anti-rabbit IgG H&L Alexa Fluor 488	Abcam	Cat# ab150077; RRID: AB_2630356
Goat anti-rabbit IgG H&L Alexa Fluor 647	Abcam	Cat# ab150079; RRID: AB_2722623
Chemicals, Peptides, and Recombinant Proteins		
Quipazine maleate salt	MilliporeSigma	Cat# Q1004
Buspirone hydrochloride	MilliporeSigma	Cat# B7148
4-chloro-DL-phenylalanine methyl ester hydrochloride (pCPA)	MilliporeSigma	Cat# C3635

Metronidazole	MP Biomedicals	Cat# 0215571080
Euthasol	VWR	Cat# 102094-104
Fluoxetine HCl	Enzo Life Sciences	Cat# BML-NS140-0050
O.C.T. compound	VWR	Cat# 102094-104
16% paraformaldehyde	ThermoFisher Sci.	Cat# 15710
Normal goat serum	ThermoFisher Sci.	Cat# NC9660079
Collagenase	MilliporeSigma	Cat# C9891
Vectashield	Vector laboratories	Cat# H-1000; RRID:AB_2336789
Fluoromount G with DAPI	ThermoFisher Sci.	Cat# 00-4959-52
alpha-bungarotoxin	Tocris	Cat# 2133
tricaine	MilliporeSigma	Cat# A5040
Experimental Models: Organisms/Strains		
Zebrafish: *tph2* ct817 mutant	(Chen et al., 2013)	RRID: ZDB-ALT-131122-14
Zebrafish: *aanat2* ct801 mutant	(Gandhi et al., 2015)	RRID: ZDB-ALT-131122-2
Zebrafish: *Tg(tph2:eGFP)* ct864Tg	This paper	RRID: ZDB-ALT-190508-1
Zebrafish: *Tg(tph2:ChR2-YFP)* ct865Tg	This paper	RRID: ZDB-ALT-190508-2
Zebrafish: *Tg(tph2:eNTR-YFP)* ct866Tg	This paper	RRID: ZDB-ALT-190508-3
Mouse: SERT-cre (Zhuang et al., 2005)	Jackson Laboratory	Stock No: 014554; RRID:IMSR_JAX:014554

Mouse: ePet-cre (Scott et al., 2005)	Jackson Laboratory	Stock No: 012712; RRID:IMSR_JAX:012712
Oligonucleotides		
Primer: *tph2* promoter Forward: TGTCTTCCTGCCATTAGTCTG	This paper	N/A
Primer: *tph2* promoter Reverse: TTAATATGGCAAAGGTAGTTTTTTTTATC	This paper	N/A
Primer: *tph2* mutant genotyping primer 1: AGAACTTACAAAACTCTATCCAACTC	This paper	N/A
Primer: *tph2* mutant genotyping primer 2: AGAGAGGACAACATCTGGGG	This paper	N/A
Primer: *tph2* mutant genotyping primer 3: TAATCATGCAGTCCGTTAATACTC	This paper	N/A
Virus strains		
AAV5-Syn-FLEX-GCaMP6s	Penn Vector Core	AV-5-PV2821
AAV5-Syn-FLEX-GCaMP6s	Addgene	100845-AAV5
AAV5-Ef1a-DIO-ChR2(H134R)-eYFP	Penn Vector Core	AV-5-20298P
AAV5-Ef1a-DIO-eYFP	Penn Vector Core	AV-5-27056
AAV5-mCherry-flex-dtA	UNC Vector Core	N/A
AAV5-CAG-GFP	Addgene	37825-AAV5
Software and Algorithms		
MATLAB R2017b	Mathworks	RRID:SCR_001622
EEGLAB plug-in	Swartz Center for Comp. Neuro.	RRID:SCR_007292
SleepSign 3.0	Kissei Comtec	http://www.sleepsign.com

Prism6	GraphPad	RRID:SCR_002798
Image J	PMID: 22930834	RRID:SCR_002285
Other		
96-well plate	GE Healthcare Life Sciences	Cat#:7701-1651
MicroAmp Optical Adhesive Film	Thermo Fisher Scientific	Cat#: 4311971

LEAD CONTACT AND MATERIALS AVAILABILITY

Further information and requests for resources and reagents from zebrafish or mouse experiments should be directed to and will be fulfilled by David Prober (dprober@caltech.edu).

EXPERIMENTAL MODEL AND SUBJECT DETAILS

Animal husbandry and all experimental procedures involving animals were performed in accordance with the California Institute of Technology Institutional Animal Care and Use Committee (IACUC) guidelines and by the Office of Laboratory Animal Resources at the California Institute of Technology (animal protocols 1580 (zebrafish) and 1672 (mice)).

Zebrafish

All experiments used healthy larvae between 4 and 7 dpf; at this stage of development, sex is not yet defined. Larvae were housed in Petri dishes with 50 animals per dish. E3 medium (5 mM NaCl, 0.17 mM KCl, 0.33 mM $CaCl_2$, 0.33 mM $MgSO_4$) was used for housing and experiments. All lines were derived from the TLAB hybrid strain. Animals were not involved in any previous procedures and were naive to the test and drugs used.

Mice

SERT-cre (Zhuang et al., 2005) and ePet-cre (Scott et al., 2005) mice were crossed to wild type C57BL/6 mice (Charles River). All animals had a normal immune status. Only male animals heterozygous for the Cre transgene were used for experiments. After weaning, animals of the same gender were group-housed until they underwent surgery at the age of 6-12 weeks. After surgery,

subjects were single-housed for at least five days in a residence room for full recovery before animals were moved to a behavioral room. In the behavioral room, animals were housed on a 12:12 h light/dark cycle (light off at 6 a.m. and light on at 6 p.m.) with ad libitum access to food and water. Mice were acclimated to the new behavioral room and light/dark cycle for at least 2 weeks before experiments were started. Animals used for experiments were not involved in any previous procedures and were naive to the test and drugs used.

METHOD DETAILS

Zebrafish Methods and Data Analysis

Pharmacology (zebrafish)

Quipazine maleate salt (Q1004, MilliporeSigma, Burlington, MA, USA), buspirone hydrochloride (B7148, MilliporeSigma, Burlington, MA, USA) and 4-Chloro-DL-phenylalanine methyl ester hydrochloride (pCPA) (C3635, MilliporeSigma, Burlington, MA, USA) were dissolved in dimethyl sulfoxide (DMSO) and added to E3 medium (5 mM NaCl, 0.17 mM KCl, 0.33 mM $CaCl_2$, 0.33 mM $MgSO_4$, pH 7.4) for a final concentration of 0.1% DMSO and 10 μM quipazine, 25 μM buspirone or 7.5 μM pCPA. These concentrations were determined through dose-response experiments (0.1 μM to 100 μM), and allow for robust behavioral phenotypes without apparent toxicity or abnormal responses to a gentle stimulus. Controls were exposed to 0.1% DMSO alone. For sleep/wake experiments, drugs were added during the evening of the 4th day of development; reported data is from the 5th day and night of development.

Transgenic and mutant animals (zebrafish)

For the construction of *Tg(tph2:ChR2-YFP)* and *Tg(tph2:eNTR-YFP)* lines, a 1.2 kb genomic fragment from the promoter region of *tph2* was amplified using primers 5'-TGTCTTCCTGCCATTAGTCTG-3' (forward) and 5'-TTAATATGGCAAAGGTAGTTTTTTTT ATC-3' (reverse) into a vector containing NRSE elements and Tol2 recognition sequences. This promoter fragment is subject to positional effects; depending on the integration site in the genome it can drive expression in all or subsets of the reported CNS *tph2* expression sites (pineal gland, pretectal area, raphe). *Tg(tph2:ChR2-YFP)* animals showed YFP immunoreactivity in the pineal gland and the raphe, while *Tg(tph2:eNTR-YFP)* animals only showed expression in the raphe. Both lines also show sparse expression in the spinal cord, as previously shown for other *tph2* transgenic

lines (Yokogawa et al., 2012). For the construction of *tph2* mutants, TALEN-based genomic editing was used to introduce a 4 bp insertion in exon 6 of *tph2* (ENSDARG00000057239) (Chen et al., 2013), which causes a frameshift at nucleotide 721 (out of 1427) of the open reading frame and introduces multiple premature stop codons (first stop codon appears at nucleotide 841). For genotyping, genomic DNA was prepared using standard methods (Westerfield, 2000) and PCR was performed using a set of 3 primers (5'-AGAACTTACAAAACTCTATCCAACTC-3', 5'-AGAGAGGACAACATCTGGGG-3', 5'-TAATCATGCAGTCCGTTAATACTC-3'), which produce one band for homozygous wild-type animals (255 bp), two bands for homozygous mutant animals (177 bp and 259 bp), and three bands for heterozygous mutant animals (177 bp, 255 bp and 259 bp). PCR products were run on a 4% agarose gel.

Immunohistochemistry (zebrafish)

Samples were fixed in 4% PFA/4% sucrose in PBS overnight at 4°C and then washed with 0.25% Triton X-100/PBS (PBTx). Immunolabeling was generally performed using dissected brains because dissection allows for superior antibody penetration. However, for pineal gland imaging whole-mount staining was performed because the pineal gland is often damaged by dissection. Whole larvae or dissected brains were incubated for 1 h in 1 mg/mL collagenase (C9891, MilliporeSigma, St. Louis, Missouri, USA) and blocked overnight in 2% NGS/2% DMSO in PBTx at 4°C. Antibody incubations were performed in blocking solution overnight at 4°C. Primary antibodies were rabbit anti-5-HT (1:1000; S5545, MilliporeSigma, Burlington, MA, USA) and chicken anti-GFP (1:400; GFP-1020, Aves Labs, Tigard, OR, USA). Secondary antibodies were goat anti-Chicken IgY (H+L), Alexa Fluor 488 (1:500; A-11039; Invitrogen, Carlsbad, CA, USA) and goat anti-Rabbit IgG (H+L) cross-adsorbed, Alexa Fluor 568 (1:500; A-11011; Invitrogen, Carlsbad, CA, USA). Samples were mounted in Vectashield (H-1000; Vector Laboratories, Burlingame, CA) and imaged using a Zeiss LSM 780 or Zeiss LSM 880 confocal microscope (Zeiss, Oberkochen, Germany).

Electrophysiological recordings (zebrafish)

For cell-attached recordings of raphe neurons, we used 4- to 6-dpf *Tg(tph2:eGFP)* animals, in which serotonergic raphe neurons were visualized using a fluorescent microscope (BX50WI, Olympus, Tokyo, Japan) and an infrared CCD camera (IR1000, DAGE-MTI, Michigan City, IN, USA). Animals were paralyzed by bath application of 0.1% α-bungarotoxin (2133, Tocris Bioscience,

Bristol, UK) for 10-15 min, then embedded in a custom-made glass-bottom Petri dish with 1.5% low-melting agarose (A9414, MilliporeSigma, Burlington, MA, USA) dorsal side up, and immersed in extracellular solution (134 mM NaCl, 2.9 mM KCl, 2.1 mM $CaCl_2$, 1.2 mM $MgCl_2$, 10 mM HEPES, 10 mM glucose; 290 mOsmol/L, pH = 7.8). A small incision was made at the skin above the ventricle between cerebellum and hindbrain using a glass micropipette. Micropipettes were made from borosilicate glass (BF100-58-10, Sutter Instrument, Novato, CA, USA) by a Flaming/Brown micropipette puller P-87 (Sutter Instrument, Novato, CA, USA). The recording pipette (~10 MΩ in resistance, ~2 μm tip opening) was filled with extracellular solution, and advanced into the brain through a motorized micromanipulator (MP-225, Sutter Instruments, CA, USA). Contact of the micropipette onto raphe neurons was confirmed by visualizing eGFP-positive membranes within the tip of the recording micropipette. Spike firing was detected by a MultiClamp 700B amplifier (Molecular Devices, San Jose, CA, USA) and a 1550B4 Digidata data acquisition system (Molecular devices, CA, USA). Signals were filtered at 2 kHz and sampled at 10 kHz. To avoid baseline fluctuations, signals were recorded with a 1 Hz high pass filter.

Chemogenetic ablation (zebrafish)

Animals were treated with 5 mM metronidazole (MTZ) (0215571080, MP Biomedicals, Santa Ana, CA, USA) diluted in E3 medium containing 0.2% DMSO, starting in the afternoon at 2 dpf, and refreshed every 24 h. Animals were kept in dim light during the day to prevent MTZ photodegradation. In the evening at 4 dpf, the animals were rinsed 3 times in E3 medium and then transferred to behavioral plates. Reported data is from the 5th day and night of development.

2-Photon laser ablation (zebrafish)

4 dpf *Tg(tph2:eGFP)*; *nacre* animals were anesthetized in E3 medium containing 0.016% tricaine (A5040, MilliporeSigma, Burlington, MA, USA) and mounted in 1.5% low-melting agarose (A9414, MilliporeSigma, Burlington, MA, USA) dorsal side up. 2-Photon laser ablation of the raphe was performed using a Zeiss LSM 880 microscope (Zeiss, Oberkochen, Germany) equipped with a Titanium:Sapphire two-photon laser (Chameleon Ultra II, Coherent, Santa Clara, CA) and 20x water immersion objective (1.0 NA). To create local lesions the bleaching function of the Zen Black software (Zeiss, Oberkochen, Germany) was used with the following parameters: pixel dwell time 2.06 μsec, pixel size 0.42 μm, laser power 100% (~3700 mW), 30 iterations. All GFP positive cells

around a 200 μm caudal-to-rostral axis along the midline starting from the caudal tip of the superior raphe were ablated (approximately 100 cells/animal). This area includes all of the superior raphe and the majority of the inferior raphe. Cells were ablated one at a time, or in case of closely arranged cells, in groups no larger than 3-4 cells. Ablations were considered successful when no GFP was observable and a small cavitation was briefly visible after treatment. Mock ablated controls were mounted next to the ablated animals. After ablation/mock ablation, animals were unmounted, transferred to the videotracking system and allowed to recover overnight before assaying behavior at 5 dpf.

Optogenetics (zebrafish)

The video-tracking system was modified to include a custom array containing three sets of blue LEDs (470 nm, MR-B0040-10S, Luxeon V-star, Brantford, Canada) mounted 15 cm above and 7 cm away from the center of the 96-well plate to ensure uniform illumination. The LEDs were controlled using a custom-built driver and software written in BASIC stamp editor. A power meter (1098293, Laser-check, Santa Clara, CA, United States) was used before each experiment to verify uniform light intensity (~500 μW at the surface of the 96-well plate). In the morning of the fifth day of development, single larvae were placed into each well of a 96-well plate and placed in the video tracker. Larvae were exposed to blue light for 30 min with at least 60 min of recovery between trials. Total locomotor activity for each larva was monitored for 30 min before and after light onset. Light onset induces a startle response, which causes a short burst of locomotor activity. For this reason, we excluded 5 min of behavioral recording centering around the peak of the startle response from analysis. The two minutes before light offset was also excluded from analysis. For normalization, the locomotor activity and sleep of each larva during light exposure was divided by the average baseline locomotor activity and sleep for all larvae of the same genotype. For baseline, we used a time period equal to blue light treatment, but prior to light onset.

Sleep/wake analysis (zebrafish)

Sleep/wake analysis was performed as previously described (Prober et al., 2006). Larvae were raised on a 14:10 h light:dark (LD) cycle at 28.5°C with lights on at 9 a.m. and off at 11 p.m. Dim white light was used to raise larvae for optogenetic experiments to prevent stimulation of ChR2 by ambient light. Individual larvae were placed into each well of a 96-well plate (7701-1651, Whatman,

Pittsburgh, PA, United States) containing 650 µl of E3 embryo medium. Locomotor activity was monitored using a video-tracking system (Viewpoint Life Sciences, Lyon, France) with a Dinion one-third inch Monochrome camera (Dragonfly 2, Point Grey, Richmond, Canada) fitted with a variable-focus megapixel lens (M5018-MP, Computar, Cary, NC, United States) and infrared filter. The movement of each larva was recorded using the quantization mode. The 96-well plate and camera were housed inside a custom-modified Zebrabox (Viewpoint Life Sciences) that was continuously illuminated with infrared lights. The 96-well plate was housed in a chamber filled with recirculating water to maintain a constant temperature of 28.5ºC. The parameters used for movement detection were: detection threshold, 15; burst, 29; freeze, 3; bin size, 60 s, which were determined empirically. Data were analyzed using custom Perl and Matlab (Mathworks, Natick, MA, United States) scripts (Source code 1), which conform to the open source definition. For this and all behavioral assays, animals were genotyped after the experiment to identify mutant, transgenic and control animals.

Sleep deprivation (zebrafish)

Sleep deprivation (SD) was performed on 6 dpf animals during the first 6 h of the subjective night by maintaining daytime levels of illumination. Animals that failed to show at least a 50% reduction in sleep during the first 4 h of sleep deprivation (SD Sleep) compared to sleep during the first 4 h of the previous night (Baseline Sleep) were excluded from analysis. For each genotype we defined Sleep Lost as the difference between Baseline Sleep and SD sleep averaged for all animals of that genotype. Normalized SD Response was defined as the ratio of Recovery Sleep (i.e. sleep during the first 4 h after sleep deprivation) for each animal to Sleep Lost. Only 4 h of Recovery Sleep (and hence Baseline Sleep) were used in order to ensure that all sleep data were confined to the circadian night (6 h of SD + 4 h of Recovery Sleep for a total of 10 h of circadian night per standard zebrafish rearing protocols).

Arousal analysis (zebrafish)

The video-tracking system was modified by adding an Arduino (http://www.arduino.cc/) based automated driver to control two solenoids (28P-I-12, Guardian Electric, Woodstock, IL, United States) that delivered a tap to a 96-well plate containing zebrafish larvae (Gandhi et al., 2015). This setup allowed us to drive the solenoids with voltage ranging from 0 V to 20 V over a range of 4095

settings (from 0.01 to 40.95). In our experiments, we used taps ranging from a power setting of 1–36.31. Taps of 14 different intensities were applied in a pseudo-random order from 12:30 a.m. to 7:30 a.m. during the fifth night of development with an inter-trial-interval (ITI) of 1 min. Previous studies showed that a 15 s interval between repetitive stimuli is sufficient to prevent behavioral habituation (Burgess and Granato, 2007). The background probability of movement was calculated by identifying for each genotype the fraction of larvae that moved 5 s prior to all stimuli delivered during an experiment (14 different tap powers x 30 trials per experiment = 420 data points per larva; average background movement). This value was subtracted from the average response fraction value for each tap event (corrected response = average response – average background movement). For sleep depth analysis, taps were delivered every 5 min at powers low enough to allow discrimination between awake and sleeping fish. The response of larvae to the stimuli was monitored using the video-tracking software and was analyzed using Matlab (Mathworks) and Excel (Microsoft, Redmond, WA, United States). Statistical analysis was performed using the Variable Slope log(dose) response curve fitting module of Prism (Graphpad, La Jolla, CA, United States) for 1 min ITI and the Kruskal-Wallis test for 5 min ITI.

Mouse Methods and Data Analysis

Surgical Procedures (mouse)

General. Adult mice were anesthetized with isoflurane (5% induction, 1% maintenance). After weighing the animal, ketoprofen (5 mg/kg) and buprenorphine SR (1 mg/kg) were subcutaneously injected. The mouse was placed on a stereotaxic frame (David Kopf Instruments, CA, USA) and body temperature was kept stable throughout the surgery with a heating pad. The hair covering the skin above the skull was removed and the skin was sterilized with chlorhexidine. A sterile scalpel was used to make an incision. The skull was cleaned with autoclaved cotton swabs. Bregma and lambda were leveled to be on the same z-axis. Two points on the surface of the skull 2.5 mm to either side of lambda were used to level the skull with regard to the y-axis. After further surgical procedures detailed below, Bupivacaine (up to 1 mg/kg) is applied subcutaneously to the skin margins at the site of the incision to provide local analgesia before closing the wound. Tissue adhesive was used to close the incision. During the post-operative care period, mice were provided with ibuprofen (30 mg/kg) in the drinking water.

Viral injection. To inject virus and implant optical fibers for optogenetic and fiber photometry experiments, craniotomy holes were made over the dorsal raphe nucleus (DRN; antero-posterior (AP) axis: -4.65 mm; medio-lateral (ML) axis: ±1.3 mm; relative to Bregma). Virus was injected using a blunt 33 or 35-gauge microinjection needle within a 10 uL microsyringe (NanoFil, World Precision Instruments, FL, USA). The injection needle was lowered at an angle into the DRN (AP: -4.65 mm; ML: ±1.30 mm; dorsoventral (DV): -2.9~3.05 mm, at a 20 degree angle relative to vertical axis). Injection volume was controlled by a microsyringe pump (UMP3, World Precision Instruments), which was connected to a controller (Micro4, World Precision Instruments). 0.5-1 μL of AAV was infused per site at a rate of 100 nL per min. After injection, the needle was kept in place for an additional 10 min to allow the virus to diffuse into the tissue. To avoid backflow, the needle was withdrawn over approximately 10 min. Following each injection, the needle was rinsed multiple times with sterile saline to prevent clogging in subsequent injections. For fiber photometry experiments, mice were unilaterally injected with 1 μL AAV5-Syn-FLEX-GCaMP6s ($1x10^{13}$ genome copies/mL) or AAV5-Ef1a-DIO-eYFP ($1x10^{13}$ genome copies/mL). For optogenetic experiments, mice were bilaterally injected with 0.5 μL AAV5-Ef1a-DIO-ChR2(H134R)-eYFP (1-$2.5x10^{13}$ genome copies/mL) or AAV5-Ef1a-DIO-eYFP ($1x10^{13}$ genome copies/mL).

The procedure was the same for ablation experiments, but the number of craniotomies, injection coordinates and volumes were different (AP: -4.1, -4.4, -4.4, -4.6 mm; ML: -1.65, -1.3, +1.6, +1.3 mm; dorsoventral (DV): -4.85, -3.1, -4.8, -3.1 mm, at a 20 degree angle relative to vertical axis; injection volumes from anterior to posterior: 0.5, 1, 0.5, 0.5 μL).

For our ablation experiments we targeted all non-medullary 5-HT populations (groups B5-B9) as opposed to only the DRN (groups B6-B7) which were the target of our fiber photometry and optogenetics experiments. We made this choice for three reasons: First, in our chemogenetic and 2-photon ablations in zebrafish we ablated all non-medullary populations. Therefore, ablating groups B5-B9 in mice would allow for direct comparison between the two species. Second, previous work has suggested that other non-medullary raphe nuclei beyond the DRN are involved in sleep regulation (Jouvet, 1968). Third, ablating specifically groups B6-B7 (DRN) is technically challenging as they are anatomically very close to the smaller groups B5, B8 and B9. Indeed, interpretation of past ablation-based work has at times been complicated by questions of specificity. In optogenetic and fiber photometry experiments possible transfection of non-DRN populations is not an issue, since the localization of the optical fiber and the limited ability of light to travel through

tissue allow for precise targeting (and also only allow a small area to be targeted). In the case of AAV5-EF1a-mCherry-FLEX-dtA injections, diffusion of AAVs through the tissue does not allow for precise targeting; efforts to limit dtA expression to only groups B6-B7 would result in a cohort of mice with varying levels of ablation coverage. Therefore, to ensure consistency, we decided to target all non-medullary groups instead, in agreement with a previous raphe-ablation study (Whitney et al., 2016). Importantly, this strategy spares the B1-B3 groups (Figure 6B), ablation of which has been shown to secondarily disrupt sleep due to the role of these groups in thermoregulation.

Whenever possible, cage mates were split into experimental and control groups. Allocation of animals to experimental and control groups was random. Behavioral experiments were started no earlier than 14 days after injection to ensure sufficient viral transgene expression.

Optical fiber implantation. After the injection needle was withdrawn, optical fibers with cut length of 4 mm (optogenetics: MFC_300/330-0.37_4mm_ZF1.25_FLT, fiber photometry: MFC_400/430-0.48_4mm_ZF1.25_FLT, Doric lenses, Quebec, QC, Canada) were mounted in a stereotaxic holder (1766AP, David Kopf Instruments, CA, USA) and inserted into the tissue targeting the DRN (AP: -4.65 mm; ML: ±1.30 mm; DV: -2.5~2.75 mm, at a 20 degree angle relative to vertical axis, see Figures S6A and S7E). For fiber photometry experiments only one optical fiber was implanted per animal, whereas two optical fibers were bilaterally inserted for optogenetic experiments. To fix the optical fibers to the skull, a layer of adhesive cement (C&B Metabond, Parkell Inc., NY, USA) was applied to the surface of the skull around the optical fiber. In addition, a layer of dental cement (51458, Stoelting Co., IL, USA) was used to secure the optical fiber.

EEG and EMG implantation. For EEG/EMG recordings, three craniotomy holes were made (for reference and ground: AP: -3.2 mm; ML: -2.8 mm; for first EEG channel: AP: 1.7 mm; ML: 0.8 mm; for second EEG channel: AP: -1.3 mm; ML: 1.3 mm) with a drill bit (#73, 105-0240.340, Kyocera, Kyoto, Japan). 0.10” electrodes with wire lead (8403, Pinnacle Technology Inc., KS, USA) were screwed into the craniotomy holes. Electrodes were covered and fixed to the skull with adhesive cement. Lead wires from the screw electrodes were connected to an EEG/EMG headmount (8201, Pinnacle Technology Inc.). Connections between lead wires and headmount were covered with silver epoxy (MG Chemicals, BC, Canada) to ensure electrical conduction. EMG wires from the headmount were inserted into the trapezius muscles. Dental cement was used to cover wires and their connection to the headmount.

Histology (mouse)

Perfusion. Animals were euthanized with 100 mg/kg euthasol i.p. injection and transcardially perfused with ice-cold 1x phosphate buffered saline (PBS) followed by ice-cold 4% paraformaldehyde (PFA) in 1x PBS. Mouse brains were post-fixed in 4% PFA at 4°C overnight on a shaker. Samples were immersed in 30% sucrose in 1x PBS solution for >2 days. Mouse brains were then embedded in Tissue-Tek O.C.T. Compound (102094-104, VWR) before freezing in dry ice for 1 h. Samples were then transferred to a -80°C freezer for long-term storage or directly sliced on a cryostat (Leica Biosystems). Samples from optogenetic and fiber photometry experiments were sectioned into 30 μm slices covering the superior (pontine) raphe. Samples from ablation experiments covered both the superior and inferior (medullary) raphe and were hence sectioned into 50 μm slices to reduce the number of sections to process.

Immunohistochemistry. After sectioning, brain slices were washed once with 1x PBS to remove O.C.T. Compound. Samples were then incubated overnight at 4°C on a shaker in a 1x PBS solution containing 0.1% Triton X-100, 10% normal goat serum (NGS; Jackson ImmunoResearch, PA, USA) and primary antibodies. Sections were washed three times for 15 min each in 1x PBS. Next, brain slices were incubated at 4°C overnight on a shaker in a 1x PBS solution containing 0.1% Triton X-100, 10% NGS and secondary antibodies. Sections were washed again three times for 15 min each in 1x PBS. Finally, slices were mounted on glass microscope slides (Adhesion Superfrost Plus Glass Slides, #5075-Plus, Brain Research Laboratories, MA, USA). After the brain slices dried, DAPI-containing mounting media (Fluoromount G with DAPI, 00-4959-52, eBioscience, CA, USA) was added before protecting the slices with a coverglass (Cover glass, #4860-1, Brain Research Laboratories, MA, USA). Confocal images were acquired on a Zeiss LSM 880 confocal microscope (Zeiss, Oberkochen, Germany). For quantification of viral transduction efficiency of DRN^{SERT} and DRN^{ePet} neurons and ablation of 5-HT neurons, brain slices were imaged on a Keyence BZ-X700 microscope (Keyence, IL, USA). The following primary antibodies were used: chicken polyclonal anti-GFP (1:500; GFP-1020; Aves Labs, OR, USA), chicken polyclonal anti-mCherry (1:500; ab205402; Abcam, MA, USA), rabbit polyclonal anti-Tryptophan Hydroxylase 2 (1:500; ABN60; Millipore, MA, USA). The following secondary antibodies were used: goat anti-chicken IgY H&L Alexa Fluor 488 (1:500; ab150169; Abcam, MA, USA), goat anti-chicken IgY H&L Alexa Fluor 647 (1:500; ab150175; Abcam, MA, USA), goat anti-rabbit IgG H&L Alexa Fluor 488 (1:500;

ab150077; Abcam, MA, USA), goat anti-rabbit IgG H&L Alexa Fluor 647 (1:500; ab150079; Abcam, MA, USA).

Fiber photometry (mouse)

Fiber photometry was performed as previously described (Cho et al., 2017). Briefly, we used a 490 nm (211 Hz) LED for GCaMP6s excitation and a 405 nm (531 Hz) LED for isosbestic wavelength (M490F1 and M405F1, Thorlabs Inc., NJ, USA). A real-time processor (RX8-2, Tucker David Technologies, FL, USA) and custom-written software (provided by Drs. Karl Deisseroth and Tom Davidson, Stanford University) were used to control the modulation at two different frequencies. GFP and violet cleanup excitation filters (FF02-472/30-25 and FF01-400/40-25, Semrock, NY, USA) were used for excitation wavelengths. The two different excitation lights were reflected off dichroic mirrors (DMLP425 and MD498, Thorlabs) and coupled into a low auto-fluorescence 400 μm patch cord (MFP_400/430/1100-0.48_2m_FC-ZF1.25, Doric lenses) with a high NA coupler/collimator (F240FC-A, Thorlabs). The patch cord was attached to a ceramic optical fiber implanted into the mouse brain. The LED powers for both excitation wavelengths were measured with a power meter (PM100D, Thorlabs) and set to be ~70 μW at the end of the patch cord. The emitted GCaMP6s fluorescence was guided back into the patch cord to the collimator, and passed through a dichroic mirror (MD498, Thorlabs). The signal was passed through a GFP emission filter (MF525-39, Thorlabs) and then relayed to a femtowatt photoreceiver (Model 2151, Newport Co., Irvine, CA, USA) using a focusing lens (62-561, Edmunds Optics, Barrington, NJ, USA). Photoreceiver signals were fed into an RX8-2 processor through a BNC cable and were demodulated into two signals, corresponding to each LED excitation wavelength based on its modulation frequency. These signals were then digitized at a sampling rate of 382 Hz and low-pass filtered at 15 Hz. To synchronize fiber photometry and EEG/EMG recordings, a BNC cable carrying TTL pulses from a TTL pulse generator (OTPG_8, Doric lenses, Quebec, QC, Canada) was connected to a digital input channel.

Polysomnographic recordings (mouse)

During polysomnographic recordings animals were singly housed in clear Plexiglas cylindrical tubes (diameter = 15”, height = 20”) with ad libitum food and water. Mice were connected to a customized pre-amplifier (10x gain, 0.5 Hz high-pass filter, 10 Hz high-pass filter for EMG; Pinnacle

Technology Inc., Lawrence, KS, USA) which was attached to a commutator (8204, Pinnacle Technology Inc.) enabling free movement. Before experiments began, mice were habituated to the recording conditions for at least 2 days. EEG/EMG signals were digitized using the OmniPlex System (Plexon, TX, USA) with a sampling rate of 1 kHz. Once data was acquired, Plexon's proprietary file format (pl2) was converted to European data format (.edf) with MATLAB (MathWorks, MA, USA) using the EEGLAB plug-in (Schwartz Center for Computational Neuroscience, La Jolla, CA, USA).

Sleep deprivation (mouse)

During the first 6 h of the light phase animals were sleep deprived by gentle handling (Eban-Rothschild et al., 2016) while monitoring their EEG and EMG signals on a computer screen. A paint brush was used to softly touch the animal whenever it exhibited reduced EMG tone and/or its EEG signal amplitudes increased. Following sleep deprivation, EEG and EMG signals were recorded for the remaining 6 h of the light phase.

Optogenetic stimulation (mouse)

Patch cords connected 447 nm lasers (MDL-III-447/200mW, Opto Engine LLC, Midvale, UT, USA) via swivel commutators (fiber-optic rotary joints, FRJ_1x1_FC-FC, Doric lenses) to the optical fibers implanted in animals. Laser pulses were controlled by a TTL pulse generator (OTPG_8, Doric lenses, Quebec, QC, Canada). TTL pulses were sent simultaneously to the lasers and the Plexon acquisition system through an analog input to record stimulation time with regard to EEG/EMG recording time. Pulse width was 10 ms and an optical power meter (PM100D, Thorlabs) was used to set the laser output to 5 mW at the tip of the optical fiber. Burst optical stimulation consisted of a 3 s train of pulses at 25 Hz delivered every 10 s for 5 min. This stimulation pattern was referred to as a single trial and was repeated every 30-40 min during the light phase. Tonic optical stimulation consisted of 12.5 min of pulses at a frequency of 3 Hz, which amounts to the same number of optical stimuli per trial as for the burst stimulation condition. Trials using tonic stimulation were repeated every 30-40 min during the dark phase. In order to collect enough single trials per animal and condition, experiments were repeated three times such that every other day an animal was subject to optical stimulation. For optogenetic experiments in conjunction with fluoxetine injection, 10-20

mg/kg fluoxetine (BML-NS140-0050, Enzo Life Sciences, Inc., NY, USA) was delivered by i.p. injection 30-60 min before the start of the experiment (i.e. 30-60 min before lights on or off).

Sleep/wake analysis (mouse)

SleepSign analysis software (SleepSign for Animal, Kissei Comtec Co., Nagano, Japan) was used for sleep-wake classification. Wake state was characterized by desynchronized EEG and high EMG activity. NREM sleep was identified by synchronized EEG with high power at < 4 Hz and low EMG activity. REM sleep was defined by desynchronized EEG with high power at theta frequencies (6-9 Hz) and very low EMG tone. Sleep-wake states were assigned to 5 s non-overlapping windows of EEG/EMG signals. EEG/EMG signals from experiments were automatically scored according to arbitrarily defined threshold for delta power, theta ratio and EMG integral. Classification was then manually corrected by an experimenter (M.A.) who was blind to expressed transgene and experimental conditions.

Fiber photometry data processing and analysis (mouse)

Pre-processing of fiber photometry data was performed as previously described (Cho et al., 2017; Lerner et al., 2015). First, a 4^{th} order Butterworth filter with zero-phase distortion was applied to low-pass filter at 2 Hz fiber photometry signals from the two excitation wavelengths, 490 nm and 405 nm. Using a least-squares linear fit, the 405 nm signal was aligned to the 490 nm signal. $\Delta F/F$ was then calculated according to: (490 nm signal – fitted 405 nm signal)/(fitted 405 nm signal). To analyze temporal dynamics of DRN^{SERT} activity during sleep-wake states, photometry signals from each state including 20% of the traces before and after state transitions were extracted and down-sampled to a defined sample number in order to normalize timescale (Figure 5D). After down-sampling, each episode has a total duration of 1 (a.u.). For further analysis of significant dynamics within one state episode, $\Delta F/F$ values between 10-20 percentile time range of an episode were compared to values between 80-90 percentile time range. In Figure S6E these time ranges are referred to as early and late, respectively. Only sleep-wake states which lasted for >= 30 s were considered for this analysis.

EEG spectrogram and power spectral density (mouse)

EEG spectrogram plots were generated as previously described (Cho et al., 2017). Briefly, time-frequency decomposition of EEG signals was accomplished using Morlet wavelet and convolved with a complex Morlet wavelet having a Gaussian shape both in time and frequency domain around its central frequency. To estimate the power spectral density of EEG signals, the Welch method was applied. Window size was defined to be 5 s with 50% overlap between windows. Power was estimated at frequencies from 0.5 Hz to 100 Hz at 1 Hz step sizes. For optogenetic experiments, changes in power spectral density during the first minute of burst stimulation or last five minutes of tonic stimulation are shown as percentages of power estimates of one minute or five minutes before optical stimulation onset, respectively. For sleep deprivation experiments, only EEG signals from NREM bouts (>= 30 s) were considered for spectral analysis. In Figures S7J and S7K, BL refers to the average delta power in EEG signals from all NREM episodes across 12 h of undisturbed light phase. These EEG/EMG recordings were obtained during the previous light phase and were part of the 24 h EEG/EMG recordings whose analysis is shown in Figures 6C-6E. Likewise, in Figure 6F delta power in EEG signals from NREM episodes after sleep deprivation were compared to delta power in EEG signals from NREM episodes during the previous light phase EEG/EMG recordings without sleep deprivation. However, as opposed to Figures S7J and S7K, Figure 6F used NREM episodes from the corresponding time window as a comparison. Thus, average delta power from NREM episodes occurring within 0-2 h after SD were compared to average delta power from NREM episodes occurring within 6-8 h after light phase onset in the previous light phase recording. One control animal was excluded from spectral analysis due to a large number of artifacts in EEG traces.

Quantification of efficiency and specificity of viral transgene expression (mouse)

To quantify efficiency and specificity of viral transduction, optical sections were obtained via structured illumination on a Keyence BZ-X700 microscope (Keyence, IL, USA). Manual quantification was performed using the Cell Counter plugin, present in the Fiji distribution (Schindelin et al., 2012) of ImageJ (National Institutes of Health, Bethesda, MD). For samples from optogenetic and fiber photometry experiments, fluorescence micrographs were cropped to a 700 μm circle centered on the DRN. Seven to eight adjacent coronal sections, in which the tip of the optical fiber was clearly demarcated, were quantified, containing 1238 ± 98 TPH2+ cells. Efficiency was calculated as the total number of double-positive cells (i.e. transgene and TPH2 immunoreactive

cells) divided by the total number of TPH2 immunoreactive cells. Specificity was calculated as the total number of double-positive cells divided by the total number of transgene-immunoreactive cells. To quantify the degree of virus-mediated ablation, epifluorescence micrographs were used. The number of TPH2 immunoreactive cells was counted in serial coronal sections, starting at the most posterior aspect of the hypothalamus and ending 15 sections posterior to the first appearance of the central lobule of the cerebellar vermis. Animals in our control cohort had >7000 and >360 5-HT neurons in the B5-B9 groups and B1-B3 groups (up to appearance of the central lobule of the cerebellar vermis), respectively. Experimental animals were excluded from analysis if they had >520 and/or <360 5-HT neurons in the B5-B9 groups and B1-B3 groups, respectively.

QUANTIFICATION AND STATISTICAL ANALYSIS

Zebrafish

For all behavioral experiments the unit of analysis for statistics is a single animal during the day or night; for optogenetic experiments the unit of analysis for statistics is a single trial (Figure 4: 6 trials per animal; Figure S5: 3 trials per animal). Number of animals whose data are shown in a panel are indicated by "n=". Normality tests (D'Agostino & Pearson omnibus normality test; Shapiro-Wilk normality test) demonstrated that most behavioral parameters were not normally distributed. We therefore used non-parametric tests for most statistical analyses (Mann-Whitney test for two unpaired groups; Kruskal-Wallis test with Dunn's correction for multiple comparisons for more than two unpaired groups). The data represented in Figure 2C were normally distributed, hence we used unpaired t test. Tukey boxplots were used for data presentation, and are constructed as follows: the main rectangle (box) extends from the 25^{th} to the 75^{th} percentile with the median marked by a horizontal line through the box. The inter-quantile range (IQR) is the distance between these two quartiles. The lower whisker extends to the smallest datum that is larger than 25^{th} percentile - 1.5*IQR. The upper whisker extends to the largest datum that is smaller than 75^{th} percentile + 1.5*IQR. Data points outside the Tukey range were not represented in the graphs to facilitate data presentation but were included in statistical analyses. All statistical analyses were performed using Prism 6 (GraphPad Software, San Diego, CA, USA). Data are considered to be statistically significant if $p < 0.05$.

Mouse

All data shown in the figures, except for the representative examples, are represented as mean ± S.E.M. The unit of analysis for statistics is a single animal. The single trials from one animal are averaged and the average value from each animal is then used to calculate mean ± S.E.M. and to test for statistical significance. Number of animals whose data are shown in a panel are indicated by "n=". Probability in Figures 7 and S7 is calculated by taking the ratio of number of times the animal spent in a particular behavioral state at a given time point with regard to optical stimulation over the total number of single trials. The Kolmogorov-Smirnov test, Lilliefors test and Shapiro-Wilk normality test were used to test for normality. Paired and unpaired t tests were applied when all the data shown in a given panel is normally distributed, otherwise the non-parametric Wilcoxon rank sum test was applied. To compare more than two groups, one-way ANOVA was used with Bonferroni correction for multiple comparisons. The Statistics and Machine Learning toolbox in MATLAB (Mathworks) was used for statistical analyses. Data are considered to be statistically significant if $p < 0.05$.

DATA AND CODE AVAILABILITY

The datasets generated and analyzed in this study are available from the corresponding author upon request.

2.11 References

Adrien, J. (2008). Sleep and waking in mutant mice that do not express various proteins involved in serotonergic neurotransmission such as the serotonergic transporter, monoamine oxidase A, and 5-HT1A, 5-HT1B, 5-HT2A, 5-HT2C and 5-HT7 receptors. In serotonin and sleep: Molecular, functional and clinical aspects, J.M. Monti, S.R. Pandi-Perumal, B.L. Jacobs, and D.J. Nutt, eds. (Birkhäuser), pp. 457–475.

Airhart, M.J., Lee, D.H., Wilson, T.D., Miller, B.E., Miller, M.N., Skalko, R.G., and Monaco, P.J. (2012). Adverse effects of serotonin depletion in developing zebrafish. Neurotoxicol. Teratol. *34*, 152–160.

Alenina, N., Kikic, D., Todiras, M., Mosienko, V., Qadri, F., Plehm, R., Boyé, P., Vilianovitch, L., Sohr, R., Tenner, K., et al. (2009). Growth retardation and altered autonomic control in mice lacking brain serotonin. Proc. Natl. Acad. Sci. U. S. A. *106*, 10332–10337.

Allers, K.A., and Sharp, T. (2003). Neurochemical and anatomical identification of fast- and slow-firing neurones in the rat dorsal raphe nucleus using juxtacellular labelling methods in vivo. Neuroscience *122*, 193–204.

Aston-Jones, G., and Cohen, J.D. (2005). An integrative theory of locus coeruleus-norepinephrine function: Adaptive gain and optimal performance. Annu. Rev. Neurosci. *28*, 403–450.

Azmitia, E.C., and Segal, M. (1978). An autoradiographic analysis of the differential ascending projections of the dorsal and median raphe nuclei in the rat. J. Comp. Neurol. *179*, 641–667.

Bellipanni, G., Rink, E., and Bally-Cuif, L. (2002). Cloning of two tryptophan hydroxylase genes expressed in the diencephalon of the developing zebrafish brain. Mech. Dev. *119 (Suppl 1)*, S215–S220.

Borbély, A.A. (1982). A two process model of sleep regulation. Hum. Neurobiol. *1*, 195–204.

Borbély, A.A., and Neuhaus, H.U. (1979). Sleep-deprivation: Effects on sleep and EEG in the rat. J. Comp. Physiol. *133*, 71–87.

Bouhuys, A.L., and Van Den Hoofdakker, R.H. (1977). Effects of midbrain raphe destruction on sleep and locomotor activity in rats. Physiol. Behav. *19*, 535–541.

Buchanan, G.F., and Richerson, G.B. (2010). Central serotonin neurons are required for arousal to CO2. Proc. Natl. Acad. Sci. *107*, 16354–16359.

Burgess, H.A., and Granato, M. (2007). Sensorimotor gating in larval zebrafish. J. Neurosci. *27*, 4984–4994.

Cespuglio, R., Walker, E., Gomez, M.-E., and Musolino, R. (1976). Cooling of the nucleus raphe dorsalis induces sleep in the cat. Neurosci. Lett. *3*, 221–227.

Chen, S., Oikonomou, G., Chiu, C.N., Niles, B.J., Liu, J., Lee, D.A., Antoshechkin, I., and Prober, D.A. (2013). A large-scale in vivo analysis reveals that TALENs are significantly more mutagenic than ZFNs generated using context-dependent assembly. Nucleic Acids Res. *41*, 2769–2778.

Cho, J.R., Treweek, J.B., Robinson, J.E., Xiao, C., Bremner, L.R., Greenbaum, A., and Gradinaru, V. (2017). Dorsal raphe dopamine neurons modulate arousal and promote wakefulness by salient stimuli. Neuron *94*, 1205-1219.

Cohen, J.Y., Amoroso, M.W., and Uchida, N. (2015). Serotonergic neurons signal reward and punishment on multiple timescales. eLife *4*, e06346.

Curado, S., Stainier, D.Y.R., and Anderson, R.M. (2008). Nitroreductase-mediated cell/tissue ablation in zebrafish: A spatially and temporally controlled ablation method with applications in developmental and regeneration studies. Nat. Protoc. *3*, 948–954.

Dahlstroem, A., and Fuxe, K. (1964). Evidence for the existence of monoamine-containing neurons in the central nervous system. I. Demonstration of monoamines in the cell bodies of brain stem neurons. Acta Physiol. Scand. Suppl. SUPPL 232:1-55.

Dreosti, E., Lopes, G., Kampff, A.R., and Wilson, S.W. (2015). Development of social behavior in young zebrafish. Front. Neural Circuits *9*, 39.

Dugovic, C., and Wauquier, A. (1987). 5-HT2 receptors could be primarily involved in the regulation of slow-wave sleep in the rat. Eur. J. Pharmacol. *137*, 145–146.

Eban-Rothschild, A., Rothschild, G., Giardino, W.J., Jones, J.R., and de Lecea, L. (2016). VTA dopaminergic neurons regulate ethologically relevant sleep-wake behaviors. Nat. Neurosci. *19*, 1356–1366.

Fisher, S.P., Foster, R.G., and Peirson, S.N. (2013). The circadian control of sleep. Handb. Exp. Pharmacol. *217*, 157–183.

Frank, M.G., Stryker, M.P., and Tecott, L.H. (2002). Sleep and sleep homeostasis in mice lacking the 5-HT2c receptor. Neuropsychopharmacology *27*, 869–873.

Gandhi, A.V., Mosser, E.A., Oikonomou, G., and Prober, D.A. (2015). Melatonin is required for the circadian regulation of sleep. Neuron *85*, 1193–1199.

Gent, T.C., Bandarabadi, M., Herrera, C.G., and Adamantidis, A.R. (2018). Thalamic dual control of sleep and wakefulness. Nat. Neurosci. *21*, 974–984.

Goto, Y., Otani, S., and Grace, A.A. (2007). The Yin and Yang of dopamine release: A new perspective. Neuropharmacology *53*, 583–587.

Idzikowski, C., Mills, F.J., and Glennard, R. (1986). 5-Hydroxytryptamine-2 antagonist increases human slow wave sleep. Brain Res. *378*, 164–168.

Iwasaki, K., Komiya, H., Kakizaki, M., Miyoshi, C., Abe, M., Sakimura, K., Funato, H., and Yanagisawa, M. (2018). Ablation of central serotonergic neurons decreased REM sleep and attenuated arousal response. Front. Neurosci. *12*, 535.

Jacobs, B.L., and Azmitia, E.C. (1992). Structure and function of the brain serotonin system. Physiol. Rev. *72*, 165–229.

Jacobs, B.L., and Fornal, C.A. (2010). Activity of brain serotonergic neurons in relation to physiology and behavior. In handbook of the behavioral neurobiology of serotonin, C.P. Müller and B.L. Jacobs, eds. (Elsevier/Academic Press), pp. 153–162.

Jouvet, M. (1968). Insomnia and decrease of cerebral 5-hydroxytryptamine after destruction of the raphe system in the cat. Adv. Pharmacol. *6* (Pt B), 265–279.

Jouvet, M. (1972). The role of monoamines and acetylcholine-containing neurons in the regulation of the sleep-waking cycle. Ergeb. Physiol. *64*, 166–307.

Jouvet, M. (1999). Sleep and serotonin: An unfinished story. Neuropsychopharmacology *21* (2 Suppl), 24S-27S.

Kawashima, T., Zwart, M.F., Yang, C.-T., Mensh, B.D., and Ahrens, M.B. (2016). The serotonergic system tracks the outcomes of actions to mediate short-term motor learning. Cell *167*, 933-946.

Kirby, L.G., Pernar, L., Valentino, R.J., and Beck, S.G. (2003). Distinguishing characteristics of serotonin and non-serotonin-containing cells in the dorsal raphe nucleus: Electrophysiological and immunohistochemical studies. Neuroscience *116*, 669–683.

Koella, W.P., Feldstein, A., and Czicman, J.S. (1968). The effect of para-chlorophenylalanine on the sleep of cats. Electroencephalogr. Clin. Neurophysiol. *25*, 481–490.

Lebrand, C., Cases, O., Adelbrecht, C., Doye, A., Alvarez, C., El Mestikawy, S., Seif, I., and Gaspar, P. (1996). Transient uptake and storage of serotonin in developing thalamic neurons. Neuron *17*, 823–835.

Lerner, T.N., Shilyansky, C., Davidson, T.J., Evans, K.E., Beier, K.T., Zalocusky, K.A., Crow, A.K., Malenka, R.C., Luo, L., Tomer, R., et al. (2015). Intact-brain analyses reveal distinct information carried by SNc dopamine subcircuits. Cell *162*, 635–647.

Lillesaar, C. (2011). The serotonergic system in fish. J. Chem. Neuroanat. *41*, 294–308.

Lillesaar, C., Stigloher, C., Tannhäuser, B., Wullimann, M.F., and Bally-Cuif, L. (2009). Axonal projections originating from raphe serotonergic neurons in the developing and adult zebrafish, Danio rerio, using transgenics to visualize raphe-specific pet1 expression. J. Comp. Neurol. *512*, 158–182.

Lin, J.Y., Lin, M.Z., Steinbach, P., and Tsien, R.Y. (2009). Characterization of engineered channelrhodopsin variants with improved properties and kinetics. Biophys. J. *96*, 1803–1814.

Liu, Z., Zhou, J., Li, Y., Hu, F., Lu, Y., Ma, M., Feng, Q., Zhang, J., Wang, D., Zeng, J., et al. (2014). Dorsal raphe neurons signal reward through 5-HT and glutamate. Neuron *81*, 1360–1374.

Lovett-Barron, M., Andalman, A.S., Allen, W.E., Vesuna, S., Kauvar, I., Burns, V.M., and Deisseroth, K. (2017). Ancestral circuits for the coordinated modulation of brain state. Cell *171*, 1411–1423.

Marcinkiewcz, C.A., Mazzone, C.M., D'Agostino, G., Halladay, L.R., Hardaway, J.A., DiBerto, J.F., Navarro, M., Burnham, N., Cristiano, C., Dorrier, C.E., et al. (2016). Serotonin engages an anxiety and fear-promoting circuit in the extended amygdala. Nature *537*, 97–101.

Mathias, J.R., Zhang, Z., Saxena, M.T., and Mumm, J.S. (2014). Enhanced cell-specific ablation in zebrafish using a triple mutant of Escherichia coli nitroreductase. Zebrafish *11*, 85–97.

McGinty, D.J., and Harper, R.M. (1976). Dorsal raphe neurons: Depression of firing during sleep in cats. Brain Res. *101*, 569–575.

McLean, D.L., and Fetcho, J.R. (2004). Ontogeny and innervation patterns of dopaminergic, noradrenergic, and serotonergic neurons in larval zebrafish. J. Comp. Neurol. *480*, 38–56.

Montgomery, J.E., Wiggin, T.D., Rivera-Perez, L.M., Lillesaar, C., and Masino, M.A. (2016). Intraspinal serotonergic neurons consist of two, temporally distinct populations in developing zebrafish. Dev. Neurobiol. *76*, 673–687.

Monti, J.M. (2011). Serotonin control of sleep-wake behavior. Sleep Med. Rev. *15*, 269–281.

Monti, J.M., Pandi-Perumal, S.R., Jacobs, B.L., and Nutt, D.J. (2008). Serotonin and sleep: Molecular, functional and clinical aspects (Birkhäuser).

Mouret, J., Bobillier, P., and Jouvet, M. (1968). Insomnia following parachlorophenylalanin in the rat. Eur. J. Pharmacol. *5*, 17–22.

Müller, C.P., and Jacobs, B.L. (2010). Handbook of the behavioral neurobiology of serotonin (Elsevier/Academic Press).

Murray, N.M., Buchanan, G.F., and Richerson, G.B. (2015). Insomnia caused by serotonin depletion is due to hypothermia. Sleep (Basel) *38*, 1985–1993.

Narboux-Neme, N., Angenard, G., Mosienko, V., Klempin, F., Pitychoutis, P.M., Deneris, E., Bader, M., Giros, B., Alenina, N., and Gaspar, P. (2013). Postnatal growth defects in mice with constitutive depletion of central serotonin. ACS Chem. Neurosci. *4*, 171–181.

Oikonomou, G., and Prober, D.A. (2017). Attacking sleep from a new angle: Contributions from zebrafish. Curr. Opin. Neurobiol. *44*, 80–88.

Popa, D., Léna, C., Fabre, V., Prenat, C., Gingrich, J., Escourrou, P., Hamon, M., and Adrien, J. (2005). Contribution of 5-HT2 receptor subtypes to sleep–wakefulness and respiratory control, and functional adaptations in knock-out mice lacking 5-HT2A receptors. J. Neurosci. *25*, 11231–11238.

Porkka-Heiskanen, T., Strecker, R.E., Thakkar, M., Bjørkum, A.A., Greene, R.W., and McCarley, R.W. (1997). Adenosine: A mediator of the sleep-Inducing effects of prolonged wakefulness. Science *276*, 1265–1268.

Portas, C.M., and Grønli, J. (2008). Involvement of the 5-HT1A and the 5-HT1B receptor in the regulation of sleep and waking. In Serotonin and sleep: Molecular, functional and clinical aspects, J.M. Monti, S.R. Pandi-Perumal, B.L. Jacobs, and D.J. Nutt, eds. (Birkhäuser), pp. 325–369.

Portas, C.M., Bjorvatn, B., and Ursin, R. (2000). Serotonin and the sleep/wake cycle: Special emphasis on microdialysis studies. Prog. Neurobiol. *60*, 13–35.

Prober, D.A., Rihel, J., Onah, A.A., Sung, R.-J., and Schier, A.F. (2006). Hypocretin/orexin overexpression induces an insomnia-like phenotype in zebrafish. J. Neurosci. *26*, 13400–13410.

Qian, Y., Cao, Y., Deng, B., Yang, G., Li, J., Xu, R., Zhang, D., Huang, J., and Rao, Y. (2017). Sleep homeostasis regulated by 5HT2b receptor in a small subset of neurons in the dorsal fan-shaped body of Drosophila. eLife *6*, e26519.

Ren, J., Friedmann, D., Xiong, J., Liu, C.D., Ferguson, B.R., Weerakkody, T., DeLoach, K.E., Ran, C., Pun, A., Sun, Y., et al. (2018). Anatomically defined and functionally distinct dorsal raphe serotonin sub-systems. Cell *175*, 472-487.

Rihel, J., Prober, D.A., Arvanites, A., Lam, K., Zimmerman, S., Jang, S., Haggarty, S.J., Kokel, D., Rubin, L.L., Peterson, R.T., et al. (2010). Zebrafish behavioral profiling links drugs to biological targets and rest/wake regulation. Science *327*, 348–351.

Saper, C.B., Scammell, T.E., and Lu, J. (2005). Hypothalamic regulation of sleep and circadian rhythms. Nature *437*, 1257–1263.

Scammell, T.E., Arrigoni, E., and Lipton, J.O. (2017). Neural circuitry of wakefulness and sleep. Neuron *93*, 747–765.

Schindelin, J., Arganda-Carreras, I., Frise, E., Kaynig, V., Longair, M., Pietzsch, T., Preibisch, S., Rueden, C., Saalfeld, S., Schmid, B., et al. (2012). Fiji: An open-source platform for biological-image analysis. Nat. Methods *9*, 676–682.

Schweimer, J.V., and Ungless, M.A. (2010). Phasic responses in dorsal raphe serotonin neurons to noxious stimuli. Neuroscience *171*, 1209–1215.

Scott, M.M., Wylie, C.J., Lerch, J.K., Murphy, R., Lobur, K., Herlitze, S., Jiang, W., Conlon, R.A., Strowbridge, B.W., and Deneris, E.S. (2005). A genetic approach to access serotonin neurons for in vivo and in vitro studies. Proc. Natl. Acad. Sci. U. S. A. *102*, 16472–16477.

Simonneaux, V., and Ribelayga, C. (2003). Generation of the melatonin endocrine message in mammals: A review of the complex regulation of melatonin synthesis by norepinephrine, peptides, and other pineal transmitters. Pharmacol. Rev. *55*, 325–395.

Singh, C., Oikonomou, G., and Prober, D.A. (2015). Norepinephrine is required to promote wakefulness and for hypocretin-induced arousal in zebrafish. eLife *4*, e07000.

Smith, H.R., Leibold, N.K., Rappoport, D.A., Ginapp, C.M., Purnell, B.S., Bode, N.M., Alberico, S.L., Kim, Y.-C., Audero, E., Gross, C.T., et al. (2018). Dorsal raphe serotonin neurons mediate CO2-induced arousal from sleep. J. Neurosci. *38*, 1915–1925.

Solarewicz, J.Z., Angoa-Perez, M., Kuhn, D.M., and Mateika, J.H. (2015). The sleep-wake cycle and motor activity, but not temperature, are disrupted over the light-dark cycle in mice genetically depleted of serotonin. Am. J. Physiol. Regul. Integr. Comp. Physiol. *308*, R10-R17.

Sommerfelt, L., and Ursin, R. (1993). The 5-HT2 antagonist ritanserin decreases sleep in cats. Sleep *16*, 15–22.

Tabor, K.M., Bergeron, S.A., Horstick, E.J., Jordan, D.C., Aho, V., Porkka-Heiskanen, T., Haspel, G., and Burgess, H.A. (2014). Direct activation of the Mauthner cell by electric field pulses drives ultrarapid escape responses. J. Neurophysiol. *112*, 834–844.

Tan, C.L., and Knight, Z.A. (2018). Regulation of body temperature by the nervous system. Neuron *98*, 31–48.

Teraoka, H., Russell, C., Regan, J., Chandrasekhar, A., Concha, M.L., Yokoyama, R., Higashi, K., Take-Uchi, M., Dong, W., Hiraga, T., et al. (2004). Hedgehog and Fgf signaling pathways regulate the development of tphR-expressing serotonergic raphe neurons in zebrafish embryos. J. Neurobiol. *60*, 275–288.

Torda, C. (1967). Effect of brain serotonin depletion on sleep in rats. Brain Res. *6*, 375–377.

Trueta, C., and De-Miguel, F.F. (2012). Extrasynaptic exocytosis and its mechanisms: A source of molecules mediating volume transmission in the nervous system. Front. Physiol. *3*, 319.

Trulson, M.E., and Jacobs, B.L. (1979). Raphe unit activity in freely moving cats: Correlation with level of behavioral arousal. Brain Res. *163*, 135–150.

Ursin, R. (2008). Changing concepts on the role of serotonin in the regulation of sleep and waking. In serotonin and sleep: Molecular, functional and clinical aspects, (Birkhäuser), pp. 3–21.

Vanhatalo, S., and Soinila, S. (1998). Serotonin is not synthesized, but specifically transported, in the neurons of the hypothalamic dorsomedial nucleus. Eur. J. Neurosci. *10*, 1930–1935.

Veasey, S.C., Fornal, C.A., Metzler, C.W., and Jacobs, B.L. (1995). Response of serotonergic caudal raphe neurons in relation to specific motor activities in freely moving cats. J. Neurosci. *15*, 5346–5359.

Weitzman, E.D., Rapport, M.M., McGregor, P., and Jacoby, J. (1968). Sleep patterns of the monkey and brain serotonin concentration: Effect of p-chlorophenylalanine. Science *160*, 1361–1363.

Westerfield, M. (2000). The zebrafish book. A guide for the laboratory use of zebrafish (Danio rerio) (Univ. of Oregon Press).

Whitney, M.S., Shemery, A.M., Yaw, A.M., Donovan, L.J., Glass, J.D., and Deneris, E.S. (2016). Adult brain serotonin deficiency causes hyperactivity, circadian disruption, and elimination of siestas. J. Neurosci. *36*, 9828–9842.

Yokogawa, T., Hannan, M.C., and Burgess, H.A. (2012). The dorsal raphe modulates sensory responsiveness during arousal in zebrafish. J. Neurosci. *32*, 15205–15215.

Yu, H., Dickson, E.J., Jung, S.-R., Koh, D.-S., and Hille, B. (2016). High membrane permeability for melatonin. J. Gen. Physiol. *147*, 63–76.

Yuan, Q., Joiner, W.J., and Sehgal, A. (2006). A sleep-promoting role for the Drosophila serotonin receptor 1A. Curr. Biol. CB *16*, 1051–1062.

Zhdanova, I.V., Wang, S.Y., Leclair, O.U., and Danilova, N.P. (2001). Melatonin promotes sleep-like state in zebrafish. Brain Res. *903*, 263–268.

Zhuang, X., Masson, J., Gingrich, J.A., Rayport, S., and Hen, R. (2005). Targeted gene expression in dopamine and serotonin neurons of the mouse brain. J. Neurosci. Methods *143*, 27–32.

Chapter 3

DIRECTED EVOLUTION OF A SELECTIVE AND SENSITIVE SEROTONIN SENSOR VIA MACHINE LEARNING

Unger, E.K.*, Keller, J.P.*, Altermatt, M.*, Liang, R., Matsui, A., Dong, C., Hon, O.J., Yao, Z., Sun, J., Banala, S., Flanigan, M.E., Jaffe, D.A., Hartanto, S., Carlen, J., Mizuno, G.O., Borden, P.M., Shivange, A.V., Cameron, L.P., Sinning, S., Underhill, S.M., Olson, D.E., Amara, S.G., Lang, D.T., Rudnick, G., Marvin, J.S., Lavis, L.D., Lester, H.A., Alvarez, V.A., Fisher, A.J., Prescher, J.A., Kash, T.L, Yarov-Yarovoy, V., Gradinaru, V., Looger, L.L., and Tian, L. (2019). Directed evolution of a selective and sensitive serotonin sensor via machine learning. Cell *183*, 1986-2002.e26. doi: 10.1016/j.cell.2020.11.040.
*equal contribution

3.1 Summary

Serotonin plays a central role in cognition and is the target of most pharmaceuticals for psychiatric disorders. Existing drugs have limited efficacy; creation of improved versions will require better understanding of serotonergic circuitry, which has been hampered by our inability to monitor serotonin release and transport with high spatial and temporal resolution. We developed and applied a binding-pocket redesign strategy, guided by machine learning, to create a high-performance, soluble, fluorescent serotonin sensor (iSeroSnFR), enabling optical detection of millisecond-scale serotonin transients. We demonstrate that iSeroSnFR can be used to detect serotonin release in freely behaving mice during fear conditioning, social interaction, and sleep/wake transitions. We also developed a robust assay of serotonin transporter function and modulation by drugs. We expect that both machine-learning-guided binding-pocket redesign and iSeroSnFR will have broad utility for the development of other sensors and *in vitro* and *in vivo* serotonin detection, respectively.

3.2 Introduction

Serotonergic systems profoundly modulate diverse behaviors (Berger et al., 2009; Charnay and Leger, 2010). Serotonin (5-HT) dysregulation has been implicated in mental disorders, including depression and anxiety (Belmaker and Agam, 2008; Calhoon and Tye, 2015). Most antidepressants

target some aspect of the serotonergic system; selective serotonin reuptake inhibitors (SSRIs) specifically target the 5-HT transporter (SERT) (Bos et al., 2012; Cipriani et al., 2018). Despite the critical importance of 5-HT, development of novel and more effective therapies has been challenging due to poor understanding of 5-HT dynamics, specifically the inabililty to measure 5-HT with high spatiotemporal resolution. Existing methods for measuring 5-HT, including microdialysis and fast-scan cyclic voltammetry (FSCV) (Abdalla et al., 2017; Jaquins-Gerstl and Michael, 2015; Peñalva et al., 2003; Schultz and Kennedy, 2008), as well as transporter assays relying primarily on radiolabeled 5-HT or analogs (Clarke and Khalid, 2015), lack the spatial or temporal resolution to adequately probe 5-HT dynamics and targetability.

A genetically encoded 5-HT sensor could potentially overcome these technical challenges (for review see (Broussard et al., 2014; Lin and Schnitzer, 2016; Looger and Griesbeck, 2012)). We and others have recently produced single-fluorescent protein (FP)-based sensors for neurotransmitters and neuromodulators based on either microbial periplasmic binding proteins (PBPs) or G-protein-coupled-receptors (GPCRs). Combined with modern microscopy, these sensors enable direct and specific measurements of diverse neurotransmitters and neuromodulators including glutamate (Marvin et al., 2013), GABA (Marvin et al., 2019), ATP (Lobas et al., 2019), dopamine (Patriarchi et al., 2018; Sun et al., 2018), acetylcholine (ACh) (Borden et al., 2020; Jing et al., 2020), and norepinephrine (Feng et al., 2019) with the necessary resolution for use in behaving animals (Corre et al. 2018; Madisen et al., 2015).

Although GPCR-based sensors can yield sensitive indicators, their response to pharmaceutical manipulations makes them problematic for use in any studies involving drug administration. Furthermore, it is difficult to target GPCR-based sensors to intracellular locations (*e.g.* to study 5-HT transport). PBP-based sensors are soluble and can therefore readily be targeted to subcellular locations, are amenable to high-throughput screening in bacteria, and easily allow detailed characterization in purified protein (Marvin et al., 2011). Naturally evolved PBPs typically bind few, if any, drugs targeting host proteins. In addition, microbial PBPs are bio-orthogonal to pathways in model organisms, promising minimal interference with endogenous signaling, a particular concern following long-term expression. Importantly, ligand binding in PBPs induces large conformational changes, resulting in very large dynamic ranges (Marvin et al., 2011, 2013, 2018). However, with no annotated PBPs for 5-HT, we opted to redesign the binding pocket of an existing PBP-based sensor to selectively bind 5-HT.

There are several complementary approaches available for binding-site redesign (Baker, 2019; Khoury et al., 2014). Site-saturated mutagenesis (SSM) combined with rational design can optimize sensor properties such as brightness, dynamic range, kinetics and affinity (Cobb et al., 2013; Packer and Liu, 2015). However, SSM, while sufficient to convert our ACh sensor to one binding the cholinergic agonist nicotine (Shivange et al., 2019), cannot plausibly cover sufficient sequence space to radically change binding specificity to the structurally very different 5-HT. Computational design (Rosetta) can successfully predict proteins with high affinity and selectivity for a given small molecule (Richter et al., 2011), but has never been used for sensors. Recently, machine-learning approaches of varying complexity have been applied to optimize protein function (Bedbrook et al., 2019; Biswas et al., 2018; Ehren et al., 2008; Liao et al., 2007; Saito and Nakatsuji, 2001; Wu et al., 2019). Our approach combined computational design and machine learning to guide an SSM pipeline. Using this method, we developed the first PBP-based 5-HT sensor (iSeroSnFR) by redesigning the binding pocket of the ACh sensor iAChSnFR0.6 (Borden et al., 2020). iSeroSnFR contains 19 mutations relative to iAChSnFR0.6; these conferred >5,000-fold improvement in 5-HT affinity while eliminating choline and ACh binding. We demonstrate that iSeroSnFR enables imaging of 5-HT dynamics in brain slices and freely moving mice. In addition, we highlight the clinical relevance of iSeroSnFR for pharmacological assays.

3.3 Results

Sensor design

Before redesigning a binding pocket for structurally disparate molecules, we established our machine learning pipeline on structurally similar molecules (Figure S1; Table S1; Data S1; STAR Methods). As a starting scaffold for our sensor, we chose an early version of iAChSnFR, based on a choline-binding PBP, OpuBC, from the hyperthermophile *Thermoanaerobacter sp. X513* (Miller et al., 2011). In addition, this variant displayed detectable binding to 5-HT (apparent K_d > 1 mM) (Figure S2A), making it a good starting template. We used a multi-stage pipeline to iteratively improve 5-HT binding and sensor response (Figure 1A). We first performed computational binding-pocket redesign using Rosetta, then iterative rounds of SSM guided by machine learning.

Step I: Computational binding-pocket redesign

To perform computational modeling, we started with the structures of open, ligand-free iAChSnFR0.6 (6URU) and closed, choline-bound *Bacillus subtilis* OpuBC (3R6U), and created a model of the closed, ACh-bound form of iAChSnFR using Rosetta (Figure 1B). 5-HT conformers (rotation of the β-aminoethyl and hydroxy moieties) were generated using Open Eye Omega (Hawkins et al., 2010), and docked into the closed-iAChSnFR model using RosettaLigand (Bender et al., 2016; Davis and Baker, 2009) (Figures 1B and 1C). Next, Rosetta protein redesign (Taylor et al., 2016; Tinberg et al., 2013) was used to optimize the 5-HT-binding pocket. In total, 250,000 variants were predicted and ranked based on computed ligand interaction (STAR Methods). The top 18 predicted variants were synthesized, purified, and examined for fluorescence response to 5-HT and other ligands including ACh (Figures S2B and S2C). Among the 18 variants, variant 7 showed the largest fluorescence response to 10 mM 5-HT ($\Delta F/F_0$ = 87% ± 20%) with no ACh response ($\Delta F/F_0$ = -4% ± 1%), representing an 18-fold improvement in 5-HT selectivity (Figure S2C). This mutated variant, named iSeroSnFR0.0 (Table S2), was then selected for further optimization.

Step II: Random forest modeling

We next optimized iSeroSnFR0.0 with SSM to improve 5-HT affinity. We used a random forest (RF) model to estimate the importance of each position interrogated by computational design (Table S2). We took the four highest-ranked positions from RF (66 > 170 > 143 > 188) (Figure 1D) and performed SSM at each site separately and in pairs (using degenerate NNK codons). We screened a total of 2,576 variants, including 92 from each single-site library and 368 from each dual-site library, for fluorescence response to 5-HT (10 mM). The library size was determined using the TopLib online library calculator (Nov, 2012). Of the screened variants, ~100 variants showed an improved response (~2- to 3-fold) compared to iSeroSnFR0.0 (Figure 1E). Subsequent analysis showed that top-performing variants frequently contained mutations at multiple positions, and the ordered contribution of each position (66 > 143 > 170 > 188) (Table S2) to the fluorescence response was nearly identical to that predicted by RF (66 > 170 > 143 > 188) (Figure 1F). No single mutation drastically improved 5-HT affinity, but combinations of mutations were frequently better than single mutations (Figure S2D). These results suggest that RF effectively predicts important positions contributing to sensor response, and simultaneous, beneficial contributions of multiple residues are essential to large-scale improvements.

Step III: Generalized linear model

Because single mutations offered only small improvements, whereas combinations gave much better results, mutations were clearly not additive. For example, we found a top-performing variant containing T66Y/H170A with 140% improved response, whereas T66Y and H170A alone showed only 40% and 10% improvements, respectively (Figure S2D). We next applied GLM to our dataset. This allowed us to identify individual mutations from our libraries that contribute to synergistic interactions – allowing us to design small targeted libraries.

GLM predicted that several amino acid mutations at each position would be beneficial (Figure 1F; Table S3), with 66Y, 66P, 143M, 170A, 188G, 188P, and 188T showing the strongest positive predictions. Given the beneficial T66Y/H170A mutant that we had already identified, we decided to synthesize variants combining those with GLM-predicted amino acid residues at positions 143 and 188. Out of 13 variants synthesized, 12 showed larger fluorescence response to 10 mM 5-HT than iSeroSnFR0.0 (Figure 1G) (GLM was moderately predictive: pseudo-R^2 = 0.31). One variant displayed 4.5-fold improved response over iSeroSnFR0.0, well above any SSM-screened variant. In purified protein, this variant (T66Y/F143M/H170A/H188T, named iSeroSnFR0.1) showed >9-fold increased fluorescence response $(\Delta F/F_0)_{max}$ relative to iSeroSnFR0.0 ($(\Delta F/F_0)_{max}$ = 480% ± 14% *vs*. 50% ± 4%), and 2-fold increased 5-HT affinity (900 ± 110 µM *vs*. 1.8 ± 0.5 mM) (Figure 1H).

In light of the substantial improvements from a single round of GLM-guided mutagenesis, we performed two more rounds of screening followed by GLM prediction, recruiting additional positions predicted by RF, and added others based on prior experience optimizing biosensors (*e.g.* linkers connecting the cpGFP to the binding protein, the interface between cpGFP and binding protein, and random mutations from previous rounds of screening) (Table S2). These subsequent rounds were screened at progressively lower 5-HT concentrations (round 2: 500 µM and round 3: 50 µM) to enrich for variants with tighter affinity. After each round, the top-performing variants were sequenced and reanalyzed using GLM to create a focused library; in total, ~13,000 variants were tested, of which 244 were sequenced. The best variant from round 2 (Figure 1I) came from the GLM-driven focused library, had 8-fold improved response over its parent iSeroSnFR0.1, and was named iSeroSnFR0.2. The best variant from round 3 (Figure 1J**)** was 5-fold improved over its parent iSeroSnFR0.2 (Figure 2A; Table S2). We named this final version iSeroSnFR, which contains 19

mutations relative to iAChSnFR0.6 (Figure 2A, PDB: 6PER); In purified protein, this variant exhibits 310 ± 30 μM affinity for 5-HT, and 800% $(\Delta F/F_0)_{max}$ (Figure 2B).

Our data show that GLM is highly effective at identifying beneficial mutations (Figures 1I and 1J): the average performance of GLM variants was significantly higher than SSM variants (1st, 2nd, and 3rd rounds: $p < 0.001$, Wilcoxon rank-sum test) and more importantly, the top variants in each round (including the top 15 variants from round 2) were from the GLM-inspired library as opposed to the SSM library. Thus, our machine-learning-guided mutagenesis pipeline can improve protein-ligand binding selectivity and affinity even for target molecules structurally distant from cognate ones, while still maintaining sensor function.

In vitro characterization

iSeroSnFR is highly specific for 5-HT over a wide array of endogenous molecules and drugs (Figures 2C and S3). Only tryptamine and dopamine showed detectable responses, but with 8- and 16-times weaker affinity (apparent K_d = 2.4 mM for tryptamine and 5.6 mM for dopamine), respectively. Other endogenous molecules showed marginal responses, with very low or negative responses, and/or titrations that did not fit a single-site binding isotherm.

To determine the *in situ* affinity in mammalian (HEK293T) cells, we cloned iSeroSnFR into the pMinDisplay expression vector (pDisplay lacking the HA epitope tag) (Marvin et al., 2013) such that iSeroSnFR would be displayed on the outer cell surface; we also cloned a version targeted to the post-synapse using full-length neuroligin (Nlgn) (STAR Methods). We observed robust membrane localization (Figure 2D) and clear response to 1.6 μM 5-HT (~50% $\Delta F/F_0$) (Figures 2E and S4A). The *in situ* affinity of the sensor on HEK293T cells was similar (390 ± 110 μM) to that in purified protein. Fortuitously, the fluorescence response of iSeroSnFR on HEK293T cells was significantly increased ($[\Delta F/F_0]_{max}$ = 1,700%). To characterize the utility of iSeroSnFR for physiologically relevant concentrations, we focused on the range from high-pM (338 pM) to mid-μM (60 μM) (Figures 2F and S4B). We observed small but reliable responses to all concentrations tested ($\Delta F/F_0$ = 16.8% ± 1.9% at 338 pM; similar responses up to 246 nM 5-HT) (Figure S4B). We quantified the ability of iSeroSnFR to faithfully report 5-HT by comparing 5-HT responses to Hank's balanced salt solution (HBSS) buffer responses (Figure S4C) with two metrics from signal detection theory: the receiver operating characteristic (ROC) (Figure S4D) and the discriminability index (*d'*) (Figure S4E). ROC analysis indicates that 5-HT responses show essentially perfect discrimination

(area under the curve = 0.990) (Figure S4D, bottom) of true-positives from false-positives, whereas buffer responses have no power (Figure S4D, top). Similarly, *d'* analysis shows that 5-HT responses have very strong separation from system noise (*d'* > 3) (Figure S4E, bottom), but buffer responses show essentially no separation (Figure S4E, top). Results on the surface of dissociated hippocampal neurons were similar to those on HEK293 cells ($\Delta F/F_0$ = 15.8% ± 2.0% at 16 nM 5-HT) (Figures 2G-2I and S4F).

We next sought to assess sensor kinetics. Using stopped-flow fluorescence, we found that the sensor reached saturation after ~10-40 s (Figures 3A and 3B). With a single exponential fit, $\tau_{apparent}$ was between 5 and 18 s (Figure 3C). We noted, however, that there appeared to be a very fast and robust initial rise (Figures 3D and 3E). We therefore fit a double-exponential curve with two phases of activation: a fast initial rise (Figure 3F), and a slower rise to saturation. Our double-exponential fit the data much more precisely and showed that the two phases occur with a rise τ of 0.5-10 ms (fast) and 5-18 s (slow). We postulate that ligand binding rapidly activates fluorescence of the sensor (Figure 3G, $K_{5\text{-HT}}$), but that the sensor in purified protein exists in an "inactive" (iSeroSnFR) and an "active" (iSeroSnFR*) conformation, and the transition between these states is slow (Figure 3G, k_+).

We then validated the kinetics of iSeroSnFR by using light-evoked release of 5-HT from a caged version (PA-N-5HT). Single pulses (1 ms) of uncaged 5-HT were robustly detected on the surface of cultured neurons (Figures 3H and 3I), and the amplitude of fluorescence changes increased with uncaging pulse duration (Figures 3I-3L). Decay to baseline featured a fast component (τ_{decay} ~ 4 ms at 10 ms pulse duration) followed by a slower component (τ_{decay} ~ 150 ms at 10 ms pulse duration) (Figures 3J and 3K). Diffusion of uncaged 5-HT away from the imaging location likely explains the slower component. To determine how iSeroSnFR responds to repeated 5-HT bursts, we used various combinations of uncaging pulse durations and frequencies. One-photon line-scans at 5,000 Hz or 250 Hz, and frame-scans at 40 Hz revealed robust, reproducible fluorescence increases to trains of uncaging pulses at various frequencies over prolonged imaging (line scans: 10 ms uncaging pulses at 5 Hz, Figure 3M, and 75 ms uncaging pulses at 1 Hz, Figure 3N; frame scan: 15 ms uncaging pulses at 0.4, 0.8 and 4 Hz, Figure 3O). Fluorescence response amplitude increased with uncaging pulse duration under frame-scan (Figure 3P). However, when line-scan mode was used, the amplitude decreased with increased pulse frequency (Figures 3O and S5A), possibly due to accumulation of 5-HT in the bath and resulting sensor saturation. It is also possible that this results

from the slow phase of the sensor response, as described above. 5-HT uncaged at one dendrite produced a negligible response in dendrites ~10 µm away (Figure 3Q). Although 5-HT uncaging readily activated iSeroSnFR, it failed to activate iAChSnFR0.6 (Figure 3R), indicating that the fluorescence response is specific to release of 5-HT, and not artefactual.

Imaging endogenous release of 5-HT in brain slice

Serotonergic fibers from the raphe nuclei innervate many brain regions, with dense projections found in medial prefrontal cortex (mPFC), orbitofrontal cortex (OFC), striatum, bed nucleus of the stria terminalis (BNST), and basolateral amygdala (BLA) (Bang et al., 2012; Belmer et al., 2017; Zhou et al., 2015). To demonstrate iSeroSnFR's utility in mouse brain slices, we first examined the expression level of iSeroSnFR in striatum and in mPFC. We cloned iSeroSnFR into regular and Cre-dependent adeno-associated virus (AAV) backbones, producing AAV2/9.*CAG*.iSeroSnFR.Nlgn and AAV2/9.*CAG*.FLEx.iSeroSnFR.PDGFR. We injected AAV2/9.*CAG*.iSeroSnFR.Nlgn into dorsal striatum of C57BL/6J mice (Figure 4A), and a mix of AAV2/9.*CAG*.FLEx.iSeroSnFR.PDGFR and AAV2/9.*CMV*.Cre (9:1 ratio) into mPFC of *Rosa*$^{Ai14/+}$ (Cre-dependent tdTomato expression) (Madisen et al., 2010) (Figure S5B). After 2 weeks recovery, iSeroSnFR expression was obvious in dorsal striatum as evidenced by widespread green fluorescence (Figure 4B) and in mPFC as evidenced by green fluorescence on membranes and processes of red, Cre-positive neurons (Figure S5C). We demonstrated robust functionality by imaging iSeroSnFR with two-photon frame-scan imaging while applying exogenous 5-HT *via* micro-injection (Figures S5D-S5F), or by imaging iSeroSnFR with one-photon photometry and applying exogenous 5-HT *via* bath application (Figure S5G).

We next imaged iSeroSnFR responses to electrically triggered release in mouse brain slices using one-photon photometry. Brief electrical stimuli triggered 5-HT release, readily detected by iSeroSnFR (1 pulse: $\Delta F/F_0 = 0.71\% \pm 0.12\%$); response amplitudes correlated with the number of electrical stimuli ($\Delta F/F_0 = 1.1\% \pm 0.1\%$ [2 pulses], $2.0\% \pm 0.4\%$ [5 pulses], $2.8\% \pm 0.5\%$ [10 pulses], $4.1\% \pm 0.7\%$ [20 pulses], and $5.8\% \pm 0.9\%$ [40 pulses], n = 7) (Figures 4C and 4D). Surprisingly, neither amplitude nor decay kinetics of fluorescence transients was affected by bath application of cocaine (10 µM), citalopram (1 µM), or reserpine (1 µM) (Figure S5H). Importantly, however, tetrodotoxin (TTX, 300 nM) (Figure 4E) completely abolished electrically evoked fluorescence transients, indicating that signals are indeed action potential-dependent.

Imaging endogenous release of 5-HT in freely behaving mice

We then examined the utility of iSeroSnFR in reporting physiologically relevant 5-HT dynamics in freely behaving mice across multiple brain regions (Figures 4F-4O). Serotonergic DRN neurons respond to both rewarding and aversive stimuli, but little is known about the dynamics of 5-HT release in regions receiving inputs from DRN (Li et al., 2016; Ren et al., 2018). Multiple lines of evidence highlight 5-HT as a critical neuromodulator of fear learning (Bocchio et al., 2016; Burghardt et al., 2007; Marcinkiewcz et al., 2016). Therefore, we injected AAV2/9.*CAG*.iSeroSnFR.Nlgn or AAV2/9.*CAG*.GFP into BLA (Figures 4F and 4G) and mPFC (Figures 4K and 4L), followed by fiber photometry during a fear learning paradigm. Mice were trained for 15 trials (Curzon et al., 2009), during which a cue period (10 s tone and light) was followed by a 1-s pause, and then a 1-s footshock (Figures 4H-4J and 4M-4O**).** We observed a rise in 5-HT during the cue period that was immediate in mPFC but slower in BLA, followed by a dip during the footshock and further rise afterward that decayed slowly in both brain regions, which was reliable across individual trials (Figures 4H and 4M). In control GFP-expressing mice, smaller deflections were associated with cue onset and foot shock, likely due to motion artifacts (Figures 4I and 4N).

We next imaged 5-HT release in response to social interaction in multisite recordings in three brain regions simultaneously: OFC, BNST and BLA, which are suggested to mediate this behavior in different ways (Kiser et al., 2012). We injected AAV2/9.*CAG*.iSeroSnFR.Nlgn into all three regions (Figures S6A-S6D) followed by multi-site fiber photometry during introduction of a same-sex intruder (Figure S6E). Wheel running has been shown to buffer behavioral consequences of stress in rodents, with concomitant changes in presynaptic 5-HT receptor and transporter expression in DRN (Greenwood et al., 2005). To assess this, we allowed mice access to a functional running wheel for 6 weeks prior to social interaction testing (Figure S6E). We found that iSeroSnFR reliably detected changes in 5-HT release during intruder presentation (Figures S6F-S6K**;** both in red "run" and blue "locked" trials), consistent with reports that $DRN^{5\text{-}HT}$ cells are activated by social interaction (Li et al., 2016). This increase was similar across all three regions, reaching statistical significance in OFC and BLA (Figures S6I-S6K). Free access to the wheel significantly increased 5-HT signal peak during social interaction, but only in OFC (Figures S6F-S6K**;** red "run" *vs.* blue "locked"). Taken together, these data suggest that iSeroSnFR permits robust recording of 5-HT release triggered

by fear conditioning and social interaction and behavioral modulation by wheel-running in multiple brain regions.

Imaging 5-HT dynamics in sleep-wakefulness cycles

We next tested the utility of iSeroSnFR in reporting 5-HT dynamics over long time intervals in sleep-wakefulness cycles (Portas et al., 2000). Electroencephalographic (EEG) and electromyographic (EMG) electrodes were implanted for simultaneous polysomnographic (sleep) recordings (Figures 5A and S7A). iSeroSnFR tracked 5-HT fluctuations across sleep-wake cycles over prolonged times, correlating well with EEG/EMG signals (Figures 5B and S7B**)**. When variable durations of sleep-wake states were normalized, iSeroSnFR signal amplitude was highest in wakefulness, decreased during non-rapid eye movement (NREM, "slow-wave") and was lowest during rapid eye movement (REM, "paradoxical") sleep (Figures 5C and S7C). We then examined 5-HT dynamics during state transitions. Fluorescence signals rose sharply at waking, peaked during wakefulness, and decreased immediately after sleep onset, further decreasing during REM sleep. The largest signal increase occurred during the REM-to-wakefulness transition, and the largest decrease was from NREM-to-REM (Figures 5D and S7D), clearly visible in individual trials. In control mice expressing GFP, no behavioral state-dependent changes in fluorescence were observed. Similar patterns were observed in both mPFC and BLA, however, in BLA, we observed more prominent fluorescence decreases during wakefulness-to-NREM transitions.

SERT function and pharmacology in cell culture

Given the clinical significance of drugs affecting 5-HT signaling and transport, we developed an iSeroSnFR-based assay to functionally characterize hSERT and drugs modulating it. We previously developed the oscillating stimulus transporter assay (OSTA) using intracellularly expressed fluorescent sensors for glutamate (Keller and Looger, 2016) and glucose (Keller et al., 2019). Because iSeroSnFR is intracellularly targetable, and does not respond to most clinical drugs, it is ideal for use with OSTA to asses hSERT-mediated transport (Figure 6A).

We first confirmed reported ionic requirements for hSERT function (reviewed in Rudnick and Sandtner, 2019). Extracellular sodium (10 or 160 mM) and chloride (10 or 160 mM) were both required for 5-HT uptake, while high extracellular potassium (150 mM) in the absence of sodium and 5-HT drove efflux, without dependence on chloride (Figures 6B and 6C). We next measured

hSERT's K_m for sodium in 5-HT uptake by subjecting cells to a smoothly varying ramp of external sodium concentration, interleaved with high sodium (150 mM) bouts, verified using the dye sulforhodamine 101 (200 mM) (Figure 6D). Uptake rates in individual cells were plotted as a function of $[Na^+]$ and fitted using the Hill equation, yielding an average K_m of 6.5 ± 0.1 mM and a Hill coefficient of 1.9 ± 0.1 (Figures 6E and 6F), similar to published values (Koldsø et al., 2011; Sneddon, 1969). These results demonstrate that intracellularly expressed iSeroSnFR can precisely quantify transporter biophysical properties.

We next used this technique to investigate drugs targeting hSERT. Drugs were added to both influx and efflux buffers to ensure consistent exposure. As expected, 5-HT transport was reduced by the competitive inhibitor cocaine (10 µM) (Figure 6G). Similarly, the SSRI escitalopram rapidly diminished 5-HT transport by >50% at 500 nM and abolished it at 1 µM (Figures 6H and 6I). The tricyclic antidepressant clomipramine (100 nM) also inhibited 5-HT transport, but with slower on- and off-rates than escitalopram (Wang et al., 2013) (Figure 6J). A newer antidepressant, vilazodone, caused transport function to rapidly disappear, and despite washouts of >20 minutes, did not return to baseline (Figure 6K). Because vilazodone's reported K_i (0.5 nM) (Heinrich et al., 2004) is comparable to that of clomipramine (0.3 nM) (Tatsumi et al., 1997), this result was unexpected and requires further investigation. We next measured longitudinal effects of stimulation of the protein kinase C pathway through addition of phorbol 12-myristate 13-acetate (PMA), which decreases 5-HT transport (400 nM) (Bermingham and Blakely, 2016). PMA induced a slow decrement in transport rate over ~40 minutes, consistent with its reported effects (Figure 6L) (Bermingham and Blakely, 2016). Since the decrement was relatively slow, it is likely that it represents extraction of transporters from cell membranes, also consistent with literature (Bermingham and Blakely, 2016).

Finally, we examined pharmacologically driven efflux of 5-HT, which has been proposed to underlie the psychoactive effects of psychedelics such as 3,4-methyl enedioxy methamphetamine (MDMA, "ecstasy"; acting mainly via SERT) (Rudnick and Sandtner, 2019). We omitted KCl from the efflux buffer, so oscillations were instead driven solely by presence or absence of 5-HT (0 or 10 µM). 20 µM MDMA was then added to the 5-HT-free buffer to probe its capacity for driving 5-HT efflux. We observed a 2-fold enhancement in efflux in the presence of 20 µM MDMA (Figure 6M). The ratio of efflux magnitude was about 1:2:3 for Na^+-, MDMA-, and K^+-driven effluxes, respectively (Figure 6N). The smaller magnitude of efflux driven by 5-HT removal alone results from the ability of extracellular Na^+ to stabilize hSERT in an outward-facing conformation, thereby

slowing down reverse transport (Zhang et al., 2016). MDMA-driven efflux probably reflects a different process in which hSERT catalyzes exchange of intracellular 5-HT with extracellular MDMA, without utilizing the entire transport cycle (Rudnick and Wall, 1992). As a whole, these experiments show that iSeroSnFR coupled with OSTA is a powerful tool for rapid, precise pharmacological characterization.

3.4 Discussion

Use of machine learning to accelerate directed evolution

Our combined Rosetta and machine-learning-guided directed evolution approach was quite effective. After just one round of each, we screened fewer than 2,600 variants, but made dramatic improvements to the sensor's affinity, specificity, and fluorescence response. After just two more rounds of machine-learning-guided directed evolution, we had screened a total of ~16,000 variants, interrogated more than 60 different protein scaffold positions, and introduced 19 mutations into our final sensor, increasing its 5-HT affinity by >5000-fold, abolishing choline/ACh binding, and increasing fluorescence response by 3-fold compared to the starting scaffold, iAChSnFR0.6. The efficacy of the design cycle diminished somewhat with each round. However, these results validate the rankings of the initial RF model, which predicted high impacts for the top 4 positions and progressively lower impacts for each successive position. Nonetheless, in each round, the best variant came from the GLM-predicted library; in rounds 1 and 2, these variants were nearly twice as good as the best-performing variant from the SSM library. Because RF uses an ensemble method, we could identify the most important features (protein positions) and provide guidance for subsequent stages. GLM is a good classifier even for small (<10,000) training datasets and is ideal for first-pass data analysis (Yang et al., 2019a). Our entire dataset was used for training (no test data), because our models were used only to guide one round of library design at a time.

Headroom remains in the iSeroSnFR scaffold, particularly for higher-affinity versions for better detection of sparse signaling events. It is likely that the machine-learning-guided approach detailed here can produce further gains, although each round thus far produced diminishing returns. A high-resolution structure of ligand-bound iSeroSnFR could reinvigorate this process, but we have been as yet unable to obtain such a structure. Alternatively, the addition of more biophysical parameters to the model, or more advanced ML models such as universal transformers (Dehghani et al., 2019), Bayesian optimization (Yang et al., 2019b), or neural networks (Kato et al., 2005), could

extract sequence/function relationships that we missed. On a related note, it will be broadly useful for the field to somehow incorporate ML-gleaned insights back into the biophysical potential functions underlying structure-based computational protein design. Regardless, the method described here was highly effective for our purposes, and we expect that it can be used to engineer other PBP-based neuromodulator sensors, and more generally to tackle other challenging protein-engineering tasks.

Molecular properties of iSeroSnFR

iSeroSnFR is highly selective for 5-HT over other endogenous signaling molecules and drugs (Figures 2C and S3). The physiological concentration of 5-HT has been estimated using FSCV to be in the high-nM to low-µM range (Bunin and Wightman, 1998; Bunin et al., 1998). The functional affinity of iSeroSnFR is in the high-µM range, much larger than endogenous monoamine receptors. However, its very large fluorescence response $(\Delta F/F_0)_{max}$, which is 3- to 30-fold larger than that of GPCR-based sensors (Jing et al., 2019; Mizuno et al., 2019; Wan et al., 2020), means that low concentrations are still readily detectible. On mammalian cells, iSeroSnFR reliably detected concentrations as low as ~350 pM (Figures 2F and S4B). Indeed, this high dynamic range and weaker affinity offers the additional advantages of fast kinetics (Helassa et al., 2018; Marvin et al., 2018) and low 5-HT buffering potential. Furthermore, the bio-orthogonal nature of the sensor reduces concerns of interference with endogenous receptors due to sensor overexpression. We have shown that the kinetics of iSeroSnFR are in the low millisecond range, both by stopped-flow (Figures 3D-3F) and by uncaging (Figures 3I-3K). We calculated both slow and fast components of the on-kinetics in purified protein, also observed with iGABASnFR and iGluSnFR (Marvin et al., 2019). Further investigation is needed to determine the mechanism underlying the apparently two-component on-kinetics. Nonetheless, we were able to demonstrate robust *in vivo* detection of millisecond-level release events. We believe that two-component on-kinetics could potentially serve as an advantage, in that the sensor could rapidly report lower concentration events, and then slowly read out larger changes in baseline occurring over several seconds. A higher-affinity sensor would quickly max out after low concentration events, and miss larger changes in baseline. However, the sensor is not without its limitations, and low concentration events might still be missed. Future engineering efforts will focus on producing a complementary sensor with higher affinity such that both high and low concentration events can be detected.

Imaging endogenous 5-HT release *ex vivo* and *in vivo*

With iSeroSnFR, we replicated several salient biological results using photometry, with much higher temporal resolution than previously possible. We detected electrically-evoked release, which was blocked by TTX. Surprisingly, we could not perturb observed fluorescent transients using blockers for SERT such as cocaine or citalopram, nor by the VMAT inhibitor reserpine. We expected cocaine and citalopram to prolong the 5-HT transients measured in slice by inhibiting 5-HT reuptake, as we showed *in vitro* (Figure 6G). Given the fast off-kinetics (Figures 3K and 3L), it is unlikely that sensor unbinding dominates the response waveform and obscures drug effects. Alternatively, in the brain slice preparation, released 5-HT potentially diffuses away, with SERT playing a minimal role in observed waveforms. Although possible, this is unlikely, given previous results using FSCV (Matsui and Alvarez, 2018). However, other groups have seen similar negative results, e.g., the inability of the SERT blocker fluoxetine to affect electrical stimulation-evoked 5-HT release amplitude and kinetics in the mouse dorsal raphe nucleus (Bunin and Wightman, 1998). It is also unclear why inhibition of VMAT with reserpine failed to block the transients by depleting 5-HT storage in synaptic vesicles. It is possible that reserpine only slowly depletes 5-HT from vesicles in brain slice. We also noticed that the apparent affinity in slice is right-shifted from that in dissociated neuronal culture. This is not unexpected, given the added confounds of tissue penetration for bath applied 5-HT and dilution of micropipetted 5-HT in the slice environment, which do not exist in monolayered cultured cells. Reassuringly, the successful *in vivo* detection of endogenously released 5-HT suggests that this reflects an artifact of the slice preparation in this context and not a true weakening of affinity following long-term expression. Future experiments will focus on direct comparison with FSCV and microdialysis to further characterize the properties—and deficiencies—of the sensor.

Our *in vivo* studies very clearly show functionality of the sensor across multiple brain regions and multiple behaviors, across both short and long time windows. iSeroSnFR signals are consistent with 5-HT microdialysis studies in fear conditioning in both BLA and mPFC (Ferrés-Coy et al., 2013; Forster et al., 2006; Fujino et al., 2002; Hashimoto et al., 1999; Kawahara et al., 1993; Rueter and Jacobs, 1996; Yokoyama et al., 2005), but offer much improved temporal resolution, indicating that iSeroSnFR is a viable alternative to these techniques. iSeroSnFR revealed obvious 5-HT increases in mPFC and BLA during cued fear conditioning, consistent with previous studies (Bauer, 2015). OFC responds robustly to social interaction (Figure S6I), and it is clear that serotonergic input

to frontal cortex and other brain regions is complex and heterogeneous. The high sensitivity and millisecond-level temporal resolution of iSeroSnFR will be instrumental in working out such details. Furthermore, the causes and consequences of endogenous 5-HT release, and how closely optogenetically triggered release mimics it, remain uncertain (Correia et al., 2017; Garcia-Garcia et al., 2018; Marcinkiewcz et al., 2016; Ohmura et al., 2014; Seo et al., 2019). *In vivo* recording in target brain regions using iSeroSnFR will provide new opportunities to study 5-HT modulation by electrical, opto/chemogenetic, or behavioral manipulations, 5-HT interaction with other neurotransmitters such as glutamate or dopamine, and 5-HT function in the context of various behavioral states.

For initial *in vivo* demonstration of iSeroSnFR, we opted for fiber photometry, a simple and widely used technique. We replicated published FSCV results as a proof-of-principle, in multiple behavioral paradigms, across multiple brain regions. This technique, however, does not demonstrate the full potential of optical sensors, because essentially all spatial resolution is lost. *In vivo* two-photon imaging is the gold standard for high-resolution tracking of neural signaling in intact animals. iSeroSnFR is completely compatible with two-photon imaging, as we have demonstrated in brain slice (Figures S5B-S5F). Its spectral and biophysical properties are similar to that of iGluSnFR and GCaMP, routinely used in *in vivo* two-photon imaging. We thus anticipate no sensor-specific challenges for *in vivo* two-photon iSeroSnFR imaging in diverse preparations.

Finally, while we have demonstrated the uses of iSeroSnFR for several neuroscience applications, the vast majority of 5-HT is produced in the gut, and indeed 5-HT receptors exist throughout the body. Studies of 5-HT in peripheral systems would be exciting and informative, and we expect that iSeroSnFR could be adapted for these purposes.

Screening 5-HT transporter modulators

The soluble nature of iSeroSnFR provides an additional advantage over the use of integral-membrane GPCR-based scaffolds. The excellent dynamic range of the sensor, combined with its robust cytoplasmic expression, allowed us to easily monitor time-resolved kinetics of 5-HT influx and efflux, and how transport is distinctly modulated by various drugs, including two drugs of abuse and three antidepressants. GPCR-based sensors would be incompatible with this application, because they cannot be expressed cytoplasmically, and GPCRs respond directly to many of the very drugs such an assay is designed to characterize. iSeroSnFR, on the other hand, is far more specific, allowing

these critical pharmacological experiments. Given the clinical significance of hSERT and its mutants in psychological disorders (Jarrett et al., 2007; Margoob and Mushtaq, 2011; Ozaki et al., 2003; Wankerl et al., 2014), this assay will greatly facilitate serotonergic drug discovery by identifying and quantifying the underlying properties of drug-hSERT interactions, paving the way for screening patient-specific drugs and doses for SSRIs or other drugs.

3.5 Acknowledgements

We would like to thank Drs. Liqun Luo (Stanford University) and Jing Ren (MRC) for their critical reading and feedback. This work is based upon research conducted at the Northeastern Collaborative Access Team beamlines, which are funded by the National Institute of General Medical Sciences from the NIH (P30-GM124165). The Pilatus 6M detector on the 24-ID-C beamline is funded by an NIH-ORIP HEI grant (S10-RR029205). This research used resources of the Advanced Photon Source, as US Department of Energy (DOE) Office of Science User Facility operated for the DOE Office of Science by Argonne National Laboratory under contract DE-AC02-06CH11357. This work was supported by funding to L.T. (BRAIN Inititiave U01NS090604, U01NS013522, and DP2MH107056 from NIH), to E.K.U. (Mistletoe Foundation Research Fellowship), and to G.O.M. (ARCS Scholarship), as well as by the Howard Hughes Medical Institute. V.G. is a Heritage Principal Investigator supported by the Heritage Medical Research Institute, the NIH (BRAIN RF1MH117069), the Center for Molecular and Cellular Neuroscience of the Chen Institute, and the Beckman Institute for CLARITY, Optogenetics and Vector Engineering Research. V.A.A. is funded by Intramural Programs of NIAAA and NINDS ZIA-AA000421 and Innovation Award from NIH-DDIR. T.L.K. is funded by the NIH (R01AA019454, P60AA011605, and U24AA025475), and O.J.H. is funded by the NIH (5T32NS007431-20).

3.6 Author contributions

E.K.U., J.P.K., M.A., L.L.L., and L.T. conceived of and designed the study. E.K.U. designed the machine-learning method, screened and optimized sensors, and characterized them in purified protein, mammalian cells, cultured neurons, and brain slice, with significant contribution from C.D., D.A.J., and J.S. J.P.K., S.S., and G.R. designed OSTA and stopped-flow experiments, and J.P.K. performed them. M.A. and V.G. designed and performed *in vivo* fiber photometry and EEG/EMG recording in BLA and mPFC in fear learning and sleep/wake cycles. O.J.H., M.E.F., and T.L.K.

designed and performed *in vivo* fiber photometry experiments in BLA, OFC and BNST during social interaction. R.L. and V.Y.-Y. designed and performed computational Rosetta modeling. Z.Y. and J.A.P. provided luciferase experimental data for establishing machine-learning methods. J.C. and D.T.L. provided significant insight for the machine-learning methods. J.S. characterized the sensor in acute slice using two-photon imaging. A.M. and V.A.A. designed and performed photometry imaging in acute slice. S.H. and A.J.F. performed crystallography. J.S.M., P.M.B., A.V.S., H.A.L., and L.L.L. provided iAChSnFR0.6 and performed preliminary experiments on serotonin binding. S.B. and L.D.L. synthesized caged serotonin. G.O.M. provided dissociated neuronal cultures. L.P.C. and D.E.O. produced chemical reagents. S.M.U. and S.G.A. provided SSRIs and guidance in cell-assay design. E.K.U., J.P.K., L.L.L. and L.T. wrote the manuscript with significant input from other authors.

3.7 Declaration of interests:

L.T. and G.O.M. are co-founders of Seven Biosciences. D.E.O. is a founder of Delics.

3.8 Main figures

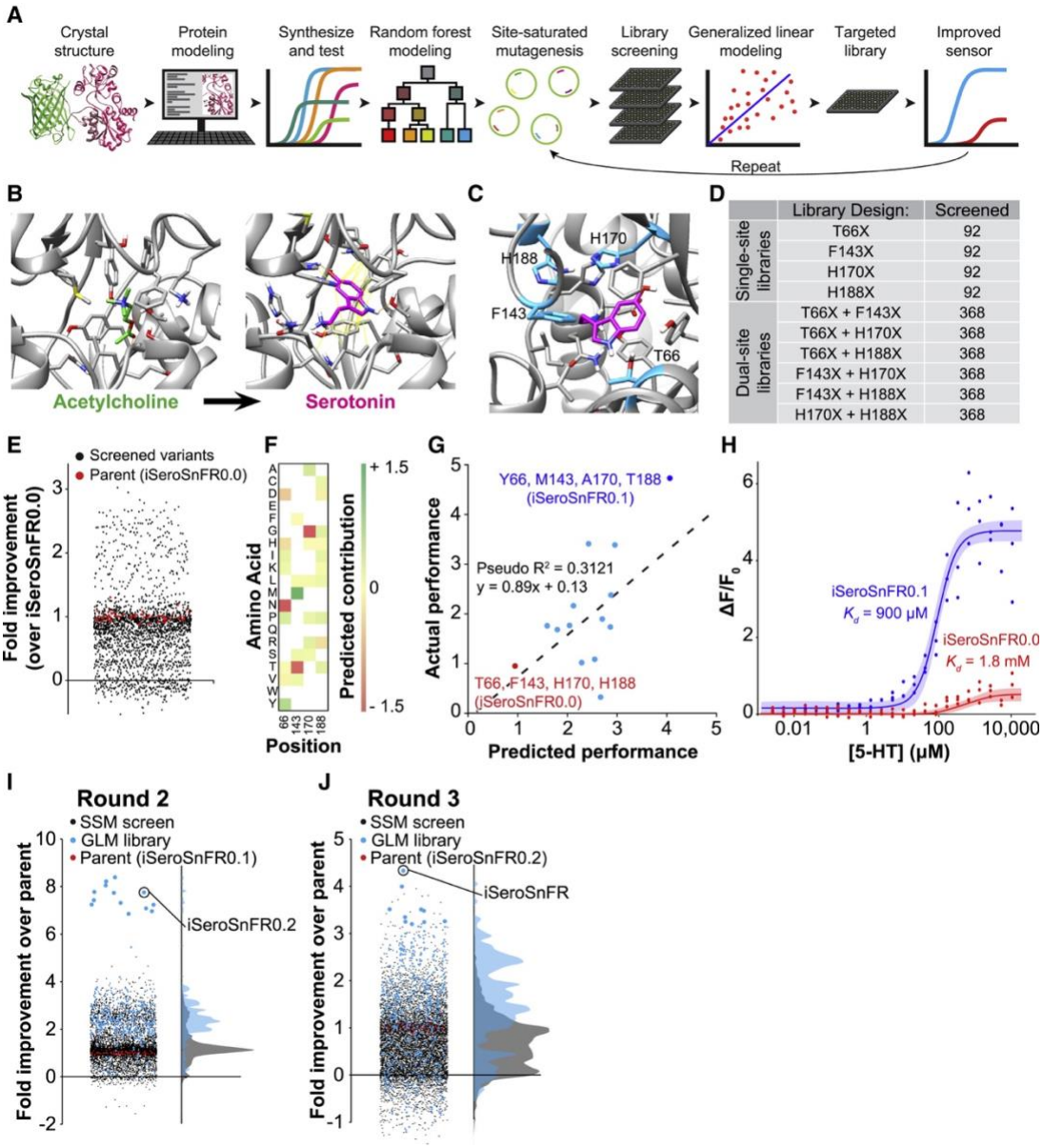

Figure 1. Using machine learning to evolve binding proteins

(A) Overview of machine learning method.

(B) Schematic showing conversion of an acetylcholine (ACh)-binding protein to a serotonin (5-HT)-binding protein. ACh and 5-HT were docked into the binding pocket of AChSnFR0.6 using Rosetta. Statistical modeling was performed on these models, and promising mutations were synthesized and tested (see Figure S2 and Table S3). iSeroSnFR0.0 was chosen as a starting point for statistical modeling. Positions 66, 143, 170 and 188 were selected for further mutation.

(C) The binding pocket of iSeroSnFR0.0 was simulated using Rosetta and 5-HT (magenta) docked. Top-ranked positions are labeled (cyan).

(D) Table of DNA libraries created, and number of variants screened from each library.

(E) DNA libraries were generated, transformed into bacteria, grown, and lysed. Lysate was then screened with 10 mM 5-HT and compared to the parent sensor (iSeroSnFR0.0).

(F) Heat map of the contribution of each mutation at each position screened, as predicted by the generalized linear model (GLM) (for additional information see Table S3).

(G) Combinations of mutations predicted to be better than the parent (iSeroSnFR0.0) were synthesized and tested as purified protein with 10 mM 5-HT. Dashed line represents linear regression.

(H) Protein from iSeroSnFR0.0 and the top variant (iSeroSnFR0.1) was purified and tested against multiple concentrations of 5-HT. Fits were determined using the Hill equation. Shaded area denotes 95% confidence interval. The apparent K_d is defined as the concentration of the ligand producing 50% of the maximum fluorescence change.

(I) Raincloud plot where iSeroSnFR0.1 was used as the parent for a second round of screening followed by GLM analysis. A small library (32 possible combinations) was generated based on the GLM results and screened (cyan), which led to the discovery of iSeroSnFR0.2.

(J) Raincloud plot similar to (I), but using iSeroSnFR0.2 as the parent. This GLM-guided targeted library (96 possible combinations) was created and screened, leading to the discovery of iSeroSnFR. See also Figures S1 and S2 and Data S1.

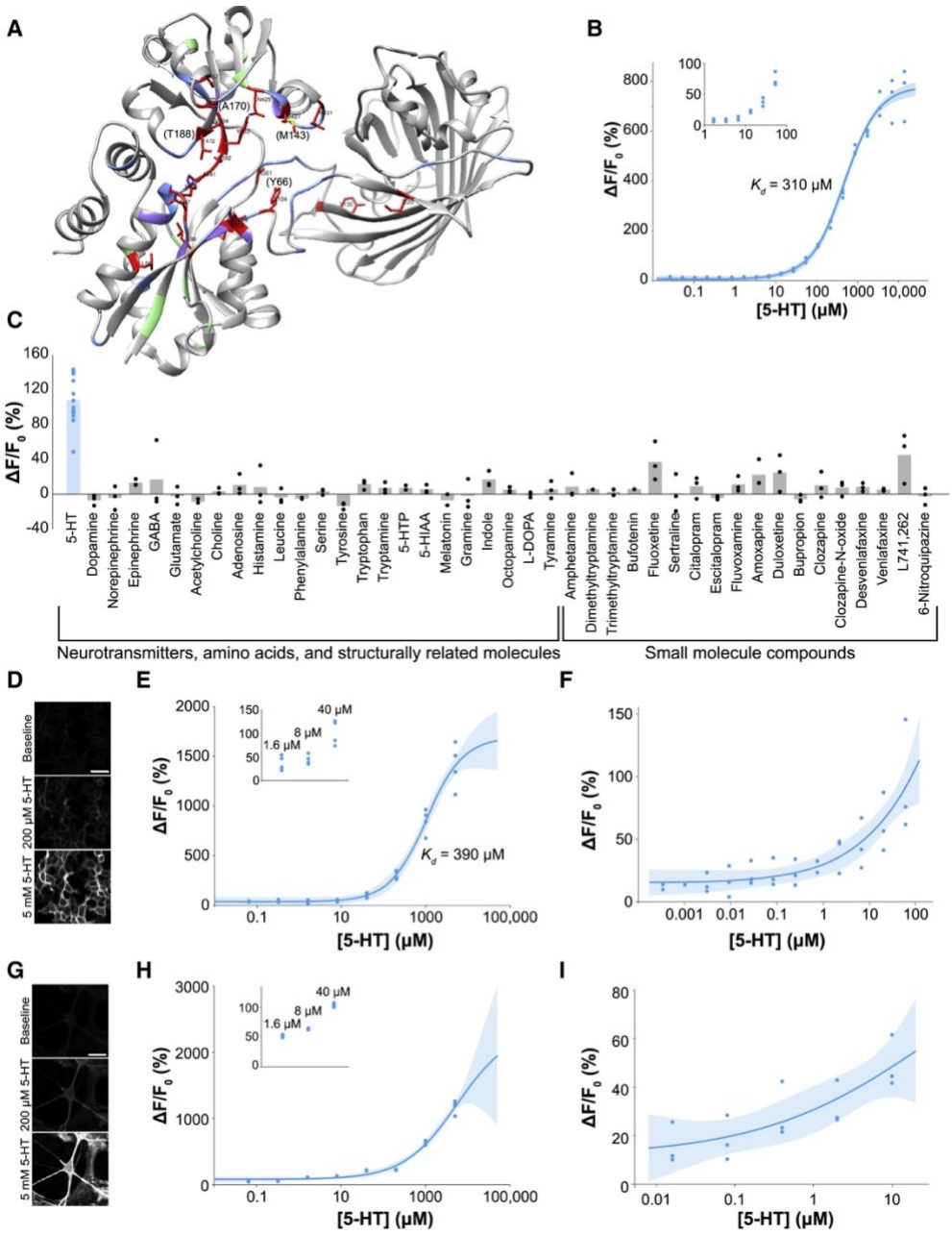

Figure 2. Affinity and specificity of the sensor

(A) Crystal structure of unliganded iSeroSnFR (PDB: 6PER). Mutations in iSeroSnFR relative to iAChSnFR0.6 are mapped onto the crystal structure (red). Positions interrogated by site-saturated mutagenesis (but not mutated in iSeroSnFR) are displayed in blue, mutations interrogated by Rosetta, but not SSM, in purple, and positions that were randomly mutated, in green.

(B) Purified iSeroSnFR binding to 5-HT.

(C) Purified iSeroSnFR binding to multiple ligands. Due to differential compound solubility, the values displayed match the following concentrations: octopamine, L-phenylalanine, 80 μM; 5-HTP,

85 µM; sertraline, 110 µM; L-DOPA, tyramine, escitalopram, citalopram, amoxapine, 125 µM; all other compounds were tested at either 100 or 105 µM. For the full concentration curve for each compound, see Figure S3.

(D-F) Response of membrane-displayed iSeroSnFR in HEK293T cells. Representative images (D), and dose-response curves for higher concentrations (E) and lower concentrations (F). n = 3-4.

(G-I) Response of membrane-displayed iSeroSnFR-PDGFR in cultured neurons. (G-I) Representative images (G), and dose-response curve for higher concentrations (H) and lower concentrations (I). n = 3-4. For raw traces, see Figure S4.

(B, E, F, H, and I) Fits were determined using the Hill equation. Shaded area denotes 95% confidence interval. Scale bars represent 50 µm. Insets show magnifications of the points at low concentrations. See also Figures S3 and S4.

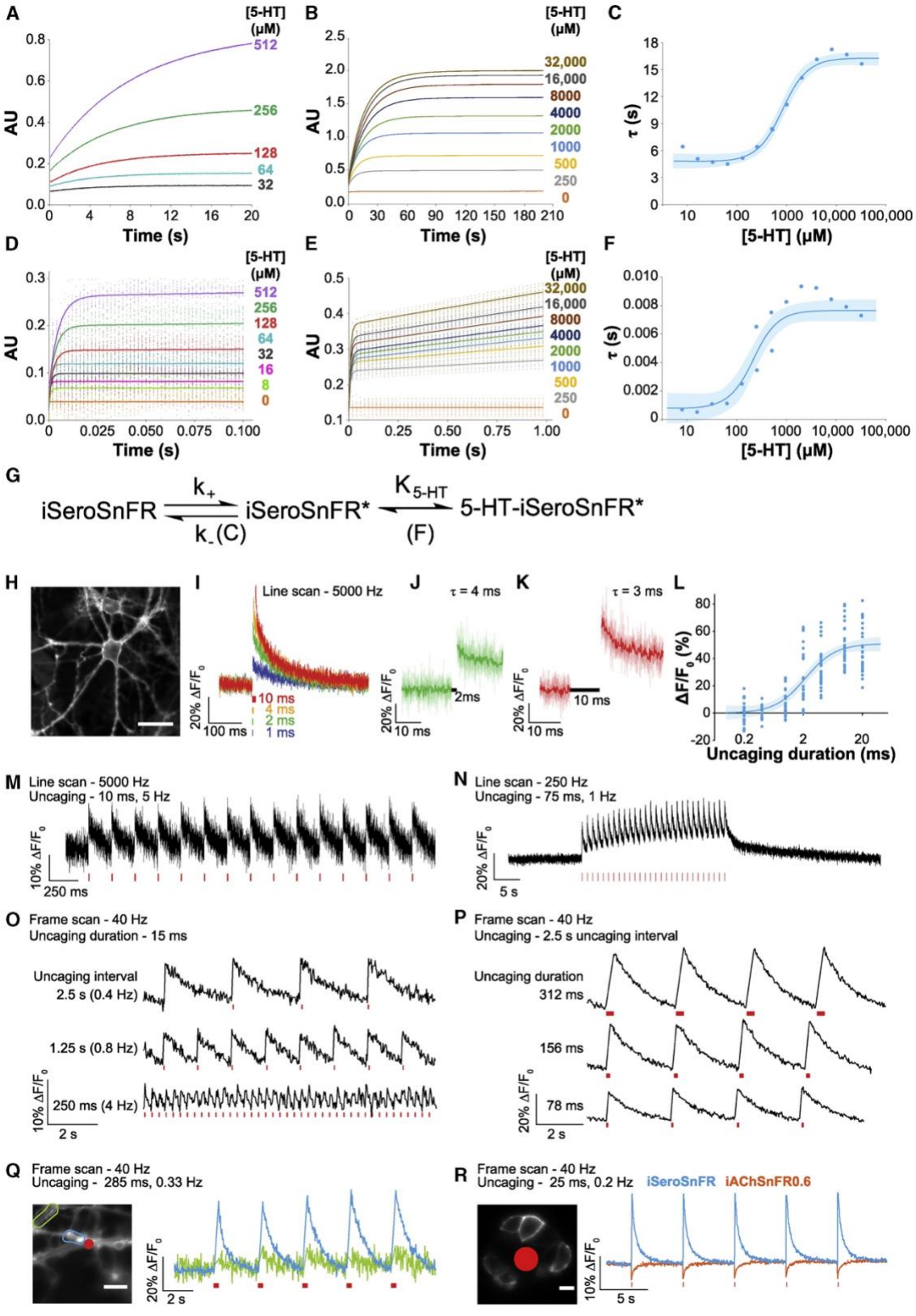

Figure 3. Sensor kinetics

(A-F) iSeroSnFR was purified and tested in a stopped-flow apparatus, with increasing concentrations of 5-HT.

(A and B) Average traces showing full time courses for low (A) and high (B) concentrations.

(D and E) Magnification of the first 100 ms and 1 s, respectively, of the data in (A) and (B), respectively, with double exponential fits shown.

(C and F) The τ (1/rate constant) for each concentration for the slow phase (C) and the fast phase (F) was fit using the Hill equation. Shaded area denotes 95% confidence interval.

(G) Model of iSeroSnFR function showing two rate-limiting steps: Isomerization between the inactive and active states, followed by binding of serotonin, for full fluorescence activation. n = 16-18 trials for each concentration.

(H-R) Primary cultured neurons (H-Q) and HEK cells (R) were exposed to 200 µM caged-5-HT (PA-N-5-HT) and uncaged using 405 nm laser stimulation.

(H) Representative image.

(I) 5-HT was uncaged as noted. Traces represent a 9-trial average for each replicate. Biological replicates = 3. There was no image acquisition during 405 nm laser stimulation.

(J and K) Data expanded from (I). Faded lines depict raw traces, dark lines represent average traces.

(L) Data from (I) was plotted and fit with using the Hill equation. Shaded area denotes 95% confidence interval.

(M-R) 5-HT was uncaged as noted. Red lines represent uncaging epochs.

(M and N) Line scans (128 x 1 pixel) at 5 kHz (M) and 250 Hz (N).

(O-R) Frame scans (128 x 128 pixel) at 40 Hz. For raw traces, see Figure S5.

(Q) Red dot represents uncaging spot. Blue and green traces represent data from regions of interest outlined on the image (~2 µm and ~20 µm from the uncaged region). (R) Response of membrane-displayed iSeroSnFR and iAChSnFR0.6 to serotonin uncaging on HEK293T cells. Scale bars represent 50 µm (H) and 10 µm (Q and R).

See also Figure S5.

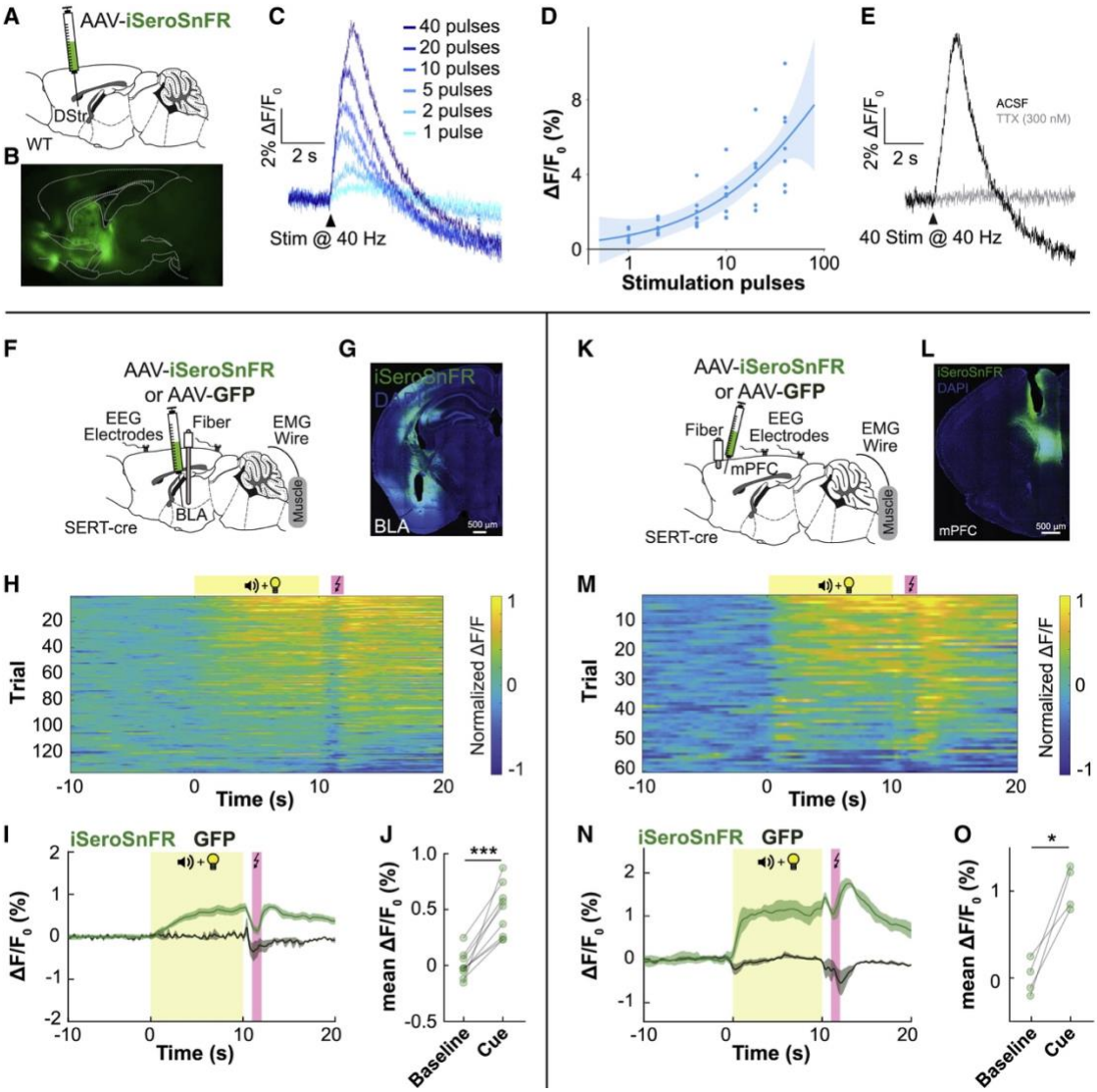

Figure 4. Detection of electrically or behaviorally triggered release of 5-HT

(A-D) WT mice were injected with AAV2/9.*CAG*.iSeroSnFR.Nlgn into the dorsal striatum (DStr). Slices were prepared (300 µm) and imaged using one-photon photometry.

(A and B) Schematic (A) and representative (B) image of sensor injection and expression.

(C) Slices were stimulated using a monopolar saline-filled glass electrode (0.5 ms; 50 µA) at the frequencies noted.

(D) Data from (C) fitted using the Hill equation. Shaded area represents 95% confidence interval.

(E) Tetrodotoxin (TTX; 300 nM) was added to the perfusion solution, and the slice was stimulated at 40 Hz for 1 s (n = 11 slices from 3 mice). For more information, see Figure S5.

(F-O) Fiber-photometry recording of 5-HT release in response to fear-conditioning in BLA (F-J) and mPFC (K-O). Mice were injected with either AAV2/9.*CAG*-iSeroSnFR.Nlgn or AAV2/5.*CAG*-GFP

(as a negative control) followed by optical fiber implantation into BLA (F and G) or mPFC (K and L). Yellow box indicates unconditioned stimulus (tone + house lights); pink box illustrates foot shock. Single-trial traces (H and M) or average trace across all trials (I and N). Shaded area represents SEM. Statistical comparison was made based on the average fluorescence for the 10 s before the cue onset (baseline) and the 10 s of cue presentation (J and O). n = 15 trials/animal, n = 9 $BLA^{iSeroSnFR}$, 3 BLA^{GFP}, 4 $mPFC^{iSeroSnFR}$, 3 $mPFC^{GFP}$). *$p < 0.05$, ***$p < 0.001$, paired Student's t test.
See also Figure S5 and S6.

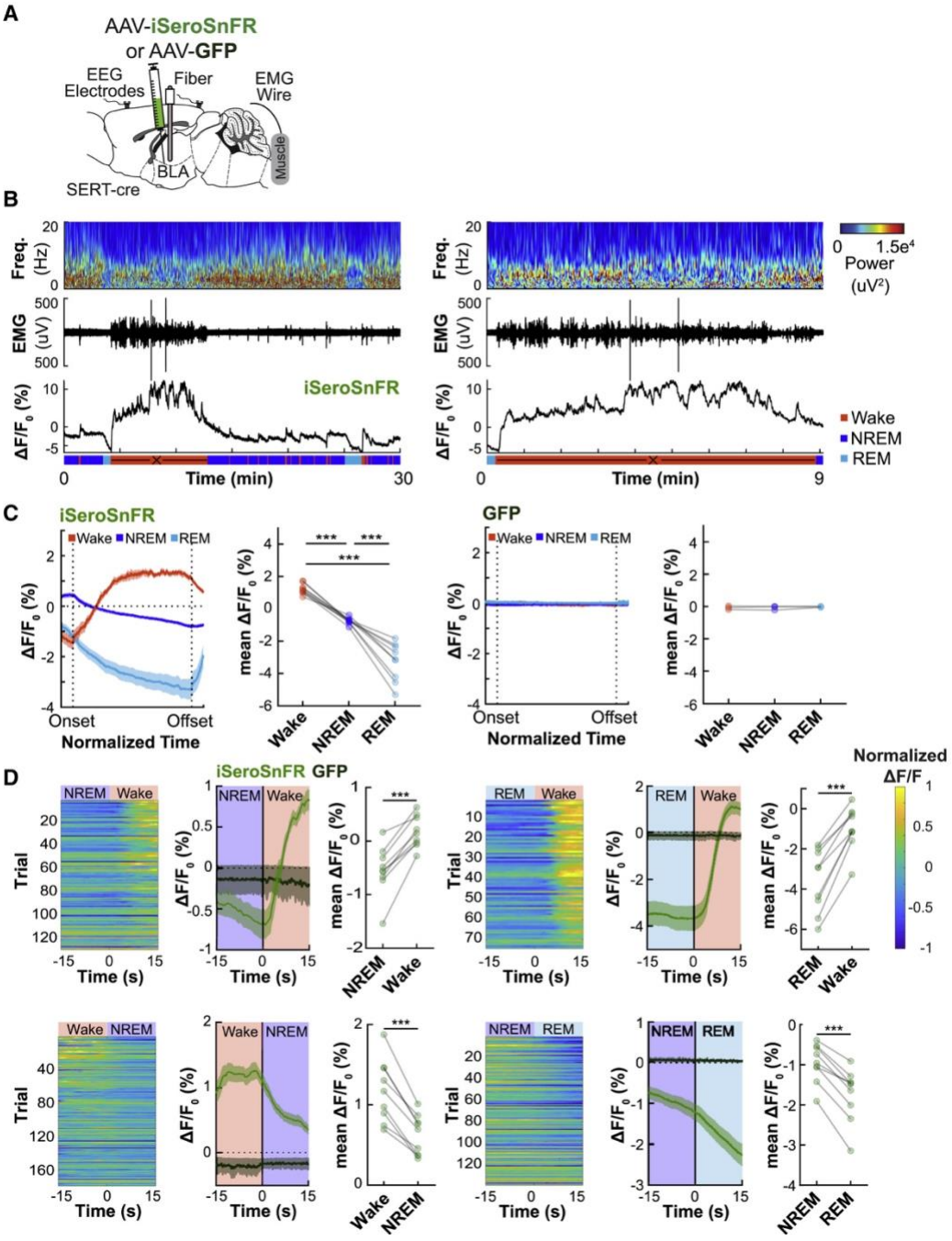

Figure 5. Detection of 5-HT release during sleep-wakefulness cycles in BLA

(A) Mice were injected with either AAV2/9.*CAG*-iSeroSnFR.Nlgn or AAV2/5.*CAG*-GFP (as a negative control), and an optical fiber was implanted into basolateral amygdala (BLA). EEG screw electrodes and EMG wires were implanted to classify sleep-wake states.

(B) Representative BLA^{iSeroSnFR} EEG spectrograms, EMG, and fiber photometry traces over time across sleep-wake cycles (left) and walking episode (right).

(C) Temporal dynamics of iSeroSnFR (left) and GFP (right) activity during waking, NREM, and REM episodes (data from panel B, left) across time, normalized from onset to offset. Statistical comparisons of fluorescence levels were performed on the last 10% of data within each behavioral state (one-way ANOVA with Bonferroni correction).

(D) Single-trial or averaged fluorescence change across all trials of iSeroSnFR from NREM to wake, REM to wake, wake to NREM and NREM to REM transitions. Statistical comparisons of changes in fluorescence using and $BLA^{iSeroSnFR}$ were made based on the average fluorescence over 15 s before and 15 s after the behavioral state transition. n = 15 trials/animal, n = 3 BLA^{GFP}, and n = 9 $BLA^{iSeroSnFR}$. Data represent mean ± SEM. ***$p < 0.001$, paired Student's *t*-test.

See also Figure S7.

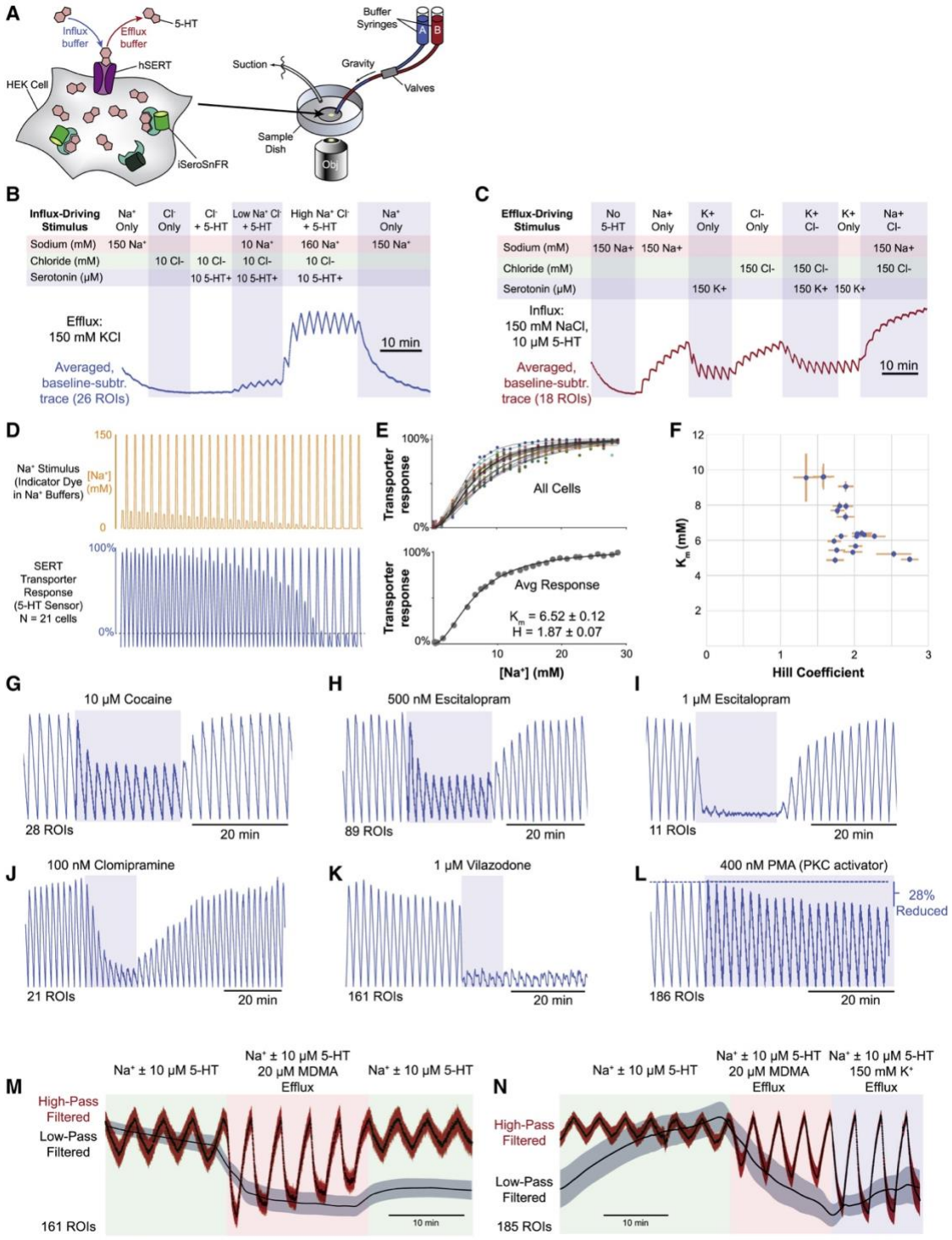

Figure 6. Application to monitoring hSERT transport

(A) Schematic of the oscillating stimulus transporter assay (OSTA).

(B) Confirmation of ionic requirements of hSERT for 5-HT uptake: Influx only occurs in the presence of 5-HT, Na^+, and Cl^-.

(C) Ions driving hSERT-mediated 5-HT efflux: Rates of efflux increase with K^+ and are insensitive to Cl^-.

(D-F) Sodium dependence of 5-HT transport through hSERT.

(D) Cells were subjected to a decreasing linear gradient of Na^+ in the influx buffer, with standardized "fiducial" bouts at saturating sodium concentration interleaved. Red fluorescence (sulforhodamine 101 at 200 nM in fiducials) was used as a readout for the sodium stimulus (top panel), and green fluorescence (iSeroSnFR) reflected changes in cytosolic [5-HT] due to hSERT function (bottom panel).

(E) Fits of single-cell (top) and grouped (bottom) 5-HT transport responses to the stimulus shown in (D).

(F) Scatterplot of fitted parameters for individual cells: Hill coefficient versus K_m.

(G-L) hSERT-mediated 5-HT transport responses to various pharmacological agents (as indicated) under a standardized stimulus.

(M and N) MDMA-mediated 5-HT efflux: MDMA at 20 μM in the efflux buffer significantly increased the rate of 5-HT efflux compared to Na^+ alone. (N) In the last epoch of the experiment, K^+ was substituted for Na^+ in the efflux buffer for comparison to other experiments.

3.9 Supplementary figures

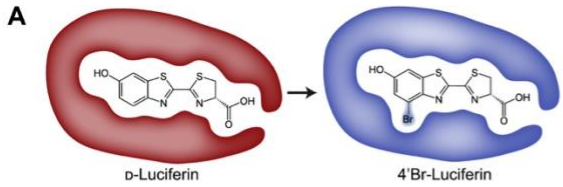

B

Position	RF rank	Native	Mutation	GLM
218	97	R	A	0.6817
247	63	F	Y	0.5138
255	39	Y	N	0.8542
316	69	G	S	0.5065
342	0	L	A	1.8681
347	86	S	G	1.8726

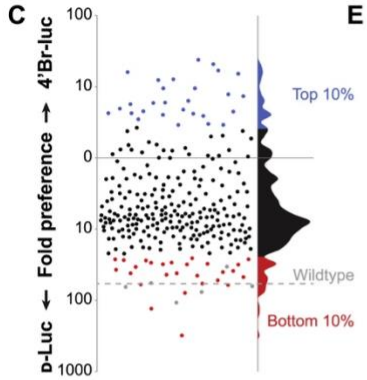

D

# Mutations	0	1	2	3	4	5	6
Top 10%	0	1	7	15	4	0	0
Bottom 10%	7	1	7	8	8	0	0

p = 0.2853

E

Position	Residue	Top 10% Freq.	Top 10% %	Bottom 10% Freq.	Bottom 10% %	Bottom 10% p*	Input data Freq.	Input data %	Input data p* (top)	Input data p* (bot.)
218	R	22	81.5	8	25.8	6.6E-4	181	81.5	1	1.8E-6
	A	5	18.5	16	51.6		2	0.9		
	other	NA		NA			39	17.6		
247	F	9	33.3	12	38.7	0.2651	195	87.8	2.4E-9	3.4E-5
	Y	18	66.7	12	38.7		11	5.0		
	other	NA		NA			16	7.2		
255	Y	21	77.8	18	58.1	1	175	78.8	1	0.6106
	N	6	22.2	6	19.4		2	0.9		
	other	NA		NA			45	20.3		
316	G	15	55.6	12	38.7	0.7819	127	57.2	1	0.5223
	S	12	44.4	12	38.7		28	12.6		
	other	NA		NA			67	30.2		
342	L	18	66.7	3	9.7	1.5E-4	210	94.6	6.7E-5	<2E-16
	A	9	33.3	21	67.7		1	0.5		
	other	NA		NA			11	5.0		
347	S	1	3.7	19	61.3	2.6E-8	199	89.6	<2E-16	0.1661
	G	26	96.3	5	16.1		4	1.8		
	other	NA		NA			19	8.6		

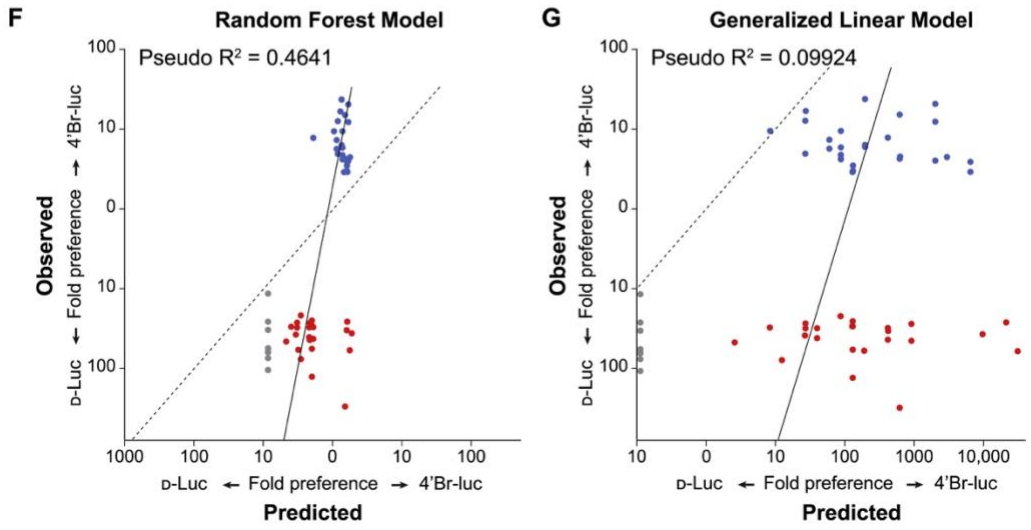

Figure S1. Development of a machine-learning-guided library design paradigm, related to Figure 1

(A) Schematic showing the evolution of substrate preference from D-luc to 4'Br-luc.

(B) Random forest (RF) modeling and generalized linear modeling (GLM) were performed on 222 variants (see Table S2).

(C) The combination library in (B) was generated and 276 variants were screened for their preference for D-luc or 4'Br-luc. The top and bottom 10% of variants were sequenced.

(D) Table showing no difference between the mutation rate of the top and bottom 10% of variants (Fisher's exact test). Variants with no mutations were omitted from statistical analysis.

(E) Table showing the frequency of different mutations predicted by statistical modeling. *p values were calculated by Fisher's exact test, comparing the mutated amino acid(s) to the native amino acid, and the top 10% to either the bottom 10% or the input data as noted.

(F and G) Comparison between the RF (F) and GLM (G) prediction and the actual data.

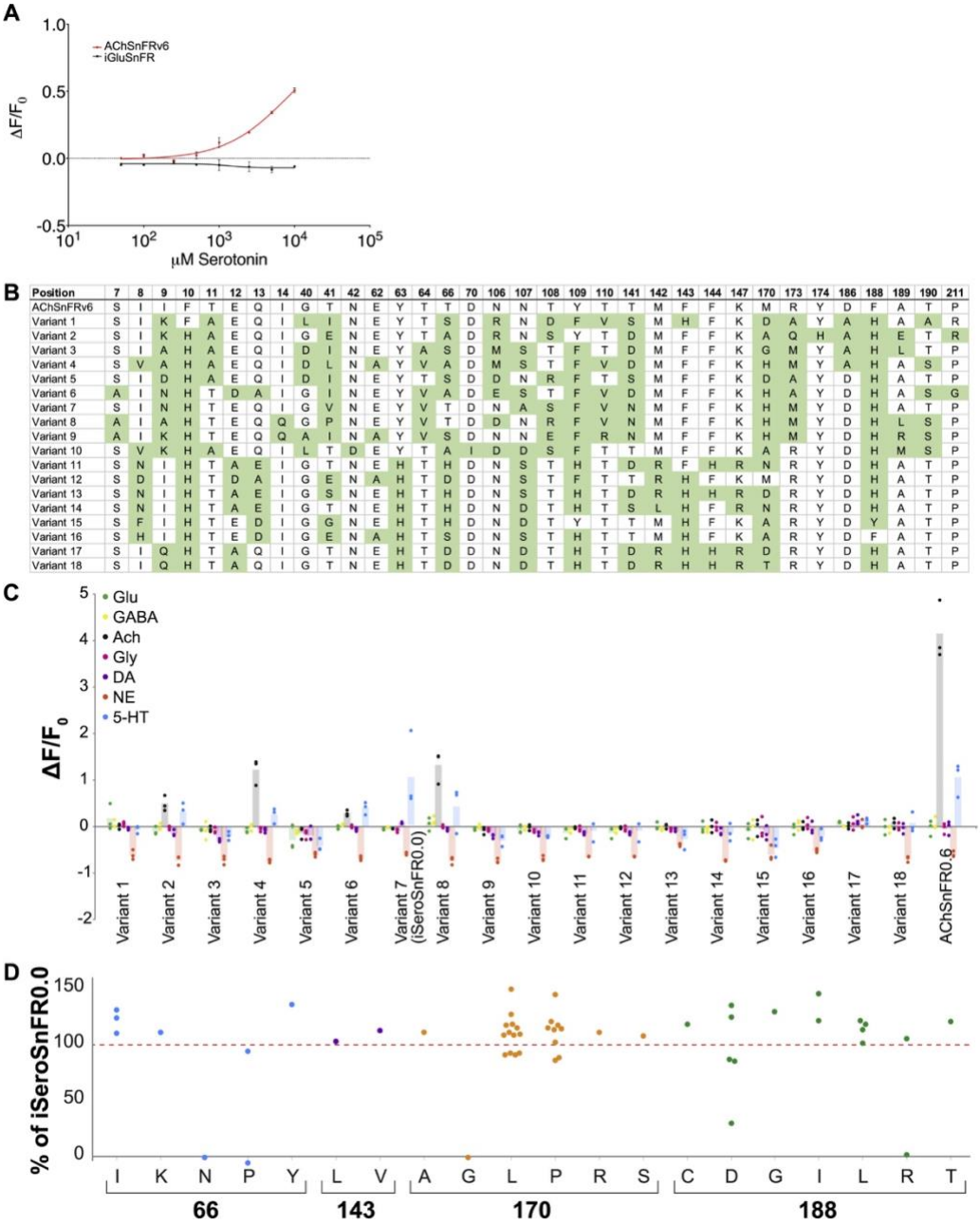

Figure S2. iSeroSnFR design, related to Figure 1

(A) Purified protein of iAChSnFR0.6 and iGluSnFR were tested against multiple concentrations of 5-HT. n = 3. Data represent mean ± SEM.

(B) Table showing the top 18 variants predicted by Rosetta modeling. Mutations are highlighted in green, compared to iAChSnFR0.6.

(C) The top 18 variants were synthesized and tested as purified protein against multiple ligands. Protein concentration: 100 nM, ligand concentration: 10 mM. Shaded bars represent the mean.

(D) Single mutants from the first SSM screen were tested with 10 mM 5-HT and compared to iSeroSnFR0.0. Red dashed line indicates iSeroSnFR0.0 (set to 100%).

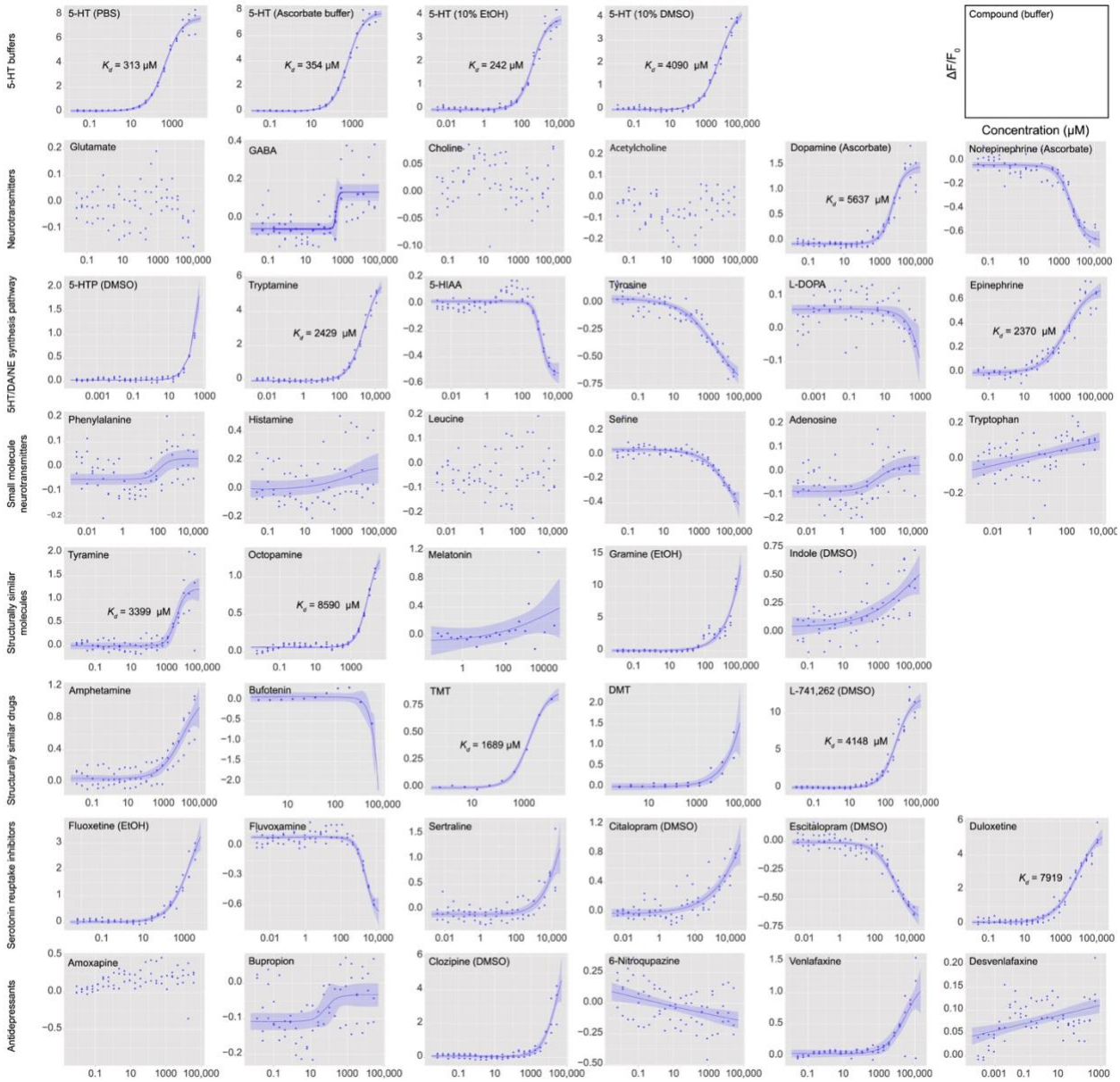

Figure S3. Specificity of iSeroSnFR, related to Figure 2

iSeroSnFR was purified and tested at 100 nM against multiple ligands as noted. Some ligands were tested in alternative buffers as noted. If no buffer is listed, the ligand was dissolved in PBS. Lines were fitted and K_d's were determined using the drc package in R. Shaded areas represent the 95% confidence interval. If no line is present, convergence failed, and no fit was calculated.

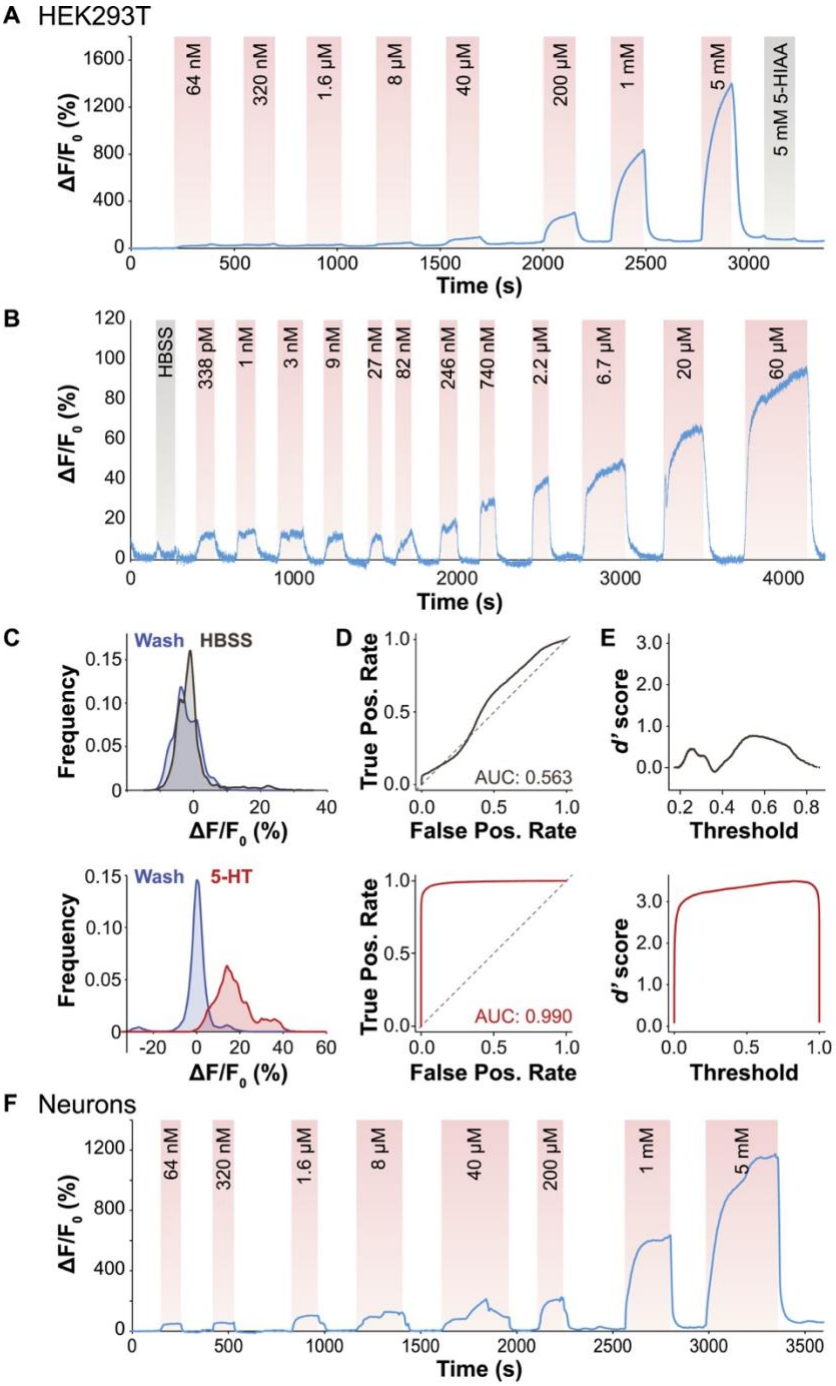

Figure S4. *In situ* titration, related to Figure 2

Representative traces from HEK293T cells (A,B) and primary cultured E18 rat hippocampal neurons (F) for which the images and dose response curves are displayed in Figures 2D-2F (HEK cells) and Figures 2G and 2H (neurons).

(C-E) HBSS (top) and concentrations of 5-HT between 338 pM and 246 nM (bottom) were further analyzed for sensor sensitivity.

(C) Distribution of responses is shown.

(D) ROC analysis was performed where responses during the “wash” period were defined as a false positive, and responses during the “HBSS” or “5-HT” period were defined as a true positive.

(E) A *d’* score was calculated based on the ROC analysis.

(A) and (F) were imaged at 1 Hz, (B) was imaged at 5 Hz. n = 3-4 dishes.

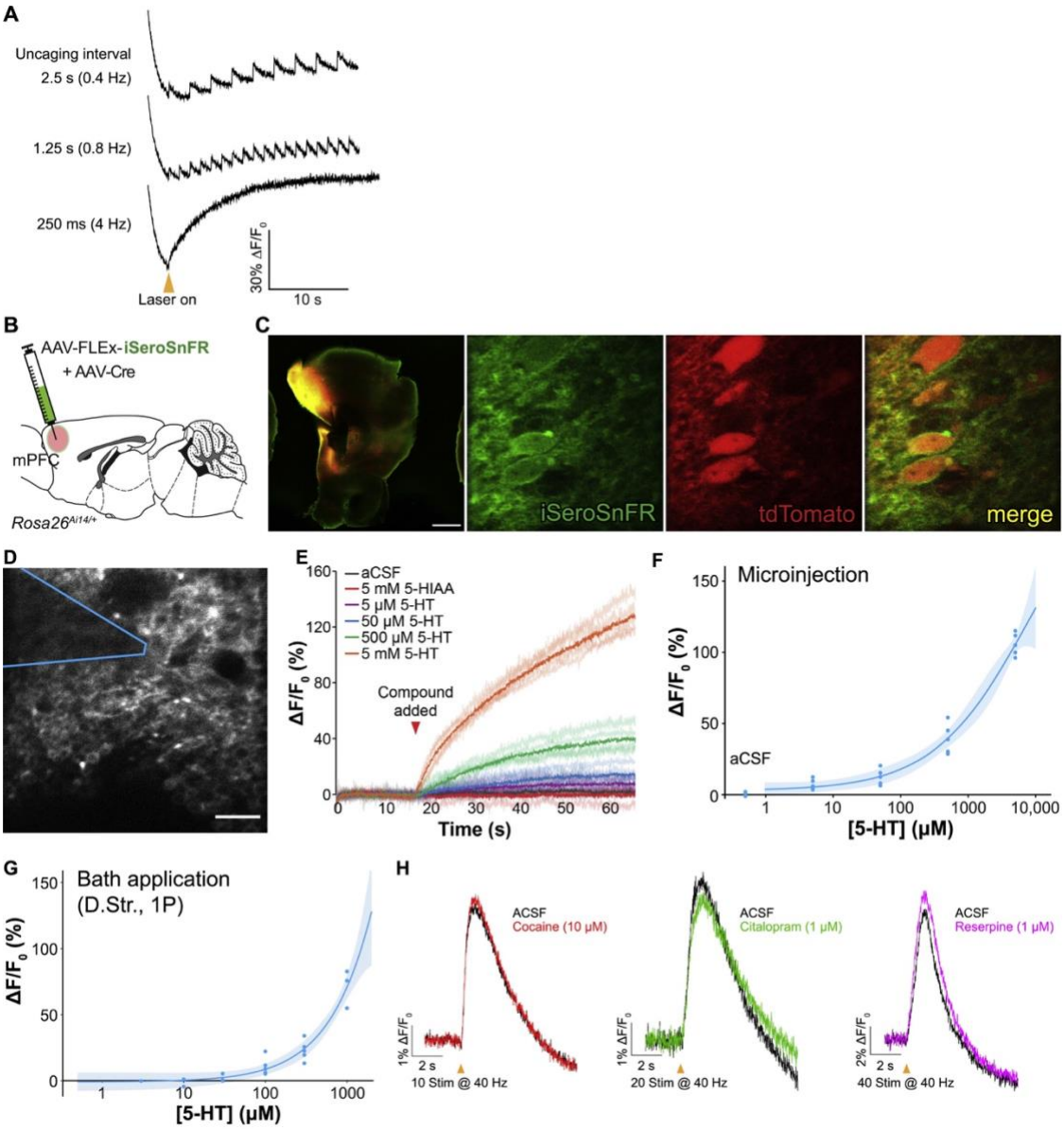

Figure S5. Kinetics and two-photon characterization of iSeroSnFR expression in mPFC, related to Figures 3 and 4

(A) Representative raw traces from Figure 3O, showing significant bleaching followed by gradual accumulation of 5-HT. Biological replicates = 3.

(B-F) AAV2/9.*CAG*.FLEx.iSeroSnFR.PDGFR combined with AAV2/1.*CMV*.Cre was injected into the medial prefrontal cortex (mPFC) of *Rosa*$^{Ai14/+}$ mice. Acute slices were prepared (300 µm) and imaged using a 2-photon microscope (920 nm).

(C and D) Representative images. Scale bars represent 500 µm (low mag.) and 10 µm (high mag.).

(E) Different concentrations of 5-HT (in aCSF) were microinjected using a pulled glass pipette positioned at the surface of the slice (outlined in blue in (D)). 5-HT was expelled manually. (n = 5 slices from 3 mice). Saturated lines indicate mean, pale lines indicate raw traces.

(F) Average values from the period between 30 and 60 s in (E) were plotted and fitted using the Hill equation. Shaded area represents 95% confidence interval.

(G) Mouse brain slices from Figures 4A-4D were perfused with different concentrations of 5-HT.

(H) Mouse brain slices from Figures 4A-4D were perfused with either ACSF or the drug noted and stimulated with a monopolar saline-filled glass electrode (0.5 ms, 50 μA).

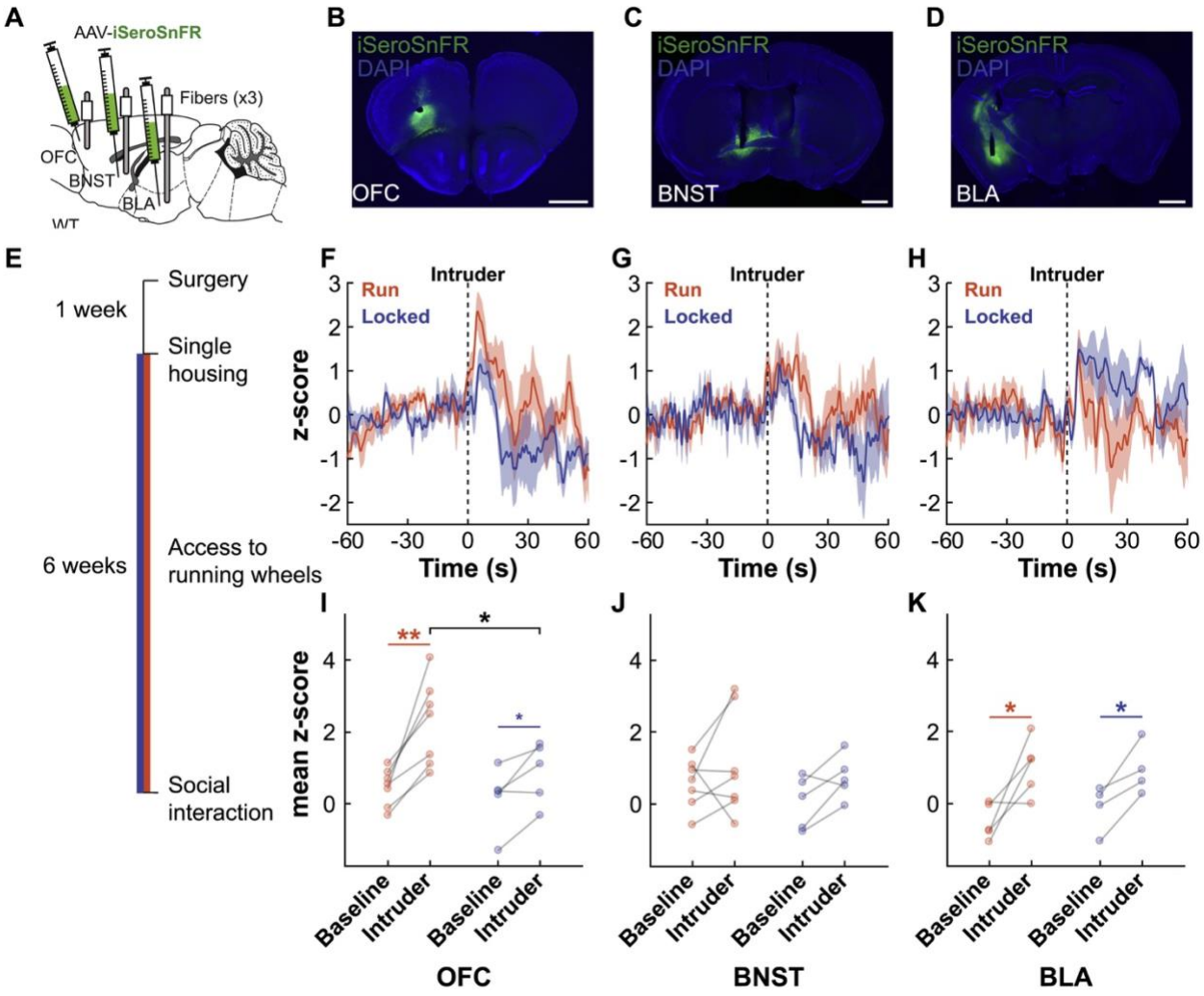

Figure S6. Imaging 5-HT dynamics in social interaction, related to Figure 4

(A) WT C57BL/6J mice were injected with AAV.*CAG*.iSeroSnFR.Nlgn into orbitofrontal cortex (OFC), bed nucleus of the stria terminalis (BNST) and basolateral amygdala (BLA). For multi-site fiber photometry recordings, optical fibers were inserted targeting all three brain regions.

(B-D) Representative images of iSeroSnFR expression and fiber location.

(E) Graphical representation of the timeline of surgery and behavioral experiments. After 1 week of recovery animals were provided access to running wheels, but only half were functional (run) and the other half were fixed (locked).

(F-H) Average fluorescence changes before and after introduction of an intruder.

(I-K) Mean z-scores from each animal from the -2-0 s prior to intruder presentation (baseline) and 4-6 s after intruder presentation (intruder). Single trials per animal; n = 4-7 mice. Data represent mean ± SEM. *$p < 0.05$, **$p < 0.01$, 2-way ANOVA. Scale bars represent 1 mm.

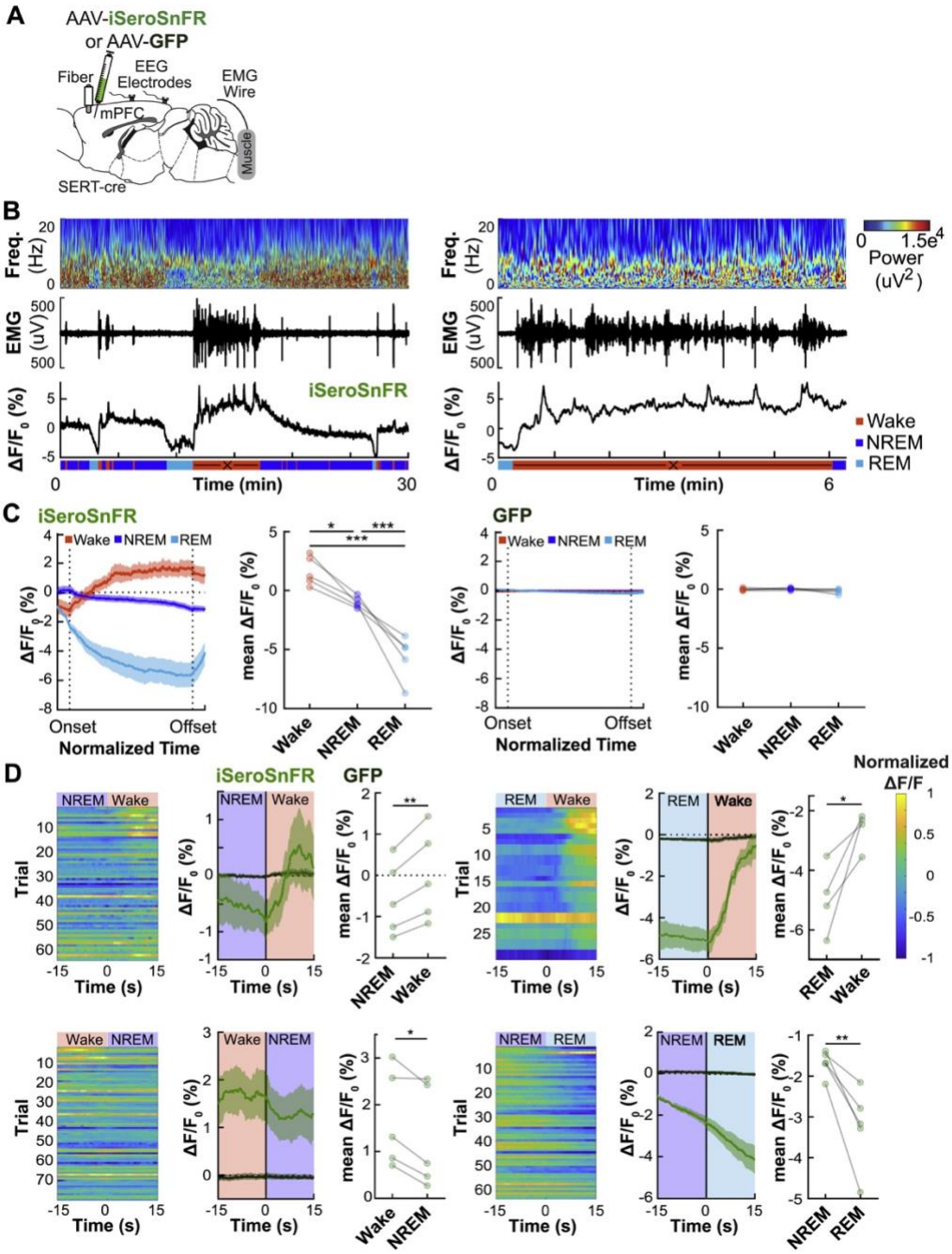

Figure S7. 5-HT dynamics in sleep-wake cycle in mPFC, related to Figure 5

(A) Mice were injected with either AAV2/9.*CAG*-iSeroSnFR.Nlgn or AAV2/5.*CAG*-GFP (as a negative control). For fiber photometry recordings, an optical fiber was inserted targeting mPFC. EEG screw electrodes and EMG wires were implanted to classify sleep-wake states.

(B) Representative mPFC^{iSeroSnFR} EEG spectrograms, EMG and fiber photometry traces over time across sleep-wake cycles (left) and walking episode (right).

(C) Temporal dynamics of $mPFC^{iSeroSnFR}$ (left) and $mPFC^{GFP}$ (right) activity during waking, NREM, and REM episodes within normalized time. Statistical comparisons of fluorescence levels were performed on the last 10% of data within each behavioral state (one-way ANOVA with Bonferroni correction).

(D) Fluorescence changes of iSeroSnFR and GFP across NREM to wake, REM to wake, wake to NREM and NREM to REM transitions. Statistical comparisons of changes in fluorescence using $mPFC^{iSeroSnFR}$ were made based on the average fluorescence over 15 s before and 15 s after the behavioral state transition. Data represent mean (dark lines) ± SEM (shaded areas). Each row of the heatmap represents one instance of a state transition. n = 3 $mPFC^{GFP}$; n = 4 $mPFC^{iSeroSnFR}$. $*p < 0.05$, $**p < 0.01$, $***p < 0.001$, paired Student's *t*-test.

3.10 Supplementary tables

Position	Native Amino Acid	Frequency	Random Forest Ranking	Mutation	Frequency	Estimate (log(D-luc/4'Br)	Standard Error	t value	Pr(>|t|)	Significance
211	P	196	18.67	A	7	0.30839	0.18982	1.625	0.10762	
				S	6	-0.0713	0.23635	-0.302	0.76367	
				T	2	0.08635	0.27811	0.31	0.75689	
214	T	208	10.42	A	2	0.22054	0.25565	0.863	0.39053	
				S	1	0.31082	0.31859	0.976	0.33179	
218	R	181	97.4	A	2	-0.6817	0.23314	-2.924	0.00434	**
				H	5	-0.1292	0.31859	-0.405	0.68605	
				K	23	0.66895	0.09273	7.214	1.43E-10	***
220	S	198	19.33	N	13	0.16193	0.33322	0.486	0.62813	
226	I	209	-3.28	V	2	-0.4745	0.73781	-0.643	0.52173	
227	F	198	0.35	C	1	-0.2112	0.31843	-0.663	0.5089	
				W	4	-0.0487	0.28951	-0.168	0.86683	
				Y	8	0.07492	0.13087	0.572	0.5684	
229	N	190	15.7	T	21	-0.2349	0.18888	-1.244	0.21673	
232	I	210	0	T	1	0.17555	0.32366	0.542	0.58883	
237	I	200	-4.78	V	11	0.05426	0.15272	0.355	0.72317	
239	S	196	-2.99	I	1	0.55528	0.46132	1.204	0.23177	
				T	13	0.30491	0.20534	1.485	0.14096	
				V	1	-0.3416	0.39311	-0.869	0.38714	
240	V	194	22.89	A	9	0.27524	0.17373	1.584	0.11652	
				G	1	0.23078	0.3638	0.634	0.52741	
				I	3	-0.0028	0.25232	-0.011	0.99113	
				L	2	0.62078	0.3638	1.706	0.09128	.
				M	2	0.11961	0.29372	0.407	0.68477	
241	V	198	8.13	A	9	0.00528	0.18827	0.028	0.97767	
				F	1	-0.9705	0.48142	-2.016	0.0467	*
				L	1	NA	NA	NA	NA	
				M	2	-0.4318	0.29795	-1.449	0.15067	
243	F	201	15.33	L	1	-0.0997	0.39904	-0.25	0.80329	
				M	9	-0.0694	0.13886	-0.5	0.61837	
246	G	192	9.84	A	19	-0.4631	0.24468	-1.893	0.06151	.
247	F	195	63.21	L	4	-0.2604	0.24334	-1.07	0.28725	
				S	1	NA	NA	NA	NA	
				Y	11	-0.5138	0.18159	-2.83	0.00571	**
249	M	150	35.41	F	9	0.19395	0.2297	0.844	0.40065	
				I	6	0.44579	0.27541	1.619	0.10892	
				L	46	0.03409	0.08591	0.397	0.69239	
250	F	178	23.77	A	4	-0.2625	0.2519	-1.042	0.30012	
				C	6	0.25221	0.19822	1.272	0.20641	
				G	1	0.57044	0.46814	1.219	0.22611	
				H	2	-0.5907	0.23678	-2.495	0.01437	*
				M	6	-0.2362	0.1506	-1.568	0.12021	
				S	2	0.72441	0.30415	2.382	0.01927	*
				T	7	-0.08	0.19599	-0.408	0.68395	
				V	1	0.15515	0.4816	0.322	0.74807	
				Y	4	-0.1121	0.16827	-0.666	0.5068	
251	T	210	0	I	1	NA	NA	NA	NA	
252	T	208	-4.28	S	3	-0.0501	0.54804	-0.091	0.92729	
255	Y	175	39.24	F	21	-0.4338	0.19608	-2.212	0.02938	*
				H	12	-0.4664	0.17548	-2.658	0.00926	**
				I	1	-0.7957	0.67763	-1.174	0.24332	
				N	2	-0.8542	0.31773	-2.688	0.00851	**
256	L	196	5.34	I	7	-0.2893	0.24769	-1.168	0.24579	
				M	6	-0.0489	0.21685	-0.225	0.82224	
				V	2	-0.1631	0.47519	-0.343	0.73221	
257	I	159	30.32	A	1	-0.5082	0.31734	-1.602	0.11266	
				C	3	-0.0694	0.38171	-0.182	0.85618	
				F	5	0.38618	0.28158	1.371	0.17353	
				L	14	0.06181	0.20057	0.308	0.75864	
				M	13	0.12343	0.17659	0.699	0.48633	
				R	3	0.27062	0.22695	1.192	0.23612	
				S	3	-0.0553	0.23705	-0.233	0.81617	
				V	8	0.42431	0.23297	1.821	0.07178	.
				Y	2	0.75755	0.40014	1.893	0.06144	.

Position	Native Amino Acid	Frequency	Random Forest Ranking	Mutation	Frequency	Estimate (log(D-luc/4'Br)	Standard Error	t value	Pr(>|t|)	Significance
260	F	207	9.51	G	1	-0.1392	0.31859	-0.437	0.66321	
				I	1	-0.2192	0.31859	-0.688	0.49317	
				N	1	-0.2792	0.31859	-0.876	0.38311	
				Y	1	0.10082	0.31859	0.316	0.75238	
264	L	189	31.8	F	1	-0.2897	0.37298	-0.777	0.43932	
				M	13	-0.3601	0.21138	-1.704	0.09179	.
				V	8	0.00896	0.2792	0.032	0.97448	
265	M	210	0	T	1	-0.8745	0.73781	-1.185	0.23893	
266	Y	209	2.65	H	2	-0.0988	0.87985	-0.112	0.91087	
267	L	210	0	F	1	0.05555	0.32366	0.172	0.86409	
269	E	209	2.47	G	2	-0.0795	0.25565	-0.311	0.75664	
279	D	210	0	N	1	0.7202	0.7657	0.941	0.34936	
281	K	210	0	E	1	-0.064	0.7331	-0.087	0.93062	
282	I	209	-5.28	T	1	NA	NA	NA	NA	
				V	1	0.08489	0.49072	0.173	0.86304	
283	Q	210	0	R	1	0.17555	0.32366	0.542	0.58883	
284	S	208	-2.78	V	3	0.08257	0.21939	0.376	0.70749	
286	L	196	24.55	I	2	-0.9751	0.48336	-2.017	0.04654	*
				M	4	-0.281	0.20038	-1.402	0.16411	
				V	9	0.55493	0.31594	1.756	0.08231	.
287	L	196	17.08	A	1	0.43402	0.46005	0.943	0.34791	
				I	1	-0.6259	0.42133	-1.486	0.14079	
				M	4	-0.2324	0.24791	-0.938	0.35089	
				V	9	0.36644	0.20177	1.816	0.07257	.
288	V	188	20.36	A	4	0.10941	0.42788	0.256	0.79875	
				F	2	0.78822	0.285	2.766	0.00685	**
				G	1	-0.2254	0.65275	-0.345	0.73062	
				I	1	0.65384	0.7185	0.91	0.36517	
				L	8	0.05214	0.23996	0.217	0.82845	
				M	6	-0.2228	0.32173	-0.693	0.49029	
				N	1	0.86248	0.63283	1.363	0.17621	
290	T	210	0	A	1	0.00446	0.50387	0.009	0.99295	
293	S	210	0	N	1	0.19511	0.85279	0.229	0.81953	
294	F	208	-2.12	L	1	-0.0444	0.32366	-0.137	0.89107	
				S	2	0.06635	0.38763	0.171	0.86446	
295	F	203	-11.5	L	8	0.23481	0.66098	0.355	0.72321	
301	I	210	0	T	1	NA	NA	NA	NA	
305	D	210	0	E	1	NA	NA	NA	NA	
310	H	209	6.41	R	2	0.10082	0.31859	0.316	0.75238	
311	E	197	22.44	C	14	0.16082	0.31859	0.505	0.61491	
312	I	209	0.37	V	2	-0.0492	0.31859	-0.154	0.87764	
313	A	197	22.27	G	14	NA	NA	NA	NA	
314	S	88	43.43	A	2	0.24328	0.23923	1.017	0.31181	
				C	51	-0.021	0.10384	-0.202	0.84049	
				T	58	-0.0921	0.10553	-0.873	0.38493	
				V	12	0.12736	0.14241	0.894	0.37344	
315	G	209	3.81	H	1	-0.3713	0.39338	-0.944	0.3477	
				T	1	-0.2377	0.48899	-0.486	0.62805	
316	G	127	68.74	A	13	-0.3285	0.12704	-2.586	0.01126	*
				R	1	NA	NA	NA	NA	
				S	28	-0.5065	0.08789	-5.763	1.07E-07	***
				T	42	-0.1567	0.09474	-1.654	0.10148	
321	L	209	-0.74	R	2	NA	NA	NA	NA	
326	A	207	-7.86	V	4	NA	NA	NA	NA	
334	P	208	3.67	S	3	-0.2754	0.48692	-0.566	0.57299	
337	R	208	-14.1	K	2	-0.6126	0.25525	-2.4	0.01838	*
				P	1	-0.0598	0.33262	-0.18	0.85769	
338	Q	207	25	C	2	-0.4257	0.42175	-1.009	0.31547	
				L	1	-0.69	0.46969	-1.469	0.14521	
				V	1	-0.4423	0.47466	-0.932	0.35384	
342	L	210	0	A	1	-1.8681	0.32673	-5.718	1.30E-07	***
347	S	199	86.35	A	8	-1.2661	0.1773	-7.141	2.02E-10	***
				G	4	-1.8726	0.22135	-8.46	3.68E-13	***
348	A	210	0	G	1	NA	NA	NA	NA	

Supplementary table 1. Additional information related to Figure 1

Positive values in the "Estimate" column indicate a preference for D-luc, while negative values indicate a preference for 4'Br-luc. · $p < 0.1$, *$p < 0.05$, **$p < 0.01$, *** $p < 0.001$.

					Round				Version				
Position	PDB#	Region	Rosetta	RF	1	2	3	AA's in sequenced variants	iAChSnFR0.6	iSeroSnFR0.0	iSeroSnFR0.1	iSeroSnFR0.2	iSeroSnFR
3	41	Lower lobe					Rand.	F,V	V				
4	42	Lower lobe					Rand.	F,V	V				
7	45	Lower lobe	X	-2.01				A,S	S				
8	46	Binding pocket	X	0.28		SSM	SSM	E,H,I,L,P,Q,S,T,V,Y	I				
9	47	Binding pocket	X	2.30		SSM	SSM	A,D,I,K,L,N,P,Q,V,Y	I	N			
10	48	Binding pocket	X	-1.06		SSM	SSM	C,D,F,H,L,P	F	H			
11	49	Binding pocket	X	1.60			SSM	A,T	T				
12	50	Binding pocket	X	0.23			SSM	A,E,D	E				
13	51	Binding pocket	X	-1.55			SSM	A,D,E,Q,P,T	Q				
14	52	Lower lobe	X	-1.00				I,Q	I				
19	57	Lower lobe					Rand.	L,M	M				
20	58	Lower lobe					Rand.	L,V	V				L
29	67	Lower lobe					SSM	D,P,Y	D				Random mutation in round 3 in improved variant
34	72	Lower lobe					SSM	A,C,R,T	R				Random mutation in round 3 in improved variant
38	76	Lower lobe					SSM	C,F,K,L	L				Random mutation in round 3 in improved variant
40	78	Binding pocket/lower lobe	X	-0.25				A,D,G,L	G				
41	79	Binding pocket/lower lobe	X	-0.02		SSM		A,E,F,G,I,L,P,Q,S,T,V	T	V			
42	80	Binding pocket/lower lobe	X	1.11				D,N	N				
55	93	Lower lobe				Rand.		N,Y	N				
59	97	Lower lobe					Rand.	F,I	I				Mutation occured after iSeroSnFR was discovered
61	99	Lower lobe				Rand.	SSM	A,G,L,M,V	V			L	
62	100	Binding pocket/lower lobe	X	-0.55				A,E	E				
63	101	Binding pocket/lower lobe	X	0.72				H,Y	Y				
64	102	Binding pocket/lower lobe	X	0.11			SSM	A,H,L,T,V	T	V			
65	103	Binding pocket/lower lobe					SSM	G	G				
66	104	Binding pocket/lower lobe	X	7.74	SSM			A,D,H,I,K,N,P,S,T,V,Y	T		Y		
70	108	Interface	X	-1.00				D,I	D				
73	111	Linker adjacent loop					SSM	A,S,T	T				
L1.1	112	Linker 1					SSM		Y				
L1.2	113	Linker 1					SSM	F,P	P				
L1.3	114	Linker 1					SSM	E,L,R	E				
L1.4	115	Linker 1					SSM		P				
GFP153	120	GFP/strand 7			Rand.		SSM	I,L,T	T		I		Effect of I was negligable by GLM, but was never confirmed
GFP157	124	GFP/7-8 loop					Rand.	H,Q	Q				Mutation occured after iSeroSnFR was discovered
GFP169	136	GFP/strand 8					SSM	H,L,Y	H			Y	
GFP192	159	GFP/9-10 loop					SSM		P			S	P
GFP196	163	GFP/9-10 loop					SSM	A,L,P,S	P			L	P L eliminates all mammalian expression
GFP231	198	GFP/11-1 linker					Rand.	F,L	L				
L2.1	357	Linker 2					SSM	P,S	P				
L2.2	358	Linker 2					SSM	A,K,Q,P	P				
L2.3	359	Linker 2					SSM	A,P	P				
L2.4	360	Linker 2					SSM	C,G,P,S,T	G				
77	361	Linker adjacent loop			Rand.	SSM		I,T	T			A	
102	386	Lower lobe				Rand.		L,P	P				
106	390	Binding pocket/hinge	X	0.71				D,E,M,N,R	N				
107	391	Binding pocket/hinge	X	-0.42		SSM		A,D,N,S	N	A			
108	392	Binding pocket/hinge	X	-2.21		SSM		A,D,E,P,R,S,T	T	S			
109	393	Binding pocket/upper lobe	X	0.39		SSM		F,H,W,Y	Y	F		Y	
110	394	Binding pocket/upper lobe	X	1.60				R,T,V	T	V			
112	396	Upper lobe				SSM	SSM	A,V	A				
130	414	Upper lobe					Rand.	A,S	A				Mutation occured after iSeroSnFR was discovered
140	424	Upper lobe					Rand.	A,V	A				
141	425	Binding pocket/upper lobe	X	0.72		SSM	SSM	D,N,Q,S,T	T	N			
142	426	Binding pocket/upper lobe	X	1.42			SSM	A,I,L,M,P,R,T	M				
143	427	Binding pocket/upper lobe	X	3.42	SSM			F,H,L,M,P,S,T,V	F		M		
144	428	Binding pocket/upper lobe	X	1.53				F,H	F				
147	431	Binding pocket/upper lobe	X	-0.46			SSM	D,K,N,Q,R,S,T	K				N
148	432	Binding pocket/upper lobe					SSM	H,P	P				
149	433	Binding pocket/upper lobe					SSM	D,Y	D				
169	453	Binding pocket/upper lobe					SSM	A,D,V	D				
170	454	Binding pocket/upper lobe	X	4.57	SSM			A,D,G,H,L,M,N,P,R,S,T	M	H	A		
173	457	Binding pocket/upper lobe	X	-0.59			SSM	A,L,M,P,Q,R,T	R	M			P
174	458	Binding pocket/upper lobe	X	0			SSM	A,F,H,P,S,Y	Y				
176	460	Upper lobe			Rand.			A,V	A				
186	470	Binding pocket/upper lobe	X	-1.16				A,D	D				
188	472	Binding pocket/upper lobe	X	2.51	SSM	SSM		C,D,F,G,H,I,K,L,M,P,R,T,Y	F		T		
189	473	Binding pocket/upper lobe	X	0.06			SSM	A,E,L,M,R	A				
190	474	Binding pocket/upper lobe	X	0.52			SSM	A,H,S,T	T				
191	475	Binding pocket/upper lobe					SSM	C,D,S	D				
211	495	Binding pocket/hinge	X	0.06				G,P,R	P				
212	496	Binding pocket/hinge				SSM		H,Y	Y				
221	505	Lower lobe					Rand.	D,E	D				
252	536	Binding pocket/lower lobe					SSM	R	R				

Supplementary table 2. Additional information related to Figure 1

Summary of positions tested during sensor engineering, and mutations introduced.

Summary of the Gaussian Regression model (built using glm):

Note Singularities were found in the modeling
and are indicated by an NA in the following table.
This is often the case when variables are linear
combinations of other variables, or the variable
has a constant value. These variables will be ignored
when using the model to score new data and will not be
included as parameters in the exported scoring routine.

Call:
glm(formula = Norm5HT ~ ., family = gaussian(identity), data = crs$dataset[,
c(crs$input, crs$target)])

Deviance Residuals:

Min	1Q	Median	3Q	Max
-0.23834	-0.013295	0.004073	0.017042	0.23219

Coefficients: (2 not defined because of singularities)

	Estimate	Std. Error	t value	Pr(>|t|)	
(Intercept)	0.264147	0.007505	35.167	<2E-16	***
Pos66D	-0.074688	0.06343	-1.177	0.24107	
Pos66H	-0.04404	0.067121	-0.656	0.51285	
Pos66I	0.06477	0.037844	1.711	0.08929	.
Pos66K	0.036014	0.064759	0.556	0.57905	
Pos66N	-0.265513	0.064759	-4.1	7.10E-05	***
Pos66P	0.111056	0.048996	2.267	0.025	*
Pos66V	-0.009171	0.067121	-0.137	0.89153	
Pos66Y	0.230738	0.030511	7.563	5.46E-12	***
Pos143L	0.017094	0.040089	0.426	0.6705	
Pos143M	0.505723	0.106518	4.748	5.18E-06	***
Pos143S	0.040451	0.028731	1.408	0.16145	
Pos143T	-0.240873	0.072141	-3.339	0.00109	**
Pos143V	0.040291	0.064759	0.622	0.53488	
Pos170A	0.133016	0.031509	4.222	4.43E-05	***
Pos170G	-0.267192	0.064759	-4.126	6.42E-05	***
Pos170L	0.02359	0.019403	1.216	0.2262	
Pos170P	0.055877	0.020024	2.79	0.00603	**
Pos170R	0.077359	0.049535	1.562	0.1207	
Pos170S	0.027526	0.064759	0.425	0.67147	
Pos188C	0.055963	0.064759	0.864	0.38903	
Pos188D	-0.016659	0.027657	-0.602	0.54796	
Pos188G	0.084843	0.064759	1.31	0.19237	
Pos188I	0.064468	0.064759	0.996	0.32127	
Pos188K	0.01733	0.070855	0.245	0.80715	
Pos188L	0.044601	0.027743	1.608	0.11025	
Pos188P	0.089914	0.05036	1.785	0.07644	.
Pos188R	-0.042585	0.03299	-1.291	0.19897	
Pos188T	0.078718	0.046043	1.71	0.08963	.
GFP153I	NA	NA	NA	NA	

Signif. codes: 0 '***' 0.001 '**' 0.01 '*' 0.05 '.' 0.1 ' ' 1

(Dispersion parameter for gaussian family taken to be 0.004414231)

Null deviance: 4.11291 on 168 degrees of freedom
Residual deviance: 0.55921 on 135 degrees of freedom
AIC: -415.58

Number of Fisher Scoring iterations: 2

==== ANOVA ====

Analysis of Deviance Table

Model: gaussian, link: identity

Response: Norm5HT

Terms added sequentially (first to last)

	Df	Deviance	Resid. Df	Resid. Dev
NULL	168	4.1129		
Pos41	1	0.0972	167	4.0157
Pos66	8	2.7726	159	1.2431
Pos109	1	0.0126	158	1.2305
Pos143	5	0.1450	153	1.0855
Pos170	6	0.2231	147	0.8624
Pos188	9	0.0634	138	0.7990
Pos55	1	0.0074	137	0.7917
Pos78	1	0.1359	136	0.6558
Pos176	1	0.0965	135	0.5992
GFP153	0	0	135	0.5592

[1] "\n"
Time taken: 0.02 secs

Rattle timestamp: 2016-06-21 12:24:20 EKUnger
==========

Supplementary table 3. Additional information related to Figure 1

Summary of the Gaussian regression model (GLM) performed after the first round of site-saturated mutagenesis. Note that these are raw values. In Figure 1, values have been normalized such that the parent (iSeroSnFR0.0) would be equal to 1.

3.11 STAR methods

KEY RESOURCES TABLE

REAGENT or RESOURCE	SOURCE	IDENTIFIER
Antibodies		
Chicken polyclonal anti-GFP	Aves Labs	GFP-1020; RRID: AB_2307313
Goat anti-chicken IgY H&L Alexa Fluor 488	Abcam	RRID: AB_150169
Bacterial and Virus Strains		
Top10	Fisher	C404003
BL21 (DE3)	NEB	C25271
LOBSTR-BL21 (DE3)	Kerafast	EC1001
CJ236	NEB	E4141
AAV-*CAG*-iSeroSnFR-Nlgn	In house	N/A
AAV-*CAG*.FLEx.iSeroSnFR-PDGFR	In house	N/A
AAV-*CAG*.FLEx.iSeroSnFRNull-PDGFR	In house	N/A
AAV1-*CMV*-PI-Cre-rBG	Penn Vector Core	AV-1-PV1090
AAV5-*CMV*-HI-eGFP-Cre.WPRE.SV40	Penn Vector Core	AV-5-PV2004
Biological Samples		
Hippocampal dissociated neuronal culture	In house	N/A
Chemicals, Peptides, and Recombinant Proteins		
Serotonin	Enzo	ALX-550-328-G001
Glutamate	Sigma	G1251
GABA	Sigma	A5835
Choline	Fisher	AC110290010
Acetylcholine	Sigma	A2661-100G
Tyrosine	Sigma	T3754-50G
L-DOPA	Sigma	378850
Dopamine	Sigma	H8502-25G
Norepinephrine	Sigma	74480
Epinephrine	Sigma	E4642-5G
L-Tryptophan	Sigma	T0254-25G
5-Hydroxytryptophan	Sigma	H9772-250MG
Tryptamine	Sigma	246557-5G
5-Hydroxy indole acetic acid	Sigma	H8876-500MG
L-Phenylalanine	Sigma	P2126-100G
Histamine	Sigma	H7250-10G
L-Leucine	Sigma	E811-25G
L-Serine	Sigma	S4250-5G
Adenosine	Sigma	A9251
Tyramine	Sigma	T2879-1G
Octopamine	Sigma	O0250-1G
Melatonin	Calbiochem	444300
Gramine	Sigma	G10806-25G

Indole	Sigma	W259306-SAMPLE-K
Amphetamine	Sigma	A5880-1G
Bufotenine	Gift from DEO	N/A
Trimethyltryptamine	Gift from DEO	N/A
Dimethyltryptamine	Gift from DEO	N/A
L-741,626	Tocris	1003
Fluoxetine	Tocris	0927
Fluoxamine	Tocris	1033
Sertraline	Tocris	2395
Citalopram (racemic)	Tocris	5763
Escitalopram	Tocris	4796
Duloxetine	Tocris	4798
Amoxapine	Sigma	A129-100MG
Bupropion	Tocris	2831
Clozapine	Tocris	0444
Clozapine-N-Oxide	Tocris	6329
6-Nitroqupazine	Sigma	Q109-100MG
Venlafaxine	Tocris	2917
Desvenlafaxine	Sigma	D2069-50MG
PA-N caged serotonin	Made by LDLand SB	N/A
NPEC caged serotonin	Tocris	3991
MDMA	Gift from DEO	N/A
TCEP	Sigma	C4706-2G
Jeffamine	Hampton	HR2-597
Citalopram	Abcam	ab120133
Tetrodotoxin	Tocris	1078
Buprenorphine	MWI	O56163
Carprofen	Henry Schein	024751
Ketamine	Henry Schein	010177
Xylazine	Henry Schein	033198
Critical Commercial Assays		
DNA miniprep kit	Qiagen	27104
PCR purification kit	Qiagen	28104
ZymoPURE Plasmid Miniprep Kit	Zymo	D4208T
MCSG-2 crystallization screen	Anatrance	MCSG-2
Endo-free Plasmid Maxi kit	Qiagen	12362
jetPrime	Polypus	114-75
AAVance concentration reagent	SBI	AAV100A-1
Effectine	Qiagen	301425
Deposited Data		
pRSET-iSeroSnFR	This paper	Addgene 128483
pMinDisplay-iSeroSnFR	This paper	Addgene 128484
pAAV-CAG-iSeroSnFR-Nlgn	This paper	Addgene 128485
pAAV-CAG.FLEx.iSeroSnFR	This paper	Addgene 128486
pMinDisplay-iSeroSnFR-EnhancedExport	This paper	Addgene 128941

pAAV-CAG.FLEx.iSeroSnFR-EnhancedExport	This paper	Addgene 129180
iSeroSnFR open conformation crystal structure	This paper	PDB: 6PER
Sequence of iSeroSnFR	This paper	Genebank:MN083270
Experimental Models: Cell Lines		
HEK293T	ATCC	1573
AAV293	Agilent	240073
Experimental Models: Organisms/Strains		
Timed-pregnant rats	Charles River	N/A
C57BL/6J	Jackson Laboratory	000664
SERT-Cre	MMRRC	017260-UCD RRID: MMRRC_017260-UCD
SERT-Cre	Jackson Laboratory	(Zhuang et al., 2005) RRID:IMSR_JAX:014554
Ai14	Jackson Laboratory	(Madisen et al., 2010) 007914
Recombinant DNA		
pRSET-A	Invitrogen	V35120
pMinDisplay	Invitrogen	V66020
pAAV	Addgene	98932
Software and Algorithms		
Rosetta	Rosetta Commons	https://www.rosettacommons.org/
liganddock	N/A	https://www.rosettacommons.org/manuals/rosetta3_user_guide/app_ligand_docking.html
Backrub	N/A	https://www.rosettacommons.org/manuals/archive/rosetta3.4_user_guide/d1/d09/backrub.html
R (RStudio)	R-project	https://www.r-project.org/ - https://www.rstudio.com/
randomForest	N/A	https://www.rdocumentation.org/packages/randomForest/versions/4.6-14/topics/randomForest
Glm	N/A	https://www.rdocumentation.org/packages/stats/versions/3.5.3/topics/glm
MATLAB R2017b	Mathworks	RRID: SCR_001622
EEGLAB plug-in	Swartz Center for Comp. Neuro.	https://sccn.ucsd.edu/eeglab/index.php RRID: SCR_007292
SleepSign 3.0	Kissei Comtec	http://www.sleepsign.com
Ethovision 14	Noldus	https://www.noldus.com/ethovision-xt/new
Video Freeze Software	Med Associates	https://www.med-associates.com/product/video-fear-conditioning/
ScanImage (SI 2016b)	Vidrio Technologies	http://scanimage.vidriotechnologies.com/display/SIH/ScanImage+Home
OMEGA	OpenEye Scientific	https://www.eyesopen.com/
CCP4	Collaborative Computational Project No. 4	http://www.ccp4.ac.uk
Living Image	PerkinElmer	https://www.perkinelmer.com/product/li-software-for-spectrum-1-seat-add-on-128113
OmniPlex System	Plexon	https://plexon.com/products/omniplex-d-neural-data-acquisition-system-1/
ABET II	Lafayette Instruments	http://lafayetteneuroscience.com/products/abetii-operant-ctrl-software

pCLAMP10	Molecular Devices	http://mdc.custhelp.com/app/answers/detail/a_id/18779/~/axon%E2%84%A2pclamp%E2%84%A2-10-electrophysiology-data-acquisition-%26-analysis-software-download
AxoGraph X	N/A	https://axograph.com/
Other		
Mantis	Formulatrix	N/A
Fluorescent Platereader	Tecan	Infinite M200Pro
IVIS Lumina	Xenogen	N/A
Nanodrop	Thermo	2000
Small animal Stereotax	David Kopf Instruments	In vivo fiber photometry experiments 1900
2-photon microscope	Scientifica	N/A
Ti:Sapphire laser	Coherent	Chameleon ultra
Axopatch-200B amplifier	Molecular Devices	200B
Vibrating Microtome	Leica	1200
Mosquito	TTP Labtech	HTS

RESOURCE AVAILABILITY

Lead contact

Further information and requests for resources and reagents should be directed and will be fulfilled by lead contact, Lin Tian, lintian@ucdavis.edu.

Materials availability

The following plasmids have been made available through Addgene:

128483	pRSET-iSeroSnFR
128484	pMinDisplay-iSeroSnFR
128485	pAAV-CAG.iSeroSnFR-Nlgn
128486	pAAV-CAG.FLEx.iSeroSnFR
128941	pMinDisplay-iSeroSnFR-EnhancedExport
129180	pAAV-CAG.FLEx.iSeroSnFR-EnhancedExport

AAV Viruses are available through thFurther information and requests for resources
e Canadian Neurophotonics Centre.

Data and Code Availability

The full sequence of iSeroSnFR has been deposited in GenBank: MN083270. The crystal structure has been deposited in the Protein Data Bank: 6PER. Code has been provided directly in this STAR methods section.

Code updates will be provided at https://github.com/ekunger/iSeroSnFR.git.

Experimental Model and Subject Details

Mice and Rats

The experimental procedures performed on animals followed the guidelines of the Animal Care and Use Committees at the University of California Davis, the California Institute of Technology, the University of North Carolina, Chapel Hill, and the National Institute on Drug Abuse. Mice and rats were housed in a barrier facility with a 12:12 hr light:dark cycle, and food and water were available *ad libitum*. Animals were group housed by sex wherever possible. *Rosa*$^{Ai14/Ai14}$ (Madisen et al., 2010) mice were maintained as homozygous breeding pairs or crossed to wild type C57BL/6J (Jax # 000664). *SERT*$^{Cre/+}$ (Zhuang et al., 2005) mice were bred as male *SERT*$^{Cre/+}$ x female wild-type C57BL/6J (Jax # 000664) as recommended by the depositing lab. Both male and female animals were used in experiments and were between the age of 2 and 9 months. For *in vivo* mouse experiments, *SERT*-Cre (Zhuang et al., 2005; Gong et al., 2003) were crossed to wild-type C57BL/6J (Jax # 000664). Both wild-type mice and mice heterozygous for the Cre transgene were used for experiments. Following surgery, subjects were singly housed for at least five days in a residence room for full recovery before animals were moved to a behavioral room. Animals were habituated to the new light/dark cycle and behavioral room for at least 2 weeks before experiments were started. Rats were ordered as timed-pregnant females and sacrificed shortly after arrival in the facility.

Methods Details

Methods specific to luciferase

Development of a machine learning-guided library design paradigm (methods specific to luciferase)

Before pursuing the ambitious goal of drastically shifting the specificity of a choline-binding protein to 5-HT, we first established our machine learning approach on a more modestly modified ligand/binding pocket pair. We selected firefly luciferase, an enzyme that has been engineered for multicomponent imaging (Jones et al., 2017). We synthesized a brominated analogue (4'Br-Luc) of

the cognate substrate D-luciferin (D-Luc), and mutated the enzyme active site to accommodate the substitution (Figure S1A).

We first chose random forest (RF) (Liaw and Wiener, 2002) because it is tolerant of missing data points and capable of extracting information from relatively small training datasets, which are a practicality of most protein mutagenesis studies. Importantly, a strength of RF is "feature importance" detection, giving us the ability to prioritize protein positions for SSM (Figure 1A). Second, we chose generalized linear modeling (GLM, Gaussian regression) (Dobson et al., 2008) because it is a better classifier, while still tolerating small training datasets, and its linear nature provides precise, interpretable predictions about the effects of individual mutations that we could easily translate into new variants and combinations thereof (Figure 1A).

To build the models, we used sequence information from 222 published and unpublished luciferase variants as our input variables, and the experimentally determined preference for D-Luc versus 4'Br-Luc as the output variable. Each position within the protein was an independent variable with a categorical distribution (amino acid), and the preference for D-Luc versus 4'Br-Luc (fold-preference as calculated by the amplitude of photon output in the presence of D-Luc versus 4'Br-Luc) was our target with a continuous numerical distribution. We then compared the importance of each position using the RF model, and the contribution of each mutation using the GLM (identity link), followed by experimental validation of these predictions. We found that RF was effective at predicting positions, and GLM made correct predictions, but only at positions highly ranked by RF. We therefore decided that for future sensor design, we would use the two models in a sequential fashion: first we would use the RF to rank the positions for SSM, and then we would analyze the results of our SSM libraries with the GLM to identify the best individual mutations at each position.

The top residues predicted by the RF model were positions 218, 347, 316 and 247, which were frequently mutated to accommodate other 4'-substituted analogs in a previous screen (Jones et al., 2017). The GLM predicted S347G, L342A, S347A, Y255N, R218A, F247Y, and G316S as the top mutations (see table below). To experimentally validate these predictions, we created a small library covering both high-ranked and low-ranked positions predicted by RF, all of which had very statistically significant GLM predictions of improved 4'Br–Luc specificity (Figure 7B). We tested 276 variants from this library for their photon output with D-Luc and 4'Br–Luc and sequenced the top 10% favoring 4'Br–Luc (~1000x increased binding compared to the starting variant), as well as the bottom 10% favoring D-Luc (Figure 7C). The number of mutations per variant was not

significantly different between the two populations, indicating a similar overall mutation rate (Figure 7D). However, the incidence of specific mutations was different between the two populations, and when compared to the input data (Figure 7E). For example, at position 347, which was highly ranked by both RF and GLM, the incidence of the glycine mutation compared to the native serine was 26:1 (G:S) in the top 10% of variants but 5:19 in the bottom ones (Figure 7E). Conversely, at position 342, which was not ranked highly by RF, a leucine-to-alanine mutation was predicted by the GLM to heavily bias the preference toward 4'Br–Luc. This mutation appeared more frequently in the bottom variants (L:A, 18:9 – top 10% versus 3:21 – bottom 10%, Figure 7E), demonstrating a correct prediction by the RF model, and an incorrect prediction for the GLM. In general, the RF more linearly predicted the preference (pseudo-R^2 = 0.45, Figure 7F), than GLM (pseudo-R^2 = 0.10, Figure 7G).

Construction of luciferase library and mutants

DNA inserts for the luciferase shuffle library and point mutants were generated as described by Jones et al. (2017). Two sections of the luciferase gene (*pgl4-luc2*), denoted R1 and R2, were targeted for gene assembly. The R1 region comprises amino acids 199-275 and was assembled with primers R1-F0 to R1-F235 (forward primers, Table M1) and R1-R0 to R1-R119 (reverse primers). The R2 region comprises amino acids 275-347 and was assembled with primers R2-F0 to R2-F264 (forward, Table M2) and R2-R0 to R2-R228 (reverse). The gene assembly primers were designed using gene2oligo (Rouillard et al., 2004) to identify desirable T_m values. To assemble the genes encoding point mutants, primers containing the codon(s) of interest were used in place of the primers coding for the wild-type sequence. For the shuffle library inserts, mutagenic primers were mixed with wild-type primers in a 1:1 molar ratio. Libraries were assembled as described by Bessette et al. (2003). All PCR reactions were performed using Q5® High-Fidelity DNA polymerase.

Library DNA was inserted into linearized template vector pET28-R1del-mRFP as described by Rathbun et al. (2017). Library inserts were assembled with the linearized pET vectors using Gibson assembly (Gibson et al., 2009). Gibson assembly master mixes were prepared following the Prather recipe on http://www.openwetware.org/wiki/Gibson_Assembly, with all materials purchased from New England BioLabs. For each assembly, 50 ng of *Dpn*I digested, linearized vector was combined with insert (5:1 insert:vector ratio) and added to 10 mL of master mix. The mixtures were incubated at 50 °C for 60 min, then 2 mL was transformed into chemically competent cells

(TOP10 *E.* coli, Thermo-Fisher). Transformants were plated on square, agar plates containing kanamycin. Cells were plated to exceed 3X the library size. Cells were scrapped of the plates, combined, and pelleted. DNA was isolated using ZymoPURE Plasmid Miniprep Kit and saved for screening.

Primer lists

All primers were purchased from Integrated DNA Technologies, Inc. (San Diego, CA) and are written in the 5′→3′ direction. Upper case letters denote bases coding for the luciferase gene. Lower case letters denote bases added to ensure similar melting temperatures (T_m) for all primers. Bases highlighted in red denote sites targeted for mutagenesis.

Forward Primers	
R1-F0	GGATCCACCGGATTGCCCAAGGGCGTAGCCCTACC
R1-F35	GCACCGCACCGCTTGTGTCCGATTCAGTCATGCCC
R1-F70	GCGACCCCATCTTCGGCAACCAGATCATCCCCGACA
R1-F106	CCGCTATCCTCAGCGTGGTGCCATTTCACCACGGC
R1-F141	TTCGGCATGTTCACCACGCTGGGCTACTTGATCTGCG
R1-F178	GCTTTCGGGTCGTGCTCATGTACCGCTTCGAGGAG
R1-F213	GAGCTATTCTTGCGAAGCTTcggccctgtacagtcgctg
R1-F235	cagcgactgtacagggc
Reverse Primers	
R1-R0	GGGCAATCCGGTGGATCC
R1-R18	ACAAGCGGTGCGGTGCGGTAGGGCTACGCCCTT
R1-R51	GCCGAAGATGGGGTCGCGGGCATGACTGAATCGGAC
R1-R87	CCACGCTGAGGATAGCGGTGTCGGGGATGATCTGGTT
R1-R124	CGTGGTGAACATGCCGAAGCCGTGGTGAAATGGCA
R1-R159	AGCACGACCCGAAAGCCGCAGATCAAGTAGCCCAG
R1-R194	cgAAGCTTCGCAAGAATAGCTCCTCCTCGAAGCGGTACATG

Region 1 (R1, wild-type *luc2* primers). Lower case letters denote non-luciferase sequences included for maintaining proper T_m and do not appear in the final assembled gene.

Forward Primers	
R2-F0	acacatCGAGGAGGAGCTATTCTTGCGAAGCTTGCA
R2-F36	AGACTATAAGATTCAATCTGCCCTGCTGGTGCCCACAC
R2-F74	TATTTAGCTTCTTCGCTAAGAGCACTCTCATCGACAAGTACGAC
R2-F117	CTAAGCAACTTGCACGAGATCGCCAGCGGCGGG
R2-F150	GCGCCGCTCAGCAAGGAGGTAGGTGAGGCC
R2-F181	GTGGCCAAACGCTTCCACCTACCAGGCATCCG
R2-F213	CCAGGGCTACGGCCTGACAGAAACAACTAGTGCCA
R2-F248	TTCTGATCACCCCCgtcgcctccggaggaga
R2-F264	tctcctccggaggcg
Reverse Primers	
R2-R0	TAGCTCCTCCTCGatgtgt
R2-R19	GGGCAGATTGAATCTTATAGTCTTGCAAGCTTCGCAAGAA
R2-R59	GCTCTTAGCGAAGAAGCTAAATAGTGTGGGCACCAGCA
R2-R97	TCGTGCAAGTTGCTTAGGTCGTACTTGTCGATGAGAGT
R2-R135	TTGCTGAGCGGCGCCCCGCCGCTGGCGATC
R2-R165	GGAAGCGTTTGGCCACGGCCTCACCTACCTCC
R2-R197	AGGCCGTAGCCCTGGCGGATGCCTGGTAGGT
R2-R228	acGGGGGTGATCAGAATGGCACTAGTTGTTTCTGTC

Region 2 (R2, wild-type *luc2* primers). Lower case letters denote non-luciferase sequences included for maintaining proper T_m and do not appear in the final assembled gene.

Forward Primers	
R1-F35_A	GCACCGCACCGCTTGTGTCGCCTTCAGTCATGCCC
R1-F141_Y	TACGGCATGTTCACCACGCTGGGCTACTTGATCTGCG
R1-F141_N	TTCGGCATGTTCACCACGCTGGGCAATTTGATCTGCG
R1-F141_Y+N	TACGGCATGTTCACCACGCTGGGCAATTTGATCTGCG
R2-F117_S	CTAAGCAACTTGCACGAGATCGCCAGCGGCTCT
R2-F213_A	CCAGGGCTACGGCGCCACAGAAACAACTAGTGCCA
R2-F213_G	CCAGGGCTACGGCCTGACAGAAACAACTGGGGCCA
R2-F213_A+G	CCAGGGCTACGGCGCCACAGAAACAACTGGGGCCA
Reverse Primers	
R1-R51_A	GCCGAAGATGGGGTCGCGGGCATGACTGAAGGCGAC
R1-R124_Y	CGTGGTGAACATGCCGTAGCCGTGGTGAAATGGCA
R1-R159_N	AGCACGACCCGAAAGCCGCAGATCAAATTGCCCAG
R2-R135_S	TTGCTGAGCGGCGCAGAGCCGCTGGCGATC
R2-R197_A	GCGCCGTAGCCCTGGCGGATGCCTGGTAGGT
R2-R228_G	acGGGGGTGATCAGAATGGCACTAGTTGTTTCTGTG

Primers used to construct luciferase point mutants and shuffle library. The bases highlighted in red denote sites targeted for mutagenesis.

R1 insert amplifaction primers	
R1-insert-Fwd	GACAAAACCATCGCCCTGATCATGAACAGTAGT GGATCCACCGGATTGCCCAA
R1-insert-Rev	CACCAGCAGGGCAGATTGAATCTTATAGTCTTGCAAGCTTCGCAAGA ATAGCTCCTCCTC
R2 insert amplifaction primers	
R2-insert-Fwd	CGAGGAGGAGCTATTCTTGCG
R2-insert-Rev	CTTCGGGGGTGATCAGAAT
Vector amplifcation primers	
R1-vector-Rev	GCAAGACTATAAGATTCAATCTGCCCTGCTGGTG
R2-vector-Fwd	ATTCTGATCACCCCCGAAG

Primers used to amplify inserts for the R1 or R2 regions, along with the pET vector backbone.

General bioluminescence imaging protocol

All analyses were performed with bacterial cell lysates in black 96-well plates (Greiner Bio One). Plates containing luminescent reagents were imaged in a light-proof chamber with an IVIS Lumina (Xenogen) CCD camera chilled to -90 °C. The stage was kept at 37 °C during the imaging session, and the camera was controlled using Living Image software. Exposure times were set to 60 s, and data binning levels were set to medium. Regions of interests were selected for quantification, and total flux values were analyzed using Living Image software. All data were exported to Microsoft Excel for further analyses.

Lysate screening of combination library

The shuffle library was screened following the protocol previously described in Jones et al. (2017), with modifications. Library DNA was transformed into chemically competent BL21-DE3 *E. coli* cells. Transformants were plated on square, agar plates containing kanamycin. Colonies were picked and expanded in LB-Kan media in a 96-well deep well plate (500 mL/well). The plate was incubated at 37 °C overnight. An aliquot of the overnight culture (4 mL) was used to inoculate 400 mL of auto-induction LB media (Studier, 2005), and the cells were incubated at 30 °C with shaking (200 rpm) for 24 h. The remaining starter cultures were stored at 4 °C and used for subsequent plasmid recovery and sequencing analysis. The cells were pelleted and lysed in lysis buffer (600 mL). Cell lysate (90 mL) was added to 96-well black plates, followed by 10X luciferin and ATP solution (10 mL, 100 mM luciferin and 1 mM ATP final concentration) in phosphate buffer (250 mM phosphate buffer, pH = 7.8). The plate was then imaged as described above.

Methods specific to iSeroSnFR

Rosetta Modeling

Rotamers for 5-HT were generated with OMEGA from OpenEye Scientific. The closed conformation PDB structure of *Thermoanaerobacter spX513* OpuBC was combined with the open structure of iAChSnFR0.4 (provided by PMB). We used rosetta_script in Rosetta 3 (2015.19.57819) for docking with protein-ligand interface design instructed by design.xml (below). Residues within 6Å of the ligand, as well as those within 8Å and facing towards the ligand, were mutated. Residues within 10Å, as well as those within 12Å and facing the ligand, were repacked. We restricted aromatic residues (Trp, His, Tyr, and Phe) to only be mutated into other aromatic residues. We designed 48,000 models and filtered them with total_score for the top 5% and then picked the top 10 models according to the interface_delta_X score. These 10 models were further re-designed with a protocol to couple protein side-chain and backbone flexibility from the Kortemme lab (Ollikainen et al., 2015). Shape complementarity scores for the top redesigns were calculated with Sc routine in CCP4. Top designs were chosen for synthesis and characterization.

Rosetta design was performed using the following scripts:

Design.options

```
-in
   -file
   -s  SRO_X513.pdb
   -extra_res_fa SRO.params
   -packing
   -ex1
   -ex2
   -linmem_ig 10
   -parser
   -protocol design.xml
   -overwrite
   -mistakes
   -restore_pre_talaris_2013_behavior true
```

Backrub.options

```
-in
   -path
   -database ./rosetta/main/database/
   -file
   -extra_res_fa SRO.params
   -packing
   -ex1
```

```
-ex2
-extrachi_cutoff 0
-resfile X513_6A.res
-out
-nstruct 20
-coupled_moves
-mc_kt 0.6
-ntrials 1000
-initial_repack false
-ligand_mode true
-ligand_weight 2.0
-run
-ignore_zero_occupancy false
```

Backrub.bash

```
./main/source/bin/coupled_moves.linuxgccrelease  -database
./main/database/ protocols.backrub.BackrubMover -extra_res_fa
SRO.params -ex1 -ex2 -extrachi_cutoff 0 -nstruct 20 -
coupled_moves::mc_kt 0.6 -coupled_moves::ntrials 1000 -
coupled_moves::initial_repack false -coupled_moves::ligand_mode
true -coupled_moves::ligand_weight 2.0 -mute all -
coupled_moves::fix_backbone false -coupled_moves::bias_sampling
true -coupled_moves::bump_check true  -s 14_SRO_X513_0280.pdb -
resfile 14_SRO_X513_0280.res
```

Design.xml

```
<ROSETTASCRIPTS>
   <SCOREFXNS>
   <ligand_soft_rep weights=ligand_soft_rep>
   </ligand_soft_rep>
   <hard_rep weights=ligand>
   </hard_rep>
   </SCOREFXNS>
   <TASKOPERATIONS>
   <DetectProteinLigandInterface  name=design_interface  cut1=6.0
   cut2=8.0 cut3=10.0 cut4=12.0 design=1 resfile="resfile.txt"/>
   </TASKOPERATIONS>
   <LIGAND_AREAS>
   <inhibitor_dock_sc   chain=X   cutoff=6.0   add_nbr_radius=true
   all_atom_mode=false/>
   <inhibitor_final_sc   chain=X   cutoff=6.0   add_nbr_radius=true
   all_atom_mode=false/>
   <inhibitor_final_bb  chain=X  cutoff=7.0  add_nbr_radius=false
   all_atom_mode=true  alpha_restraints=0.3/>
   </LIGAND_AREAS>
   <INTERFACE_BUILDERS>
   <side_chain_for_docking ligand_areas=inhibitor_dock_sc/>
```

```
<side_chain_for_final ligand_areas=inhibitor_final_sc/>
<backbone ligand_areas=inhibitor_final_bb extension_window=3/>
</INTERFACE_BUILDERS>
<MOVEMAP_BUILDERS>
<docking sc_interface=side_chain_for_docking
minimize_water=false/>
<final sc_interface=side_chain_for_final bb_interface=backbone
minimize_water=false/>
</MOVEMAP_BUILDERS>
<MOVERS>
<FavorNativeResidue name=favor_native bonus=1.2/>
<ddG name=calculateDDG jump=1 per_residue_ddg=1
scorefxn=hard_rep/>
<PackRotamersMover name=designinterface scorefxn=hard_rep
task_operations=design_interface/>
<Translate name=translate chain=X distribution=uniform
angstroms=3 cycles=50/>
<Rotate name=rotate chain=X distribution=uniform degrees=360
cycles=50/>
<SlideTogether name=slide_together chains=X/>
<HighResDocker name=high_res_docker cycles=12
repack_every_Nth=3 scorefxn=ligand_soft_rep
movemap_builder=docking/>
<FinalMinimizer name=final scorefxn=hard_rep
movemap_builder=final/>
<InterfaceScoreCalculator name=add_scores chains=X
scorefxn=hard_rep/>
</MOVERS>
<PROTOCOLS>
<Add mover_name=translate/>
<Add mover_name=rotate/>
<Add mover_name=slide_together/>
<Add mover_name=favor_native/>
<Add mover_name=designinterface/>
<Add mover_name=high_res_docker/>
<Add mover_name=calculateDDG/>
<Add mover_name=final/>
<Add mover_name=add_scores/>
</PROTOCOLS>
</ROSETTASCRIPTS>
```

Cloning

The bacterial expression vector pRSET-A was used for library screening, which contains a His_6-tag for purification. The mammalian expression vector pMinDisplay, which contains a myc-tag, an IgK-leader secretion tag, a Kozak sequence, and a PDGFR transmembrane domain for tethering to the

membrane, was used for transfection into HEK293 cells. The viral expression vector pAAV was used for infection of HEK293 cells, primary neurons, mouse brain slices, and *in vivo* fiber photometry. All vectors were cloned with a combination of QuikChange, circular polymerase extension cloning (Quan and Tian, 2011), overlap extension cloning (Bryksin and Matsumura, 2010), digestion/ligation, or Kunkel mutagenesis (Kunkel, 1985). Due to issues arising from double-stranded break repair machinery in the bacteria, which drastically reduced the cloning efficiency into FLEx backbones, sequences inserted into pAAV containing FLEx sites were first subcloned into a custom shuttle vector, then cut with SacI and HindIII and ligated into a matching custom pAAV.

Library generation

Libraries were constructed by Kunkel mutagenesis (Kunkel, 1985). Single stranded dU-DNA was generated by transforming the plasmid to CJ236 cells and infecting with M13K07 bacteriophage. Chloramphenicol was used initially to ensure an F-pilus$^+$ host; ampicillin was used to ensure the presence of the plasmid, and kanamycin was used to ensure bacteriophage infection. Single stranded dU-DNA was harvested using a kit according to the manufacturer's instructions. Phosphorylated primers were designed in the reverse direction with either a specific mutation or a degenerate codon (NNK), and at least 10 bp on either side of the mutation. An additional primer was included in each reaction to destroy a cut site (either NheI or XbaI) in order to allow easy enrichment for mutated sequences (Huang et al., 2012). Primers were annealed to the sequence by raising the temp to 95^{o}C and lowering it slowly to 25^{o}C (2^o/min) using a thermocycler. Gaps were filled in and ligated using T7 polymerase and T4 ligase. DNA was transformed to Top10 cells and grown at 37^{o}C overnight. DNA was extracted using a miniprep kit according to the manufacturer's instructions, and digested with either NheI or XbaI. DNA was purified using a PCR cleanup kit according to the manufacturer's instructions.

Library screening

Library size was determined using the TopLib online library calculator (Nov, 2012). DNA libraries were transformed to BL21(DE3) cells, plated on LB-agar with ampicillin, and allowed to grow at 37^{o}C overnight. Colonies were picked at random into 2.3 mL deep-well 96-well plates and grown in 1 mL of autoinduction medium (2xYT + 0.5% glycerol, 0.5% glucose, 0.2% α-lactose, 25 mM Na_2HPO_4, 25 mM KH_2PO_4, 50 mM NH_4Cl, 5 mM Na_2SO_4, 20 mM $MgSO_4$) for 8 h at 37^{o}C, then

for 24-36 h at 18ºC, shaking at 250-300 rpm. 4 wells of each plate were designated for the parent protein, which was transformed and plated at the same time as the libraries. At the end of the growth period, 50 µL was removed and stored at -80ºC in 25% glycerol for subsequent DNA recovery. Cultures were then pelleted by centrifugation and washed 3x with PBS. Pellets were dried briefly, then frozen at -80ºC for 15 mins, and thawed. Pellets were resuspended in 100 µL of B-PER Complete reagent and incubated shaking at 30ºC for 1 h. Cell debris was pelleted by centrifugation and the supernatant was transferred to a clean plate. 96-well plates were expanded into optically clear 384-well plates containing 45 µL PBS and 4 µL lysate, then read on a fluorescent plate reader. Following the initial read, 5-HT was prepared fresh and 1 µL was added to experimental wells, and 1 µL of PBS was added to control wells, and the plate was read again. The performance of each variant was calculated as the difference between the first and second read, divided by the first read, and normalized to the PBS well, then compared to the parent wells. Any variant showing considerable improvement over the parent was subsequently retested at multiple concentrations, then regrown from the glycerol stock, DNA extracted by miniprep, and sequenced.

Protein purification

Plasmids were regrown from glycerol stock or transformed to LOBSTR-BL21(DE3) cells. For small yields, cells were grown in 5 mL of autoinduction medium at 37ºC for 8 h, then 18ºC for 24-36 h, shaking at 250-300 rpm. Then cultures were pelleted by centrifugation and the supernatant removed. Pellets were subjected to 3 rounds of freeze-thaw, first at -80ºC, followed by 37ºC waterbath. Then pellets were resuspended in 500 µL of B-PER Complete and incubated at 30ºC for 1 h, shaking at 250-300 rpm. Cell debris was pelleted by centrifugation and supernatant was transferred to a 96-well deep-well plate. Protein was purified using the His-tag with prepacked NiNTA tips (IMAC20) connected to an electronic multichannel with a preset protein purification protocol. Briefly, NiNTA beads were washed with 10 mM imidazole, then the lysate was bound to the NiNTA beads, and washed 8X with 25 mM imidazole, then eluted with 250 mM imidazole.

For large yields, plasmids were first grown in 5 mL of autoinduction medium at 37ºC, then expanded to 100 mL and grown at 18ºC for 36-48 h, shaking at 250-300 rpm. Then cultures were pelleted by successive rounds of centrifugation followed by supernatant removal. Pellets were subjected to 3 rounds of freeze-thaw cycles as above, then resuspended in 10 mL of B-PER Complete and incubated at 30ºC for 1 h, shaking at 250-300 rpm. Then NiNTA beads were washed with 10

mM imidazole in PBS and incubated with the lysate in 10 mM imidazole on a rotator at 4ºC for 18 h. Beads were then washed with 25 mM imidazole in PBS 6 times (600-1000 mL total wash volume), then eluted with 250 mM imidazole in PBS. Protein was then dialyzed in 1X PBS (specificity and affinity assays) or 0.1X TBS (crystallization), and subsequently concentrated using concentrator columns (10 kDa MWCO).

Specificity screening

Purified protein was measured by nanodrop, and diluted with 1X PBS to reach a final concentration of 100 nM. 40 µL was added to a 384-well plate, and read on a fluorescent plate reader. Small molecule neurotransmitters, drugs and other compounds were dissolved in either 1X PBS, ascorbate buffer (to reduce oxidation: Na-(L) Ascorbate 137 mM, KCl 5.3 mM, $CaCl_2$ 952 µM, $MgSO_4 7H_2O$ 833 µM, $MgCl_2 6H2O$ 1 mM, $Na_2PO_4 2H2O$ 423 µM, KH_2PO_4 345 µM, glucose 5.6 mM, $NaHCO_3$ 4.2 mM), 10% ethanol, or 10% DMSO. pH was carefully maintained at 7.4 for all experiments. Then 10 µL of either vehicle or compound was added to the protein and read again on the plate reader. Due to maximum solubility issues, not all compounds were tested at the same concentration.

Crystallization and data collection

Crystals were grown by hanging-drop vapor diffusion at room temperature (21°C) using iSeroSnFR (20 mg/mL, mixed with 20 mM 5-HT and 10 mM TCEP) and the commercially available crystallization screen MCSG 2. Crystals grew in condition G11, in a drop containing 200 nL protein and 200 nL reservoir solution (0.1 M HEPES:NaOH pH 7.0, 30% Jeffamine ED-2001 pH 7.0). Crystals were harvested and cryoprotected in reservoir solution containing 30% ethylene glycol before flash-cooling in liquid nitrogen. All data were collected at APS beamline 24-ID-C. Diffraction data were processed with XDS (Kabsch, 2010) and scaled with Aimless (Evans and Murshudov, 2013). iSeroSnFR crystallized in the orthorhombic space group *I*222 with unit cell parameters a = 80.67 Å, b = 99.26 Å, c = 150.56 Å. The structure of iSeroSnFR was determined by molecular replacement with PHASER (McCoy, 2007) using the GFP domain (residues 177-402) of the similarly-constructed maltose sensor (PDB: 3OSQ) and the soluble binding domain of the BilE ABC transporter from *Listeria monocytogenes* (PDB: 4Z7E) as search models. Manual model building was done with the program Coot (Emsley and Cowtan, 2004). The resulting

structure was refined with PHENIX to a final R_{factor} = 19.21% and R_{free} = 23.84%. Data collection refinement statistics are listed below.

Synchrotron (Beamline)	APS (24-ID-C)
Wavelength (Å)	0.97920
Space Group	*I*222
Unit Cell Parameters (Å)	*a* = 80.67, *b* = 99.26, *c* = 150.56
Resolution Range (Å)	85-2.10 (2.16-2.10)
No. observed reflections	107,170 (8,844)
No. unique reflections	34,796 (2,849)
Completeness (%)	98.1 (68.2)
I/σ (I)	11.4 (2.0)
R_{merge}[a] (%)	7.0 (63.8)
$CC_{1/2}$	99.8 (68.2)
Monomers per ASU	1
Matthew's Coefficient (Å^3/Da)	2.40
Solvent Content (%)	48.81
Refinement Statistics	
No. of reflections (F>0)	34,793
R_{factor}[b] (%)	18.83
R_{free}[b] (%)	23.46
RMS bond length (Å)	0.008
RMS bond angle (°)	1.077
Coordinate Error[c] (Å)	0.21
Average B Factors	
Protein (Å^2)	43.6
Water (Å^2)	40.0
Ethylene Glycols (Å^2)	46.4
Ramachandran Plot Statistics[c]	
Favored (%)	489 (96.0%)
Allowed (%)	17 (3.4%)
Outliers (%)	3 (0.6%)
No. of atoms	
Protein	4,023
Ethylene Glycols	20 (5 molecules)
Waters	226
PDBID	**6PER**

[a] $R_{merge} = [\sum_h\sum_i|\boldsymbol{I}_h - \boldsymbol{I}_{hi}|/\sum_h\sum_i\boldsymbol{I}_{hi}]$ where $\boldsymbol{I}_h$ is the mean of $\boldsymbol{I}_{hi}$ observations of reflection *h*. Numbers in parenthesis represent highest resolution shell.

[b] *R*-Factor and [c] $R_{free} = \sum||F_{obs}| - |F_{calc}|| / \sum|F_{obs}|$ x 100 for 95% of recorded data (*R*-Factor) or 5% data (R_{free})

[c] Ramachandran plot statistics from MolProbity (Chen et al., 2010)

Protein Sequences

Insertion of cpsfGFP is after residue 106, but residues 105-108 were mutated previously as part of the linker regions. Amino acid numbering matches normal N-to-C numbering of each domain. The first 29 amino acids of X513 OpuBC are an endogenous secretion signal that was omitted, and the first D of X513 OpuBC corresponds to 1 throughout the rest of the manuscript as it was the first amino acid available in the initial Rosetta modeling.

IgGκ signal peptide
X513 OpuBC 30-104
Inserted linker
sfGFP 147-238 circular permutation linker sfGFP 1-146
Inserted linker
X513 OpuBC 109-305
Myc epitope
PDGFR transmembrane domain 513-561

METDTLLLWVLLLWVPGSTGDRSANDTVVVGSINHTEQIIVANMLAEMIEAHTDLKVVRKLNLGGVNVNFEAIKR
GGANNGIDIYLEYVGYGLVDILGYPEPNVYIIADKQKNGIKANFKIRYNVEDGSVQLADHYQQNTPIGDGPVLLP
DNHYLSTQSVLSKDPNEKRDHMVLLEFVTAAGITLGMDELYKGGTGGSMSKGEELFTGVVPILVELDGGVNGHKF
SVRGEGEGDATNGKLTLKFICTTGKLPVPWPTLVTTLTYGVQCFSRYPDHMKQHDFFKSAMPEGYVQERTISFKD
DGTYKTRAEVKFEGDTLVNRIELKGIDFKEDGNILGHKLEYNFPPPGATDPEGAYETVKKEYKRKWNIVWLKPLG
FNASYVLAVKDELAKQYNLKTFSDLAKISDKLILGANMMFLENPDGYPGLQKLYNFKFKHTKSMDAGIPYTAIDN
NEVQVIDATATDGLLVSHKLKILEDDKAFFPPYYAAPIIRQDVLDKHPELKDVLNKLANQISLEEMQKLNYKRDG
EGQDPAKVAKEFLKEKGLILQVDEQKLISEEDLNAVGQDTQEVIVVPHSLPFKVVVISAILALVVLTIISLIILI
MLWQKKPR*

Neuroligin1 signal peptide
X513 OpuBC 30-104
Inserted linker
sfGFP 147-238 circular permutation linker sfGFP 1-146
Inserted linker
X513 OpuBC 109-305
Neuroligin exrtracellular predicted transmembrane intracellular

MALPRCMWPNYVWRAMMACVVHRGSGAPLTLCLLGCLLQTFHVLSQKLEFANDTVVVGSINHTEQIIVANMLAEM
IEAHTDLKVVRKLNLGGVNVNFEAIKRGGANNGIDIYLEYVGYGLVDILGYPEPNVYIIADKQKNGIKANFKIRY
NVEDGSVQLADHYQQNTPIGDGPVLLPDNHYLSTQSVLSKDPNEKRDHMVLLEFVTAAGITLGMDELYKGGTGGS
MSKGEELFTGVVPILVELDGGVNGHKFSVRGEGEGDATNGKLTLKFICTTGKLPVPWPTLVTTLTYGVQCFSRYP
DHMKQHDFFKSAMPEGYVQERTISFKDDGTYKTRAEVKFEGDTLVNRIELKGIDFKEDGNILGHKLEYNFPPPGA
TDPEGAYETVKKEYKRKWNIVWLKPLGFNASYVLAVKDELAKQYNLKTFSDLAKISDKLILGANMMFLENPDGYP
GLQKLYNFKFKHTKSMDAGIPYTAIDNNEVQVIDATATDGLLVSHKLKILEDDKAFFPPYYAAPIIRQDVLDKHP
ELKDVLNKLANQISLEEMQKLNYKRDGEGQDPAKVAKEFLKEKGLIGSTLELVPHLHNLNDISQYTSTTTKVPST
DITLRPTRKNSTPVTSAFPTAKQDDPKQQPSPFSVDQRDYSTELSVTIAVGASLLFLNILAFAALYYKKDKRRHD
VHRRCSPQRTTTNDLTHAPEEEIMSLQMKHTDLDHECESIHPHEVVLRTACPPDYTLAMRRSPDDIPLMTPNTIT
MIPNTIPGIQPLHTFNTFTGGQNNTLPHPHPHPHSHSTTRVGGSGG*

Tissue Culture

HEK293T cells were grown in DMEM, supplemented with fetal bovine serum (FBS) and Penicillin-Streptomycin (Pen Strep). Cells were transfected with Effectene per the manufacturer's instructions. Prior to imaging, cells were washed with Hank's Balanced Salt Solution (HBSS) supplemented with 2 mM $MgCl_2$ and 2 mM $CaCl_2$. All images were collected in HBSS + Mg + Ca.

Dissociated hippocampal neuronal culture

Primary hippocampal neuronal cultures were prepared as previously described. Briefly, E18 rat pups were decapitated, and the brains were dissected into ice-cold neural dissection solution (NDS, 10 mM HEPES in HBSS, pH 7.4). Hippocampi were removed, enzymatically digested with 0.25% trypsin, washed with pre-warmed plating medium (PM, Minimal Essential Medium supplemented with 10% FBS and 100 U/mL Pen Strep) and then mechanically digested by trituration. Cells were plated on 35 mm MatTek glass bottom dishes previously coated with a mixture of 20 µM poly-L-ornithine and 50 ng/mL laminin. Cells were kept at 37 °C, 5% CO_2 in PM for ~24 h and then in Neurobasal medium supplemented with 2% B27, and one third medium exchanges were performed every 3-4 days. On the seventh day *in vitro* (DIV), cells were infected with AAV2/1- or AAV2/9-*CAG*-iSeroSnFR-Nlgn or AAV2/1- or AAV2/9-*CAG*.FLEx.iSeroSnFR-PDGFR and AAV2/1-*CMV*-Cre and transferred to feeding medium (Neurobasal medium supplemented with 2% B27, 1% GlutaMAX, 1 µg/mL Gentamicin, and 10 µM FuDR).

Dose-response curves

Prior to imaging, all cultures were washed and incubated in HBSS containing 2 mM $MgCl_2$ and 2 mM $CaCl_2$ to minimize background due to fluorescent culture medium components. All data collected for the same experiment were collected with identical imaging parameters. Cultures were imaged on a laser scanning confocal microscope (Zeiss 710). Dishes were perfused using a gravity-fed inlet connecting 8 channels via a commutator and controlled by a ValveBank controller, and a pump-controlled outlet. 5-HT and 5-HIAA were made fresh. Washes and test concentrations were perfused onto the cultures at a rate of ~1 mL/minute.

Stopped-flow

iSeroSnFR protein was purified as above and kinetics were determined by mixing equal volumes of 0.2 µM protein with varying concentrations of 5-HT in PBS in an Applied Photophysics SX20 stopped-flow fluorimeter with 490 nm LED excitation and 510 nm long pass filter. Data were collected at 37ºC.

Uncaging

Prior to imaging, all cultures were washed and incubated in HBSS containing 2 mM $MgCl_2$ and 2 mM $CaCl_2$ to minimize background due to fluorescent culture medium components. All data collected for the same experiment were collected with identical imaging parameters. MatTek dishes containing primary neurons were washed 3X with HBSS, then 1 mL of HBSS with 200 µM PA-N-5HT or NPEC-5HT was added to the dish. Dishes were imaged on a laser scanning confocal (Zeiss 880). The 488 nm laser was used for imaging at 0.5% power. The 405 nm laser was used for uncaging at 100% power. Bidirectional line scans (1 x 128 pixel) were performed at 5000 Hz (200 µs/scan). Frame scans (128 x 128 pixel) were performed at 40 Hz (25 ms/scan). The uncaging area was selected using the Zen software's bleaching function, then setting the initial delay, the bleaching period, and the inter-bleach interval.

Virus production

Virus was produced as previously described (Broussard et al., 2018). Briefly, transfer plasmid, capsid plasmid and helper plasmid were grown in a large culture volume and purified using an endo-free maxiprep kit, per the manufacturer's instructions. AAV293 cells were grown in DMEM + FBS + Pen Strep, as described above, and transfected with all three plasmids (17 µg transfer, 14.5 µg helper, 8.4 µg capsid) using jetPrime reagent per the manufacturer's instructions. After 72h incubation, medium was collected and cleared by centrifugation (2000 xg, 5 min) and filtered through a 0.22 µm filter. 4ºC AAVance concentration reagent was added and incubated at 4ºC for 18-96 h. Virus was pelleted by centrifugation (1500 x g, 30 min, 4ºC), washed by resuspending in 4ºC culture medium, and pelleted again (1500 x g, 3 min). Virus was finally resuspended in 4ºC PBS. Genomic titers were determined by qPCR within the WPRE region.

Surgical procedures for slice experiments

Viral injections

Injection procedures were performed as previously described (Broussard et al., 2018). Briefly, animals were anesthetized using 0.5-2.5% isoflurane and mounted on a stereotaxic apparatus (900). For injections into the mPFC, a small craniotomy (1-2 mm diameter) was performed around Bregma to expose the mPFC. Virus injection was performed using a glass pipette beveled at 45° with a 15–20-μm opening and back-filled with mineral oil. A fitted plunger controlled by a hydraulic manipulator was inserted into the pipette and used to load and inject the viral solution. Either AAV2/9-*CAG*-iSeroSnFR-Nlgn or AAV2/9-*CAG*.FLEx.iSeroSnFR-PDGFR and AAV2/1-*CMV*-Cre was injected into $SERT^{Cre/+}$; $Rosa^{Ai14/+}$ mice in 3 to different locations on each side, ~250 μm apart, and 500-1500 μm deep such that a large area of the mPFC would be labeled. For injections into the striatum, AAV2/9-CAG-iSeroSnFR-Nlgn was injected bilaterally into striatum and nucleus accumbens using a Nanoject II or III. Virus was injected at AP +1.2; ML ± 1.0; DV -4.6, -4.1, -3.6, -3.1 mm. 250 nL was injected at each depth for a total of 1000nL/side. Mice were allowed to recover >2 weeks to allow for sensor expression.

Brain slices for 2-photon imaging

Brain slices for two-photon imaging were prepared as previously described (Broussard et al., 2018). Briefly, animals were sacrificed, and the brain was dissected out and placed into ice-cold cutting solution (73 mM NaCl, 2.5 mM KCl, 2 mM $MgCl_2x6H_2O$, 1.25 mM $NaH_2PO_4xH_2O$, 25 mM $NaHCO_3$, 25 mM glucose, 0.5 mM $CaCl_2$, 75mM sucrose). 300 μm slices were cut using a vibrating microtome. Slices were allowed to recover for 45 mins at 37ºC in cutting solution, before being transferred to artificial cerebrospinal fluid (aCSF) (125 mM NaCl, 2.5 mM KCl, 1 mM $MgCl_2x6H_2O$, 1.25 mM $NaH_2PO_4xH_2O$, 25 mM $NaHCO_3$, 10 mM glucose, 2 mM $CaCl_2$). Imaging was carried out on a custom-built 2-photon microscope. ScanImage version 5 software was used to control the microscope and collect the images. Slices were scanned at 30 Hz using 920 nm light. Ligands were applied by microinjection through a pulled glass pipette placed on the surface of the slice within the imaging area. Pressure was applied manually, and ligand expulsion was confirmed by slight deformation of the tissue.

Brain slices for 1-photon photometry

Brain slices for photometry imaging were prepared as follows. Mice were anesthetized with isoflurane and brains were removed and placed in warm (33°C) aCSF containing the following (in mM): 124 NaCl, 2.5 KCl, 1.3 $MgCl_2$, 2.5 $CaCl_2$, 1.0 NaH_2PO_4, 26.2 $NaHCO_3$, 20 glucose, 0.4 ascorbate, and 3 kynurenic acid. Sagittal slices (230 μm) were prepared in warm aCSF using a Leica vibratome. Slices were incubated in warm (33°C) 95%O_2/5%CO_2 oxygenated aCSF containing kynurenic acid (3 mM) for at least 30 min and moved to room temperature (22°C–24°C) until used. Photometric recordings were made from slices containing striatum and transferred to a recording chamber maintained at 34°C, and aCSF perfused at the rate of 2 mL/min.

5-HT transients were detected under a 40x water immersion objective on an upright fluorescent microscope connected with a photomultiplier tube (PMT). Regions of interests (ROIs) were excited using Solis LED and excitation/emission lights were filtered with a dichroic. ROIs were excited for 20 seconds every 2 minutes using TTL signals to control the LED. Monopolar saline-filled glass electrodes (~4 MΩ, stimulation: 0.5 ms, 50 μA) were used to evoke 5-HT release with various pulses and frequencies. The current produced by the PMT was digitized by Axopatch-200B amplifier and sampled with pClamp 10 software. Data were analyzed with AxoGraphX software. 5-HT transients were calculated as the ratio of the peak amplitude transient (ΔF) to the baseline value (F_0), defined as $\Delta F/F_0$.

Surgical procedures for *in vivo* mouse experiments

General

At the beginning of surgery mice were anesthetized with 5% isoflurane for induction and later 1% isoflurane was used for maintenance. After induction of anesthesia, ketoprofen (5 mg/kg) and buprenorphine SR (1 mg/kg) were subcutaneously injected. The mouse was mounted on a stereotaxic frame. During surgery, body temperature was maintained with a heating pad. Before a sterile scalpel was used to make an incision, the hair covering the skin above the skull was removed, and the skin was subsequently sterilized with chlorhexidine. To have consistent horizontal alignment of the skull, bregma and lambda were leveled to be on the same z axis while two points on the surface of the skull 2.5 mm to either side of lambda were used to level the skull with regard to the y axis. Following viral injection, optical fiber and EEG/EMG implantation, bupivacaine (up to 1 mg/kg) was applied

subcutaneously for local analgesia before the wound was closed. Tissue adhesive was applied to the closed wound. For the duration of the post-operative care period, mice were provided with ibuprofen (30 mg/kg) in the drinking water.

Viral injection

To inject virus and implant optical fibers for optogenetic and fiber photometry experiments, craniotomy holes were made over the mPFC (anterior-posterior (AP) axis: 1.3 mm; medio-lateral (ML) axis: 0.4 mm) and BLA (AP: -1.42 mm; ML: 3.0 mm). Virus was injected using a blunt 35 (mPFC) or 33-gauge (BLA) microinjection needle within a 10 μL microsyringe. The injection needle was lowered into the mPFC (dorsoventral (DV): -2.3 mm) or BLA (DV: -5.6 mm) and 0.5 μL of AAV was infused per site at a rate of 100 nL per min. Injection volume was controlled by a microsyringe pump, which was connected to a controller. Following injection, the virus was allowed to diffuse into the tissue for an additional 10 min before the needle was withdrawn over approximately 10 min.

Optical fiber implantation

After viral injection, optical fibers were mounted in a stereotaxic holder and inserted into tissue targeting the mPFC (AP: 1.3 mm; ML: 0.4 mm; DV: -1.8 mm; MFC_400/430-0.48_3mm_ZF1.25_FLT) or the BLA (AP: -1.42 mm; ML: -3.0 mm; DV: -5.1 mm; MFC_400/430-0.48_7mm_ZF1.25_FLT), or the DRN (with 20 degrees angle AP: -4.3 mm; ML: 1.1 mm; DV: -2.85 mm; MFC_400/430-0.57_5mm_ZF2.5(G)_FLT). First, a layer of adhesive cement was applied to the surface of the skull around the optical fiber followed by a layer of dental cement to secure the optical fiber.

EEG and EMG implantation

A drill bit was used to make three craniotomy holes (for reference and ground: AP: -3.2 mm; ML: -2.8 mm; for first EEG channel: AP: 1.7 mm; ML: 0.8 mm; for second EEG channel: AP: -1.3 mm; ML: 1.3 mm) into which 0.10” electrodes with wire lead were inserted. Similar to optical fiber implantation, electrodes were covered with adhesive cement to secure them to the skull. Lead wires from the screw electrodes were connected to an EEG/EMG headmount (8201, Pinnacle Technology Inc.). To improve electrical conduction, silver epoxy was spread over the connections between lead

wires and headmount. EMG wires from the headmount were inserted into the trapezius muscles. Finally, dental cement was used to cover all wires and their connections to the headmount.

Histology

Perfusion

Animals were euthanized with 100 mg/kg euthasol i.p. injection followed by trans-cardial perfusion with ice-cold 1x phosphate buffered saline (PBS) and subsequent perfusion with ice-cold 4% paraformaldehyde (PFA) in 1x PBS. After extraction of mouse brains, samples were post-fixed in 4% PFA at 4°C overnight on a shaker. Mouse brains were cryo-protected by immersion in 30% sucrose in 1x PBS solution for >2 days, before samples are embedded in O.C.T. Compound and frozen in dry ice for >1 h. Samples were then transferred to a -80°C freezer for long-term storage or directly sliced into 50 μm sections on a cryostat (Leica Biosystems).

Immunohistochemistry

Before staining, brain sections were washed 1-3 times with 1x PBS to remove O.C.T. Compound. Afterwards, slices were incubated overnight at 4°C on a shaker in a 1x PBS solution containing 0.1% Triton X-100, 10% normal goat serum (NGS) or normal donkey serum (NDS) and primary antibody chicken polyclonal anti-GFP (1:500). This was followed by a washing step in which slices were washed 3-4 times for 10-15 min each in 1x PBS. Brain slices were then incubated at 4°C overnight or RT for 2 h on a shaker in a 1x PBS solution containing 0.1% Triton X-100, 10% NGS/DGS and secondary antibody goat anti-chicken IgY H&L Alexa Fluor 488 (1:500), again followed by washing with 1x PBS. To image the slices, they were mounted on glass microscope slides. DAPI-containing mounting media and slices were covered with a glass. Images were taken on a Zeiss LSM 880 confocal microscope. Regions where fibers were misplaced of expression of iSeroSnFR or GFP was insufficient were excluded from other analysis.

Fiber photometry

Fiber photometry in mPFC, BLA and DRN was performed as in a previous study (Cho et al., 2017). A 490 nm LED operated at 211 Hz and a 405 nm LED operated at 531 Hz were used for iSeroSnFR excitation or for an isosbestic wavelength, respectively. The two LEDs were controlled by a custom-written software (provided by Drs. Karl Deisseroth and Tom Davidson at Stanford University) and

processor. Two filters were used to clean the excitation lights in the LEDs. Dichroic mirrors guided the light into a patch cord connected to an implanted optical fiber using a ferrule. The excitation wavelength light power at the end of the patch cord was measured with a power meter and set to 70 µW. iSeroSnFR emission signals were passed back through the patch cord, dichroic mirror, an emission filter and then a focusing lens until it reached the femtowatt photoreceiver. Signals from the photoreceiver were sent to an RX8-2 processor using a BNC cable and split into two signals corresponding to each LED excitation wavelength based on modulation frequency. These signals were then digitized at a 382 Hz sampling rate followed by low-pass filtering with a 15 Hz threshold. To synchronize iSeroSnFR fluorescence with EEG/EMG recordings, TTL pulses from a TTL pulse generator were fed into an additional digital input channel using a BNC cable.

For multisite fiber photometry experiments (OFC-BNST-BLA), mice were habituated to patch cord tethering for 2 days prior to the start of behavior. For photometry recordings, 470 nm light was delivered at 100-120 µW and iSeroSnFR signals were recorded for the duration of the fear conditioning protocol using a Neurophotometrics (San Diego, CA) system. Background fluorescence measurements were taken by briefly turning off LEDs while mice were tethered, but prior to the start of behavioral testing. Signals were analyzed using a custom MATLAB script. Briefly, background fluorescence was subtracted for each ROI, and the recorded traces were low-pass filtered at 2Hz. Traces were then fit to a biexponential curve, and the fit was subtracted from the signal to correct for baseline drift. The first two minutes of baseline recordings were discarded to improve curve fitting. ΔF/F% was calculated as (100*(470 signal - fitted signal) / fitted signal). Traces were then z-scored.

Polysomnographic recordings

For fiber photometry experiments with concurrent polysomnographic recordings, mice were singly housed in clear Plexiglas cylindrical tubes (diameter = 15”, height = 20”) with *ad libitum* food and water. Prior to the start of experiments, mice were habituated to the experimental setup for > 2 days. Animals were connected to a customized pre-amplifier (10x gain, 0.5 Hz high-pass filter, 10 Hz high-pass filter for EMG) attached to a commutator to allow unrestricted movement. EEG/EMG signals were digitized using the OmniPlex System with a sampling rate of 1 kHz. Plexon’s proprietary file format (pl2) was converted to European data format (.edf) with MATLAB using the EEGLAB plug-in.

Sleep/wake analysis

Sleep-wake classification based on EEG/EMG signals was conducted using the SleepSign analysis software. Wake states were defined by desynchronized EEG and high EMG activity, NREM sleep by synchronized EEG with high power at < 4 Hz and low EMG activity, and REM sleep by desynchronized EEG with high power at theta frequencies (6-9 Hz) and very low EMG tone. Non-overlapping 5 s windows of EEG/EMG signals were assigned a behavioral state. Delta power, theta ratio and EMG integral were the parameters used for automatic scoring with arbitrarily chosen thresholds. Afterwards, classification was manually corrected by an experimenter (M.A.) who was blind to expressed transgene.

Fear conditioning

Behavioral experiments were performed in an operant chamber located within a sound-attenuating box (Lafayette Instruments (mPFC/BLA), or Med Associates (DRN)). Tone (± light), and electric shock were programmed in and controlled by ABET II software (Lafayette Instruments, mPFC/BLA), or Video Freeze Software (Med Associates Inc., DRN). Each experiment consisted of 15 individual trials. A single trial consisted of a 10 s long cue and a 1 s break followed by a 1 s electric footshock of 0.6 mA (mPFC/BLA) or a 27 s long cue and a 1.5 s shock (0.6 mA). The intervals between single trials were randomly chosen from a uniform distribution between 45 and 75 s (mPFC/BLA) or set to 2 mins (DRN). The cue included a house-light (mPFC/BLA) and 70 dB 5 kHz tone (all). Fear conditioning was performed after sleep experiments.

Running wheels

In running wheel experiments, C57Bl/6J mice were singly housed starting one week after surgery, and were given continuous access to a functional or locked running wheel (Med Associates, St. Albans, VT) in the home cage. Wheel revolutions were counted wirelessly for the duration of the experiment. Behavioral testing began following 6 weeks of wheel running.

Free Social Interaction

Test mice were placed into an empty novel cage and allowed to freely explore. After a 2 min baseline period, a sex and age-matched social target (C57) was placed into the cage for a total test time of 12 min.

Oscillating Stimulus Transporter Assay

OSTA was performed as previously described (Keller and Looger, 2016). Briefly, HEK293 cells were cultured in DMEM, 10% FBS, 1% Penicillin/Streptomycin, and 1% L-glutamine and transfected using FuGENE (Promega) with plasmids encoding human serotonin transporter (hSERT, Addgene 15483) and p-cyto-iSeroSnFR, which omits the transmembrane anchor to induce cytosolic localization. Cells were seeded onto 35 mm coverslip bottomed dishes (MatTek) with 10-20 mm microwells to become 60-80% confluent when measured. A gravity-fed, four-channel perfusion system delivered solutions at 2-3 mL/min, and wide-diameter solution reservoirs (2L bottles and large beakers) were used to minimize changes in height of solution surfaces and concomitant changes in perfusion rates. A short segment of Tygon tubing with an inner diameter of 1/16" was added after the perfusion manifold to reduce the flow velocity which allowed for better cell stability. This outlet was positioned within 2-3 mm from the imaging area, and a suction tube at the edge of the dish or microwell removed the solutions. Buffer changes were estimated to be > 90% in 1 s and ~ 100% in 1.5 s. For all data in Figure 6, cells were imaged on a Zeiss 800 inverted laser scanning confocal microscope with excitation at 488 and 561 nm wavelengths, and emission at 495-550 and 570-650, respectively, and using an EC Plan-Neofluar 10x/0.30 M27 objective.

For ion substitution experiments (Figures 6B and 6C), substitutions were either equiosmolar or within 20 mOsm due to addition of salts. NMDG and gluconate were used as null substitutes for cations and anions, respectively. Each raw ROI trace was normalized by overall minimum and maximum fluorescence values, then averaged to produce the trace shown.

For quantification of sodium dependence of transport (Figure 6D-6F), perfusion buffers were oscillated between influx buffer (IB: 10 μM 5-HT, 150 mM NaCl, 10 glucose, 2 $CaCl_2$, 2 $MgCl_2$, 5 MOPS pH 7.5 with TRIS base) and efflux buffer (EB: same as IB, but without 5-HT and substituting KCl for NaCl to increase efflux and allow faster oscillation) for standardized "fiducial," full-strength sodium bouts. Sulforhodamine-101 was added as a marker at 200 nM in IB, and the microscope's red fluorescence channel gain and laser power were adjusted to provide maximum dynamic range

without saturated pixels. Once steady oscillations in fluorescence were attained under fiducial conditions, “test” bouts were interleaved between the fiducial bouts, in which a gradient mixer system gradually diluted IB with decreased-sodium IB (substituted with a dye-free NMDG-Cl version of IB). The plot of red fluorescence acted as a readout of sodium concentrations, and the fiducials remained very nearly unchanged, indicating the fidelity of the perfusion and gradient systems. For presentation in Figure 6, the red fluorescence trace was normalized by subtraction of a smoothed moving-window average with window size equal to the stimulus period, then divided by a smoothed moving window maximum with window size equal to two periods (to include always one fiducial). In the green (iSeroSnFR) channel, since heights of fiducial bouts changed gradually over time for unknown reasons, individual traces were corrected, similarly to the red channel, by normalizing the entire trace to smoothed moving window minimum and maximum functions. Residual oscillations of unknown cause, observed at zero sodium concentration, were subtracted out, and resulting peak heights of the test bouts were taken as readouts of the integrated rates of transport, assuming approximate linearity. These rates were expressed as percentages of transport observed during the fiducials, which was assumed to be saturated with regard to the effects of sodium. The data were then fit by the Hill equation in GraphPad Prizm, either individually or as a group.

For pharmacological data (Figures 6G-6L), the stimulus was the same IB/EB oscillation as in the fiducials described above, but with pharmacological agents at indicated concentrations superadded to both buffers in the middle epoch of the experiment. Oscillating signals representing transporter flux were isolated from tonic changes by a applying a high-pass frequency filter in the form of a two-sided boxcar filter with window length equal to the stimulus period. To convert this signal into a purely positive-going one, a smoothed moving-window minimum function with window length of one stimulus period was first subtracted, then the result was divided by the maximum of the entire experiment. While there is also presumably information contained in the discarded tonic signal, nothing appeared remarkable offhand, and the isolated oscillating signal gave the most straightforward readout of drug effects. Raw images are available for further inspection and alternative processing.

For experiments on MDMA (Figures 6M and 6N), the baseline stimulus was simply oscillation of IB +/- 10 μM 5-HT, without using potassium for the efflux bouts as above. Although this required longer periods, it allowed more direct probing of MDMA’s ability to cause efflux. In Figure 6N, the last segment of the trace shows, for reference, decreases of intracellular 5-HT in

response to substituting potassium for sodium, which might be used as a standard for future efflux experiments. These data were processed similarly to those above, with the exception that the minimum- and maximum functions were reversed to show more directly the down-going magnitudes of 5-HT efflux.

Cocaine and MDMA were used according to Institutional Biosafety Committee and Drug Enforcement Agency protocols of Howard Hughes Medical Institute, Janelia Research Campus and National Institute of Mental Health.

Quantification and Statistical Analysis

Image analysis

Images were analyzed using Fiji (Schindelin et al., 2012). For each experiment, a region of interest (ROI) was selected manually and stored in the ROI manager. Then all images from that experiment were analyzed by calculating the average pixel intensity within the ROI for each frame. Timestamps were extracted using the LSM toolbox plugin. For each experiment, a baseline period was collected and averaged as the basal fluorescence. $\Delta F/F_0$ was calculated for each frame as (average pixel intensity – basal fluorescence)/basal fluorescence.

Fiber photometry

Fiber photometry data processing was conducted as previously reported (Cho et al., 2017). Briefly, a 4^{th} order Butterworth filter with zero-phase distortion was applied to low-pass filter (with a threshold of 2 Hz) the fluorescent signals from the 490 nm and 405 nm excitation wavelengths. The 405 nm signal was aligned to the 490 nm signal using a least-squares linear fit. $\Delta F/F_0$ values were computed as follows: (490 nm signal – fitted 405 nm signal)/(fitted 405 nm signal).

EEG spectrogram

Fiber photometry data processing was conducted as previously reported (Cho et al., 2017). In short, a Morlet wavelet time-frequency decomposition of EEG signals was performed and convolved with a complex Morlet wavelet having a Gaussian shape both in time and frequency domain around its central frequency.

Statistical methods

Student's t-test and 2-way ANOVA were performed on *in vivo* fiber photometry data as noted using Excel or Graphpad Prism. All other statistics were performed using R (R Development Core Team, 2013), including the tidyr, tidyverse, and ggplot2 packages (Wickham, 2016; Wickham et al., 2019).

Statistical modeling was performed using the data mining GUI: Rattle (Williams, 2011), which includes the randomForest package (Breiman, 2001) and the glm function.

Random forest was performed using the following call:

```
randomForest(formula = x5HT ~ .,
data = crs$dataset[, c(crs$input, crs$target)],
ntree = 500, mtry = 14, importance = TRUE, replace = FALSE,
na.action = randomForest::na.roughfix)

Type of random forest: regression
Number of trees: 500
No. of variables tried at each split: 14
Missing value imputation is active.
```

Generalized linear modeling was performed using the following call:

```
glm(formula = x5HT ~ ., family = gaussian(identity), data =
crs$dataset[,
c(crs$input, crs$target)])
```

Hill Equation fitting was performed using the drc package (Ritz et al., 2015)**, with the following code:**

```
library(tidyr)
library(drc)
library(ggplot2)

#copy data to clipboard, concentrations are rows, trials are columns
read.excel <- function(header=TRUE, ...){read.table("clipboard",
sep="\t", header = header, ...)}
rawdata=read.excel()

#Tidy data
colnames(rawdata)[1]<- "concs"
longdata <- gather(rawdata, Trial, dFFs, -concs)

#Fit the Hill equation
```

```
mycurve <- drm(longdata$dFFs ~ longdata$concs, fct = LL.4())

#Calculate 95% confidence intervals
minconc <- min(longdata$concs, na.rm=TRUE)
maxconc <- max(longdata$concs, na.rm=TRUE)
newdata        <-        expand.grid(concs=exp(seq(log(minconc/2),
log(maxconc*2), length=maxconc*2)))
pm <- predict(mycurve, newdata = newdata, interval = "confidence")
newdata$p <- pm[,1]
newdata$pmin <- pm[,2]
newdata$pmax <- pm[,3]

#b = (-)Hill coefficient, c = min offset, d = max, e = Kd/EC50
summary(mycurve)

#for saving and opening in illustrator, use eps, max path = 30,000
points
ggplot(longdata, aes(x=concs, y=dFFs)) + geom_point(color="blue")
+
     geom_line(data=newdata, aes(x=concs, y=p), color="blue") +
     scale_x_log10() +
     xlab("[5HT] (uM)") + ylab("dF/F") +
     geom_line(data=newdata, aes(x=concs, y=pmin)) +
     geom_line(data=newdata, aes(x=concs, y=pmax)) +
     ggtitle("Dose Response Curve")

ggsave(plot                        =                        last_plot(),
file="C:\\Users\\EKUnger\\Desktop\\5HTcurves.eps",  width  =  14,
height = 8)
```

Fisher's Exact Test was performed using the fisher.test package with the following code:

```
fisher.test(rbind(c(x1,x2, ...),c(y1,y2, ...)));
```

Wilcoxon rank-sum test was performed using the wilcox.test package with the following code:

```
wilcox.test(ssmmuts ~ glmmuts, data = mydata)
```

ROC and d' analysis was performed using the following code:

```
library(tidyverse)
library(pROC)
library(psycho)
```

```
read.excel <- function(header=TRUE, ...){read.table("clipboard",
sep="\t", header = header, ...)}
rawdata=read.excel() #read in data: cols = trials/ROIs, rows =
timepoints

longdata <- gather(rawdata, ROI, dFFs, -Baseline.Signal) #tidy data
dffs <- longdata$dFFs
signoise <- longdata$Baseline.Signal #Baseline.Signal = classifier
column, 0 = baseline, 1 = signal

plot(x=dffs, y=signoise) #frequency distribution
glm.fit=glm(signoise ~ dffs, family = binomial) #establish
classifier
lines(dffs, glm.fit$fitted.values) #check classifier fidelity

par(pty = "s") #plot constrained to square
roc(signoise, glm.fit$fitted.values,
    plot=TRUE,
    legacy.axes=TRUE,
    xlab="False Positive Rate",
    ylab="True Positive Rate",
    print.auc=TRUE) #ROC plot
roc.info <- roc(signoise, glm.fit$fitted.values, legacy.axes=TRUE)
roc.df <- data.frame(
    truepos = roc.info$sensitivities*100,
    falsepos = (1-roc.info$specificities)*100,
    misses = (1-roc.info$sensitivities)*100,
    correj = roc.info$specificities*100,
    thresholds = roc.info$thresholds) #data for d' analysis

indices <- psycho::dprime(
    n_hit = roc.df$truepos,
    n_fa = roc.df$falsepos,
    n_miss = roc.df$misses,
    n_cr = roc.df$correj)
plot(x=roc.df$thresholds, y=indices[[1]], xlab = "Threshold", ylab
= "d' score")

par(pty = "m") #plot fills space by default
```

Double exponential fits were estimated using the nls function with the following code:

```
library(ggplot2)
library(tidyverse)
```

```
read.excel <- function(header=TRUE, ...){read.table("clipboard",
sep="\t", header = header, ...)}
rawdata=read.excel()
colnames(rawdata)[1]<- "timesec"
longdata2 <- slice(rawdata, 1:8000) %>% gather(Trial,dFFs, -
timesec)
longdata3 <- slice(rawdata, 1:51) %>% gather(Trial,dFFs, -timesec)

#Double exponential equation
#m1 + m2*(1 - exp(-m3*x)) + m4*(1 - exp(-m5*x))
# Where m1 is Y-intercept
# Where m2 is ΔF1 and m3 is k1 (Slow phase)
# Where m4 is ΔF2 and m5 is k2 (fast phase)

doublexp <- function(x,m1,m2,m3,m4,m5) m1 + m2*(1-exp(-m3*x)) +
m4*(1-exp(-m5*x))
nlsfit <- nls(longdata2$dFFs ~ doublexp(x = longdata2$timesec,
m1,m2,m3,m4,m5),
     data = longdata2, start = list(m1=1.8, m2=1.2, m3=0.05, m4=.1,
m5=2000),
     nls.control(maxiter = 500, minFactor = .000001),
     lower = c(0,0,0,0,0), algorithm = "port", trace = TRUE)
summary(nlsfit))

m1=coef(nlsfit)[[1]]
m2=coef(nlsfit)[[2]]
m3=coef(nlsfit)[[3]]
m4=coef(nlsfit)[[4]]
m5=coef(nlsfit)[[5]]

ggplot(longdata3, aes(x=timesec, y=dFFs)) +
  geom_point(size = 0.1, alpha = 0.05) +
  theme_light(base_size = 16) +
  ylab("AU") + xlab("Time (s)") +
  stat_function(geom = "path", fun = function(x)
     (m1 + m2*(1 - exp(-m3*x)) + m4*(1 - exp(-m5*x))))
```

3.12 References

Abdalla, A., Atcherley, C.W., Pathirathna, P., Samaranayake, S., Qiang, B., Peña, E., Morgan, S.L., Heien, M.L., and Hashemi, P. (2017). In vivo ambient serotonin measurements at carbon-fiber microelectrodes. Anal. Chem. *89*, 9703–9711.

Baker, D. (2019). What has de novo protein design taught us about protein folding and biophysics? Protein Sci. *28*, 678–683.

Bang, S.J., Jensen, P., Dymecki, S.M., and Commons, K.G. (2012). Projections and interconnections of genetically defined serotonin neurons in mice. Eur. J. Neurosci. *35*, 85–96.

Bauer, E.P. (2015). Serotonin in fear conditioning processes. Behav. Brain Res. *277*, 68–77.

Bedbrook, C.N., Yang, K.K., Robinson, J.E., Gradinaru, V., and Arnold, F.H. (2019). Machine learning-guided channelrhodopsin engineering enables minimally-invasive optogenetics. bioRxiv. https://doi.org/10.1101/565606.

Belmaker, R.H., and Agam, G. (2008). Major depressive disorder. N. Engl. J. Med. *358*, 55–68.

Belmer, A., Klenowski, P.M., Patkar, O.L., and Bartlett, S.E. (2017). Mapping the connectivity of serotonin transporter immunoreactive axons to excitatory and inhibitory neurochemical synapses in the mouse limbic brain. Brain Struct. Funct. *222*, 1297–1314.

Bender, B.J., Cisneros, A., Duran, A.M., Finn, J.A., Fu, D., Lokits, A.D., Mueller, B.K., Sangha, A.K., Sauer, M.F., Sevy, A.M., et al. (2016). Protocols for molecular modeling with Rosetta3 and RosettaScripts. Biochemistry *55*, 4748–4763.

Berger, M., Gray, J.A., and Roth, B.L. (2009). The expanded biology of serotonin. Annu. Rev. Med. *60*, 355–366.

Bermingham, D.P., and Blakely, R.D. (2016). Kinase-dependent regulation of monoamine neurotransmitter transporters. Pharmacol. Rev. *68*, 888–953.

Bessette, P.H., Mena, M.A., Nguyen, A.W., and Daugherty, P.S. (2003). Construction of designed protein libraries using gene assembly mutagenesis. Methods Mol. Biol. *231*, 29–37.

Biswas, S., Kuznetsov, G., Ogden, P.J., Conway, N.J., Adams, R.P., and Church, G.M. (2018). Toward machine-guided design of proteins. bioRxiv. https://doi.org/10.1101/337154.

Bocchio, M., McHugh, S.B., Bannerman, D.M., Sharp, T., and Capogna, M. (2016). Serotonin, amygdala and fear: Assembling the puzzle. Front. Neural Circuits *10*, 24.

Borden, P.M., Zhang, P., Shivange, A.V., Marvin, J.S., Cichon, J., Dan, C., Podgorski, K., Figueiredo, A., Novak, O., Tanimoto, M., et al. (2020). A fast genetically encoded fluorescent sensor for faithful in vivo acetylcholine detection in mice, fish, worms and flies. bioRxiv. https://doi.org/10.1101/2020.02.07.939504.

Bos, N., Dreier, S., Jørgensen, C.G., Nielsen, J., Guerrieri, F.J., and d'Ettorre, P. (2012). Learning and perceptual similarity among cuticular hydrocarbons in ants. J. Insect Physiol. *58*, 138–146.

Breiman, L. (2001). Breiman and Cutler's random forests for classification and regression. Mach. Learn. *45*, 5–32.

Broussard, G.J., Liang, R., and Tian, L. (2014). Monitoring activity in neural circuits with genetically encoded indicators. Front. Mol. Neurosci. *7*, 97.

Broussard, G.J., Unger, E.K., Liang, R., McGrew, B.P., and Tian, L. (2018). Imaging glutamate with genetically encoded fluorescent sensors. In biochemical approaches for glutamatergic neurotransmission, S. Parrot and L. Denoroy, eds. (Springer New York), pp. 117–153.

Bryksin, A.V., and Matsumura, I. (2010). Overlap extension PCR cloning: A simple and reliable way to create recombinant plasmids. Biotechniques *48*, 463–465.

Bunin, M.A., and Wightman, R.M. (1998). Quantitative evaluation of 5-hydroxytryptamine (serotonin) neuronal release and uptake: An investigation of extrasynaptic transmission. J. Neurosci. *18*, 4854–4860.

Bunin, M.A., Prioleau, C., Mailman, R.B., and Wightman, R.M. (1998). Release and uptake rates of 5-hydroxytryptamine in the dorsal raphe and substantia nigra reticulata of the rat brain. J. Neurochem. *70*, 1077–1087.

Burghardt, N.S., Bush, D.E.A., McEwen, B.S., and LeDoux, J.E. (2007). Acute selective serotonin reuptake inhibitors increase conditioned fear expression: Blockade with a 5-HT(2C) receptor antagonist. Biol. Psychiatry *62*, 1111–1118.

Calhoon, G.G., and Tye, K.M. (2015). Resolving the neural circuits of anxiety. Nat. Neurosci. *18*, 1394–1404.

Charnay, Y., and Leger, L. (2010). Brain serotonergic circuitries. Dialogues Clin. Neurosci. *12*, 471–487.

Chen, V.B., Arendall, W.B., Headd, J.J., Keedy, D.A., Immormino, R.M., Kapral, G.J., Murray, L.W., Richardson, J.S., and Richardson, D.C. (2010). MolProbity: All-atom structure validation for macromolecular crystallography. Acta. Crystallogr. D Biol. Crystallogr. *66*, 12–21.

Cho, J.R., Treweek, J.B., Robinson, J.E., Xiao, C., Bremner, L.R., Greenbaum, A., and Gradinaru, V. (2017). Dorsal raphe dopamine neurons modulate arousal and promote wakefulness by salient stimuli. Neuron *94*, 1205-1219.

Cipriani, A., Furukawa, T.A., Salanti, G., Chaimani, A., Atkinson, L.Z., Ogawa, Y., Leucht, S., Ruhe, H.G., Turner, E.H., Higgins, J.P.T., et al. (2018). Comparative efficacy and acceptability of

21 antidepressant drugs for the acute treatment of adults with major depressive disorder: A systematic review and network meta-analysis. Lancet *391*, 1357–1366.

Clarke, R.J. and Khalid, M.A.A. (2015). Pumps, channels and transporters: Methods of functional analysis (John Wiley & Sons).

Cobb, R.E., Chao, R., and Zhao, H. (2013). Directed evolution: Past, present and future. AIChE J. *59*, 1432–1440.

Corre, J., van Zessen, R., and Pascoli, V. (2018). Dopamine neurons projecting to medial shell of the nucleus accumbens drive heroin reinforcement. eLife 7, e39945.

Correia, P.A., Lottem, E., Banerjee, D., Machado, A.S., Carey, M.R., and Mainen, Z.F. (2017). Transient inhibition and long-term facilitation of locomotion by phasic optogenetic activation of serotonin neurons. eLife *6*, e20975.

Curzon, P., Rustay, N.R., and Browman, K.E. (2009). Cued and contextual fear conditioning for rodents. In methods of behavior analysis in neuroscience, J.J. Buccafusco, ed. (CRC Press/Taylor & Francis).

Davis, I.W., and Baker, D. (2009). RosettaLigand docking with full ligand and receptor flexibility. J. Mol. Biol. *385*, 381–392.

Dehghani, M., Gouws, S., Vinyals, O., Uszkoreit, J., and Kaiser, L. (2019). Universal transformers (ICLR).

Dobson, A.J., Barnett, A.G., and Barnett, A.G. (2008). An introduction to generalized linear models (Chapman and Hall/CRC).

Ehren, J., Govindarajan, S., Morón, B., Minshull, J., and Khosla, C. (2008). Protein engineering of improved prolyl endopeptidases for celiac sprue therapy. Protein Eng. Des. Sel. *21*, 699–707.

Emsley, P., and Cowtan, K. (2004). Coot: Model-building tools for molecular graphics. Acta Crystallogr. D Biol. Crystallogr. *60*, 2126–2132.

Evans, P.R., and Murshudov, G.N. (2013). How good are my data and what is the resolution? Acta Crystallogr. D Biol. Crystallogr. *69*, 1204–1214.

Feng, J., Zhang, C., Lischinsky, J.E., Jing, M., Zhou, J., Wang, H., Zhang, Y., Dong, A., Wu, Z., Wu, H., et al. (2019). A genetically encoded fluorescent sensor for rapid and specific in vivo detection of norepinephrine. Neuron *102*, 745-761.

Ferrés-Coy, A., Pilar-Cuellar, F., Vidal, R., Paz, V., Masana, M., Cortés, R., Carmona, M.C., Campa, L., Pazos, A., Montefeltro, A., et al. (2013). RNAi-mediated serotonin transporter suppression rapidly increases serotonergic neurotransmission and hippocampal neurogenesis. Transl. Psychiatry *3*, e211.

Forster, G.L., Feng, N., Watt, M.J., Korzan, W.J., Mouw, N.J., Summers, C.H., and Renner, K.J. (2006). Corticotropin-releasing factor in the dorsal raphe elicits temporally distinct serotonergic responses in the limbic system in relation to fear behavior. Neuroscience *141*, 1047–1055.

Fujino, K., Yoshitake, T., Inoue, O., Ibii, N., Kehr, J., Ishida, J., Nohta, H., and Yamaguchi, M. (2002). Increased serotonin release in mice frontal cortex and hippocampus induced by acute physiological stressors. Neurosci. Lett. *320*, 91–95.

Garcia-Garcia, A.L., Canetta, S., Stujenske, J.M., Burghardt, N.S., Ansorge, M.S., Dranovsky, A., and Leonardo, E.D. (2018). Serotonin inputs to the dorsal BNST modulate anxiety in a 5-HT 1A receptor-dependent manner. Mol. Psychiatry *23*, 1990–1997.

Gibson, D.G., Young, L., Chuang, R.-Y., Venter, J.C., Hutchison, C.A., and Smith, H.O. (2009). Enzymatic assembly of DNA molecules up to several hundred kilobases. Nat. Methods *6*, 343–345.

Gong, S., Zheng, C., Doughty, M.L., Losos, K., Didkovsky, N., Schambra, U.B., Nowak, N.J., Joyner, A., Leblanc, G., Hatten, M.E., et al. (2003). A gene expression atlas of the central nervous system based on bacterial artificial chromosomes. Nature *425*, 917-925.

Greenwood, B.N., Foley, T.E., Day, H.E.W., Burhans, D., Brooks, L., Campeau, S., and Fleshner, M. (2005). Wheel running alters serotonin (5-HT) transporter, 5-HT1A, 5-HT1B, and alpha 1b-adrenergic receptor mRNA in the rat raphe nuclei. Biol. Psychiatry *57*, 559–568.

Hashimoto, S., Inoue, T., and Koyama, T. (1999). Effects of conditioned fear stress on serotonin neurotransmission and freezing behavior in rats. Eur. J. Pharmacol. *378*, 23–30.

Hawkins, P.C.D., Skillman, A.G., Warren, G.L., Ellingson, B.A., and Stahl, M.T. (2010). Conformer generation with OMEGA: Algorithm and validation using high quality structures from the protein databank and cambridge structural database. J. Chem. Inf. Model. *50*, 572–584.

Heinrich, T., Böttcher, H., Gericke, R., Bartoszyk, G.D., Anzali, S., Seyfried, C.A., Greiner, H.E., and van Amsterdam, C. (2004). Synthesis and structure−activity relationship in a class of indolebutylpiperazines as dual 5-HT(1A) receptor agonists and serotonin reuptake inhibitors. J. Med. Chem. *47*, 4684–4692.

Helassa, N., Dürst, C.D., Coates, C., Kerruth, S., Arif, U., Schulze, C., Wiegert, J.S., Geeves, M., Oertner, T.G., and Török, K. (2018). Ultrafast glutamate sensors resolve high-frequency release at Schaffer collateral synapses. Proc. Natl. Acad. Sci. USA *115*, 5594–5599.

Huang, R., Fang, P., and Kay, B.K. (2012). Improvements to the Kunkel mutagenesis protocol for constructing primary and secondary phage-display libraries. Methods *58*, 10–17.

Jaquins-Gerstl, A., and Michael, A.C. (2015). A review of the effects of FSCV and microdialysis measurements on dopamine release in the surrounding tissue. Analyst (Lond.) *140*, 3696–3708.

Jarrett, M.E., Kohen, R., Cain, K.C., Burr, R.L., Poppe, A., Navaja, G.P., and Heitkemper, M.M. (2007). Relationship of SERT polymorphisms to depressive and anxiety symptoms in irritable bowel syndrome. Biol. Res. Nurs. *9*, 161–169.

Jing, M., Zhang, Y., Wang, H., and Li, Y. (2019). G-protein-coupled receptor-based sensors for imaging neurochemicals with high sensitivity and specificity. J. Neurochem. *151*, 279–288.

Jing, M., Li, Y., Zeng, J., Huang, P., Skirzewski, M., Kljakic, O., Peng, W., Qian, T., Tan, K., Zou, J., et al. (2020). An optimized acetylcholine sensor for monitoring in vivo cholinergic activity. Nat. Methods *17*, 1139-1146.

Jones, K.A., Porterfield, W.B., Rathbun, C.M., McCutcheon, D.C., Paley, M.A., and Prescher, J.A. (2017). Orthogonal luciferase-luciferin pairs for bioluminescence imaging. J. Am. Chem. Soc. *139*, 2351–2358.

Kabsch, W. (2010). XDS. Acta Crystallogr. D Biol. Crystallogr. *66*, 125–132.

Kato, R., Nakano, H., Konishi, H., Kato, K., Koga, Y., Yamane, T., Kobayashi, T., and Honda, H. (2005). Novel strategy for protein exploration: High-throughput screening assisted with fuzzy neural network. J. Mol. Biol. *351*, 683–692.

Kawahara, H., Yoshida, M., Yokoo, H., Nishi, M., and Tanaka, M. (1993). Psychological stress increases serotonin release in the rat amygdala and prefrontal cortex assessed by in vivo microdialysis. Neurosci. Lett. *162*, 81–84.

Keller, J.P., and Looger, L.L. (2016). The oscillating stimulus transporter assay, OSTA: Quantitative functional imaging of transporter protein activity in time and frequency domains. Mol. Cell *64*, 199–212.

Keller, J.P., Marvin, J.S., Lacin, H., Lemon, W.C., Shea, J., Kim, S., Lee, R.T., Koyama, M., Keller, P.J., and Looger, L.L. (2019). In vivo glucose imaging in multiple model organisms with an engineered single-wavelength sensor. bioRxiv. https://doi.org/10.1101/571422.

Khoury, G.A., Smadbeck, J., Kieslich, C.A., and Floudas, C.A. (2014). Protein folding and de novo protein design for biotechnological applications. Trends Biotechnol. *32*, 99–109.

Kiser, D., Steemers, B., Branchi, I., and Homberg, J.R. (2012). The reciprocal interaction between serotonin and social behaviour. Neurosci. Biobehav. Rev. *36*, 786-798.

Koldsø, H., Noer, P., Grouleff, J., Autzen, H.E., Sinning, S., and Schiøtt, B. (2011). Unbiased simulations reveal the inward-facing conformation of the human serotonin transporter and Na(+) ion release. PLoS Comput. Biol. *7*, e1002246.

Kunkel, T.A. (1985). Rapid and efficient site-specific mutagenesis without phenotypic selection. Proc. Natl. Acad. Sci. U.S.A. *82*, 488–492.

Li, Y., Zhong, W., Wang, D., Feng, Q., Liu, Z., Zhou, J., Jia, C., Hu, F., Zeng, J., Guo, Q., et al. (2016). Serotonin neurons in the dorsal raphe nucleus encode reward signals. Nat. Commun. *7*, 10503.

Liao, J., Warmuth, M.K., Govindarajan, S., Ness, J.E., Wang, R.P., Gustafsson, C., and Minshull, J. (2007). Engineering proteinase K using machine learning and synthetic genes. BMC Biotechnol. *7*, 16.

Liaw, A., and Wiener, M. (2002). Classification and regression by randomForest. https://rdrr.io/cran/randomForest/.

Lin, M.Z., and Schnitzer, M.J. (2016). Genetically encoded indicators of neuronal activity. Nat. Neurosci. *19*, 1142–1153.

Lobas, M.A., Tao, R., Nagai, J., Kronschläger, M.T., Borden, P.M., Marvin, J.S., Looger, L.L., and Khakh, B.S. (2019). A genetically encoded single-wavelength sensor for imaging cytosolic and cell surface ATP. Nat. Commun. *10*, 711.

Looger, L.L., and Griesbeck, O. (2012). Genetically encoded neural activity indicators. Curr. Opin. Neurobiol. *22*, 18–23.

Madisen, L., Zwingman, T.A., Sunkin, S.M., Oh, S.W., Zariwala, H.A., Gu, H., Ng, L.L., Palmiter, R.D., Hawrylycz, M.J., Jones, A.R., et al. (2010). A robust and high-throughput Cre reporting and characterization system for the whole mouse brain. Nat. Neurosci. *13*, 133–140.

Madisen, L., Garner, A.R., Shimaoka, D., Chuong, A.S., Klapoetke, N.C., Li, L., van der Bourg, A., Niino, Y., Egolf, L., Monetti, C., et al. (2015). Transgenic mice for intersectional targeting of neural sensors and effectors with high specificity and performance. Neuron *85*, 942–958.

Marcinkiewcz, C.A., Mazzone, C.M., D'Agostino, G., Halladay, L.R., Hardaway, J.A., DiBerto, J.F., Navarro, M., Burnham, N., Cristiano, C., Dorrier, C.E., et al. (2016). Serotonin engages an anxiety and fear-promoting circuit in the extended amygdala. Nature *537*, 97–101.

Margoob, M.A., and Mushtaq, D. (2011). Serotonin transporter gene polymorphism and psychiatric disorders: Is there a link? Indian J. Psychiatry *53*, 289–299.

Marvin, J.S., Schreiter, E.R., Echevarría, I.M., and Looger, L.L. (2011). A genetically encoded, high-signal-to-noise maltose sensor. Proteins *79*, 3025–3036.

Marvin, J.S., Borghuis, B.G., Tian, L., Cichon, J., Harnett, M.T., Akerboom, J., Gordus, A., Renninger, S.L., Chen, T.-W., Bargmann, C.I., et al. (2013). An optimized fluorescent probe for visualizing glutamate neurotransmission. Nat. Methods *10*, 162–170.

Marvin, J.S., Scholl, B., Wilson, D.E., Podgorski, K., Kazemipour, A., Müller, J.A., Schoch, S., Quiroz, F.J.U., Rebola, N., Bao, H., et al. (2018). Stability, affinity, and chromatic variants of the glutamate sensor iGluSnFR. Nat. Methods *15*, 936–939.

Marvin, J.S., Shimoda, Y., Magloire, V., Leite, M., Kawashima, T., Jensen, T.P., Kolb, I., Knott, E.L., Novak, O., Podgorski, K., et al. (2019). A genetically encoded fluorescent sensor for in vivo imaging of GABA. Nat. Methods. *16*, 763-770.

Matsui, A., and Alvarez, V.A. (2018). Cocaine inhibition of synaptic transmission in the ventral pallidum is pathway-specific and mediated by serotonin. Cell Rep. *23*, 3852–3863.

McCoy, A.J. (2007). Solving structures of protein complexes by molecular replacement with Phaser. Acta Crystallogr. D Biol. Crystallogr. *63*, 32–41.

Miller, D.A., Suen, G., Bruce, D., Copeland, A., Cheng, J.-F., Detter, C., Goodwin, L.A., Han, C.S., Hauser, L.J., Land, M.L., et al. (2011). Complete genome sequence of the cellulose-degrading bacterium Cellulosilyticum lentocellum. J. Bacteriol. *193*, 2357–2358.

Mizuno, G.O., Unger, E.K., and Tian, L. (2019). Real-time monitoring of neuromodulators in behaving animals using genetically-encoded indicators. In compendium on in vivo monitoring in real-time molecular neuroscience, G.S. Wilson and A.C. Michael, eds. (World Scientific), pp. 1-18.

Nov, Y. (2012). When second best is good enough: Another probabilistic look at saturation mutagenesis. Appl Environ. Microbiol. *78*, 258–262.

Ohmura, Y., Tanaka, K.F., Tsunematsu, T., Yamanaka, A., and Yoshioka, M. (2014). Optogenetic activation of serotonergic neurons enhances anxiety-like behaviour in mice. Int. J. Neuropsychopharmacol. *17*, 1777–1783.

Ollikainen, N., de Jong, R.M., and Kortemme, T. (2015). Coupling protein side-chain and backbone flexibility improves the re-design of protein-ligand specificity. PLoS Comput. Biol. *11*, e1004335.

Ozaki, N., Goldman, D., Kaye, W.H., Plotnicov, K., Greenberg, B.D., Lappalainen, J., Rudnick, G., and Murphy, D.L. (2003). Serotonin transporter missense mutation associated with a complex neuropsychiatric phenotype. Mol. Psychiatry *8*, 933–936.

Packer, M.S., and Liu, D.R. (2015). Methods for the directed evolution of proteins. Nat. Rev. Genet. *16*, 379–394.

Patriarchi, T., Cho, J.R., Merten, K., Howe, M.W., Marley, A., Xiong, W.-H., Folk, R.W., Broussard, G.J., Liang, R., Jang, M.J., et al. (2018). Ultrafast neuronal imaging of dopamine dynamics with designed genetically encoded sensors. Science *360*, eaat4422.

Peñalva, R.G., Lancel, M., Flachskamm, C., Reul, J.M.H.M., Holsboer, F., and Linthorst, A.C.E. (2003). Effect of sleep and sleep deprivation on serotonergic neurotransmission in the hippocampus: A combined in vivo microdialysis/EEG study in rats. Eur. J. Neurosci. *17*, 1896–1906.

Portas, C.M., Bjorvatn, B., and Ursin, R. (2000). Serotonin and the sleep/wake cycle: Special emphasis on microdialysis studies. Prog. Neurobiol. *60*, 13–35.

Quan, J., and Tian, J. (2011). Circular polymerase extension cloning for high-throughput cloning of complex and combinatorial DNA libraries. Nat. Protoc. *6*, 242–251.

Rathbun, C.M., Porterfield, W.B., Jones, K.A., Sagoe, M.J., Reyes, M.R., Hua, C.T., and Prescher, J.A. (2017). Parallel screening for rapid identification of orthogonal bioluminescent tools. ACS Cent. Sci. *3*, 1254–1261.

Ren, J., Friedmann, D., Xiong, J., Liu, C.D., Ferguson, B.R., Weerakkody, T., DeLoach, K.E., Ran, C., Pun, A., Sun, Y., et al. (2018). Anatomically defined and functionally distinct dorsal raphe serotonin sub-systems. Cell *175*, 472-487.

Richter, F., Leaver-Fay, A., Khare, S.D., Bjelic, S., and Baker, D. (2011). De novo enzyme design using Rosetta3. PLoS ONE *6*, e19230.

Ritz, C., Baty, F., Streibig, J.C., and Gerhard, D. (2015). Dose-response analysis using R. PLoS ONE *10*, e0146021.

Rouillard, J.-M., Lee, W., Truan, G., Gao, X., Zhou, X., and Gulari, E. (2004). Gene2Oligo: Oligonucleotide design for in vitro gene synthesis. Nucleic Acids Res. *32*, W176-180.

Rudnick, G., and Sandtner, W. (2019). Serotonin transport in the 21st century. J. Gen. Physiol. *151*, 1248–1264.

Rudnick, G., and Wall, S.C. (1992). p-Chloroamphetamine induces serotonin release through serotonin transporters. Biochemistry *31*, 6710–6718.

Rueter, L.E., and Jacobs, B.L. (1996). A microdialysis examination of serotonin release in the rat forebrain induced by behavioral/environmental manipulations. Brain Res. *739*, 57–69.

Saito, T., and Nakatsuji, N. (2001). Efficient gene transfer into the embryonic mouse brain using in vivo electroporation. Dev. Biol. *240*, 237–246.

Schindelin, J., Arganda-Carreras, I., Frise, E., Kaynig, V., Longair, M., Pietzsch, T., Preibisch, S., Rueden, C., Saalfeld, S., Schmid, B., et al. (2012). Fiji: An open-source platform for biological-image analysis. Nat. Methods *9*, 676–682.

Schultz, K.N., and Kennedy, R.T. (2008). Time-resolved microdialysis for in vivo neurochemical measurements and other applications. Annu. Rev. Anal. Chem. (Palo Alto Calif) *1*, 627–661.

Seo, C., Guru, A., Jin, M., Ito, B., Sleezer, B.J., Ho, Y.-Y., Wang, E., Boada, C., Krupa, N.A., Kullakanda, D.S., et al. (2019). Intense threat switches dorsal raphe serotonin neurons to a paradoxical operational mode. Science *363*, 538–542.

Shivange, A.V., Borden, P.M., Muthusamy, A.K., Nichols, A.L., Bera, K., Bao, H., Bishara, I., Jeon, J., Mulcahy, M.J., Cohen, B., et al. (2019). Determining the pharmacokinetics of nicotinic drugs in the endoplasmic reticulum using biosensors. J. Gen. Physiol. *151*, 738–757.

Sneddon, J.M. (1969). Sodium-dependent accumulation of 5-hydroxytryptamine by rat blood platelets. Br. J. Pharmacol. *37*, 680–688.

Studier, F.W. (2005). Protein production by auto-induction in high density shaking cultures. Protein Expr. Purif. *41*, 207–234.

Sun, F., Zeng, J., Jing, M., Zhou, J., Feng, J., Owen, S.F., Luo, Y., Li, F., Wang, H., Yamaguchi, T., et al. (2018). A genetically encoded fluorescent sensor enables rapid and specific detection of dopamine in flies, fish, and mice. Cell *174*, 481-496.

Tatsumi, M., Groshan, K., Blakely, R.D., and Richelson, E. (1997). Pharmacological profile of antidepressants and related compounds at human monoamine transporters. Eur. J. Pharmacol. *340*, 249–258.

Taylor, N.D., Garruss, A.S., Moretti, R., Chan, S., Arbing, M.A., Cascio, D., Rogers, J.K., Isaacs, F.J., Kosuri, S., Baker, D., et al. (2016). Engineering an allosteric transcription factor to respond to new ligands. Nat. Methods *13*, 177–183.

R Development Core Team (2013). R: A language and environment for statistical computing (R Foundation for Statistical Computing).

Tinberg, C.E., Khare, S.D., Dou, J., Doyle, L., Nelson, J.W., Schena, A., Jankowski, W., Kalodimos, C.G., Johnsson, K., Stoddard, B.L., et al. (2013). Computational design of ligand-binding proteins with high affinity and selectivity. Nature *501*, 212–216.

Wan, J., Peng, W., Li, X., Qian, T., Song, K., Zeng, J., Deng, F., Hao, S., Feng, J., Zhang, P., et al. (2020). A genetically encoded GRAB sensor for measuring serotonin dynamics in vivo. bioRxiv. https://doi.org/10.1101/2020.02.24.962282.

Wang, H., Goehring, A., Wang, K.H., Penmatsa, A., Ressler, R., and Gouaux, E. (2013). Structural basis for action by diverse antidepressants on biogenic amine transporters. Nature *503*, 141–145.

Wankerl, M., Miller, R., Kirschbaum, C., Hennig, J., Stalder, T., and Alexander, N. (2014). Effects of genetic and early environmental risk factors for depression on serotonin transporter expression and methylation profiles. Transl. Psychiatry *4*, e402.

Wickham, H. (2016). ggplot2: Elegant graphics for data analysis (Springer).

Wickham, H., Averick, M., Bryan, J., Chang, W., McGowan, L., François, R., Grolemund, G., Hayes, A., Henry, L., Hester, J., et al. (2019). Welcome to the Tidyverse. J. Open Source Softw. *4*, 1686.

Williams, G. (2011). Data mining with Rattle and R: The Art of excavating data for knowledge discovery (New York: Springer-Verlag).

Wu, Z., Kan, S.B.J., Lewis, R.D., Wittmann, B.J., and Arnold, F.H. (2019). Machine learning-assisted directed protein evolution with combinatorial libraries. Proc. Natl. Acad. Sci. U.S.A. *116*, 8852–8858.

Yang, K.K., Wu, Z., and Arnold, F.H. (2019a). Machine-learning-guided directed evolution for protein engineering. Nat. Methods *16*, 687-694.

Yang, K.K., Chen, Y., Lee, A., and Yue, Y. (2019b). Batched stochastic Bayesian optimization via combinatorial constraints design. arXiv, arXiv:1904.08102.

Yokoyama, M., Suzuki, E., Sato, T., Maruta, S., Watanabe, S., and Miyaoka, H. (2005). Amygdalic levels of dopamine and serotonin rise upon exposure to conditioned fear stress without elevation of glutamate. Neurosci. Lett. *379*, 37–41.

Zhang, Y.-W., Turk, B.E., and Rudnick, G. (2016). Control of serotonin transporter phosphorylation by conformational state. Proc. Natl. Acad. Sci. U.S.A. *113*, E2776-2783.

Zhou, X., Lu, J.Y.-F., Darling, R.D., Simpson, K.L., Zhu, X., Wang, F., Yu, L., Sun, X., Merzenich, M.M., and Lin, R.C.S. (2015). Behavioral training reverses global cortical network dysfunction induced by perinatal antidepressant exposure. Proc. Natl. Acad. Sci. U.S.A. *112*, 2233–2238.

Zhuang, X., Masson, J., Gingrich, J.A., Rayport, S., and Hen, R. (2005). Targeted gene expression in dopamine and serotonin neurons of the mouse brain. J. Neurosci. Methods *143*, 27–32.

Chapter 4

FUTURE RESEARCH DIRECTIONS ON THE ROLE OF SEROTONIN IN MURINE SLEEP

4.1 Changing view of serotonin's role in sleep

In the following section, findings from murine sleep experiments presented in Chapters 2 and 3 are revisited and their contribution to our understanding of the role of 5-HT in sleep will be discussed.

Activity pattern of serotonergic neurons across sleep-wake states

Earlier studies describing the activity pattern of 5-HT neurons across sleep-wake states employed electrophysiology to record the firing activity and focused on a few cells within the DRN (McGinty and Harper, 1976; Trulson and Jacobs, 1979). In these experiments, low-frequency firing (0.5-5 spikes/sec) and regular interspike intervals were used as electrophysiological markers to identify 5-HT neurons. However, subsequent studies applying immunohistochemistry to define cell types demonstrated that these electrophysiological criteria are not unique to 5-HT neurons and disregard 5-HT neurons that fire at higher frequencies (Allers and Sharp, 2003; Kirby et al., 2003; Kocsis et al., 2006). In Chapter 2, we took advantage of existing transgenic animals expressing Cre recombinase in 5-HT neurons in order to Cre-dependently express the activity reporter GCaMP6s in 5-HT neurons within the DRN. We simultaneously performed polysomnographic (EEG/EMG) and fiber photometry recordings to record the activity of large numbers of genetically-defined 5-HT neurons across sleep-wake states. Our results show that the overall activity of 5-HT neurons in the DRN is highest during wakefulness, decreases over the course of NREM sleep and is lowest during REM sleep. These observations confirm and expand upon previous reports based on *in vivo* single-unit recordings of putative 5-HT neurons and describe the genetically-defined 5-HT population activity across states and state transitions.

Serotonergic neurons in the superior raphe are necessary for normal amounts of sleep

As discussed in Chapter 1, physical ablation of the raphe as well as systemic injection of pCPA results in a reduction in sleep (Koella et al., 1968; Mouret et al., 1968; Weitzman et al., 1968).

However, these experiments were later criticized for lacking specificity (Jouvet, 1999; Ursin, 2002). Lesion experiments were confounded by off-target effects such as ablation of somas and fibers belonging to other cell types in the raphe, and pCPA also inhibits the synthesis of 5-HT in the periphery and directly affects the levels of other monoamines (Jouvet, 1999; Tagliamonte et al., 1973; Ursin, 2002). These pharmacology and lesion studies were followed by experiments conducting genetic ablation of 5-HT synthesis in the CNS. While the genetic loss-of-function approach is more specific, interpretation of the results are difficult due to severe developmental retardation and postnatal lethality in these genetically-modified animals (Alenina et al., 2009). Furthermore, emerging sleep phenotypes following the CNS-wide disruption of 5-HT signaling in these studies were complicated by the role of the medullary raphe in thermoregulation (Madden and Morrison, 2019; Tan and Knight, 2018). Indeed, animals lacking 5-HT neurons in the CNS sleep less at an ambient temperature of 23° C, but not at the thermoneutral temperature of 33 ° C suggesting that sleep phenotypes are due to shivering (Buchanan and Richerson, 2010; Murray et al., 2015). However, no attempts have been made to investigate sleep phenotypes after abolishing 5-HT signaling in the superior raphe while sparing 5-HT neurons in the caudal inferior raphe and thereby avoiding the confounding factor of thermoregulation disruption. Inhibition of 5-HT synthesis specifically in the superior raphe caused an alteration of daily locomotion activity patterns which encouraged analysis of sleep phenotypes (Whitney et al., 2016). In Chapter 2, we selectively ablated 5-HT neurons of the superior raphe in adult animals, while leaving intact the thermoregulatory populations in the medulla. Our results from polysomnographic recordings show that ablation leads to an increased amount of wakefulness at the expense of NREM and REM sleep during both the day and night. Since neither lesion nor activation of 5-HT neurons in the DRN have an effect on body temperature (Holschbach et al., 2018; Venner et al., 2020), our results clearly demonstrate that 5-HT neurons of the superior raphe are necessary for normal amounts of sleep.

Serotonergic neurons in the superior raphe play a role in sleep homeostasis

Results discussed in the last two paragraphs generate an apparent paradox: how can a sleep-promoting system be more active during wakefulness? In an effort to reconcile this paradox, Michel Jouvet proposed that 5-HT neurons are part of the sleep-homeostasis system (Jouvet, 1999). According to this hypothesis, the activity of 5-HT neurons and concomitant release of 5-HT serve to build sleep pressure by measuring the duration and intensity of waking. Work presented in Chapters

2 and 3 provide evidence for such a role in sleep homeostasis. In Chapter 2, animals lacking 5-HT neurons in the superior raphe were subjected to 6 h of sleep deprivation. When compared to control animals, animals lacking 5-HT neurons in the superior raphe displayed a significantly smaller increase in delta power during NREM sleep following sleep deprivation. An increase in delta power during NREM sleep is considered a critical feature of recovery sleep in order to make up for the lost sleep (Borbély and Neuhaus, 1979). A less pronounced increase in delta power during NREM sleep suggests that sleep deprivation in animals lacking 5-HT neurons led to a smaller increase in homeostatic sleep pressure. In Chapter 3, we recorded changes in iSeroSnFR fluorescence across sleep-wake cycles and noticed an increase in baseline fluorescence over the course of wake states, a decrease during NREM sleep and a further decline during REM sleep. This observation is in agreement with the proposed role of 5-HT to build up sleep pressure over the course of wakefulness followed by gradual decrease over subsequent sleep episodes.

Our ablation results complement the ones from 5-HT receptor and *tph* mutant experiments. *Drosophila 5HT1* mutants show reduced sleep and reduced rebound sleep following sleep deprivation, in accordance with a role for 5-HT in measuring sleep debt (Yuan et al., 2006). Flies mutant for *trh* (equivalent to *tph*) or the serotonin receptor *5HT2b* have reduced homeostatic response to sleep deprivation (Qian et al., 2017). Mice mutant for *5-HT2A* sleep less and show a smaller delta power increase compared to controls following sleep deprivation (Popa et al., 2005).

Our iSeroSnFR experiments verify microdialysis studies showing that extracellular concentration of 5-HT is highest during waking, lower during NREM, and lowest during REM (Peñalva et al., 2003; Portas et al., 2000). In addition, microdialysis experiments also demonstrated that sleep deprivation leads to increased 5-HT levels in the basal forebrain and hippocampus providing further evidence for a role of 5-HT in sleep homeostasis (Peñalva et al., 2003; Zant et al., 2011).

Serotonergic neurons have a bidirectional firing mode-dependent effect on sleep

In addition to the typical tonic (~1-6 Hz) baseline firing pattern during wakefulness (Jacobs and Azmitia, 1992; McGinty and Harper, 1976), 5-HT neurons can also fire in bursts (up to ~30 Hz) (Cohen et al., 2015; Liu et al., 2014; Schweimer and Ungless, 2010; Veasey et al., 1995). However, the effects of different firing modes on sleep-wake regulation have not been characterized yet. In Chapter 2, we demonstrated that burst optogenetic stimulation of 5-HT neurons in the DRN caused

a sudden decrease in NREM and REM sleep, and an increase in wakefulness. Similar to burst stimulation, tonic stimulation caused an inhibition of REM sleep, however, it also led to an increase in NREM sleep and a reduction in wakefulness. The induction of sleep during tonic optogenetic activation of 5-HT neurons, a stimulation pattern imitating the baseline firing activity, could be due to a transient increase in sleep pressure, in line with Jouvet's hypothesis (Jouvet, 1999).

Repeating these optogenetic experiments with transgenic animals lacking serotonin synthesis in the DRN of adult animals is an important future research direction in order to verify that 5-HT is the signaling molecule responsible for the observed sleep phenotypes. Elimination of 5-HT synthesis from the adult superior raphe has already been demonstrated by stereotaxic injection of an AAV expressing Cre recombinase into mice carrying a loxP-conditional *Tph2* allele (Whitney et al., 2016). Subsequent injection of an AAV expressing ChR2 regulated by the Ple67 promoter (Chan et al., 2017; de Leeuw et al., 2016; Portales-Casamar et al., 2010) would allow optogenetic stimulation of 5-HT neurons lacking the ability to release 5-HT. However, the fact that systemic injection of fluoxetine could partially recover the optogenetically-evoked sleep phenotypes in ePet-cre mice with less efficient opsin expression strongly suggests that 5-HT is the underlying molecule causing these actions.

Although opposing effects during tonic versus burst activity are a new observation for 5-HT neurons, they have been reported for other monoaminergic systems, including dopamine (Goto et al., 2007) and noradrenaline (Aston-Jones and Cohen, 2005). Furthermore, tonic activation of centromedial thalamic neurons in mice was shown to induce wakefulness, while burst activation induced slow-wave-like activity and enhanced cortical synchrony (Gent et al., 2018).

In summary, our data reject the previously prevailing view of 5-HT neurons being purely wake-promoting (Saper et al., 2005; Scammell et al., 2017) and instead suggest a more complex role that may be further elucidated by closer inspection of differences between firing modes and/or 5-HT subpopulations.

4.2 *In vivo* investigation of activity mode-dependent serotonin release

A potential explanation for the opposing effects on sleep-wake regulation is that tonic and burst stimulation modes evoke distinct patterns of 5-HT release and thereby modulate different downstream neuronal populations. Chapter 3 discussed the development and characterization of

iSeroSnFR, a fluorescent 5-HT sensor which enables to measure *in vivo* changes in extracellular 5-HT concentration during behavior of various timescales. In contrast to previous tools used for measuring extracellular 5-HT concentrations, iSeroSnFR, along with other recently developed protein-based sensors (Wan et al., 2020; Zhang et al., 2020), has the potential to visualize *in vivo* the presumed complex spatiotemporal 5-HT release patterns described in Chapter 1. iSeroSnFR's protein-based nature permits cell type specific expression and sub-cellular localization, and the fluorescence-based readout enables high spatial resolution.

Studies in leech Retzius neurons demonstrated that 5-HT release from clear small vesicles occurs in response to single action potentials, whereas extrasynaptic exocytosis from electrodense large vesicles occurs upon multiple stimulation at high frequency and leads to prolonged 5-HT release (Bruns and Jahn, 1995; Trueta et al., 2003, 2012). In the mammalian DRN, electron microscopic studies visualized 5-HT filled small clear and large dense-core vesicles (Chazal and Ralston, 1987; Kapadia et al., 1985; Liposits et al., 1985; Trueta and De-Miguel, 2012). Therefore, it is plausible to assume that tonic and burst optogenetic stimulation applied in experiments presented in Chapter 2 caused different spatiotemporal 5-HT release. Experiments combining optogenetic stimulation of 5-HT neurons in the DRN with fiber photometry recordings of iSeroSnFR in a downstream brain area could reveal such differential 5-HT release dynamics during tonic versus burst stimulation. According to studies in leech, a larger and prolonged increase in extracellular 5-HT concentration is expected upon burst stimulation.

Although fiber photometry reveals bulk changes in extracellular 5-HT concentration at high temporal resolution, it falls short of capturing spatial differences in 5-HT release. To that end, two-photon imaging of iSeroSnFR dynamics could provide valuable insights into extrasynaptic and synaptic release of 5-HT. As mentioned in Chapter 3, iSeroSnFR like $GRAB_{5\text{-}HT}$ (Wan et al., 2020) are compatible with two-photon imaging. The technical feasibility of such a research endeavor has already been demonstrated with imaging calcium or glutamate dynamics in axons and dendritic spines with either genetically encoded calcium indicators (GCaMP) or intensity-based glutamate-sensing reporters (iGluSnFR) (Chen et al., 2013; Dana et al., 2019; Marvin et al., 2018; Petreanu et al., 2012).

4.3 Distinct roles of different serotonin subpopulations

Alternatively, tonic and burst modes of activity could recruit different serotonergic sub-systems *(Ren et al., 2018)*. These sub-systems may employ inherently different modes of activity and hence are preferentially recruited by burst versus tonic inputs. According to this hypothesis, these 5-HT subpopulations will also differ in their innervation and modulation of various sleep-wake regulation centers.

Varying electrophysiological properties of serotonergic neurons

Although whole-cell recordings from brain slices verified that ChR2-expressing 5-HT neurons in the DRN are capable of reliably firing action potentials upon blue light pulses at high frequencies of 20 Hz (Liu et al., 2014), only 8 cells were tested in this study and it remains possible that certain 5-HT neurons in the DRN are unable to faithfully follow high-frequency burst stimulations. Indeed, electrophysiological characteristics are known to vary across 5-HT neurons in the DRN and correlate with behavioral activation of neurons (Crawford et al., 2010; Fernandez et al., 2016; Okaty et al., 2020; Shikanai et al., 2012).

For example, 5-HT neurons located in the lateral wings of the DRN have been shown to exhibit higher excitability and faster firing rates than other DRN 5-HT neurons (Crawford et al., 2010). Furthermore, a positive correlation between rostral position and increased excitability was observed within the ventromedial DRN. This pattern of increased excitability matches stressor induced patterns of activation of 5-HT neurons (Berton et al., 2007; Bouwknecht et al., 2007; Chung et al., 1999; Commons, 2008; Crawford et al., 2010; Gardner et al., 2005; Hale et al., 2008; Johnson et al., 2008, 2004; Martinez et al., 1998, 2002; Roche et al., 2003).

In addition to electrophysiological properties varying with anatomy, these characteristics have been demonstrated to differ according to the projection patterns (Fernandez et al., 2016). 5-HT neurons projecting to the BLA showed lower excitability and significantly less action potentials upon current injection than 5-HT neurons projection to the mPFC and dorsal hippocampus.

Altogether, these observations make it plausible that different effects on sleep-wake states caused by tonic and burst stimulation can be attributed to the biased activation of electrophysiological distinct 5-HT subpopulations in the DRN.

A recent scRNA-seq study uncovered potential genetic handles to specifically access these distinct subpopulations (Okaty et al., 2020). In total, at least four electrophysiological types were

discovered based on four key properties: 1) rheobase (input sensitivity), 2) delay to first spike (ability to phasically activate), 3) spike-frequency adaptation, 4) maximum firing rate. For example, a 5-HT subpopulation enriched with transcripts of *P2ry1* (purinergic receptor P2Y1) and located in the caudal DRN was shown to have dramatically lower excitability, long-latency to spike and three-fold lower maximum firing rate compared to other 5-HT neurons in the DRN. Furthermore, 5-HT neurons located in the dorsomedial and lateral wing areas of the DRN were found to have enriched expression of *Trh* (thyrotropin releasing hormone). Unfortunately, the study performed no electrophysiological characterization of this genetically-defined 5-HT subpopulation in order to verify the increased excitability and faster firing rates typical for this region of the DRN.

Varying projection patterns of serotonergic neurons

As discussed in Chapter 1, different 5-HT subpopulations are topographically organized (Bang et al., 2012; Brust et al., 2014; Fernandez et al., 2016; Imai et al., 1986; Lowry, 2002; Lowry et al., 2008; Muzerelle et al., 2016; Niederkofler et al., 2016; O'Hearn and Molliver, 1984; Ren et al., 2018) and subpopulations with different projection patterns have distinct behavioral functions (Niederkofler et al., 2016; Ren et al., 2018). However, a comprehensive investigation of the role of different 5-HT subpopulations in sleep-wake regulation is still lacking. Transcriptomic data sets provided by studies characterizing 5-HT neurons with scRNA-seq can be searched for genetic markers that potentially allow to specifically access genetically-defined 5-HT subpopulations projecting to sleep-wake regulation centers in the CNS (Huang et al., 2019; Okaty et al., 2020; Ren et al., 2019; Zeisel et al., 2018). In fact, these transcriptomic studies have already revealed 5-HT subpopulations with differing innervation of several relevant brain areas involved in sleep-wake regulation (Huang et al., 2019; Niederkofler et al., 2016; Ren et al., 2018, 2019). The following paragraphs will discuss a selection of these relevant brain areas which are essential for controlling sleep-wake states and for which there is existing mechanistic insights on the action of 5-HT. The discovery of genetically-defined 5-HT populations selectively innervating these regions may allow to segregate the opposing effects on sleep observed during bulk optogenetic stimulation of 5-HT neurons in the DRN.

The **thalamus** has long been known to be important for the generation of sleep rhythms observed in cortical EEG recordings (McCormick and Bal, 1997). NREM sleep is characterized by cortical slow waves (0.5-4 Hz) resulting from the synchronized activity of thalamocortical neuronal

networks alternating between active (UP) and quiescent (Down) states (David et al., 2013; Hughes et al., 2002; Lemieux et al., 2014; Sheroziya and Timofeev, 2014; Steriade et al., 1993a, 1993b, 1993c). These synchronized oscillations are generated through the interaction between GABAergic neurons of the thalamic reticular nuclei and the recipient thalamocortical neurons, and characterized by rhythmic burst firing (Krosigk et al., 1993; Steriade and Deschenes, 1984; Steriade et al., 1993d). The transition from sleep to wake state is associated with an abolition of rhythmic burst firing in thalamic neurons due to depolarization of the membrane potential and subsequent inactivation of the low-threshold Ca^{2+} current underlying these bursts (Hirsch et al., 1983; Steriade et al., 1986). Strong activation of 5-HT receptors on GABAergic neurons of the thalamic reticular results in a slow depolarization which leads to a suppression of rhythmic burst firing and promotion of single-spike activity which is characteristic of wake states (Lee and McCormick, 1996; McCormick and Wang, 1991).

The **ventrolateral preoptic area (VLPO)** contains NREM sleep-active neurons (Alam et al., 2014; Sherin et al., 1996) and lesions of this area produce reductions in sleep (John and Kumar, 1998; Lu et al., 2000). VLPO sleep-active neurons are GABAergic and galaninergic and innervate and inhibit arousal-promoting brain regions (Saito et al., 2013; Sherin et al., 1998). In addition to promoting NREM sleep, VLPO neurons are involved in mediating the homeostatic response to sleep deprivation. VLPO neurons fire faster with increasing sleep pressure during sleep deprivation and displayed increased activity during subsequent sleep recovery (Alam et al., 2014). *In vitro* experiments demonstrated that half of the GABAergic VLPO neurons were excited by 5-HT whereas the other half were inhibited (Gallopin et al., 2000, 2005). Since VLPO sleep neurons excited by 5-HT are also excited by adenosine via the A2AR-mediated pathway, it was hypothesized that these VLPO neurons mediate sleep induction (Gallopin et al., 2005). Individual 5-HT neurons innervating the VLPO may have either a bi-directional effect on sleep or selectively synapse onto VLPO neurons expressing one particular 5-HT receptor type.

The **basal forebrain** extends from the medial septum to the substantia innominata and contains cholinergic, GABAergic and glutamatergic neurons innervating the cortex (Xu et al., 2015; Zant et al., 2016). The basal forebrain is considered to be part of the arousal system as stimulation of the basal forebrain promotes wakefulness whereas lesions produce EEG slow waves and coma (Buzsaki et al., 1988; Fuller et al., 2011). Lesions or inhibition of cholinergic neurons increases slow EEG rhythms and reduces awakenings from NREM sleep, but fail to reduce the amount of

wakefulness (Chen et al., 2016; Fuller et al., 2011; Shi et al., 2015). Activation of these neurons suppresses EEG slow-wave activity during NREM sleep, interrupts NREM sleep and prolongs wakefulness (Anaclet et al., 2015; Chen et al., 2016; Ozen Irmak and de Lecea, 2014; Xu et al., 2015). Activation of glutamatergic neurons increases wakefulness (Anaclet et al., 2015; Xu et al., 2015). Inhibition of GABAergic neurons increases NREM sleep while their activation increases wakefulness (Anaclet et al., 2015). Similar to the VLPO, 5-HT has bi-directional effects on neurons in the basal forebrain, depending on which 5-HT receptor is expressed neurons can be either inhibited or excited (Fort et al., 1998; Guo et al., 2009; Hammack et al., 2009; Khateb et al., 1993; Levita et al., 2004). However, microinjection of 5-HT into the basal forebrain has been shown to decrease high-frequency EEG rhythms (Cape and Jones, 1998). Furthermore, since sleep deprivation leads to a slow and gradual build-up of serotonin in the basal forebrain similar to adenosine, and 5-HT inhibits cholinergic neurons, the actions of 5-HT in this region were hypothesized to be part of the homeostatic sleep response (Kalinchuk et al., 2006; Porkka-Heiskanen et al., 1997; Zant et al., 2011).

The **lateral hypothalamus** contains neurons producing orexin neuropeptides which are essential for regulating wake and REM sleep (Lecea et al., 1998; Sakurai et al., 1998). Activation of orexin neurons increases wakefulness and suppresses REM sleep (Adamantidis et al., 2007; Sasaki et al., 2011). Loss of orexin neurons leads to shorter wake bouts, although total amount of wake is only slightly reduced (Branch et al., 2016). 5-HT has been shown to inhibit orexin neurons in vitro (Li et al., 2002) as well as in vivo (Kumar et al., 2007).

The **pedunculopontine** (**PPT**) and **laterodorsal tegmental nuclei** (**LDT**) are located at the junction of the pons and midbrain in the brainstem. PPT/LDT contain cholinergic, GABAergic and glutamatergic neurons (Wang and Morales, 2009). These neurons are active during wakefulness and REM sleep (Boucetta et al., 2014; Cox et al., 2016) and the activation of cholinergic and glutamatergic neurons decreases lower-frequency EEG activity (Furman et al., 2015; Kroeger et al., 2017; Steriade et al., 1991). The activation of cholinergic neurons, in particular, promotes transition from NREM to REM sleep (Dort et al., 2015). While it is unknown whether cholinergic neurons promote wakefulness, stimulation of glutamatergic neurons has been demonstrated to increase wakefulness, whereas inhibition reduced wakefulness and increased NREM sleep (Kroeger et al., 2017). 5-HT is released in these nuclei in a behavioral state-related manner, highest during waking and lowest during REM sleep (Strecker et al., 1999). PPT/LDT neurons active during REM sleep

are inhibited by 5-HT (Luebke et al., 1992; Thakkar et al., 1998), but neurons active during wakefulness are not (Thakkar et al., 1998). Consistent with this, microinjection of serotonin or 5-HT_{1A} receptor agonist into the LDT nucleus suppresses REM sleep, while 5-HT_{1A} receptor antagonist injection increased REM sleep (Horner et al., 1997; Monti and Jantos, 2003; Sanford et al., 1994). Together with observations of a decrease in firing rate of 5-HT neurons in REM sleep (McGinty and Harper, 1976; Trulson and Jacobs, 1979), these results suggest that 5-HT plays an important role in the regulation of REM sleep (McCarley et al., 1995).

Overall, currently available data provide evidence that opposing effects on sleep-wake states may arise from genetically-distinct 5-HT subpopulations with varying projection patterns and electrophysiological characteristics. For this reason, future investigations into dissecting 5-HT sub-systems are promising and have the potential to further advance our understanding of the role of 5-HT in sleep-wake regulation.

4.4 References

Adamantidis, A.R., Zhang, F., Aravanis, A.M., Deisseroth, K., and de Lecea, L. (2007). Neural substrates of awakening probed with optogenetic control of hypocretin neurons. Nature *450*, 420–424.

Alam, M.A., Kumar, S., McGinty, D., Alam, M.N., and Szymusiak, R. (2014). Neuronal activity in the preoptic hypothalamus during sleep deprivation and recovery sleep. J. Neurophysiol. *111*, 287–299.

Alenina, N., Kikic, D., Todiras, M., Mosienko, V., Qadri, F., Plehm, R., Boyé, P., Vilianovitch, L., Sohr, R., Tenner, K., et al. (2009). Growth retardation and altered autonomic control in mice lacking brain serotonin. Proc. Natl. Acad. Sci. U.S.A. *106*, 10332–10337.

Allers, K.A., and Sharp, T. (2003). Neurochemical and anatomical identification of fast- and slow-firing neurones in the rat dorsal raphe nucleus using juxtacellular labelling methods in vivo. Neuroscience *122*, 193–204.

Anaclet, C., Pedersen, N.P., Ferrari, L.L., Venner, A., Bass, C.E., Arrigoni, E., and Fuller, P.M. (2015). Basal forebrain control of wakefulness and cortical rhythms. Nat. Commun. *6*, 8744.

Aston-Jones, G., and Cohen, J.D. (2005). An integrative theory of locus coeruleus-norepinephrine function: Adaptive gain and optimal performance. Annu. Rev. Neurosci. *28*, 403–450.

Bang, S.J., Jensen, P., Dymecki, S.M., and Commons, K.G. (2012). Projections and interconnections of genetically defined serotonin neurons in mice. Eur. J. Neurosci. *35*, 85–96.

Berton, O., Covington, H.E., Ebner, K., Tsankova, N.M., Carle, T.L., Ulery, P., Bhonsle, A., Barrot, M., Krishnan, V., Singewald, G.M., et al. (2007). Induction of ΔFosB in the periaqueductal gray by stress promotes active coping responses. Neuron *55*, 289–300.

Borbély, A.A., and Neuhaus, H.U. (1979). Sleep-deprivation: Effects on sleep and EEG in the rat. J. Comp. Physiol. *133*, 71–87.

Boucetta, S., Cissé, Y., Mainville, L., Morales, M., and Jones, B.E. (2014). Discharge profiles across the sleep–waking cycle of identified cholinergic, GABAergic, and glutamatergic neurons in the pontomesencephalic tegmentum of the rat. J. Neurosci. *34*, 4708–4727.

Bouwknecht, J.A., Spiga, F., Staub, D.R., Hale, M.W., Shekhar, A., and Lowry, C.A. (2007). Differential effects of exposure to low-light or high-light open-field on anxiety-related behaviors: Relationship to c-Fos expression in serotonergic and non-serotonergic neurons in the dorsal raphe nucleus. Brain Res. Bull. *72*, 32–43.

Branch, A.F., Navidi, W., Tabuchi, S., Terao, A., Yamanaka, A., Scammell, T.E., and Diniz Behn, C. (2016). Progressive loss of the orexin neurons reveals dual effects on wakefulness. Sleep *39*, 369–377.

Bruns, D., and Jahn, R. (1995). Real-time measurement of transmitter release from single synaptic vesicles. Nature *377*, 62–65.

Brust, R.D., Corcoran, A.E., Richerson, G.B., Nattie, E., and Dymecki, S.M. (2014). Functional and developmental identification of a molecular subtype of brain serotonergic neuron specialized to regulate breathing dynamics. Cell Rep. *9*, 2152–2165.

Buchanan, G.F., and Richerson, G.B. (2010). Central serotonin neurons are required for arousal to CO2. Proc. Natl. Acad. Sci. U.S.A. *107*, 16354–16359.

Buzsaki, G., Bickford, R.G., Ponomareff, G., Thal, L.J., Mandel, R., and Gage, F.H. (1988). Nucleus basalis and thalamic control of neocortical activity in the freely moving rat. J. Neurosci. *8*, 4007–4026.

Cape, E.G., and Jones, B.E. (1998). Differential modulation of high-frequency γ-electroencephalogram activity and sleep–wake state by noradrenaline and serotonin microinjections into the region of cholinergic basalis neurons. J. Neurosci. *18*, 2653–2666.

Chan, K.Y., Jang, M.J., Yoo, B.B., Greenbaum, A., Ravi, N., Wu, W.-L., Sánchez-Guardado, L., Lois, C., Mazmanian, S.K., Deverman, B.E., et al. (2017). Engineered AAVs for efficient noninvasive gene delivery to the central and peripheral nervous systems. Nat. Neurosci. *20*, 1172–1179.

Chazal, G., and Ralston, H.J. (1987). Serotonin-containing structures in the nucleus raphe dorsalis of the cat: An ultrastructural analysis of dendrites, presynaptic dendrites, and axon terminals. J. Comp. Neurol. *259*, 317–329.

Chen, L., Yin, D., Wang, T.-X., Guo, W., Dong, H., Xu, Q., Luo, Y.-J., Cherasse, Y., Lazarus, M., Qiu, Z., et al. (2016). Basal forebrain cholinergic neurons primarily contribute to inhibition of electroencephalogram delta activity, rather than inducing behavioral wakefulness in mice. Neuropsychopharmacology *41*, 2133–2146.

Chen, T.W., Wardill, T.J., Sun, Y., Pulver, S.R., Renninger, S.L., Baohan, A., Schreiter, E.R., Kerr, R.A., Orger, M.B., Jayaraman, V., et al. (2013). Ultrasensitive fluorescent proteins for imaging neuronal activity. Nature *499*, 295–300.

Chung, K.K.K., Martinez, M., and Herbert, J. (1999). c-fos expression, behavioural, endocrine and autonomic responses to acute social stress in male rats after chronic restraint: Modulation by serotonin. Neuroscience *95*, 453–463.

Cohen, J.Y., Amoroso, M.W., and Uchida, N. (2015). Serotonergic neurons signal reward and punishment on multiple timescales. eLife *4*, e06346.

Commons, K.G. (2008). Evidence for topographically organized endogenous 5-HT-1A receptor-dependent feedback inhibition of the ascending serotonin system. Eur. J. Neurosci. *27*, 2611–2618.

Cox, J., Pinto, L., and Dan, Y. (2016). Calcium imaging of sleep–wake related neuronal activity in the dorsal pons. Nat. Commun. *7*, 10763.

Crawford, L.K., Craige, C.P., and Beck, S.G. (2010). Increased intrinsic excitability of lateral wing serotonin neurons of the dorsal raphe: A mechanism for selective activation in stress circuits. J. Neurophysiol. *103*, 2652–2663.

Dana, H., Sun, Y., Mohar, B., Hulse, B.K., Kerlin, A.M., Hasseman, J.P., Tsegaye, G., Tsang, A., Wong, A., Patel, R., et al. (2019). High-performance calcium sensors for imaging activity in neuronal populations and microcompartments. Nat. Methods *16*, 649–657.

David, F., Schmiedt, J.T., Taylor, H.L., Orban, G., Giovanni, G.D., Uebele, V.N., Renger, J.J., Lambert, R.C., Leresche, N., and Crunelli, V. (2013). Essential thalamic contribution to slow waves of natural sleep. J. Neurosci. *33*, 19599–19610.

Dort, C.J.V., Zachs, D.P., Kenny, J.D., Zheng, S., Goldblum, R.R., Gelwan, N.A., Ramos, D.M., Nolan, M.A., Wang, K., Weng, F.-J., et al. (2015). Optogenetic activation of cholinergic neurons in the PPT or LDT induces REM sleep. Proc. Natl. Acad. Sci. U.S.A. *112*, 584–589.

Fernandez, S.P., Cauli, B., Cabezas, C., Muzerelle, A., Poncer, J.C., and Gaspar, P. (2016). Multiscale single-cell analysis reveals unique phenotypes of raphe 5-HT neurons projecting to the forebrain. Brain Struct. Funct. *221*, 4007–4025.

Fort, P., Khateb, A., Serafin, M., Mühlethaler, M., and Jones, B.E. (1998). Pharmacological characterization and differentiation of non-cholinergic nucleus basalis neurons in vitro. NeuroReport *9*, 61–65.

Fuller, P., Sherman, D., Pedersen, N.P., Saper, C.B., and Lu, J. (2011). Reassessment of the structural basis of the ascending arousal system. J. Comp. Neurol. *519*, 933–956.

Furman, M., Zhan, Q., McCafferty, C., Lerner, B.A., Motelow, J.E., Meng, J., Ma, C., Buchanan, G.F., Witten, I.B., Deisseroth, K., et al. (2015). Optogenetic stimulation of cholinergic brainstem neurons during focal limbic seizures: Effects on cortical physiology. Epilepsia *56*, e198–e202.

Gallopin, T., Fort, P., Eggermann, E., Cauli, B., Luppi, P.H., Rossier, J., Audinat, E., Muhlethaler, M., and Serafin, M. (2000). Identification of sleep-promoting neurons in vitro. Nature *404*, 992–995.

Gallopin, T., Luppi, P.-H., Cauli, B., Urade, Y., Rossier, J., Hayaishi, O., Lambolez, B., and Fort, P. (2005). The endogenous somnogen adenosine excites a subset of sleep-promoting neurons via A2A receptors in the ventrolateral preoptic nucleus. Neuroscience *134*, 1377–1390.

Gardner, K.L., Thrivikraman, K.V., Lightman, S.L., Plotsky, P.M., and Lowry, C.A. (2005). Early life experience alters behavior during social defeat: Focus on serotonergic systems. Neuroscience *136*, 181–191.

Gent, T.C., Bandarabadi, M., Herrera, C.G., and Adamantidis, A.R. (2018). Thalamic dual control of sleep and wakefulness. Nat. Neurosci. *21*, 974–984.

Goto, Y., Otani, S., and Grace, A.A. (2007). The Yin and Yang of dopamine release: A new perspective. Neuropharmacology *53*, 583–587.

Guo, J.-D., Hammack, S.E., Hazra, R., Levita, L., and Rainnie, D.G. (2009). Bi-directional modulation of bed nucleus of stria terminalis neurons by 5-HT: Molecular expression and functional properties of excitatory 5-HT receptor subtypes. Neuroscience *164*, 1776–1793.

Hale, M.W., Hay-Schmidt, A., Mikkelsen, J.D., Poulsen, B., Bouwknecht, J.A., Evans, A.K., Stamper, C.E., Shekhar, A., and Lowry, C.A. (2008). Exposure to an open-field arena increases c-Fos expression in a subpopulation of neurons in the dorsal raphe nucleus, including neurons projecting to the basolateral amygdaloid complex. Neuroscience *157*, 733–748.

Hammack, S.E., Guo, J.-D., Hazra, R., Dabrowska, J., Myers, K.M., and Rainnie, D.G. (2009). The response of neurons in the bed nucleus of the stria terminalis to serotonin: Implications for anxiety. Prog. Neuropsychopharmacol. Biol. Psychiatry *33*, 1309–1320.

Hirsch, J.C., Fourment, A., and Marc, M.E. (1983). Sleep-related variations of membrane potential in the lateral geniculate body relay neurons of the cat. Brain Res. *259*, 308–312.

Holschbach, M.A., Vitale, E.V., and Lonstein, J.S. (2018). Serotonin-specific lesions of the dorsal raphe disrupt maternal aggression and caregiving in postpartum rats. Behav. Brain Res. *348*, 53–64.

Horner, R.L., Sanford, L.D., Annis, D., Pack, A.I., and Morrison, A.R. (1997). Serotonin at the laterodorsal tegmental nucleus suppresses rapid-eye-movement sleep in freely behaving rats. J. Neurosci. *17*, 7541–7552.

Huang, K.W., Ochandarena, N.E., Philson, A.C., Hyun, M., Birnbaum, J.E., Cicconet, M., and Sabatini, B.L. (2019). Molecular and anatomical organization of the dorsal raphe nucleus. eLife *8*, e46464.

Hughes, S.W., Cope, D.W., Blethyn, K.L., and Crunelli, V. (2002). Cellular mechanisms of the slow (<1 Hz) oscillation in thalamocortical neurons in vitro. Neuron *33*, 947–958.

Imai, H., Steindler, D.A., and Kitai, S.T. (1986). The organization of divergent axonal projections from the midbrain raphe nuclei in the rat. J. Comp. Neurol. *243*, 363–380.

Jacobs, B.L., and Azmitia, E.C. (1992). Structure and function of the brain serotonin system. Physiol. Rev. *72*, 165–229.

John, J., and Kumar, V.M. (1998). Effect of NMDA lesion of the medial preoptic neurons on sleep and other functions. Sleep *21*, 587–598.

Johnson, P., Lowry, C., Truitt, W., and Shekhar, A. (2008). Disruption of GABAergic tone in the dorsomedial hypothalamus attenuates responses in a subset of serotonergic neurons in the dorsal raphe nucleus following lactate-induced panic. J. Psychopharmacol. *22*, 642–652.

Johnson, P.L., Lightman, S.L., and Lowry, C.A. (2004). A functional subset of serotonergic neurons in the rat ventrolateral periaqueductal gray implicated in the inhibition of sympathoexcitation and panic. Ann. N. Y. Acad. Sci. *1018*, 58–64.

Jouvet, M. (1999). Sleep and serotonin: An unfinished story. Neuropsychopharmacology *21*, 24S-27S.

Kalinchuk, A.V., Lu, Y., Stenberg, D., Rosenberg, P.A., and Porkka-Heiskanen, T. (2006). Nitric oxide production in the basal forebrain is required for recovery sleep. J. Neurochem. *99*, 483–498.

Kapadia, S.E., de Lanerolle, N.C., and LaMotte, C.C. (1985). Immunocytochemical and electron microscopic study of serotonin neuronal organization in the dorsal raphe nucleus of the monkey. Neuroscience *15*, 729–746.

Khateb, A., Fort, P., Alonso, A., Jones, B.E., and Muhlethaler, M. (1993). Pharmacological and immunohistochemical evidence for serotonergic modulation of cholinergic nucleus basalis neurons. Eur. J. Neurosci. *5*, 541–547.

Kirby, L.G., Pernar, L., Valentino, R.J., and Beck, S.G. (2003). Distinguishing characteristics of serotonin and non-serotonin-containing cells in the dorsal raphe nucleus: Electrophysiological and immunohistochemical studies. Neuroscience *116*, 669–683.

Kocsis, B., Varga, V., Dahan, L., and Sik, A. (2006). Serotonergic neuron diversity: Identification of raphe neurons with discharges time-locked to the hippocampal theta rhythm. Proc. Natl. Acad. Sci. U.S.A. *103*, 1059–1064.

Koella, W.P., Feldstein, A., and Czicman, J.S. (1968). The effect of para-chlorophenylalanine on the sleep of cats. Electroencephalogr. Clin. Neurophysiol. *25*, 481–490.

Kroeger, D., Ferrari, L.L., Petit, G., Mahoney, C.E., Fuller, P.M., Arrigoni, E., and Scammell, T.E. (2017). Cholinergic, glutamatergic, and GABAergic neurons of the pedunculopontine tegmental nucleus have distinct effects on sleep/wake behavior in mice. J. Neurosci. *37*, 1352–1366.

Krosigk, M. von, Bal, T., and McCormick, D.A. (1993). Cellular mechanisms of a synchronized oscillation in the thalamus. Science *261*, 361–364.

Kumar, S., Szymusiak, R., Bashir, T., Rai, S., McGinty, D., and Alam, M.N. (2007). Effects of serotonin on perifornical-lateral hypothalamic area neurons in rat. Eur. J. Neurosci. *25*, 201–212.

Lecea, L. de, Kilduff, T.S., Peyron, C., Gao, X.-B., Foye, P.E., Danielson, P.E., Fukuhara, C., Battenberg, E.L.F., Gautvik, V.T., Bartlett, F.S., et al. (1998). The hypocretins: Hypothalamus-specific peptides with neuroexcitatory activity. Proc. Natl. Acad. Sci. U.S.A. *95*, 322–327.

Lee, K.H., and McCormick, D.A. (1996). Abolition of spindle oscillations by serotonin and norepinephrine in the ferret lateral geniculate and perigeniculate nuclei in vitro. Neuron *17*, 309–321.

de Leeuw, C.N., Korecki, A.J., Berry, G.E., Hickmott, J.W., Lam, S.L., Lengyell, T.C., Bonaguro, R.J., Borretta, L.J., Chopra, V., Chou, A.Y., et al. (2016). rAAV-compatible MiniPromoters for restricted expression in the brain and eye. Mol. Brain *9*, 52.

Lemieux, M., Chen, J.-Y., Lonjers, P., Bazhenov, M., and Timofeev, I. (2014). The impact of cortical deafferentation on the neocortical slow oscillation. J. Neurosci. *34*, 5689–5703.

Levita, L., Hammack, S.E., Mania, I., Li, X.Y., Davis, M., and Rainnie, D.G. (2004). 5-hydroxytryptamine1A-like receptor activation in the bed nucleus of the stria terminalis: Electrophysiological and behavioral studies. Neuroscience *128*, 583–596.

Li, Y., Gao, X.-B., Sakurai, T., and van den Pol, A.N. (2002). Hypocretin/Orexin excites hypocretin neurons via a local glutamate neuron—A potential mechanism for orchestrating the hypothalamic arousal system. Neuron *36*, 1169–1181.

Liposits, Z., Görcs, T., and Trombitás, K. (1985). Ultrastructural analysis of central serotoninergic neurons immunolabeled by silver-gold-intensified diaminobenzidine chromogen. Completion of immunocytochemistry with X-ray microanalysis. J. Histochem. Cytochem. *33*, 604–610.

Liu, Z., Zhou, J., Li, Y., Hu, F., Lu, Y., Ma, M., Feng, Q., Zhang, J.E., Wang, D., Zeng, J., et al. (2014). Dorsal raphe neurons signal reward through 5-HT and glutamate. Neuron *81*, 1360–1374.

Lowry, C.A. (2002). Functional subsets of serotonergic neurones: Implications for control of the hypothalamic-pituitary-adrenal axis. J. Neuroendocrinol. *14*, 911–923.

Lowry, C.A., Evans, A.K., Gasser, P.J., Hale, M.W., Staub, D.R., and Shekhar, A. (2008). Topographic organization and chemoarchitecture of the dorsal raphe nucleus and the median raphe nucleus. In serotonin and sleep: Molecular, functional and clinical aspects, J.M. Monti, S.R. Pandi-Perumal, B.L. Jacobs, and D.J. Nutt, eds. (Basel: Birkhäuser), pp. 25–67.

Lu, J., Greco, M.A., Shiromani, P., and Saper, C.B. (2000). Effect of lesions of the ventrolateral preoptic nucleus on NREM and REM sleep. J. Neurosci. *20*, 3830–3842.

Luebke, J.I., Greene, R.W., Semba, K., Kamondi, A., McCarley, R.W., and Reiner, P.B. (1992). Serotonin hyperpolarizes cholinergic low-threshold burst neurons in the rat laterodorsal tegmental nucleus in vitro. Proc. Natl. Acad. Sci. U.S.A. *89*, 743–747.

Madden, C.J., and Morrison, S.F. (2019). Central nervous system circuits that control body temperature. Neurosci. Lett. *696*, 225–232.

Martinez, M., Phillips, P.J., and Herbert, J. (1998). Adaptation in patterns of c-fos expression in the brain associated with exposure to either single or repeated social stress in male rats. Eur. J. Neurosci. *10*, 20–33.

Martinez, M., Calvo-Torrent, A., and Herbert, J. (2002). Mapping brain response to social stress in rodents with c-fos expression: A review. Stress *5*, 3–13.

Marvin, J.S., Scholl, B., Wilson, D.E., Podgorski, K., Kazemipour, A., Müller, J.A., Schoch, S., Quiroz, F.J.U., Rebola, N., Bao, H., et al. (2018). Stability, affinity, and chromatic variants of the glutamate sensor iGluSnFR. Nat. Methods *15*, 936–939.

McCarley, R.W., Greene, R.W., Rainnie, D., and Portas, C.M. (1995). Brainstem neuromodulation and REM sleep. Semin. Neurosci. *7*, 341–354.

McCormick, D.A., and Bal, T. (1997). Sleep and arousal: Thalamocortical mechanisms. Annu. Rev. Neurosci. *20*, 185–215.

McCormick, D.A., and Wang, Z. (1991). Serotonin and noradrenaline excite GABAergic neurones of the guinea-pig and cat nucleus reticularis thalami. J. Physiol. *442*, 235–255.

McGinty, D.J., and Harper, R.M. (1976). Dorsal raphe neurons: Depression of firing during sleep in cats. Brain Res. *101*, 569–575.

Monti, J.M., and Jantos, H. (2003). Differential effects of the 5-HT1A receptor agonist flesinoxan given locally or systemically on REM sleep in the rat. Eur. J. Pharmacol. *478*, 121–130.

Mouret, J., Bobillier, P., and Jouvet, M. (1968). Insomnia following parachlorophenylalanine in the rat. Eur. J. Pharmacol. *5*, 17–22.

Murray, N.M., Buchanan, G.F., and Richerson, G.B. (2015). Insomnia caused by serotonin depletion is due to hypothermia. Sleep *38*, 1985–1993.

Muzerelle, A., Scotto-Lomassese, S., Bernard, J.F., Soiza-Reilly, M., and Gaspar, P. (2016). Conditional anterograde tracing reveals distinct targeting of individual serotonin cell groups (B5-B9) to the forebrain and brainstem. Brain. Struct. Funct. *221*, 535–561.

Niederkofler, V., Asher, T.E., Okaty, B.W., Rood, B.D., Narayan, A., Hwa, L.S., Beck, S.G., Miczek, K.A., and Dymecki, S.M. (2016). Identification of serotonergic neuronal modules that affect aggressive behavior. Cell Rep. *17*, 1934–1949.

O'Hearn, E., and Molliver, M.E. (1984). Organization of raphe-cortical projections in rat: A quantitative retrograde study. Brain Res. Bull. *13*, 709–726.

Okaty, B.W., Sturrock, N., Escobedo Lozoya, Y., Chang, Y., Senft, R.A., Lyon, K.A., Alekseyenko, O.V., and Dymecki, S.M. (2020). A single-cell transcriptomic and anatomic atlas of mouse dorsal raphe Pet1 neurons. eLife *9*, e55523.

Ozen Irmak, S., and de Lecea, L. (2014). Basal forebrain cholinergic modulation of sleep transitions. Sleep *37*, 1941–1951.

Peñalva, R.G., Lancel, M., Flachskamm, C., Reul, J.M.H.M., Holsboer, F., and Linthorst, A.C.E. (2003). Effect of sleep and sleep deprivation on serotonergic neurotransmission in the hippocampus: A combined in vivo microdialysis/EEG study in rats. Eur. J. Neurosci. *17*, 1896–1906.

Petreanu, L., Gutnisky, D.A., Huber, D., Xu, N., O'Connor, D.H., Tian, L., Looger, L., and Svoboda, K. (2012). Activity in motor–sensory projections reveals distributed coding in somatosensation. Nature *489*, 299–303.

Popa, D., Léna, C., Fabre, V., Prenat, C., Gingrich, J., Escourrou, P., Hamon, M., and Adrien, J. (2005). Contribution of 5-HT2 receptor subtypes to sleep–wakefulness and respiratory control, and functional adaptations in knock-out mice lacking 5-HT2A receptors. J. Neurosci. *25*, 11231–11238.

Porkka-Heiskanen, T., Strecker, R.E., Thakkar, M., Bjørkum, A.A., Greene, R.W., and McCarley, R.W. (1997). Adenosine: A mediator of the sleep-inducing effects of prolonged wakefulness. Science *276*, 1265–1268.

Portales-Casamar, E., Swanson, D.J., Liu, L., Leeuw, C.N. de, Banks, K.G., Sui, S.J.H., Fulton, D.L., Ali, J., Amirabbasi, M., Arenillas, D.J., et al. (2010). A regulatory toolbox of MiniPromoters to drive selective expression in the brain. Proc. Natl. Acad. Sci. U.S.A. *107*, 16589–16594.

Portas, C.M., Bjorvatn, B., and Ursin, R. (2000). Serotonin and the sleep/wake cycle: Special emphasis on microdialysis studies. Prog. Neurobiol. *60*, 13–35.

Qian, Y., Cao, Y., Deng, B., Yang, G., Li, J., Xu, R., Zhang, D., Huang, J., and Rao, Y. (2017). Sleep homeostasis regulated by 5HT2b receptor in a small subset of neurons in the dorsal fan-shaped body of Drosophila. eLife *6*, e26519.

Ren, J., Friedmann, D., Xiong, J., Liu, C.D., Ferguson, B.R., Weerakkody, T., DeLoach, K.E., Ran, C., Pun, A., Sun, Y., et al. (2018). Anatomically defined and functionally distinct dorsal raphe serotonin sub-systems. Cell *175*, 472-487.e20.

Ren, J., Isakova, A., Friedmann, D., Zeng, J., Grutzner, S.M., Pun, A., Zhao, G.Q., Kolluru, S.S., Wang, R., Lin, R., et al. (2019). Single-cell transcriptomes and whole-brain projections of serotonin neurons in the mouse dorsal and median raphe nuclei. eLife *8*, e49424.

Roche, M., Commons, K.G., Peoples, A., and Valentino, R.J. (2003). Circuitry underlying regulation of the serotonergic system by swim stress. J. Neurosci. *23*, 970–977.

Saito, Y., Tsujino, N., Hasegawa, E., Akashi, K., Abe, M., Mieda, M., Sakimura, K., and Sakurai, T. (2013). GABAergic neurons in the preoptic area send direct inhibitory projections to orexin neurons. Front. Neural Circuits *7*, 192.

Sakurai, T., Amemiya, A., Ishii, M., Matsuzaki, I., Chemelli, R.M., Tanaka, H., Williams, S.C., Richardson, J.A., Kozlowski, G.P., Wilson, S., et al. (1998). Orexins and orexin receptors: A family of hypothalamic neuropeptides and G protein-coupled receptors that regulate feeding behavior. Cell *92*, 573–585.

Sanford, L.D., Ross, R.J., Seggos, A.E., Morrison, A.R., Ball, W.A., and Mann, G.L. (1994). Central administration of two 5-HT receptor agonists: Effect on REM sleep initiation and PGO waves. Pharmacol. Biochem. Behav. *49*, 93–100.

Saper, C.B., Scammell, T.E., and Lu, J. (2005). Hypothalamic regulation of sleep and circadian rhythms. Nature *437*, 1257–1263.

Sasaki, K., Suzuki, M., Mieda, M., Tsujino, N., Roth, B., and Sakurai, T. (2011). Pharmacogenetic modulation of orexin neurons alters sleep/wakefulness states in mice. PLoS One *6*, e20360.

Scammell, T.E., Arrigoni, E., and Lipton, J.O. (2017). Neural circuitry of wakefulness and sleep. Neuron *93*, 747–765.

Schweimer, J.V., and Ungless, M.A. (2010). Phasic responses in dorsal raphe serotonin neurons to noxious stimuli. Neuroscience *171*, 1209–1215.

Sherin, J.E., Shiromani, P.J., McCarley, R.W., and Saper, C.B. (1996). Activation of ventrolateral preoptic neurons during sleep. Science *271*, 216–219.

Sherin, J.E., Elmquist, J.K., Torrealba, F., and Saper, C.B. (1998). Innervation of histaminergic tuberomammillary neurons by GABAergic and galaninergic neurons in the ventrolateral preoptic nucleus of the rat. J. Neurosci. *18*, 4705–4721.

Sheroziya, M., and Timofeev, I. (2014). Global intracellular slow-wave dynamics of the thalamocortical system. J. Neurosci. *34*, 8875–8893.

Shi, Y.-F., Han, Y., Su, Y.-T., Yang, J.-H., and Yu, Y.-Q. (2015). Silencing of cholinergic basal forebrain neurons using archaerhodopsin prolongs slow-wave sleep in mice. PLoS One *10*, e0130130.

Shikanai, H., Yoshida, T., Konno, K., Yamasaki, M., Izumi, T., Ohmura, Y., Watanabe, M., and Yoshioka, M. (2012). Distinct neurochemical and functional properties of GAD67-containing 5-HT neurons in the rat dorsal raphe nucleus. J. Neurosci. *32*, 14415–14426.

Steriade, M., and Deschenes, M. (1984). The thalamus as a neuronal oscillator. Brain Res. *8*, 1–63.

Steriade, M., Domich, L., and Oakson, G. (1986). Reticularis thalami neurons revisited: Activity changes during shifts in states of vigilance. J. Neurosci. *6*, 68–81.

Steriade, M., Dossi, R.C., Paré, D., and Oakson, G. (1991). Fast oscillations (20-40 Hz) in thalamocortical systems and their potentiation by mesopontine cholinergic nuclei in the cat. Proc. Natl. Acad. Sci. U.S.A. *88*, 4396–4400.

Steriade, M., Nunez, A., and Amzica, F. (1993a). A novel slow (< 1 Hz) oscillation of neocortical neurons in vivo: Depolarizing and hyperpolarizing components. J. Neurosci. *13*, 3252–3265.

Steriade, M., Nunez, A., and Amzica, F. (1993b). Intracellular analysis of relations between the slow (< 1 Hz) neocortical oscillation and other sleep rhythms of the electroencephalogram. J. Neurosci. *13*, 3266–3283.

Steriade, M., Contreras, D., Dossi, R.C., and Nunez, A. (1993c). The slow (<1 Hz) oscillation in reticular thalamic and thalamocortical neurons: Scenario of sleep rhythm generation in interacting thalamic and neocortical networks. J. Neurosci. *13*, 3284–3299.

Steriade, M., McCormick, D.A., and Sejnowski, T.J. (1993d). Thalamocortical oscillations in the sleeping and aroused brain. Science *262*, 679–685.

Strecker, R.E., Thakkar, M.M., Porkka-Heiskanen, T., Dauphin, L.J., Bjørkum, A.A., and McCarley, R.W. (1999). Behavioral state-related changes of extracellular serotonin concentration in the pedunculopontine tegmental nucleus: A microdialysis study in freely moving animals. Sleep Res. Online *2*, 21–27.

Tagliamonte, A., Tagliamonte, P., Corsini, G.U., Mereu, G.P., and Gessa, G.L. (1973). Decreased conversion of tyrosine to catecholamines in the brain of rats treated with p-chlorophenylalanine. J. Pharm. Pharmacol. *25*, 101–103.

Tan, C.L., and Knight, Z.A. (2018). Regulation of body temperature by the nervous system. Neuron *98*, 31–48.

Thakkar, M.M., Strecker, R.E., and McCarley, R.W. (1998). Behavioral state control through differential serotonergic inhibition in the mesopontine cholinergic nuclei: A simultaneous unit recording and microdialysis study. J. Neurosci. *18*, 5490–5497.

Trueta, C., and De-Miguel, F.F. (2012). Extrasynaptic exocytosis and its mechanisms: A source of molecules mediating volume transmission in the nervous system. Front. Physiol. *3*, 319.

Trueta, C., Méndez, B., and De-Miguel, F.F. (2003). Somatic exocytosis of serotonin mediated by L-type calcium channels in cultured leech neurones. J. Physiol. *547*, 405–416.

Trueta, C., Kuffler, D.P., and De-Miguel, F.F. (2012). Cycling of dense core vesicles involved in somatic exocytosis of serotonin by leech neurons. Front. Physiol. *3*, 175.

Trulson, M.E., and Jacobs, B.L. (1979). Raphe unit activity in freely moving cats: Correlation with level of behavioral arousal. Brain Res. *163*, 135–150.

Ursin, R. (2002). Serotonin and sleep. Sleep Med. Rev. *6*, 55–69.

Veasey, S.C., Fornal, C.A., Metzler, C.W., and Jacobs, B.L. (1995). Response of serotonergic caudal raphe neurons in relation to specific motor activities in freely moving cats. J. Neurosci. *15*, 5346–5359.

Venner, A., Broadhurst, R.Y., Sohn, L.T., Todd, W.D., and Fuller, P.M. (2020). Selective activation of serotoninergic dorsal raphe neurons facilitates sleep through anxiolysis. Sleep *43*, zsz231.

Wan, J., Peng, W., Li, X., Qian, T., Song, K., Zeng, J., Deng, F., Hao, S., Feng, J., Zhang, P., et al. (2020). A genetically encoded GRAB sensor for measuring serotonin dynamics in vivo. bioRxiv. https://doi.org/10.1101/2020.02.24.962282.

Wang, H.-L., and Morales, M. (2009). Pedunculopontine and laterodorsal tegmental nuclei contain distinct populations of cholinergic, glutamatergic and GABAergic neurons in the rat. Eur. J. Neurosci. *29*, 340–358.

Weitzman, E.D., Rapport, M.M., McGregor, P., and Jacoby, J. (1968). Sleep patterns of the monkey and brain serotonin concentration: Effect of p-chlorophenylalanine. Science *160*, 1361–1363.

Whitney, M.S., Shemery, A.M., Yaw, A.M., Donovan, L.J., Glass, J.D., and Deneris, E.S. (2016). Adult brain serotonin deficiency causes hyperactivity, circadian disruption, and elimination of siestas. J. Neurosci. *36*, 9828–9842.

Xu, M., Chung, S., Zhang, S., Zhong, P., Ma, C., Chang, W.C., Weissbourd, B., Sakai, N., Luo, L., Nishino, S., et al. (2015). Basal forebrain circuit for sleep-wake control. Nat. Neurosci. *18*, 1641–1647.

Yuan, Q., Joiner, W.J., and Sehgal, A. (2006). A sleep-promoting role for the Drosophila serotonin receptor 1A. Curr. Biol. *16*, 1051–1062.

Zant, J.C., Leenaars, C.H.C., Kostin, A., Van Someren, E.J.W., and Porkka-Heiskanen, T. (2011). Increases in extracellular serotonin and dopamine metabolite levels in the basal forebrain during sleep deprivation. Brain Res. *1399*, 40–48.

Zant, J.C., Kim, T., Prokai, L., Szarka, S., McNally, J., McKenna, J.T., Shukla, C., Yang, C., Kalinchuk, A.V., McCarley, R.W., et al. (2016). Cholinergic neurons in the basal forebrain promote wakefulness by actions on neighboring non-cholinergic neurons: An opto-dialysis study. J. Neurosci. *36*, 2057–2067.

Zeisel, A., Hochgerner, H., Lönnerberg, P., Johnsson, A., Memic, F., van der Zwan, J., Häring, M., Braun, E., Borm, L.E., La Manno, G., et al. (2018). Molecular architecture of the mouse nervous system. Cell *174*, 999-1014.e22.

Zhang, S., Li, X., Drobizhev, M., and Ai, H. (2020). A fast high-affinity fluorescent serotonin biosensor engineered from a tick lipocalin. bioRxiv. https://doi.org/10.1101/2020.04.18.048397.

Chapter 5

DEEP PARALLEL CHARACTERIZATION OF AAV VARIANT TROPISM VIA SINGLE-CELL RNA SEQUENCING

Section 5.1 was adapted from:

Altermatt, M., Brown, D., Dobreva, T., Jang, M.J., Coughlin, G.M., Pool, A.-H., Thomson, M., Gradinaru, V. (2020). In-depth parallel profiling of tissue and cell-type tropism of AAV variants by single-cell RNA sequencing. Molecular Therapy 28, 1-592. doi: 10.1016/j.ymthe.2020.04.019.

5.1 Summary

Adeno-associated viruses (AAVs) are popular gene delivery vehicles and there is a continuing high demand for AAV variants with improved transduction efficiency and specificity. Directed evolution and/or rational design have been used extensively to engineer the capsid of naturally occurring AAVs in order to better customize their properties for research and clinical work. While these engineering approaches are scalable and have generated useful variants, the subsequent transduction profiling of these variants remains either low throughput or lacks resolution across the many relevant cell and tissue types. Single-cell RNA sequencing (scRNA-seq) via droplet-based methods allows in-depth profiling of gene expression of several thousand individual cells. We established a tissue processing and data analysis pipeline that leverages the capabilities of scRNA-seq to achieve simultaneous characterization of AAV variants across multiplexed tissue cell types. Results of viral tropism characterization using scRNA-seq correlate well with traditional *in vivo* vector characterization using immunohistochemistry (IHC). In addition, our scRNA-seq approach reveals previously undetected sub-cell type enrichments and provides data sets offering insight into potential mechanistic differences in AAV variant transduction.

5.2 Introduction

Recombinant AAVs (rAAVs) have become the preferred gene delivery vehicles for many clinical and research applications (Bedbrook et al., 2018; Samulski and Muzyczka, 2014) due to their broad viral tropism, low immunogenicity, and stable persistence as episomal DNA ensuring long-term

transgene expression (Daya and Berns, 2008; Deverman et al., 2018; Gaj et al., 2016; Naso et al., 2017; Wu et al., 2006). However, current systemic gene therapies using AAVs have a relatively low therapeutic index (Mével et al., 2020). High AAV gene delivery doses are necessary to reach sufficient transgene expression in target cell populations which can have severe adverse effects (Hinderer et al., 2018; Srivastava, 2020; Wilson and Flotte, 2020). Ideally, rAAVs should specifically and efficiently express high levels of the therapeutic transgene in the desired target tissue and cell type, which would reduce the required dose and thereby improve patient safety and alleviate demands on vector manufacturing. Several studies have demonstrated that the transduction efficiency and specificity of AAVs can be improved by engineering their capsids using rational design (Bartlett et al., 1999; Davidsson et al., 2019; Davis et al., 2015; Lee et al., 2018; Sen, 2014) or directed evolution (Bedbrook et al., 2018; Chan et al., 2017; Dalkara et al., 2013; Deverman et al., 2016; Excoffon et al., 2009; Grimm et al., 2008; Körbelin et al., 2016a; Kotterman and Schaffer, 2014; Maheshri et al., 2006; Müller et al., 2003; Ogden et al., 2019; Ojala et al., 2018; Pekrun et al., 2019; Pulicherla et al., 2011; Ravindra Kumar et al., 2020; Tervo et al., 2016; Ying et al., 2010). These engineering methods yield a diverse collection of candidates that require thorough, preferably high-throughput, *in vivo* vector characterization to obtain optimal candidates for a particular clinical or research application. Towards this end, various in situ hybridization (ISH) techniques or conventional IHC are commonly employed to profile the viral tropism based on labeling viral nucleic acids or proteins expressed by the viral transgene, respectively (Arruda et al., 2001; Chan et al., 2017; Deleage et al., 2016, 2018; Deverman et al., 2016; Grabinski et al., 2015; Hinderer et al., 2018; Hunter et al., 2019; Miao et al., 2000; Polinski et al., 2015, 2016; Puray-Chavez et al., 2017; Ravindra Kumar et al., 2020; Wang et al., 2020; Zhang et al., 2016; Zhao et al., 2020). Although these histological approaches preserve spatial information, current technical challenges limit their application to profile the viral tropism of one or two AAV variants across a few gene markers and thus fall short of efficiently characterizing multiple AAVs across the many complex cell types present in the central nervous system (CNS) (Tasic et al., 2016, 2018; Zeisel et al., 2018).

Here, we introduce an experimental and bioinformatics workflow capable of rapidly profiling the viral tropism of multiple AAV variants in parallel across numerous complex cell types by taking advantage of the transcriptomic resolution of scRNA-seq techniques (Figure 1). Our quantification results of transduction biases across major cell types using scRNA-seq correlate well with results acquired with conventional IHC. We demonstrate the power of our transcriptomic approach by going

beyond major cell types and revealing significant differences in sub-cell type transduction specificity between AAV-PHP.eB and AAV-CAP-B10. Compared to AAV-CAP-B10, AAV-PHP.eB displays biased targeting of inhibitory neurons and both variants transduce SST+ or PVALB+ inhibitory neurons more efficiently than VIP+ inhibitory neurons.

5.3 Results

Workflow of AAV tropism characterization by scRNA-seq

To address the current bottleneck in AAV tropism profiling, we devised an experimental workflow and a sophisticated data processing pipeline (Figures 1 and S1) that exploits the transcriptomic resolution of scRNA-seq to profile multiple AAV tropisms across complex cell type hierarchies. Single or multiple barcoded rAAVs are injected into the retro-orbital sinus of mice followed by tissue dissociation, single-cell library construction using the 10x Genomics Chromium system (Zheng et al., 2017), and analysis with multiplexed Illumina sequencing. Standard library construction procedure includes an enzymatic fragmentation step that shortens the cDNA amplicon such that its final size falls below the limitations of sequencing platforms. The average length of these final cDNA fragments is approximately 450 bp which poses a problem for AAV variant tropism profiling. The Woodchuck hepatitis virus posttranscriptional regulatory element (WPRE), a sequence commonly found at the 3’ end of viral transgenes and used to ensure strong transgene expression, is approximately 600 bp long. As a consequence, without modification of current library construction protocols, barcoded transgene transcripts corresponding to different rAAV capsids are indistinguishable based on Illumina sequencing results due to a shared WPRE sequence at the 3’ end. We resolved this problem by taking an aliquot of the intact cDNA library and adding standard Illumina sequencing primer recognition sites (Read 2) to the viral transcripts using PCR amplification such that the barcoded region is within the two Illumina primer target sequences and can be read out with Illumina sequencing (e.g. Figure 2 B). Cell transcriptome aliquots undergoing standard library construction protocol are sequenced using the NovaSeq 6000 system of Illumina. cDNA aliquots undergoing PCR amplification of viral transcripts are sequenced using the MiSeq system of Illumina which we found to be successful at sequencing cDNAs containing an approximately 890 bp transgene sequence. The sequencing data undergoes a comprehensive data processing pipeline (see Methods, Figure S1). Due to significant noise introduced by PCR amplification (Figure S2 A) and debris, we introduced a probabilistic representation of correct viral

transcripts to determine the transduction status of each cell (see Methods, Figure S1 B). Our data processing and analysis approach successfully recovers correct viral transcripts detected in the cell transcriptome aliquots (Figure S2 B), which include now the necessary barcode region to distinguish individual AAV variants.

Comparison of viral tropism profiling with traditional IHC and scRNA-seq

In a first step, we validated our method by comparing the quantification of AAV transduction of major cell types by means of scRNA-seq or conventional IHC. For this purpose, we characterized the tropism profiles of two previously reported AAV variants, AAV-PHP.eB (Chan et al., 2017) and AAV-CAP-B10 (Flytzanis et al., 2020) (Figure 2 A). In total, four animals received a retro-orbital injection of either AAV-PHP.eB and/or AAV-CAP-B10 with 1.5×10^{11} vg per variant. Coinjections served to test the ability of our approach to parallelize tropism profiling. After 3-4 weeks of expression, we harvested the brains and used one hemisphere for characterization by IHC and one hemisphere for scRNA-seq. For this comparison, we focused on the transduction rate of neurons (NeuN), astrocytes (S100b), and oligodendrocytes (Olig2). In the case of IHC, a cell was classified as infected based on expression of fluorophores while in scRNA-seq, transduced cells were identified based on the presence of defining viral transcripts (see Methods and Figure S1 B).

Viral transcripts expressed from genomes of different AAV variants are distinguished based on distinct XFP sequences (Figure 2 B). Primers for our viral transcript amplification step are chosen such that enough of the XFP sequence is contained between the Illumina primer target sequences to differentiate AAV variants.

Our analysis of the scRNA-seq data demonstrated that viral tropism biases across the three canonical marker genes are consistent with previous reports (Chan et al., 2017; Flytzanis et al., 2020) (Figure 2 C). In contrast to AAV-PHP.eB, AAV-CAP-B10 is preferentially targeting NeuN+ cells when compared to S100b+ and Olig2+ cells. No marked discrepancies in viral tropism characterization with single and dual injections were observed suggesting that mutual AAV variant interference with tropism is minimal and multiple AAV variants can be profiled in parallel.

In an effort to quantify the similarity between IHC and scRNA-seq with regard to AAV tropism characterization, we directly compared the transduction rate of each AAV variant for every

marker gene (i.e., NeuN, S100b or Olig2) as determined by each technique, and noticed a good correlation coefficient (Figure 2 D). In spite of different underlying biological readouts, i.e. measuring protein expression in the case of IHC and RNA molecules for scRNA-seq, the two techniques reveal similar viral tropisms.

In-depth AAV tropism characterization at transcriptomic resolution

After establishing trust in our approach, we scrutinized the tropism of AAV-PHP.eB and AAV-CAP-B10 beyond major cell types (Figure 3). In-depth cell typing of transcriptomes collected from tissues with numerous and complex cell types such as the brain, requires expert knowledge of the tissue composition, time to manually curate the data, and availability of large data sets (Zeisel et al., 2018). Since our method is envisioned to be a fast tropism profiling technique applied after vector library selection, we decided to avoid the time-consuming manual annotation of transcriptomic data by employing Cell BLAST, which is a cell-querying method built on neural network-based generative models and a customized cell-to-cell similarity metric (Cao et al., 2020). Cell BLAST allows to rapidly transfer cell type annotations from a well-curated reference data set to a newly acquired data set. As our reference data set, we selected the mouse whole cortex and hippocampus 10x data set available from the Allen Brain Institute (Yao et al., 2020).

During our in-depth characterization, we discovered several previously unnoticed sub-cell type biases for AAV-PHP.eB and AAV-CAP-B10 (Figure 3 A). The fraction of transduced cells that are glutamatergic neurons is markedly reduced for AAV-PHP.eB when compared to AAV-CAP-B10. Furthermore, both PVALB+ and SST+ inhibitory neurons represent a larger fraction of transduced cells than VIP+ cells.

To confirm the tropism biases in neuronal sub-cell types with a traditional technique, we performed fluorescent in situ hybridization chain reaction (FISH-HCR) for glutamatergic and GABAergic gene markers (Figure 3 B) (Choi et al., 2014; Patriarchi et al., 2018). As indicated by our scRNA-seq data, AAV-CAP-B10, compared to AAV-PHP.eB, has an increased transduction efficiency of glutamatergic neurons (SLC17A7) relative to GABAergic neurons (GAD1). Furthermore, FISH-HCR verified the decreasing trend in transduction efficiency of both AAV variants from PVALB+, to SST+ and VIP+ neurons.

Analyzing single-gene cross-correlation in search of mechanistic insights

Although profiling viral tropisms across complex cell type hierarchies reveals notable sub-cell type transduction biases, the categorization into different cell types masks underlying gene distributions shared across distinct sub-cell types that are transduced more efficiently by one AAV variant over the other. Several distinct cell types likely share components crucial for AAV transduction, such as receptors mediating the entry of viral particles into cells. Understanding the underlying reason of the difference in tropism profiles, thus requires to investigate the expression of genes independent of cell type categorization. To that end, we performed single-gene cross-correlation to detect genes whose expression correlates with the expression of the viral transgene (Figure 4). In particular, we studied how the correlation coefficient of genes and transgenes differ between AAV-PHP.eB and AAV-CAP-B10 for our coinjection data sets in order to gain insights into the shift in viral tropism (Figure 4 A). As expected, genes more positively correlated with AAV-PHP.eB are expressed highest in astrocytes, whereas genes more positively correlated with AAV-CAP-B10 are highly expressed in glutamatergic neurons (Figure 4 B). Among the top 20 genes more positively correlated with either AAV variant are several transmembrane proteins (highlighted in black). For example, *Mal2* which has been demonstrated to be required for transcytosis (de Marco et al., 2002), or *Npr3* and *Gpr3711*, which are receptors demonstrating ligand-induced endocytosis (Almeida et al., 1989; Maack et al., 1987; Meyer et al., 2013). Diverging affinities of AAV-PHP.eB and AAV-CAP-B10 towards these transmembrane proteins may be the underlying cause of their different tropisms. We are currently in the process of testing several hits from such transcriptomic analysis to measure the affinity of different AAV variants towards these extracellularly-displayed proteins.

5.4 Discussion

The advent of high-throughput techniques such as next-generation sequencing (NGS) made it possible to screen large libraries of AAV capsids *in vivo* by extracting viral DNA from relevant tissue followed by sequencing of capsid gene inserts or DNA barcodes corresponding to defined capsids. NGS-based screening has been successfully applied to libraries created by peptide-insertions (Davidsson et al., 2019; Körbelin et al., 2016b), DNA shuffling of capsids (De Alencastro et al., 2020; Herrmann et al., 2019; Paulk et al., 2018) or site-directed mutagenesis (Adachi et al., 2014). Although this strategy reveals broad tissue tropism differences between AAV variants, this approach falls short with regard to cell type tropism analysis, which is of utmost importance in tissues with

complex cell type compositions such as the brain (Tasic et al., 2016, 2018; Zeisel et al., 2018). For this reason, Cre recombination-based AAV targeted evolution (CREATE) was developed that positively selects for AAV capsids that more efficiently transduce cell types defined by a single gene marker and the corresponding Cre-expression (Deverman et al., 2016). Multiplexed-CREATE (M-CREATE) extended CREATE by incorporating NGS and an analysis pipeline that permits negative selection (Ravindra Kumar et al., 2020). However, focusing solely on a single canonical gene marker to represent a cell type carries the risk of ignoring cell type state changes. For example, *Cx3cr1* is commonly used as a gene marker for microglia, but recent scRNA-seq experiments have shown that this gene is down-regulated in the activated or disease-associated microglia (Jordão et al., 2019; Li et al., 2019; Masuda et al., 2019; Mrdjen et al., 2018). Cell types defined by transcriptomic methods are also rarely found to be defined by a single gene marker, but rather have distinct combinatorial expression signatures (Tasic et al., 2016, 2018; Zeisel et al., 2015). Furthermore, these NGS-based screening approaches currently neglect to take into account the discrepancy between DNA and RNA. For example, AAV5 was shown to be consistently among the most efficient vectors in the liver on the DNA level, but was outperformed on the mRNA level by numerous other capsids (Weinmann et al., 2020). For these reasons, a collection of promising candidates emerging from high-throughput engineering approaches is usually subject to a more detailed *in vivo* vector characterization. Cell type tropism analysis can be achieved with labeling RNA molecules with single molecule fluorescent *in situ* hybridization (smFISH) (Femino et al., 1998; Lein et al., 2017). The hybridization efficiency of smFISH can be close to 100%, although only a limited set of targeted genes can be labeled. A challenge with these image-based *in situ* transcriptomics approaches is the difficulty of extracting individual cells from a background with large signal interference (Liao et al., 2020). An alternative strategy to smFISH, which provides improved signal to noise ratio, is to use target-specific padlock probes to create rolling-circle amplification products for a selected set of gene transcripts. Padlock probes include gene-unique identifier barcodes that can be sequenced *in situ*. STARmap (spatially-resolved transcript amplicon readout mapping) uses this approach to simultaneously measure over 1000 genes in sections with an RNA detection efficiency similar to scRNA-seq (Wang et al., 2018). Although, scRNA-seq based on the Drop-seq method loses spatial information in the dissociation procedure, analysis packages have been developed that can infer single-cell localization by combining scRNA-seq data with preexisting information from ISH-based labeling for specific marker genes (Achim et al., 2015; Durruthy-Durruthy et al., 2015; Halpern et al., 2017; Nitzan et al.,

2019; Satija et al., 2015; Stuart et al., 2019). Furthermore, scRNA-seq is not restricted to only assay a fraction of the total transcripts as is the case for RNA-labeling methods and is superior with regard to time efficiency (Liao et al., 2020). As a result, our platform can rapidly profile the tropism of multiple AAV variants in parallel across several thousand cells defined by their entire transcriptome.

5.5 Future directions

In our experiments, AAV variants were packaging two different fluorescent protein sequences such that AAV-PHP.eB and AAV-CAP-B10 capsids could be distinguished during imaging of tissue as well as in our sequencing data. Having demonstrated that both techniques report similar tropism profiles, fluorescent sequences can now be replaced with barcodes such that more variants can be profiled in parallel. Established protocols to create pools of barcoded AAV capsid variants (Ogden et al., 2019) can be adapted to the needs of our workflow. However, the number of variants profiled in parallel will be limited by the number of cells captured during single-cell library preparation, since the maximal viral dose that can be administered to an animal is fixed. Therefore, the more variants are injected in parallel, the lower the dose per variant, and as a consequence, fewer cells will be transduced by a specific variant. The throughput of the single-cell library preparation is limited in our case since the 10x Genomics platform uses custom microfluidics and costly reagents. Future endeavors could focus on low-cost scRNA-seq techniques with higher throughput capabilities such as the recently developed split-pool ligation-based transcriptome sequencing (SPLiT-seq) which can profile the transcriptome of hundred thousands of cells (Rosenberg et al., 2018).

Our approach is not restricted to profiling capsid variants, but could be expanded in the future to screens of promoters, enhancers, or transgenes, which are other essential elements to optimize in the design of optimal gene delivery vehicles.

Collecting the entire transcriptome of infected and non-infected cells also offers the opportunity of studying the effects of AAV transduction on the host cell transcriptome. A similar investigation has been conducted with the G-deleted rabies virus (Huang and Sabatini, 2020). Results from this study demonstrated that virus infection led to the down-regulation of genes involved in metabolic processes and neurotransmission in host cells, whereas genes related to cytokine signaling and adaptive immune system were up-regulated. Furthermore, an increase in the proportion of immune cells in the surrounding tissue of host cells (microglia, myeloid, and lymphoid cells) was observed. At present, no such detailed examination of transcriptome changes upon AAV injection

has been conducted even though insights gained from such a survey would be of great value for the design of AAV-based gene delivery vehicles.

5.6 Acknowledgements

We thank the Gradinaru and Thomson labs for helpful discussions; Dr. Allan-Hermann Pool for advice on the mouse brain tissue dissociation procedure; and Jeff Park for advice on the 10x Genomics Chromium single-cell library preparation protocol. This work was supported by the NIH Pioneer DP1OD025535, Beckman Institute for CLARITY, Optogenetics and Vector Engineering Research at Caltech. V.G is a Heritage Principal Investigator supported by the Heritage Medical Research Institute.

5.7 Author contributions

M.A., D.B., T.D., and V.G. conceived the project and designed the experiments. M.A. and T.D. prepared DNA constructs. M.A., D.B., and T.D. produced the virus. M.A. performed injections, tissue dissociation, histology, imaging, and image quantification. D.B. performed single-cell library preparation and prepared samples for sequencing. M.A. and D.B. built the data processing pipeline. M.A. performed analysis shown in the main figures. M.A. wrote this chapter with inputs from D.B.

5.8 Main figures

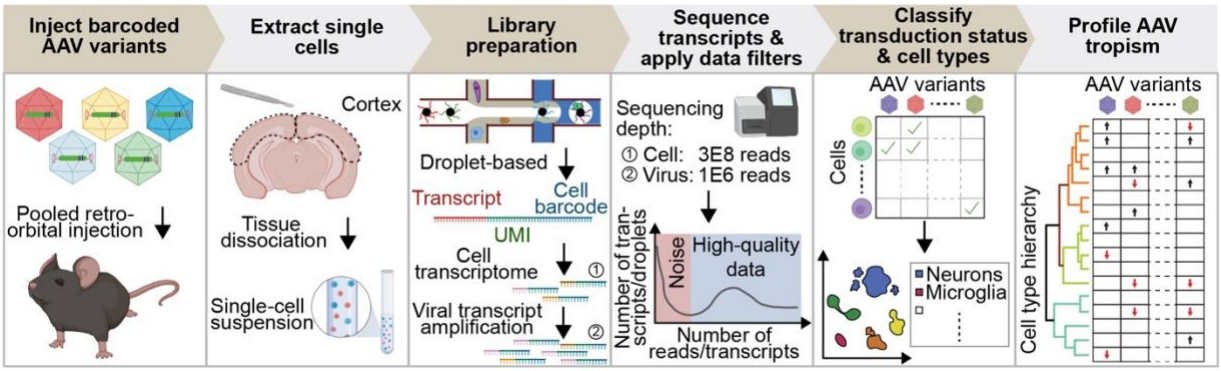

Figure 1. Workflow of AAV tropism characterization by scRNA-seq. (I) Injection of a single AAV variant or multiple barcoded AAV variants into the retro-orbital sinus. (II) After 3-4 weeks following the injection, the brain region of interest is extracted and the tissue is dissociated into a single-cell suspension. (III) The droplet-based 10x Genomics Chromium system is used to isolate cells and build transcriptomic libraries. To enable viral tropism characterization of multiple rAAVs in parallel, an aliquot of the intact cDNA library undergoes further PCR amplification of viral transcripts. During amplification, Illumina sequencing primer targets (Read 2) are added to the viral transcripts such that the sequence in between Illumina primer targets (Read 1 and 2) contains the AAV capsid barcode sequence. (IV) The cell transcriptome is sequenced using the NovaSeq 6000 system of Illumina. The aliquot with the amplified viral transcript is sequenced with the MiSeq system of Illumina. Sequencing results are filtered with a comprehensive computational pipeline to obtain a high-quality data set. (V) Transduction status of each cells is determined and cells are assigned a cell type annotation. (VI) AAV tropism profiling across numerous cell types.

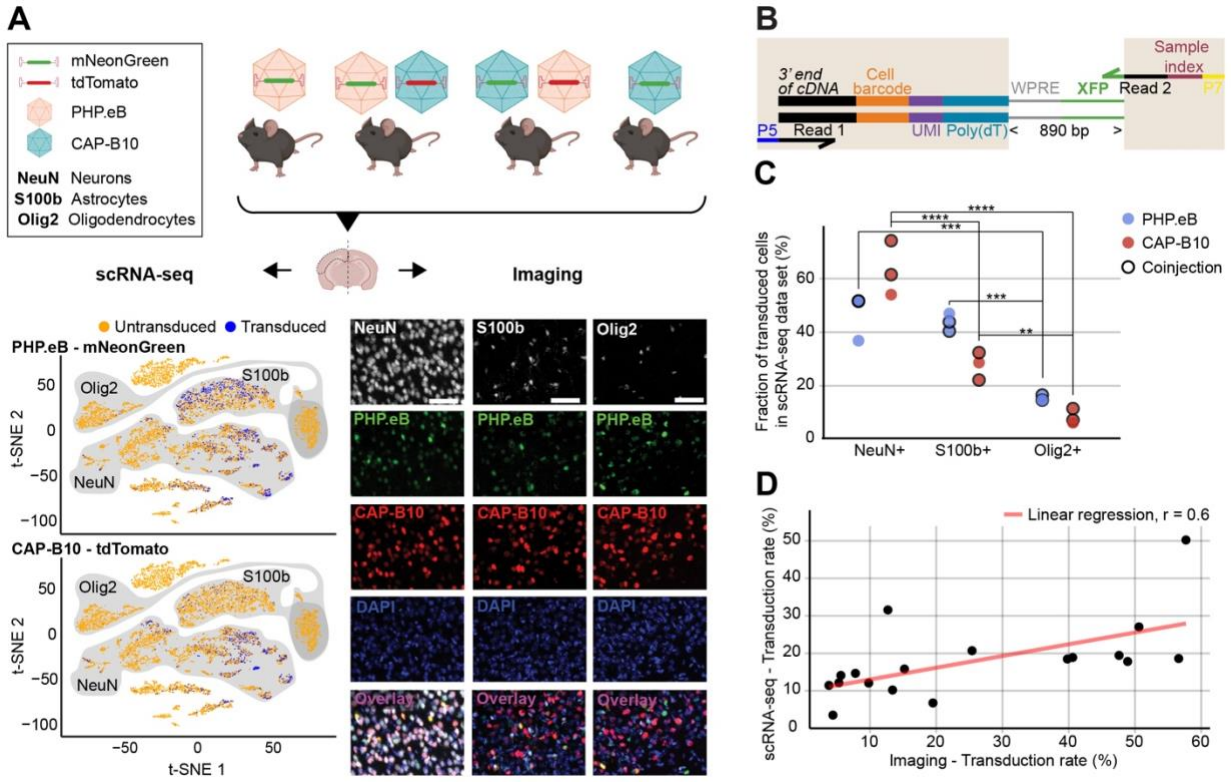

Figure 2. Comparison of viral tropism profiling with traditional IHC and scRNA-seq. (A) Overview of the experiment which compares viral tropism characterization with IHC and scRNA-seq. Four animals were injected with 1.5×10^{11} vg packaged in AAV-PHP.eB and/or 1.5×10^{11} vg packaged in AAV-CAP-B10. Bottom half shows a representative data set collected from an animal that was coinjected with AAV-PHP.eB and AAV-CAP-B10. The left side displays the scRNA-seq data set in the lower dimensional tSNE space with cells colored according to transduction status. Shaded area indicates cluster with high expression of the corresponding gene marker. The right side shows representative confocal images of cortical tissue labeled with IHC. Scale bar, 50 µm. (B) Viral transcript recovery strategy. Shaded area highlights sequences added during library construction. (C) Data shown is the fraction of the total number of transduced cells expressing one of the three selected gene markers (NeuN, S100b or Olig2). For each AAV variant, a two-way ANOVA with correction for multiple comparisons using Sidak's test is reported with adjusted P values (****P≤0.0001, ***P≤0.001, **P≤0.01, is shown, and P>0.05 is not shown on the plot). (D) Comparison of transduction rates as measured based on quantification with scRNA-seq or IHC. Transduction rate is calculated as (number of transduced cells expressing gene marker)/(total number of cells expressing gene marker). Each dot represents the transduction rate of cells expressing either NeuN,

S100b or Olig2 for one animal. Histology data are averages across three brain slices per gene marker and animal. r indicates the Pearson correlation coefficient.

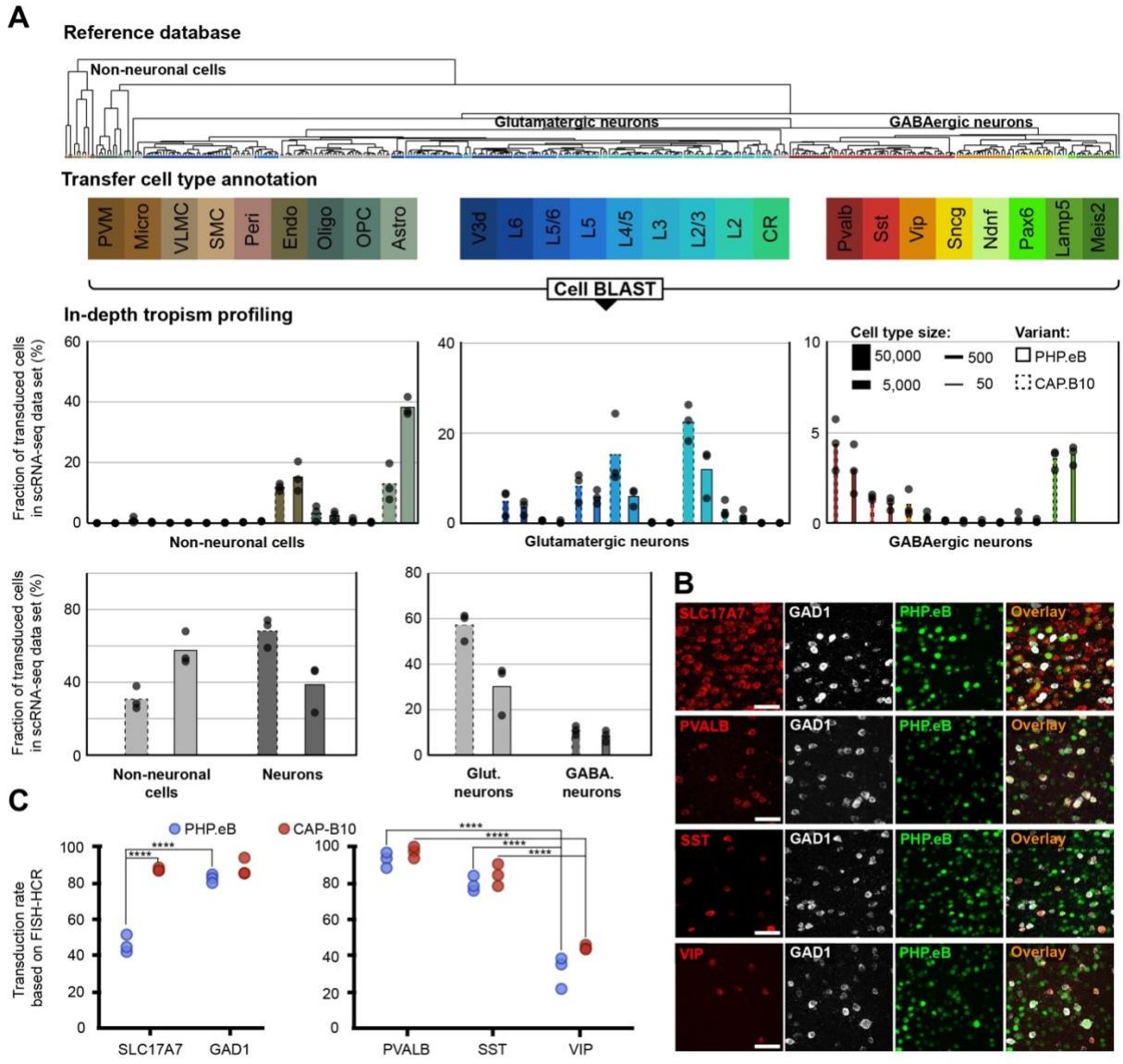

Figure 3. In-depth AAV tropism characterization at transcriptomic resolution. (A) Viral tropism profiling across cell and sub-cell types. Detailed cell annotation is transferred from a reference data set to our data set using the cell-querying method of Cell BLAST (Cao et al., 2020). Each dot represents data from one animal injected with AAV-PHP.eB and/or AAV-CAP-B10. Bar width indicates total number of cells of a particular cell type present in our data set. No V3d and Meis2 cells were detected in our data set. (B) Representative confocal images of cortical tissue from an animal injected with 1.5×10^{11} vg of AAV-PHP.eB. Tissue was labeled with FISH-HCR for gene markers of glutamatergic neurons (*Slc17a7*) and GABAergic neurons (*Gad1*, *Pvalb*, *Sst*, *Vip*). PHP.eB shows the endogenous fluorescence of mNeonGreen. Scale bar, 50 µm. (C) Confirmation of viral tropism biases across sub-cell types using FISH-HCR (3 mice per AAV

variant, 1.5×10^{11} vg dose). Dots represent average values across three brain slices of one animal. A two-way ANOVA with correction for multiple comparisons using Tukey's test is reported with adjusted P values (****$P \leq 0.0001$ is shown, and $P > 0.05$ is not shown on the plot).

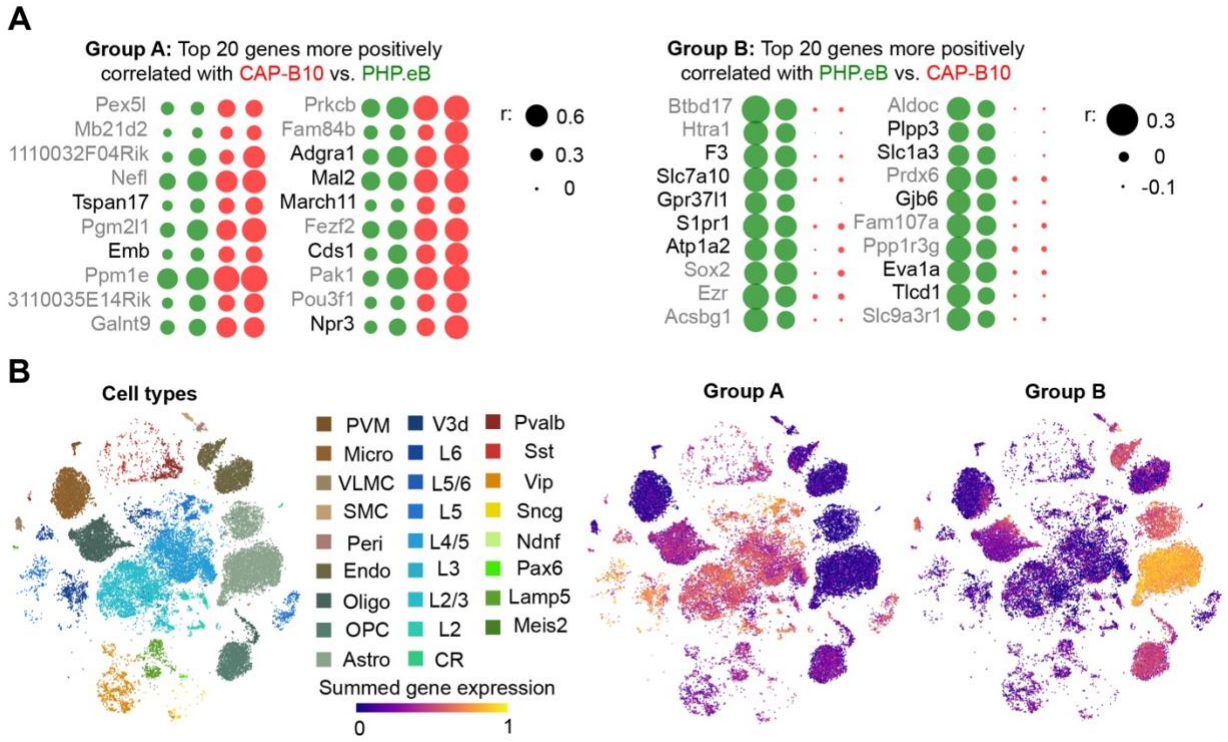

Figure 4. Analyzing single-gene cross-correlation in search of mechanistic insights. (A) Cross-correlation analysis of viral transgene and gene transcripts from animals coinjected with AAV-PHP.eB and AAV-CAP-B10. Shown are only the top 20 more positively correlated genes with either AAV variant. Genes expressing transmembrane proteins are highlighted in black. (B) First plot shows cells in the lower dimensional tSNE space and colored according to cell type annotation. The remaining two plots color cells according to the summed expression levels of all top 20 genes from either group A or B.

5.9 Supplementary figures

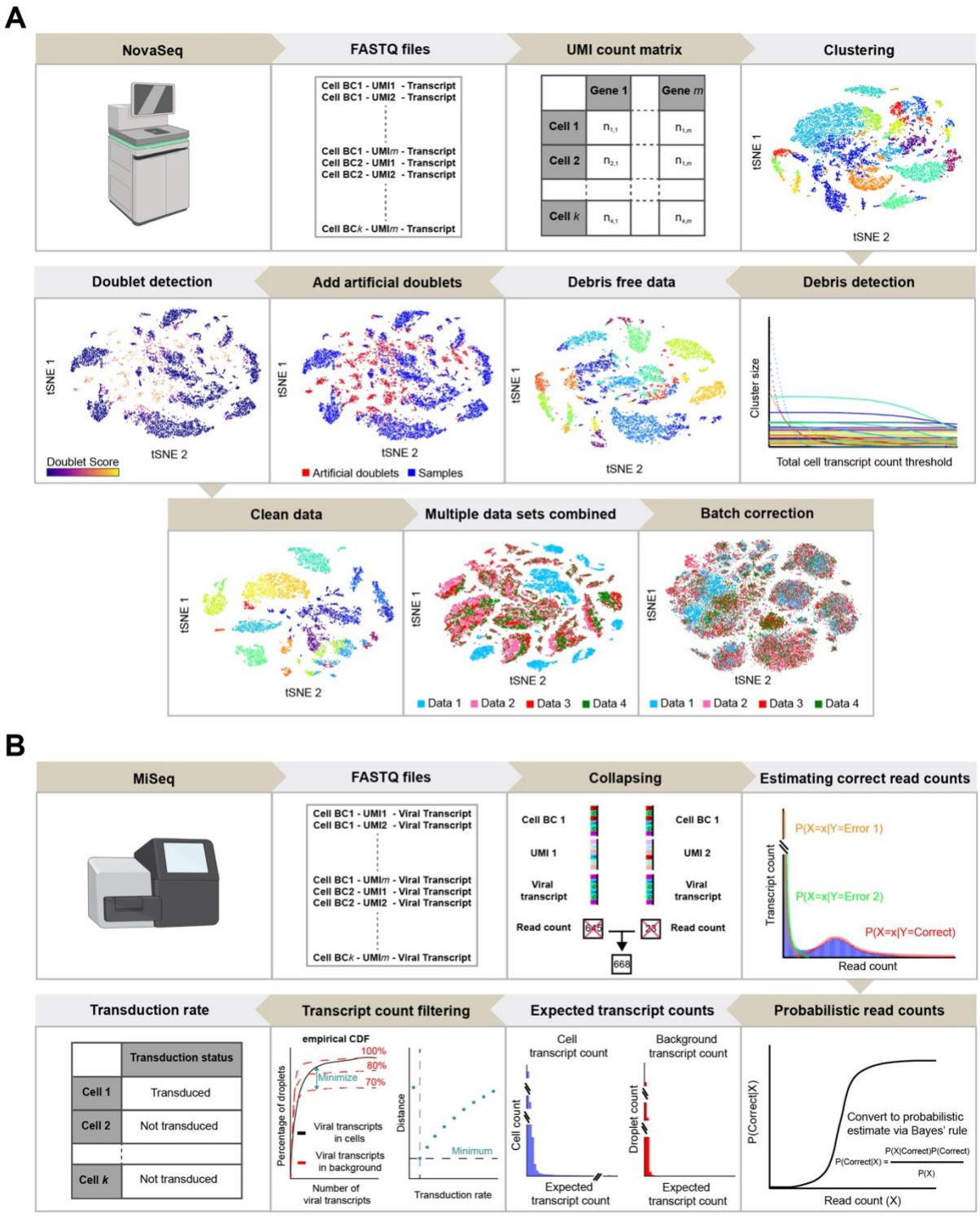

Figure S1. Data processing pipeline. (A) (I) Cell transcriptomes are sequenced on the NovaSeq 6000 system from Illumina. (II) Sequencing results are saved as FASTQ files. (III) Data from

FASTQ files is compiled into a unique molecular identifier (UMI) count matrix with genes as rows and cells (or barcodes) as columns. Matrix fields are the transcript (or UMI) counts for a given gene-cell pair. (IV) Agglomerative clustering is performed in a lower dimensional space. Cells of the same cell type cluster together, as do data points from droplets containing debris. (V) Plot shows decreasing cluster size with increasing threshold of total transcript count per cell. Debris clusters are identified by a strong decrease in cluster size at lower total transcript count thresholds. (VI) Debris free data visualized in lower dimensional tSNE space. (VII) Scrublet method (Wolock et al., 2019) creates artificial doublets by combining transcriptomes from two different cells. Data, together with artificial doublets, are shown in the lower dimensional tSNE space. (VIII) Cells are plotted in the lower dimensional tSNE space and colored according to the doublet score. Cells with a high doublet score are marked as doublets and excluded from the data set. (IX) Clean data set visualized in the lower dimensional tSNE space. (X) Multiple data sets visualized in the lower dimensional tSNE space. Certain clusters contain cells from only one data set due to batch effects. (XI) Cell BLAST algorithm (Cao et al., 2020) corrects batch effects such that distinct clusters represent distinct cell types as opposed to different data sets. (B) (I) Aliquots with cell transcriptomes and PCR amplified viral transcripts are sequenced on the MiSeq system from Illumina. (II) Sequencing results are saved as FASTQ files. (III) Sequences differing by one nucleotide are assumed to originate from the same parent sequence and their read counts are combined. (IV) One binomial and two negative binomial distributions are fitted to the read count histogram using maximum likelihood estimation. (V) Based on the fitted distribution, read counts are converted to probabilistic read counts. (VI) Probabilistic read counts yield expected viral transcript counts in droplets containing a cell and in droplets without cells (background). (VII) Empirical cumulative distribution functions (eCDF) of viral transcript counts in cells and in the background are generated and the distance between them is minimized to obtain a lower estimate of the number of transduced cells. (VIII) The final result is a table assigning a transduction status for each cell.

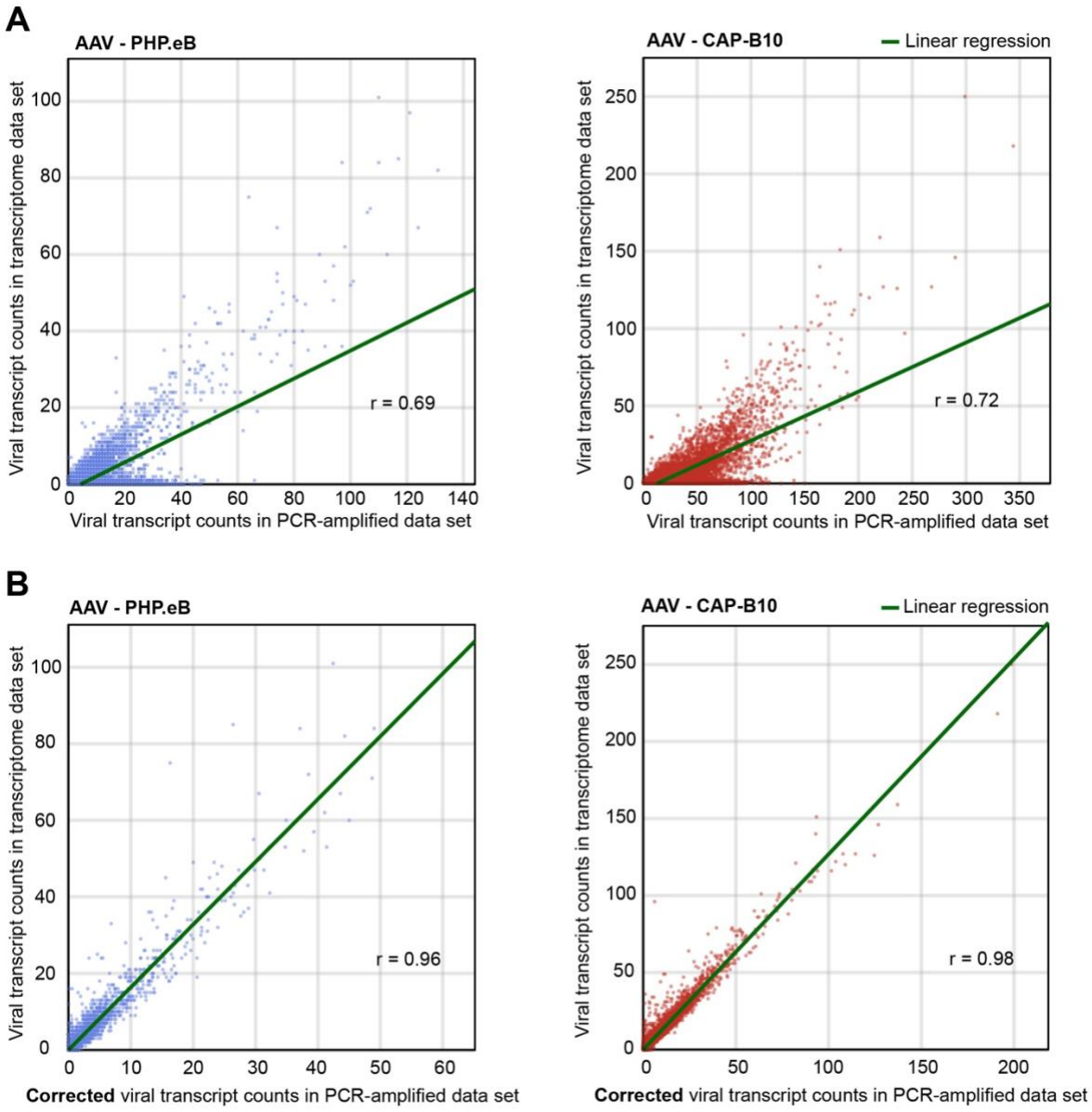

Figure S2. Data processing pipeline for PCR-amplified viral transcripts recovers correct viral transcripts. (A) Correlation of viral transcripts detected in cell transcriptome data set and viral transcripts detected in data set undergoing PCR amplification of viral transcripts. Introduction of sequence errors during PCR amplification creates artificial viral transcripts and increases overall transduction rate. Data shown are taken from data sets of single injections with either AAV-PHP.eB or AAV-CAP-B10. r indicates the Pearson correlation coefficient. (B) Similarly to (A), but with corrected viral transcript counts in PCR-amplified data set. Data processing (Figure S1 B) removes PCR amplification artefacts and recovers original viral transcript counts, but including now barcode

sequence information to distinguish different AAV variants. r indicates the Pearson correlation coefficient.

5.10 Methods

Animals

Animal husbandry and all experimental procedures involving animals were performed in accordance with the California Institute of Technology Institutional Animal Care and Use Committee (IACUC) guidelines and by the Office of Laboratory Animal Resources at the California Institute of Technology (animal protocol no. 1650). Male C57BL/6J mice (Stock No: 000664) used in this study were purchased from the Jackson Laboratory (JAX). The i.v. injection of AAV-PHP.eB and AAV-CAP-B10 was into the retro-orbital sinus of 6-7 weeks old mice.

ssAAV genomes

In vivo vector characterization of AAV-PHP.eB and AAV-CAP-B10 capsids was conducted using single-stranded (ss) rAAV genomes. pAAV:CAG-NLS-mNeonGreen and pAAV:CAG-NLS-tdTomato constructs were adapted from previous publications (Chan et al., 2017; Ravindra Kumar et al., 2020).

Viral production

We followed established protocols for the production of rAAVs (Challis et al., 2019). In short, HEK293T cells are triple transfected using polyethylenimine (PEI) with three plasmids: pAAV (see ssAAV genomes), pUCmini-iCAP-PHP.eB (Chan et al., 2017) or pUCmini-iCAP-CAP-B10 (Flytzanis et al., 2020), and pHelper. After 120 h, virus is harvested and purified using an iodixanol gradient (Optiprep, Sigma).

Tissue processing for single-cell suspension

After 3-4 weeks post injection, mice (9-10 weeks old) were briefly anaesthetized with isoflurane (5%) in an isolated plexiglass chamber followed by i.p. injection of euthasol (100 mg/kg). The following dissociation procedure of cortical tissue into a single-cell suspension was adapted with modifications from a previous report (Pool et al., 2020). Animals were transcardially perfused with ice-cold carbogenated (95% O_2 and 5% CO_2) NMDG-HEPES-ACSF (93 mM NMDG, 2.5 mM KCl, 1.2 mM NaH_2PO_4, 30 mM $NaHCO_3$, 20 mM HEPES, 25 mM glucose, 5 mM Na L-ascorbate, 2 mM thiourea, 3 mM Na-pyruvate, 10 mM $MgSO_4$, 1 mM $CaCl_2$, 1 mM kynurenic acid Na salt, pH adjusted to 7.35, osmolarity ranging 300-310 mOsm). Brains were rapidly extracted and cut in half

along the anterior-posterior axis with a razor blade. Half of the brain was used for histology using IHC while the second half of the brain was used for scRNA-seq. Tissue used for scRNA-seq was immersed in ice-cold NMDG-HEPES-ACSF while saturating with carbogen. The brain was sectioned into 300 µm slices using a vibratome (VT-1200, Leica Biosystems, IL, USA). Coronal sections starting from Bregma -0.94 mm to -2.80 mm were collected in a dissection dish on ice containing NMDG-HEPES-ACSF. Cortical tissue from the dorsal surface of the brain to ~3.5 mm ventral was cut out and further sliced into small tissue pieces. NMDG-HEPES-ACSF was replaced by trehalose-HEPES-ACSF (92 mM NaCl, 2.5 mM KCl, 1.2 mM NaH_2PO_4, 30 mM $NaHCO_3$, 20 mM HEPES, 25 mM glucose, 2 mM $MgSO_4$, 2 mM $CaCl_2$, 1 mM kynurenic acid Na salt, 0.025 mM D-(+)-trehalose dihydrate*$2H_2O$, pH adjusted to 7.35, osmolarity ranging 320-230 mOsm) containing papain (60 U/ml; P3125, Sigma Aldrich, pre-activated with 2.5 mM cysteine and a 0.5-1 h incubation at 34°C, supplemented with 0.5 mM EDTA) for the enzymatic digestion. Under gentle carbogenation, cortical tissue was incubated at 34°C for 50 min with soft agitation by pipetting every 10 min. 5 µl 2500 U/ml DNase I (04716728001 Roche, Sigma Aldrich) was added to the single-cell suspension 10 min before the end of the digestion. Solution was replaced with 200 µl trehalose-HEPES-ACSF containing 3 mg/ml ovomucoid inhibitor (OI-BSA, Worthington) and 1 µl DNase I. At room temperature, the digested cortical tissue was gently triturated with fire-polished glass Pasteur pipettes for three consecutive rounds with decreasing pipette diameters of 600, 300 and 150 µm. 800 µl of trehalose-HEPES-ACSF with 3 mg/ml ovomucoid inhibitor was added. The uniform single-cell suspension was pipetted through a 40 µm cell strainer (352340, Falcon) into a new microcentrifuge tube followed by centrifugation at 300 x g for 5 min at 4°C. Supernatant was discarded and cell pellet was resuspended in 1 ml of trehalose-HEPES-ACSF. After mixing using a Pasteur pipette with a 150 µm tip diameter, the single-cell suspension was centrifuged again. Supernatant was replaced with fresh trehalose-HEPES-ACSF and the resuspended cell pellet was strained with a 20 µm nylon net filter (NY2004700, Millipore). After resuspension in trehalose-HEPES-ACSF, cells were pelleted again and resuspended in 100 µl of ice-cold resuspension-ACSF (117 mM NaCl, 2.5 mM KCl, 1.2 mM NaH_2PO_4, 30 mM $NaHCO_3$, 20 mM HEPES, 25 mM glucose, 1 mM $MgSO_4$, 2 mM $CaCl_2$, 1 mM kynurenic acid Na salt and 0.05% BSA, pH adjusted to 7.35, osmolarity ranging 320-330 mOsm). Cells were counted with a hemocytometer and the final cell densities were verified to be in the range of 400-2,000 cells/µl. Density of single-cell suspension was adjusted with resuspension-ACSF if necessary.

Transcriptomic library construction

Cell suspension volumes containing 16,000 cells, which are expected to retrieve an estimated 10,000 single-cell transcriptomes, were added to the 10x Genomics RT reaction mix and loaded to the 10x Single Cell Chip B (2000168, 10x Genomics) per the manufacturer's protocol (Document CG000183, Revision C). We used the Chromium Single Cell 3' GEM Kit v3 (1000077, 10x Genomics) to recover and amplify cDNA, applying 11 rounds of amplification. We took 70 ng of cDNA and used the Chromium Single Cell 3' Library Kit (1000078) to prepare Illumina sequencing libraries downstream of reverse transcription following the manufacturer's protocol, applying 13 rounds of sequencing library amplification.

Viral library construction

We selectively amplified viral transcripts from 15 ng of cDNA using a cargo-specific primer binding to either mNeonGreen or tdTomato and a primer binding the partial Illumina Read 1 sequence present on the 10x capture oligos. For the single injection samples, amplification was performed only once using the primer for the delivered cargo; for dual injection animals, amplification was performed in parallel reactions from the same cDNA library using different cargo-specific primers for each reaction. We performed the amplification using 2x KAPA HiFi HotStart ReadyMix (KK2600) for 28 cycles at an annealing temperature of 53°C. Afterwards, we performed a left-sided SPRI cleanup at a concentration of 0.6X, in accordance with the manufacturer's protocol (SPRISelect, Beckman Coulter B23318). We then performed an overhang PCR on 100 ng of product with 15 cycles using primers that bind the cargo and the partial Illumina Read 1 sequence and appending the P5/P7 sequences and Illumina sample indices. We performed another 0.6X concentration SPRI cleanup, and analyzed the results via an Agilent High Sensitivity DNA Chip (Agilent 5067-4626).

- mNeonGreen: TAACTATCTGAAGAACCAGCCGATGTAC
- tdTomato: ACAACGAGGACTACACCATCGTGG
- partial Read 1: CTACACGACGCTCTTCCGATCT
- mNeonGreen overhang: CAAGCAGAAGACGGCATACGAGATNNNNNNNNGTGACTGGAGTTCAGACGTG

TGCTCTTCCGATCTTTCAAGGAGTGGCAAAAGGC (NNNNNNNN indicates Illumina sample index)

- tdTomato overhang: CAAGCAGAAGACGGCATACGAGANNNNNNNNCGTGACTGGAGTTCAGACGTG TGCTCTTCCGATCTGCATGGACGAGCTGTACAAG (NNNNNNNN indicates Illumina sample index)
- Read 1/P5: AATGATACGGCGACCACCGAGATCTACACTCTTTCCCTACACGACGCTCTTCC GAT

Sequencing

Transcriptome libraries were pooled together in equal molar ratios based on their DNA mass concentration and their mean transcript size as determined via bioanalyzer. Sequencing libraries were processed on a single Novaseq 6000 S4 300-cycle lane. The run was configured to read 150 bp from each end. Sequencing was outsourced to Fulgent Genetics and the UCSF Center for Advanced Technology.

Viral transcript libraries were pooled together in equal molar ratios into a 4 nM sequencing library, and diluted and denatured into a 12 pM library as per the manufacturer's protocol (Illumina Document #15039740v10). The resulting library was sequenced using a MiSeq v3 150-cycle reagent kit (MS-102-3001), configured to read 91 base pairs for Read 2 and 28 base pairs for Read 1. For characterizing the effect of sequencing depth, one viral transcript library was additionally processed independently on a separate MiSeq run.

Transcriptome read alignment

For transcriptome read alignment and gene expression quantification, we used 10x Cell Ranger v3.0.0 with default options to process the FASTQ files from the transcriptome sequencing library. The reads were aligned against the mus musculus reference provided by Cell Ranger (mm10 v1.2.0, based on Ensembl release 84).

Viral transcript read alignment

For viral read alignment, we aligned each Read 1 to a template derived from the plasmid. The template sequence was determined by starting at the ATG start site of the XFP cargo and ending at the AATAAA polyadenylation signal sequence. We used a Python implementation of the Striped Smith-Waterman algorithm from scikit-bio to calculate an alignment score for each read, and normalized the score by dividing by the maximum possible alignment score for a sequence of that length. For each Read 1 that had a normalized alignment score of greater than 0.9, we extracted the corresponding cell barcode and UMI from Read 2 for downstream processing.

Histology

Immunohistochemistry

Immunohistochemistry procedure was adapted from a previous publication (Oikonomou et al., 2019). Brain tissue was fixed in 4% paraformaldehyde (PFA) at 4°C overnight on a shaker. Samples were immersed in 30% sucrose in 1x phosphate buffered saline (PBS) solution for >2 days and then embedded in Tissue-Tek O.C.T. Compound (102094-104, VWR) before freezing in dry ice for 1 h. Samples were sectioned into 50 μm coronal slices on a cryostat (Leica Biosystems). Brain slices were washed once with 1x phosphate buffered saline (PBS) to remove O.C.T. Compound. Samples were then incubated overnight at 4°C on a shaker in a 1x PBS solution containing 0.1% Triton X-100, 10% normal goat serum (NGS; Jackson ImmunoResearch, PA, USA) and primary antibodies. Sections were washed three times for 15 min each in 1x PBS. Next, brain slices were incubated at 4°C overnight on a shaker in a 1x PBS solution containing 0.1% Triton X-100, 10% NGS and secondary antibodies. Sections were washed again three times for 15 min each in 1x PBS. Finally, slices were mounted on glass microscope slides (Adhesion Superfrost Plus Glass Slides, #5075-Plus, Brain Research Laboratories, MA, USA). After the brain slices dried, DAPI-containing mounting media (Fluoromount G with DAPI, 00-4959-52, eBioscience, CA, USA) was added before protecting the slices with a coverglass (Cover glass, #4860-1, Brain Research Laboratories, MA, USA). Confocal images were acquired on a Zeiss LSM 880 confocal microscope (Zeiss, Oberkochen, Germany). The following primary antibodies were used: rabbit monoclonal to NeuN (1:500; ab177487; Abcam, MA, USA), rabbit monoclonal to S100 beta (1:500; ab52642; Abcam, MA, USA), and rabbit monoclonal to Olig2 (1:500; ab109186; Abcam, MA, USA). The following

secondary antibodies were used: goat anti-rabbit IgG H&L Alexa Fluor 647 (1:500; ab150079; Abcam, MA, USA).

Fluorescent in situ hybridization chain reaction

FISH-HCR was conducted as previously reported (Patriarchi et al., 2018). Probes targeting neuronal markers were designed using a custom written software (https://github.com/GradinaruLab/HCRprobe). Probes contain a target sequence of 20 nucleotides, a spacer of 2 nucleotides, and an initiator sequence of 18 nucleotides. Criteria for the target sequences were: (1) a GC content between 45%-60%, (2) no nucleotide repeats more than three times, (3) no more than 20 hits when blasted, and (4) the ΔG had to be above -9 kcal/mol to avoid self-dimers. Last, the full probe sequence was blasted and the Smith-Waterman alignment score was calculated between all possible pairs to prevent the formation of cross-dimers. In total, we designed 26 probes for *Gad1*, 20 probes for *Vip*, 22 probes for *Pvalb*, 18 probes for *Sst*, and 28 probes for *Slc17a7*. Probes were synthesized by Integrated DNA Technologies.

Cell transcriptome sequencing data pre-processing

Major steps in the cell transcriptome sequencing data pre-processing pipeline are illustrated in Figure S1 A. Cells are excluded if the total number of transcript counts falls below 600. To remove remaining debris from the data, we reasoned that debris, similar to different cell types, would cluster together in a lower dimensional space. For this reason, we took the square root of all transcript counts in the gene count matrix, reduced the matrix to 20 dimensions using truncated singular value decomposition (SVD), and applied agglomerative clustering to obtain 30 clusters. Next, we incrementally increased the total transcript count threshold and removed cells with a total transcript count below the threshold. We noticed that this procedure identified debris clusters by a fast decrease in cluster size. Clusters dropping in size by half below a total transcript count threshold of 1500 are excluded from the data set. Beyond a simple transcript count threshold, this clustering-based procedure also enabled to detect debris with high total transcript counts. We adapted the Scrublet method (Wolock et al., 2019) to remove doublets from our data set. In brief, Scrublet simulates multiplets from our data set by artificially combining two cells and then builds a nearest neighbor classifier for detecting doublets in our data set. Overall, this data filtering procedure yielded 11,795 ± 956 cells with transcripts detected from 19,976 ± 346 genes per data set. Finally, for analysis

presented in Figures 2 and 3, we combined data sets from different scRNA-seq runs together and corrected for batch effects using the neural network-based generative models incorporated in the Cell BLAST method (Cao et al., 2020).

Viral transcript sequencing data pre-processing

Although PCR amplification of viral transcripts was necessary to profile the viral tropism of multiple AAV variants in parallel, it introduced sequence errors that had to be accounted for. Major steps in the viral transcript sequencing data pre-processing pipeline are illustrated in Figure S1 B. First, we collapsed read counts from sequences differing in one nucleotide. In dual injection animals, if the same cell barcode and UMI was detected for both viral transcripts, we also collapsed the smaller read count cell barcode/UMI combination into the larger one, since this likely arises from template switching during PCR. We next estimated the correct read counts by fitting one binomial and two negative binomial distributions to the read count histogram from our viral transcripts using maximum likelihood estimation. We modified the probability mass function for each distribution to be conditional on a count greater than 0, since we do not have access to the number of transcripts with 0 counts. Estimated correct read counts were converted to probabilistic read counts using Bayes' rule. Expected viral transcript counts were obtained from the probabilistic read counts. An additional source of noise were free floating viral transcripts that enter a droplet with an untransduced cell. We alleviated the impact of this noise by building an eCDF of viral transcripts in droplets devoid of cells and droplets containing cells. The distance between the two distributions was minimized to receive a lower estimate of the fraction of transduced cells.

Analysis of scRNA-seq data

scRNA-seq data sets were analyzed with custom-written scripts in Python 3.7.4. Annotation of transcriptomic cell types were transferred from a well-curated reference data set to our data sets using the cell-querying method of Cell BLAST (Cao et al., 2020). We used the Mouse Whole Cortex and Hippocampus 10x data set from the Allen Institute for Brain Science as our reference data set (Yao et al., 2020). The data set was subsampled to only contain at most 200 cells per cell type. Furthermore, cells are excluded if the tissue origin, based on the 'region_label' annotation provided in the table of cell metadata, is outside of the brain regions we collected from for our experiments. To ensure that overall enough cells are present per cell type in our data sets, we merged cell types

with common characteristics (e.g. expression of *Sst*) together according to the labels shown in Figure 3.

Quantification of images

Quantitative data analysis of confocal images was performed blind with regard to AAV capsid variant. Manual quantification was performed using the Cell Counter plugin, present in the Fiji distribution (Schindelin et al., 2012) of ImageJ (National Institutes of Health, Bethesda, MD). Transduction rate was calculated as the total number of double positive cells (i.e. viral transgene and cell type marker) divided by the total number of cell type marker labeled cells. For each brain slice, at least 100 cells positive for the gene markers of interest were counted in the cortex.

Statistics

Statistical analysis of the data was conducted using GraphPad Prism 8. No statistical methods were used to predetermine sample sizes. Statistical test applied, sample sizes and statistical significant effects are reported in each figure legend. The significance threshold was defined as $\alpha = 0.05$ ($P>0.05$; *$P<0.05$, **$P<0.01$, ***$P<0.001$, ****$P<0.0001$).

5.11 References

Achim, K., Pettit, J.-B., Saraiva, L.R., Gavriouchkina, D., Larsson, T., Arendt, D., and Marioni, J.C. (2015). High-throughput spatial mapping of single-cell RNA-seq data to tissue of origin. Nat. Biotechnol. *33*, 503–509.

Adachi, K., Enoki, T., Kawano, Y., Veraz, M., and Nakai, H. (2014). Drawing a high-resolution functional map of adeno-associated virus capsid by massively parallel sequencing. Nat. Commun. *5*, 3075.

Almeida, F.A., Suzuki, M., Scarborough, R.M., Lewicki, J.A., and Maack, T. (1989). Clearance function of type C receptors of atrial natriuretic factor in rats. Am. J. Physiol. *256*, R469–R475.

Arruda, V.R., Fields, P.A., Milner, R., Wainwright, L., De Miguel, M.P., Donovan, P.J., Herzog, R.W., Nichols, T.C., Biegel, J.A., Razavi, M., et al. (2001). Lack of germline transmission of vector sequences following systemic administration of recombinant AAV-2 vector in males. Mol. Ther. *4*, 586–592.

Bartlett, J.S., Kleinschmidt, J., Boucher, R.C., and Samulski, R.J. (1999). Targeted adeno-associated virus vector transduction of nonpermissive cells mediated by a bispecific F(ab'γ) 2 antibody. Nat. Biotechnol. *17*, 181–186.

Bedbrook, C.N., Deverman, B.E., and Gradinaru, V. (2018). Viral strategies for targeting the central and peripheral nervous systems. Annu. Rev. Neurosci. *41*, 323–348.

Cao, Z.-J., Wei, L., Lu, S., Yang, D.-C., and Gao, G. (2020). Searching large-scale scRNA-seq databases via unbiased cell embedding with Cell BLAST. Nat. Commun. *11*, 3458.

Challis, R.C., Kumar, S.R., Chan, K.Y., Challis, C., Beadle, K., Jang, M.J., Kim, H.M., Rajendran, P.S., Tompkins, J.D., Shivkumar, K., et al. (2019). Systemic AAV vectors for widespread and targeted gene delivery in rodents. Nat. Protoc. *14*, 379–414.

Chan, K.Y., Jang, M.J., Yoo, B.B., Greenbaum, A., Ravi, N., Wu, W.-L., Sánchez-Guardado, L., Lois, C., Mazmanian, S.K., Deverman, B.E., et al. (2017). Engineered AAVs for efficient noninvasive gene delivery to the central and peripheral nervous systems. Nat. Neurosci. *20*, 1172–1179.

Choi, H.M.T., Beck, V.A., and Pierce, N.A. (2014). Next-generation in situ hybridization chain reaction: Higher gain, lower cost, greater durability. ACS Nano *8*, 4284–4294.

Dalkara, D., Byrne, L.C., Klimczak, R.R., Visel, M., Yin, L., Merigan, W.H., Flannery, J.G., and Schaffer, D.V. (2013). In vivo-directed evolution of a new adeno-associated virus for therapeutic outer retinal gene delivery from the vitreous. Sci. Transl. Med. *5*, 189ra76.

Davidsson, M., Wang, G., Aldrin-Kirk, P., Cardoso, T., Nolbrant, S., Hartnor, M., Mudannayake, J., Parmar, M., and Björklund, T. (2019). A systematic capsid evolution approach performed in vivo

for the design of AAV vectors with tailored properties and tropism. Proc. Natl. Acad. Sci. U.S.A. *116*, 27053–27062.

Davis, A.S., Federici, T., Ray, W.C., Boulis, N.M., O'Connor, D., Clark, K.R., and Bartlett, J.S. (2015). Rational design and engineering of a modified adeno-associated virus (AAV1)-based vector system for enhanced retrograde gene delivery. Neurosurgery *76*, 216–225.

Daya, S., and Berns, K.I. (2008). Gene therapy using adeno-associated virus vectors. Clin. Microbiol. Rev. *21*, 583–593.

De Alencastro, G., Pekrun, K., Valdmanis, P., Tiffany, M., Xu, J., and Kay, M.A. (2020). Tracking adeno-associated virus capsid evolution by high-throughput sequencing. Hum. Gene Ther. *31*, 553–564.

Deleage, C., Wietgrefe, S.W., Del Prete, G., Morcock, D.R., Hao, X.P., Piatak, M., Bess, J., Anderson, J.L., Perkey, K.E., Reilly, C., et al. (2016). Defining HIV and SIV reservoirs in lymphoid tissues. Pathog. Immun. *1*, 68–106.

Deleage, C., Chan, C.N., Busman-Sahay, K., and Estes, J.D. (2018). Next-generation in situ hybridization approaches to define and quantify HIV and SIV reservoirs in tissue microenvironments. Retrovirology *15*, 4.

Deverman, B.E., Pravdo, P.L., Simpson, B.P., Kumar, S.R., Chan, K.Y., Banerjee, A., Wu, W.L., Yang, B., Huber, N., Pasca, S.P., et al. (2016). Cre-dependent selection yields AAV variants for widespread gene transfer to the adult brain. Nat. Biotechnol. *34*, 204–209.

Deverman, B.E., Ravina, B.M., Bankiewicz, K.S., Paul, S.M., and Sah, D.W.Y. (2018). Gene therapy for neurological disorders: Progress and prospects. Nat. Rev. Drug Discov. *17*, 641–659.

Durruthy-Durruthy, R., Gottlieb, A., and Heller, S. (2015). 3D computational reconstruction of tissues with hollow spherical morphologies using single-cell gene expression data. Nat. Protoc. *10*, 459–474.

Excoffon, K.J.D.A., Koerber, J.T., Dickey, D.D., Murtha, M., Keshavjee, S., Kaspar, B.K., Zabner, J., and Schaffer, D.V. (2009). Directed evolution of adeno-associated virus to an infectious respiratory virus. Proc. Natl. Acad. Sci. U.S.A. *106*, 3865–3870.

Femino, A.M., Fay, F.S., Fogarty, K., and Singer, R.H. (1998). Visualization of single RNA transcripts in situ. Science *280*, 585–590.

Flytzanis, N.C., Goeden, N., Goertsen, D., Cummins, A., Pickel, J., and Gradinaru, V. (2020). Broad gene expression throughout the mouse and marmoset brain after intravenous delivery of engineered AAV capsids. bioRxiv. https://doi.org/10.1101/2020.06.16.152975.

Gaj, T., Epstein, B.E., and Schaffer, D.V. (2016). Genome engineering using adeno-associated virus: Basic and clinical research applications. Mol. Ther. *24*, 458–464.

Grabinski, T.M., Kneynsberg, A., Manfredsson, F.P., and Kanaan, N.M. (2015). A method for combining RNAscope in situ hybridization with immunohistochemistry in thick free-floating brain sections and primary neuronal cultures. PLoS One *10*, e0120120.

Grimm, D., Lee, J.S., Wang, L., Desai, T., Akache, B., Storm, T.A., and Kay, M.A. (2008). In vitro and in vivo gene therapy vector evolution via multispecies interbreeding and retargeting of adeno-associated viruses. J. Virol. *82*, 5887–5911.

Halpern, K.B., Shenhav, R., Matcovitch-Natan, O., Tóth, B., Lemze, D., Golan, M., Massasa, E.E., Baydatch, S., Landen, S., Moor, A.E., et al. (2017). Single-cell spatial reconstruction reveals global division of labour in the mammalian liver. Nature *542*, 352–356.

Herrmann, A.-K., Bender, C., Kienle, E., Grosse, S., El Andari, J., Botta, J., Schürmann, N., Wiedtke, E., Niopek, D., and Grimm, D. (2019). A robust and all-inclusive pipeline for shuffling of adeno-associated viruses. ACS Synth. Biol. *8*, 194–206.

Hinderer, C., Katz, N., Buza, E.L., Dyer, C., Goode, T., Bell, P., Richman, L.K., and Wilson, J.M. (2018). Severe toxicity in nonhuman primates and piglets following high-dose intravenous administration of an adeno-associated virus vector expressing human SMN. Hum. Gene Ther. *29*, 285–298.

Huang, K.W., and Sabatini, B.L. (2020). Single-cell analysis of neuroinflammatory responses following intracranial injection of G-deleted rabies viruses. Front. Cell. Neurosci. *14*, 65.

Hunter, J.E., Gurda, B.L., Yoon, S.Y., Castle, M.J., and Wolfe, J.H. (2019). In situ hybridization for detection of AAV-mediated gene expression. Methods Mol. Biol. *1950*, 107–122.

Jordão, M.J.C., Sankowski, R., Brendecke, S.M., Sagar, Locatelli, G., Tai, Y.-H., Tay, T.L., Schramm, E., Armbruster, S., Hagemeyer, N., et al. (2019). Single-cell profiling identifies myeloid cell subsets with distinct fates during neuroinflammation. Science *363*, eaat7554.

Körbelin, J., Dogbevia, G., Michelfelder, S., Ridder, D.A., Hunger, A., Wenzel, J., Seismann, H., Lampe, M., Bannach, J., Pasparakis, M., et al. (2016a). A brain microvasculature endothelial cell-specific viral vector with the potential to treat neurovascular and neurological diseases. EMBO Mol. Med. *8*, 609–625.

Körbelin, J., Sieber, T., Michelfelder, S., Lunding, L., Spies, E., Hunger, A., Alawi, M., Rapti, K., Indenbirken, D., Müller, O.J., et al. (2016b). Pulmonary targeting of adeno-associated viral vectors by next-generation sequencing-guided screening of random capsid displayed peptide libraries. Mol. Ther. *24*, 1050–1061.

Kotterman, M.A., and Schaffer, D.V. (2014). Engineering adeno-associated viruses for clinical gene therapy. Nat. Rev. Genet. *15*, 445–451.

Lee, E.J., Guenther, C.M., and Suh, J. (2018). Adeno-associated virus (AAV) vectors: Rational design strategies for capsid engineering. Curr. Opin. Biomed. Eng. *7*, 58–63.

Lein, E., Borm, L.E., and Linnarsson, S. (2017). The promise of spatial transcriptomics for neuroscience in the era of molecular cell typing. Science *358*, 64–69.

Li, Q., Cheng, Z., Zhou, L., Darmanis, S., Neff, N.F., Okamoto, J., Gulati, G., Bennett, M.L., Sun, L.O., Clarke, L.E., et al. (2019). Developmental heterogeneity of microglia and brain myeloid cells revealed by deep single-cell RNA sequencing. Neuron *101*, 207-223.e10.

Liao, J., Lu, X., Shao, X., Zhu, L., and Fan, X. (2020). Uncovering an organ's molecular architecture at single-cell resolution by spatially resolved transcriptomics. Trends Biotechnol. *39*, 43–58.

Maack, T., Suzuki, M., Almeida, F.A., Nussenzveig, D., Scarborough, R.M., McEnroe, G.A., and Lewicki, J.A. (1987). Physiological role of silent receptors of atrial natriuretic factor. Science *238*, 675–678.

Maheshri, N., Koerber, J.T., Kaspar, B.K., and Schaffer, D.V. (2006). Directed evolution of adeno-associated virus yields enhanced gene delivery vectors. Nat. Biotechnol. *24*, 198–204.

de Marco, M.C., Martín-Belmonte, F., Kremer, L., Albar, J.P., Correas, I., Vaerman, J.P., Marazuela, M., Byrne, J.A., and Alonso, M.A. (2002). MAL2, a novel raft protein of the MAL family, is an essential component of the machinery for transcytosis in hepatoma HepG2 cells. J. Cell Biol. *159*, 37–44.

Masuda, T., Sankowski, R., Staszewski, O., Böttcher, C., Amann, L., Sagar, Scheiwe, C., Nessler, S., Kunz, P., van Loo, G., et al. (2019). Spatial and temporal heterogeneity of mouse and human microglia at single-cell resolution. Nature *566*, 388–392.

Mével, M., Bouzelha, M., Leray, A., Pacouret, S., Guilbaud, M., Penaud-Budloo, M., Alvarez-Dorta, D., Dubreil, L., Gouin, S.G., Combal, J.P., et al. (2020). Chemical modification of the adeno-associated virus capsid to improve gene delivery. Chem. Sci. *11*, 1122–1131.

Meyer, R.C., Giddens, M.M., Schaefer, S.A., and Hall, R.A. (2013). GPR37 and GPR37L1 are receptors for the neuroprotective and glioprotective factors prosaptide and prosaposin. Proc. Natl. Acad. Sci. U.S.A. *110*, 9529–9534.

Miao, C.H., Nakai, H., Thompson, A.R., Storm, T.A., Chiu, W., Snyder, R.O., and Kay, M.A. (2000). Nonrandom transduction of recombinant adeno-associated virus vectors in mouse hepatocytes in vivo: Cell cycling does not influence hepatocyte transduction. J. Virol. *74*, 3793–3803.

Mrdjen, D., Pavlovic, A., Hartmann, F.J., Schreiner, B., Utz, S.G., Leung, B.P., Lelios, I., Heppner, F.L., Kipnis, J., Merkler, D., et al. (2018). High-dimensional single-cell mapping of central nervous system immune cells reveals distinct myeloid subsets in health, aging, and disease. Immunity *48*, 380-395.e6.

Müller, O.J., Kaul, F., Weitzman, M.D., Pasqualini, R., Arap, W., Kleinschmidt, J.A., and Trepel, M. (2003). Random peptide libraries displayed on adeno-associated virus to select for targeted gene therapy vectors. Nat. Biotechnol. *21*, 1040–1046.

Naso, M.F., Tomkowicz, B., Perry, W.L., and Strohl, W.R. (2017). Adeno-associated virus (AAV) as a vector for gene therapy. BioDrugs *31*, 317–334.

Nitzan, M., Karaiskos, N., Friedman, N., and Rajewsky, N. (2019). Gene expression cartography. Nature *576*, 132–137.

Ogden, P.J., Kelsic, E.D., Sinai, S., and Church, G.M. (2019). Comprehensive AAV capsid fitness landscape reveals a viral gene and enables machine-guided design. Science *366*, 1139–1143.

Oikonomou, G., Altermatt, M., Zhang, R., Coughlin, G.M., Montz, C., Gradinaru, V., and Prober, D.A. (2019). The serotonergic raphe promote sleep in zebrafish and mice. Neuron *103*, 686-701.e8.

Ojala, D.S., Sun, S., Santiago-Ortiz, J.L., Shapiro, M.G., Romero, P.A., and Schaffer, D.V. (2018). In vivo selection of a computationally designed SCHEMA AAV library yields a novel variant for infection of adult neural stem cells in the SVZ. Mol. Ther. *26*, 304–319.

Patriarchi, T., Cho, J.R., Merten, K., Howe, M.W., Marley, A., Xiong, W.-H., Folk, R.W., Broussard, G.J., Liang, R., Jang, M.J., et al. (2018). Ultrafast neuronal imaging of dopamine dynamics with designed genetically encoded sensors. Science *360*, eaat4422.

Paulk, N.K., Pekrun, K., Zhu, E., Nygaard, S., Li, B., Xu, J., Chu, K., Leborgne, C., Dane, A.P., Haft, A., et al. (2018). Bioengineered AAV capsids with combined high human liver transduction in vivo and unique humoral seroreactivity. Mol. Ther. *26*, 289–303.

Pekrun, K., De Alencastro, G., Luo, Q.-J., Liu, J., Kim, Y., Nygaard, S., Galivo, F., Zhang, F., Song, R., Tiffany, M.R., et al. (2019). Using a barcoded AAV capsid library to select for clinically relevant gene therapy vectors. JCI Insight *4*, e131610.

Polinski, N.K., Gombash, S.E., Manfredsson, F.P., Lipton, J.W., Kemp, C.J., Cole-Strauss, A., Kanaan, N.M., Steece-Collier, K., Kuhn, N.C., Wohlgenant, S.L., et al. (2015). Recombinant adenoassociated virus 2/5-mediated gene transfer is reduced in the aged rat midbrain. Neurobiol. Aging *36*, 1110–1120.

Polinski, N.K., Manfredsson, F.P., Benskey, M.J., Fischer, D.L., Kemp, C.J., Steece-Collier, K., Sandoval, I.M., Paumier, K.L., and Sortwell, C.E. (2016). Impact of age and vector construct on striatal and nigral transgene expression. Mol. Ther. Methods Clin. Dev. *3*, 16082.

Pool, A.-H., Wang, T., Stafford, D.A., Chance, R.K., Lee, S., Ngai, J., and Oka, Y. (2020). The cellular basis of distinct thirst modalities. Nature *588*, 112–117.

Pulicherla, N., Shen, S., Yadav, S., Debbink, K., Govindasamy, L., Agbandje-McKenna, M., and Asokan, A. (2011). Engineering liver-detargeted AAV9 vectors for cardiac and musculoskeletal gene transfer. Mol. Ther. *19*, 1070–1078.

Puray-Chavez, M., Tedbury, P.R., Huber, A.D., Ukah, O.B., Yapo, V., Liu, D., Ji, J., Wolf, J.J., Engelman, A.N., and Sarafianos, S.G. (2017). Multiplex single-cell visualization of nucleic acids and protein during HIV infection. Nat. Commun. *8*, 1882.

Ravindra Kumar, S., Miles, T.F., Chen, X., Brown, D., Dobreva, T., Huang, Q., Ding, X., Luo, Y., Einarsson, P.H., Greenbaum, A., et al. (2020). Multiplexed Cre-dependent selection yields systemic AAVs for targeting distinct brain cell types. Nat. Methods *17*, 541–550.

Rosenberg, A.B., Roco, C.M., Muscat, R.A., Kuchina, A., Sample, P., Yao, Z., Graybuck, L.T., Peeler, D.J., Mukherjee, S., Chen, W., et al. (2018). Single-cell profiling of the developing mouse brain and spinal cord with split-pool barcoding. Science *360*, 176–182.

Samulski, R.J., and Muzyczka, N. (2014). AAV-mediated gene therapy for research and therapeutic purposes. Annu. Rev. Virol. *1*, 427–451.

Satija, R., Farrell, J.A., Gennert, D., Schier, A.F., and Regev, A. (2015). Spatial reconstruction of single-cell gene expression data. Nat. Biotechnol. *33*, 495–502.

Schindelin, J., Arganda-Carreras, I., Frise, E., Kaynig, V., Longair, M., Pietzsch, T., Preibisch, S., Rueden, C., Saalfeld, S., Schmid, B., et al. (2012). Fiji: An open-source platform for biological-image analysis. Nat. Methods *9*, 676–682.

Sen, D. (2014). Improving clinical efficacy of adeno associated vectors by rational capsid bioengineering. J. Biomed. Sci. *21*, 103.

Srivastava, A. (2020). AAV vectors: Are they safe? Hum. Gene Ther. *31*, 697–699.

Stuart, T., Butler, A., Hoffman, P., Hafemeister, C., Papalexi, E., Mauck, W.M., Hao, Y., Stoeckius, M., Smibert, P., and Satija, R. (2019). Comprehensive integration of single-cell data. Cell *177*, 1888-1902.e21.

Tasic, B., Menon, V., Nguyen, T.N., Kim, T.K., Jarsky, T., Yao, Z., Levi, B., Gray, L.T., Sorensen, S.A., Dolbeare, T., et al. (2016). Adult mouse cortical cell taxonomy revealed by single cell transcriptomics. Nat. Neurosci. *19*, 335–346.

Tasic, B., Yao, Z., Graybuck, L.T., Smith, K.A., Nguyen, T.N., Bertagnolli, D., Goldy, J., Garren, E., Economo, M.N., Viswanathan, S., et al. (2018). Shared and distinct transcriptomic cell types across neocortical areas. Nature *563*, 72–78.

Tervo, D.G., Hwang, B.Y., Viswanathan, S., Gaj, T., Lavzin, M., Ritola, K.D., Lindo, S., Michael, S., Kuleshova, E., Ojala, D., et al. (2016). A designer AAV variant permits efficient retrograde access to projection neurons. Neuron *92*, 372–382.

Wang, S.K., Lapan, S.W., Hong, C.M., Krause, T.B., and Cepko, C.L. (2020). In situ detection of adeno-associated viral vector genomes with SABER-FISH. Mol. Ther. Methods Clin. Dev. *19*, 376–386.

Wang, X., Allen, W.E., Wright, M.A., Sylwestrak, E.L., Samusik, N., Vesuna, S., Evans, K., Liu, C., Ramakrishnan, C., Liu, J., et al. (2018). Three-dimensional intact-tissue sequencing of single-cell transcriptional states. Science *361*, eaat5691.

Weinmann, J., Weis, S., Sippel, J., Tulalamba, W., Remes, A., El Andari, J., Herrmann, A.-K., Pham, Q.H., Borowski, C., Hille, S., et al. (2020). Identification of a myotropic AAV by massively parallel in vivo evaluation of barcoded capsid variants. Nat. Commun. *11*, 5432.

Wilson, J.M., and Flotte, T.R. (2020). Moving forward after two deaths in a gene therapy trial of myotubular myopathy. Hum. Gene Ther. *31*, 695–696.

Wolock, S.L., Lopez, R., and Klein, A.M. (2019). Scrublet: Computational identification of cell doublets in single-cell transcriptomic data. Cell Syst. *8*, 281-291.e9.

Wu, Z., Asokan, A., and Samulski, R.J. (2006). Adeno-associated virus serotypes: Vector toolkit for human gene therapy. Mol. Ther. *14*, 316–327.

Yao, Z., Nguyen, T.N., Velthoven, C.T.J. van, Goldy, J., Sedeno-Cortes, A.E., Baftizadeh, F., Bertagnolli, D., Casper, T., Crichton, K., Ding, S.-L., et al. (2020). A taxonomy of transcriptomic cell types across the isocortex and hippocampal formation. bioRxiv. https://doi.org/10.1101/2020.03.30.015214.

Ying, Y., Müller, O.J., Goehringer, C., Leuchs, B., Trepel, M., Katus, H.A., and Kleinschmidt, J.A. (2010). Heart-targeted adeno-associated viral vectors selected by in vivo biopanning of a random viral display peptide library. Gene Ther. *17*, 980–990.

Zeisel, A., Muñoz-Manchado, A.B., Codeluppi, S., Lönnerberg, P., Manno, G.L., Juréus, A., Marques, S., Munguba, H., He, L., Betsholtz, C., et al. (2015). Cell types in the mouse cortex and hippocampus revealed by single-cell RNA-seq. Science *347*, 1138–1142.

Zeisel, A., Hochgerner, H., Lönnerberg, P., Johnsson, A., Memic, F., van der Zwan, J., Häring, M., Braun, E., Borm, L.E., La Manno, G., et al. (2018). Molecular architecture of the mouse nervous system. Cell *174*, 999-1014.e22.

Zhang, X., Lu, W., Zheng, Y., Wang, W., Bai, L., Chen, L., Feng, Y., Zhang, Z., and Yuan, Z. (2016). In situ analysis of intrahepatic virological events in chronic hepatitis B virus infection. J. Clin. Invest. *126*, 1079–1092.

Zhao, J., Yue, Y., Patel, A., Wasala, L., Karp, J.F., Zhang, K., Duan, D., and Lai, Y. (2020). High-resolution histological landscape of AAV DNA distribution in cellular compartments and tissues following local and systemic injection. Mol. Ther. Methods Clin. Dev. *18*, 856–868.

Zheng, G.X.Y., Terry, J.M., Belgrader, P., Ryvkin, P., Bent, Z.W., Wilson, R., Ziraldo, S.B., Wheeler, T.D., McDermott, G.P., Zhu, J., et al. (2017). Massively parallel digital transcriptional profiling of single cells. Nat. Commun. *8*, 14049.